POLITECNICO DI MILANO
Dottorato di Ricerca in Bioingegneria
Ph.D. in Bioengineering

Multiscale, Multiphysics and Reduced Order Modelling Techniques for Hemodynamics

Jeroen Feher

Supervisor: *Ph.D. Coordinator:*
Prof. Dr. Gabriele Dubini   Prof. Dr. Andrea Aliverti

Advisor:
Dr. Valery Morgenthaler

XXXI Cycle

Abstract

Usage of numerical modelling techniques in a clinical setting is limited due to the computational resources and modelling expertise required. This thesis focuses on multiscale modelling and model order reduction as tools to reduce the computational cost and improving model robustness of hemodynamical models. Firstly, it is shown, using data for an aortic flow phantom, that integration of patient-specific data favours a multiscale approach due to measurement uncertainties leading to a violation of the conservation of mass and momentum. Stability of different multiscale model coupling schemes for partitioned modelling is addressed, demonstrating the superior stability of central-difference based schemes compared to more traditional explicit and semi-implicit schemes. This is highly relevant for the application of large artery modelling due to the potentially large number of models coupled simultaneously, including boundary condition models and Fluid-structure interaction (FSI). A compressible fluid model capable of representing wave propagation at reduced cost is analysed in order to suggest improvements for increased accuracy. Additionally, this part considers the limitations and functional difference between a 1D wave propagation, compressible fluid and 2-way FSI model. Lastly, a proof of concept is given for reduced order models (ROMs) of 3D field data in medicine using a singular value decomposition based approach. Effects of the choice and normalisation of training data on the SVD basis and ROM are explored. This ultimately leads to generation of a 3D transient ROM of the pressure field within a sudden expansion at an average percentual error of $0.45[\%]$.

Acknowledgements

4 years of study, work and travel have led to this thesis, which would have never been possible without the countless people I've met along the way.

I would like to thank my supervisors Prof. Gabriele Dubini at Politecnico di Milano and Dr. Valery Morgenthaler and Dr. Michel Rochette at ANSYS France SAS in Lyon, for their invaluable support, patience and providing me the opportunity to do this PhD. I am especially thankful to Valery for the many discussions we've had and for him putting up with the even greater amount of (highly enjoyable) nonsense debates.

My thanks extend to the many international teams I have had the pleasure to work with during these years. This project was part of the VPH-CaSE Marie Sklodowska-Curie ITN and coordinated by my former colleagues at the University of Sheffield, allowing me to meet the many wonderful researchers involved in this project. Secondly, I would like to thank my colleagues at ANSYS, France in Lyon and the members of the research team, past and present, for making me feel welcome into their group these past years.

Finally, I would like to thank my family and friends of whom there are too many to mention all by name. My parents for always supporting me no matter how good or bad things got. My many friends in Lyon for making sure my thoughts weren't always at work, kidnapping me to go on our many outdoor trips and for showing me every bar in Lyon. Additionally, I would like to thank my many friends in

Sheffield, in particular Aline, Kate and Amy, for keeping me in good spirits, providing me the strength to finish this thesis and making me feel like family in the process. Thank you all. Without your help I would have never been able to arrive at this point.

Contents

Glossary of acronyms

Asc	Ascending Aorta
BC	Boundary Condition
CAD	Computer Aided Design
CFL	Courant-Friedrichs-Lewy number
ceBP	Central aortic Blood Pressure
CFD	Computational Fluid Dynamics
CT	Computed Tomography
CVD	Cardiovascular Disease
Dsc	Descending Aorta
FOM	Full Order Model
FSI	Fluid-Structure Interaction
GUI	Graphical User Interface
HPC	High Performance Computing
Lca	Left Carotid Artery
Lsa	Left Subclavian Artery
MRI	Magnetic Resonance Imaging
Rca	Right Carotid Artery
Rsa	Right Subclavian Artery
RMS	Root Mean Square
ROM	Reduced Order Model
SVD	Singular Value Decomposition
TUI	Text User Interface
WK	Windkessel

List of Figures

XIV

List of tables

Chapter 1

1. Introduction

1.1. Motivation

The field of cardiovascular medicine has progressed greatly during the 20th and 21st century leading to advances in many different fields of scientific research. Cardiovascular modelling and simulation is one of those fields able to aid greatly in diagnosis, risk assessment and treatment planning. As medicine moves evermore in the direction of personalised medicine, it is becoming increasingly important to be able to provide individualised care within a reasonable timeframe and at minimal cost. For cardiovascular models to be useful in this clinical setting it is necessary to have robust model implementations and consider model order reduction techniques to speed up their evaluation. Therefore, this work is dedicated to studying cardiovascular model stability and order reduction to facilitate the translation of scientific advancement to real-world applications. The introduction below serves to introduce the general concepts treated in the remainder of the text.

1.2. Cardiovascular diseases

Cardiovascular diseases(CVDs) remain the main cause of death in many parts of the world [1, 2] and include all diseases affecting the human circulatory system. As an example, prevalence of CVDs in the United States was around 48% in 2016. Trends for prevalence of- and death rates due to CVDs however, show a decline, resulting in CVDs no longer being the leading cause of death in Western Europe [3]. However, recent evidence suggests the rate of decline is decreasing in North America and that CVDs are still the main cause of death worldwide [4]. Nevertheless, the burden of CVDs remains significant as demonstrated by the loss

of 64 million disability adjusted life years in Europe alone, a measure for the years in life lost due to disability or dying prematurely. In the opinion of the author, the real objective in medicine should not just be to prolong people's lives but to prevent premature loss of life while providing people a better quality of life than they would have had otherwise.

Trends of decline up till now, are in part attributable to risk factor modification, i.e. improvements in lifestyle choices including better dietary and exercise regimes as well as reductions in smoking rates. Aside from preventative strategies, better medical care has contributed to improved outcomes for patients affected by CVDs, with a reduction of mortality rates and an increase in hospital discharge rates overall [5] [1] [3]. However, it should be noted that these outcomes are heavily region and disease dependent.

The most prevalent CVDs include Ischaemic heart disease and stroke. As the field of CVDs is incredibly broad, it is outside the current scope to discuss individual diseases in detail. The focus of this thesis is on the dynamics within large arteries including aortic and peripheral artery diseases.

1.3. Cardiovascular physiology

The cardiovascular system functions as the body's main transport system for substances including oxygen, nutrients and waste products [6]. At the organ level, a set of pulsatile pumps, the left and right chambers of the heart, pump fluid through two networks of vessels, namely the systemic and pulmonary circulation. Both

circulations consist of an arterial part, transporting blood towards the tissues and a venous part transporting blood away from the tissues to the heart. At the microscopic level, exchange of substances takes place in the capillaries which are part of the microcirculation.

All remaining vessels between the heart and the capillaries are essentially conduits transporting blood from the heart to the tissue's capillaries. Each heartbeat, blood gets expelled at high velocity and pressure, into the large arteries of both circulations to be transported elsewhere in the body. In the capillaries, the pulsatile character of the flow is no longer present and blood flow is almost constant. As such, the main function of the larger arteries is to act as a passive pump, i.e. to store blood at sufficient pressure in order to provide a constant capillary flow from heartbeat to heartbeat.

The difference in function at different scales, leads to different structural requirements and composition of each part. Blood vessels are composed of different layers or tunics, namely the tunica intima, tunica media and tunica externa [6, 7]. The intima is the innermost layer consisting out of a layer of endothelium and connective tissue making contact with the blood. The media consists mainly of smooth muscle cells, elastin and collagen and is the main determinant of the structural properties of a vessel. Lastly the externa consists mainly of collagen and serves as a support anchor to surrounding tissues as well as protection of the vessel. Vascular walls therefore consist of a composite material and are known to exhibit

non-linear, viscoelastic and anisotropic behaviour [8, 9]. For the current work, a simplification is made neglecting these non-linear characteristics and the reader is encouraged to read the work of Fung 1993 [10] for a more thorough introduction to the subject.

Because the function of the capillaries is to facilitate a fast exchange of substances, the average blood pressure and flow velocity are low and the blood vessel wall consists almost solely out of a single layer of endothelium and they consist only out of the tunica intima. As a result, these vessels are relatively in-elastic. On the other hand, large arteries closer to the heart need to be able to expand to store blood and pressure energy. Elastin is the component allowing blood vessels to expand [10] and as such large arteries have a high proportion of tunica media.

The ability of a vessel to distend due to internal pressure is called the compliance of the vessel and is defined as the volume change of the lumen per unit pressure change [7]. Vessel compliance introduces the phenomenon of pressure and flow wave propagation. Were the vessel non-compliant, any pressure and flow waves would travel at the speed of sound of the fluid, which for blood is of order $O(10^3)$ [m s^{-1}] [11]. Whereas in reality the wave velocity is in the order of magnitude of $O(1\sim10)$[m s^{-1}] [12]. The vessel's compliance additionally has a dampening effect. In the absence of vessel compliance the heart would need to output more work due to an increased after load, the heart would need to accelerate all the fluid in the cardiovascular system with every heartbeat and [13]. And in fact, it has been found

in many instances that vascular stiffening can lead to pathologies including hypertension, promotion of atherosclerosis, myocardial hypertrophy and heart failure [14, 15, 16].

1.4. model order reduction techniques need

The use of 2D or 3D modelling and simulations can provide detailed local descriptions of physical quantities including pressure, flow, force and displacement. However, requirements regarding mesh element density and time-step sizes make these simulations computationally expensive. Although few studies report mesh independence and time-step convergence analyses, examples in literature exist. As an example, the work from de Santis et. al [17] demonstrated that over 2 million elements were required for grid independence. Their steady-state simulation of the coronary circulation, using an unstructured tetrahedral mesh, required 43 minutes for reaching convergence using a CPU with 4 cores.

For transient simulations the convergence of many time-steps is required resulting in even longer simulation times. In addition, a full fluid-structure interaction (FSI) coupling can substantially add to this time as demonstrated in the study of Brown et al. [18]. An FSI simulation with a fluid mesh of the thoracic aorta containing 500,000 elements and 35,000 structural elements for the vessel wall, required over 145 hours to complete.

The two examples mentioned above are geographically very limited in scope. Only relatively small sections of the vasculature are represented using 3D techniques. As such, simulation of the full circulatory system utilizing only 2D/3D techniques is very challenging. Increasing computational power is an option as was done in a demonstration by Zhou et al. [19] in which a simulation was performed for a large portion of the cardiovascular system containing over 1.07 billion elements. Simulation takes only 1.25[s] per time step using 163,840 CPU cores available from a high-performance computing cluster (HPC).

HPC resources tend to be out of reach of most care providers as they are very costly. It is well known that the conditions in one part of the cardiovascular system are highly dependent on conditions throughout the rest of the cardiovascular system. Correctly representing all relevant parts of the system is critical for accurate results. As it stands at the current time, the computational expense required is preventative of the use of 3D modelling techniques in a clinical setting making an excellent case for model order reduction techniques.

1.5. Modelling cardiovascular dynamics

Cardiovascular models attempt to capture the hemodynamics of the vasculature under study. Secomb [20] defines hemodynamics as "the physical study of flowing blood and of all the solid structures through which it flows". For the current context this definition is limited to the study of structural mechanics, fluid mechanics and

the interaction between them (FSI). The focus is particularly on the description of pressure and flow in the cardiovascular system.

1.5.1.   Modelling Fluid mechanics

The use of fluid mechanics models is finding its way into clinical applications in recent years. In very few instances have relevant analytical solutions been found for general problems and solutions have mostly been provided using numerical models. Computational fluid dynamics (CFD) is the branch involved with the numerical modelling of fluid Mechanics. The work of Morris et al. [21] provides a small overview of studies in recent years in which CFD has proven useful in studying various diseases or to aid in the understanding and design of medical devices including valve prostheses and vascular stents.

All methods in computational fluid dynamics attempt to provide solutions to a set of conservation differential equations. Under the assumption that thermal processes can be neglected this reduces to deriving 2D/3D pressure- and flow fields using the conservation of mass and momentum. Derivation of these equations can be found in most introductory books [22] regarding computational fluid dynamics and are given by:

<div align="center">

Mass conservation

$$\frac{D\rho}{Dt} + \boldsymbol{\nabla} \cdot (\rho \vec{v}) = 0 \qquad\qquad \text{(Eq. 1.1)}$$

Momentum conservation

$$\rho \frac{D\vec{v}}{Dt} = -\boldsymbol{\nabla}p + \boldsymbol{\nabla} \cdot \boldsymbol{\tau} + \rho \vec{f} \qquad\qquad \text{(Eq. 1.2)}$$

</div>

With ρ the fluid density, $\vec{v}$ the velocity vector, p the pressure, $\boldsymbol{\tau}$ is the viscous stress tensor and $\vec{f}$ is any remaining body force per unit mass. $\frac{D(\cdot)}{Dt}$ is the convective derivative operator of a function according to:

$$\frac{D}{Dt} = \left(\frac{\partial}{\partial t} + \vec{v} \cdot \boldsymbol{\nabla}\right) \qquad \text{(Eq. 1.3)}$$

The conservation of mass and momentum are special case derivations of the Reynolds transport theorem [23] which can be written for any scalar quantity ψ as:

$$\frac{D\psi}{Dt} = \frac{d}{dt}\int_{\Omega} \rho\varphi d\Omega + \int_{\Gamma} \rho\varphi(\vec{v_r} \cdot \vec{n})d\Gamma \qquad \text{(Eq. 1.4)}$$

In which φ is the quantity ψ per unit mass, Ω an arbitrary control volume, Γ its control surface, $\vec{v_r}$ the fluid velocity relative to the control surface velocity and $\vec{n}$ the normal vector at a point of the control surface. As such, eqs. 1.1-1.2 effectively describe the convection and diffusion of mass and momentum.

Eqs. 1.1-1.2, or for that matter any set of balance equations in continuum mechanics, can be solved using the finite difference, finite element and finite volume methods. While finite element method solvers for fluid mechanics can be found in academic applications it is most often used for solving structural mechanics problems. In commercial applications the finite volume method is much more common. Ansys Fluent (Ansys Inc., Canonsburg, Pennsylvania, USA), is a 2D/3D CFD solver utilizing the finite volume methods and will be used for the remainder of this text.

In the finite volume method, a domain is subdivided into smaller control volumes. The flow of fluid is then followed through these control volumes in an Eulerian fashion as individual fluid parcels are continuously flowing in and out of the domain. Subsequently, the integral form of eqs. 1.1-1.2 is used to derive a discretised set of equations under certain interpolation assumptions. For each control volume this leads to an equation of the form:

$$a_p \psi_p = \sum_i a_i \psi_i + b_p \qquad \text{(Eq. 1.5)}$$

With quantities with subscript p relating to the current control volume, subscript I relating to all neighbouring control volumes and b some source term. A solvable set of equations can be formed by combining the resulting equations for all control volumes. For a more thorough treatment of the finite volume method the reader is encouraged to read the introductory work by Versteeg et al. [24].

1.5.2.   *Structural Mechanics*

Whereas finite volume methods are most often used for solving fluid mechanics problems, finite element methods are most often used for structural mechanics problems. In structural mechanics the goal is to find stress and displacement fields for a given structure and boundary conditions. As the focus is on control mass, it is intuitive to define the problem from a Lagrangian standpoint. In this case conservation of mass and conservation of linear momentum can be expressed as:

Mass conservation	$$\frac{D(\rho V)}{Dt} = 0$$	(Eq. 1.6)
Momentum conservation	$$\rho \frac{\partial^2 \vec{u}}{\partial t^2} = \boldsymbol{\nabla} \cdot \boldsymbol{\sigma} + \rho \vec{f}$$	(Eq. 1.7)

Where $\vec{u}$ is the displacement vector and $\boldsymbol{\sigma}$ is the stress tensor. In the case of vascular simulations, the mass of the structure contributes little to the inertia of the system and therefore the movement can be considered to be quasi-static. For the finite element analysis this means that the goal becomes to find the solution to the system:

$$\boldsymbol{K}\vec{u} = \vec{F} \qquad \text{(Eq. 1.8)}$$

With $\boldsymbol{K}$ the stiffness matrix relating the vector of all nodal displacements $\vec{u}$ to the vector of nodal forces $\vec{F}$. The reader is referred to the introductory text by Reddy [25] for the process of arriving at the system of equations in eq. 1.8. ANSYS Mechanical (Ansys Inc., Canonsburg, Pennsylvania, USA) is the finite element analysis software used for simulation of the vascular wall. While time dependent inertial effects are deemed irrelevant, they are still included in simulations with the system being solved by ANSYS Mechanical [26] being:

$$\boldsymbol{M}\frac{\partial^2 \vec{u}(t)}{\partial t^2} + \boldsymbol{C}\frac{\partial \vec{u}(t)}{\partial t} + \boldsymbol{K}\vec{u}(t) = \vec{F}(t) \qquad \text{(Eq. 1.9)}$$

With $\boldsymbol{M}$ the structural mass matrix and $\boldsymbol{C}$ the structural dampening matrix. Inclusion of this behaviour was considered to allow for large deformations and possible non-linearities.

1.5.3.   Multiscale & Multiphysics modelling

As was mentioned before, modelling cardiovascular dynamics can be very computationally expensive. This is further complicated by the multiphysical nature of the cardiovascular system. Creating a model description of parts of the cardiovascular system, many different physical aspects and time- and geometrical scales can be considered. An example is provided for the case of modelling the human heart in the works of Zhang et al. [27] and Chabiniok et al. [28]. 3 different types of physics are involved, namely the electrophysiology involved in signal conduction, the structural mechanics involved in muscle contraction and the fluid dynamics governing the blood pumped in and out of the heart. Each of these types of physics can be considered at a protein scale, a cell scale, a tissue scale or an organ scale. As such multiscale electrophysiology modelling can mean including ion channel modelling on a protein scale while simultaneously modelling the electrical propagation on a tissue or organ level. Considering and incorporating effects on different scales has led to the discipline of multiscale modelling.

While it is important to represent all relevant parts of the cardiovascular system, not all parts need to consider the same level of detail. The term multiscale modelling in cardiovascular modelling often implies geometrical multiscale modelling. This term was introduced by Quarteroni [29] to imply the usage of different models, incorporating different characteristic scales within the cardiovascular system. A high-fidelity 3D model can be used to represent details at a very local scale of millimetres for a limited part of the circulation while at its boundaries it can be

coupled to 0D or 1D models representing details of entire compartments on a scale of centimetres to meters. This approach can significantly reduce the computational cost of these types of simulations. Arguably the most well-known pioneering works modelling large portions of the arterial circulation are done by Westerhof [30] and Anliker [31], respectively using 0D lumped parameter and 1D models. While these models are not themselves multiscale, their approach to model the cardiovascular system outside of the 3D region as 0D or 1D regions, has been used in numerous studies [29, 32, 33, 34].

As multiscale modelling techniques can significantly reduce the computational cost of simulations, they can be an asset for translating models to a clinical setting. However, few studies can be found regarding the numerical stability of these models. In the current work special attention is brought to the stability in coupling multiscale models between 3D and 0D models. For this 0D modelling is introduced in chapter 3 with the stability considerations considered in chapter 4.

1.6. Thesis Outline

As mentioned in the motivational part of the introduction, the focus of the current work is on stability considerations for multiscale models and model order reduction techniques for cardiovascular models. As such Chapter 1 has dealt with introducing the context of CVDs

Chapter 2 starts of by introducing the need for multiscale models to pose proper boundary conditions. Two boundary condition schemes posing BCs from

retrospective data highlight the potential physical incoherence between pressure and flow arising from directly posing measurement data at boundary conditions.

Chapter 3 discusses the lumped parameter models known as the Windkessel (WK) models and discusses their use as BC models. An open-source plug-in for Fluent has been created for the 2- & 3-element WK and their accuracy requirements are analysed.

Chapter 4 discusses the stability that comes with partitioned multiscale modelling approaches. Stability of BC couplings is analysed with respect to their energy conservation properties and the stability of several often used explicit and implicit schemes is considered. Based on these findings an energy conservative boundary coupling scheme is introduced.

Chapter 5 addresses speedup techniques for FSI which includes a 3D compressible fluid model. The chapter goes deeper into the discrepancies between conventional 2-Way 3D FSI method, the compressible fluid model and a 1D wave-propagation model in order to suggest improvements to the 3D compressible fluid method.

Chapter 6 lastly deals with Reduced order modelling utilizing a reduced basis approach. This chapter attempts to analyse the training-set size and the basis size Requirements for generating a singular value decomposition (SVD) basis and accompanying transient reduced order model (ROM).

Chapter 2

2. Clinically derived simulation BCs

2.1. Introduction

The goal of developing techniques for simulation of hemodynamics is to apply these techniques to realistic patient-specific cases. Due to technological advancement of computational capabilities and advancement of the field more and more attention is directed towards patient-specific modelling in recent years. Some examples include patient-specific cardiac models [35] , carotid artery simulation [36], coronary simulations [37] and investigations of the abdominal aorta [38].

A review article by Taylor and Figueroa [39] offers more examples and aptly describes the stages for patient-specific simulation of the cardiovascular system. The first stage in their process concerns the patient-specific data acquisition. In order to perform a 3D simulation, it is first necessary to derive a patient specific 3D representation of the anatomy of interest. In practice, different imaging modalities, most often Magnetic Resonance Imaging (MRI) or Computed Tomography (CT), can be used to obtain geometric information which can be processed into a computational mesh later on. Secondly, assuming a multiscale model, measurement data is required to provide appropriate boundary conditions (BCs). Lastly, the data observed dictates the physical detail required to accurately simulate the patient-specific case.

Geometrical image acquisition and image segmentation is a subject of sufficient complexity to be fully out of the scope of the current text. The current chapter focusses on the modelling choices with respect to imposing BCs derived from

patient-specific data. The work from two studies of Morbiduci et al. note the importance of those BC choices. In [40] the modelling choice between prescribing pre-set flow rate division at the outlets is compared against using a lumped-parameter model at the boundary, noting a significant difference between both approaches. In [41] the effect regarding the inlet velocity profiles, considering developed and plug flow, is compared against MRI derived data for several hydrodynamic indicators, similarly noting the importance of this choice at inlet. For the work of Gallo et al. [42] a patient-specific geometry is simulated under various combinations of plug flow outlet conditions including BCs derived from patient-specific data. One of the main conclusions of this study is that BC choices are one of the main determinants of the simulation outcome.

For measuring patient-specific physiological data, the most commonly used techniques measuring velocity and flow include ultrasonic velocimetry and MRI. Pressure is more complicated to measure non-invasively. Often only invasive measurements can be taken due to the measurement location. These can be acquired by inserting and manoeuvring a pressure wire to the vessel of interest. However due to this invasive nature and accompanying disadvantages of this procedure, these measurements are rarely available from retrospective studies while it is difficult to prospectively acquire them. Pressure can be obtained non-invasively from remote locations as for example from brachial cuff measurements, but models are required to relate these measurements to local blood pressures within the region of interest. An example includes the estimation of central aortic blood pressure(ceBP), which

is the blood pressure internal to the ascending aortic arch. Acquisition of ceBP is outside the scope of the current text but an interested reader is referred to a review article by Stergiou et al. [43] .

The focus of the current study is investigation of patient-specific boundary conditions for a thoracic aorta flow phantom. A study by Müller [44] investigated the dynamics of flow and pressure for the thoracic aorta using several imaging modalities and measurement techniques. The goal of this study was to measure flow at multiple sites along the thoracic aorta and the supra-aortic vessels for a cohort of patients. This data was used to derive flow signals representative for the cohort to be used as BCs for a mock aortic circuit. A secondary outcome of these experiments was derivation of pressure and flow curves suitable for numerical simulation using CFD. Suitability of the results by Müller [44] with respect to CFD simulation remained untested after successfully representing flow signals using characteristic feature points.

The chapter goal is to attempt patient-specific simulation from a scenario of mock retrospective data. For this mock aortic set-up pressure data is available for the rigid walled phantom from Müller, which was very kindly provided by Prof. Dr. Hendrik von Tengg-Kobligk making this chapter possible. This allows for an analysis under the best of conditions possible without confounding physical effects like vessel compliance or patient movement. Two different numerical boundary schemes are compared against measured data in order to provide insights in the difficulties regarding the treatment of retrospective data.

2.2. Mock aortic set-up

The flow phantom part of the mock aortic circuit set-up is shown below in fig. 2.1, is made out of acrylic and is therefore rigid. Locations of the vessels are indicated in white and refer to the ascending aorta (Asc), right subclavian artery (Rsa), right carotid artery (Rca), left carotid artery (Lca), left subclavian artery (Lsa) and the Descending aorta (Dsc). At the Asc inlet, the flow phantom was connected via PVC tubing to a pulsatile flow pump and a bicycle inner tire acting as a compliance. At all outlets, tubing was connected to a set of valves to regulate the resistance of each outlet, before returning to the inlet of the pump. During operation, the circuit is a fully closed circuit. To create a mean hydrostatic pressure comparable to the average pressure in the cardiovascular system a water bath is connected downstream to the flow phantom, which can be raised to a certain level. Pressure was measured through luer-lok fittings, small fittings which in this case enable connecting the flow phantom to pressure sensors by PVC tubing. Locations for these fitting are indicated in red following the naming convention of the vessels. Flow was measured in different places depending on the measurement modality used. Using MRI, for both 2D-plane and 3D+t measurements, flow measurements were derived at or close to the location of the luer-lok fittings. Ultrasound flow meters were connected in-line with the PVC tubing connecting the phantom to the remaining components of the mock aortic circuit. As such, ultrasound flow measurements are made external to the flow phantom. It is assumed that both the

PVC tubing and the acrylic flow phantom are effectively rigid and therefore all measurement modalities should theoretically represent the same flow.
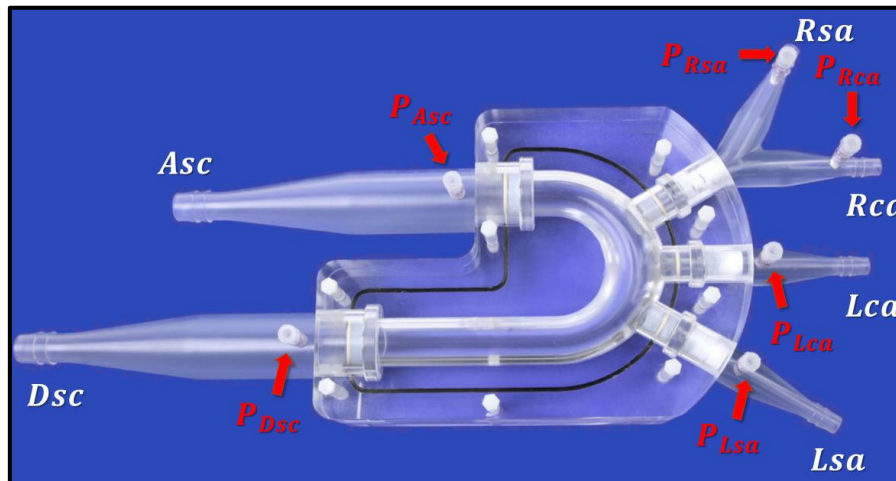
Fig. 2.1 - Flow phantom from Müller [44]. Indications in white for boundary/vessel location, indications in red for pressure measurements at integrated Luer-locks.

Conditions in the flow phantom are similar to those in the human cardiovascular system. In the physiological case, the heart exerts a pressure expelling a volume equal to the stroke volume with each heartbeat into the aorta. Due to aortic compliance, part of the stroke volume gets stored at a certain pressure within the aorta while a part flows through to the downstream vasculature. The volume that is stored, eventually flows through into the venous system, which effectively acts as a storage with a very high compliance. Pressure within the venous system is relatively constant for all practical purposes and therefore the distribution of flow is predominantly determined by the resistance encountered along the way through the different tissues. In the flow phantom conditions are similar to a degree, where

a volume can be stored at a certain pressure within the bicycle tire, while the flow distribution is determined by a set of valves. However, the venous compliance is absent. This implies that the pump effectively dictates a flow boundary distal to the resistances caused by the valves.

The flow phantom experiment is able to provide pressure and flow measurements for an incompressible flow through a known rigid geometry. The exact geometry is available from computer aided design (CAD) files used to produce the flow phantom. These will be used to attempt the numerical modelling of the flow phantom and look at the data requirements for CFD. As pressure and flow measurements at locations within the phantom are used, it is unnecessary to analyse or model the remaining components of the flow and these are considered as black-box components.

2.3. Numerical simulation setup

2.3.1. Computational scenarios

Two numerical scenarios have been designed which are classified according to their BCs. Regardless of the scenario, the Asc inlet is always prescribed as a mass flow boundary. Due to the inclusion of the compliance of the bicycle tire before the inlet, it could be argued that pressure should be prescribed instead. However, the pressure inside the tire is unknown and it is unlikely in patient-specific cases that pressure data is available. As a result, one of the outcomes of both scenarios is the pressure at inlet. Downstream, the Dsc outlet is prescribed as a pressure boundary in order

to not over-constrain the numerical setup. As a result, another outcome for both scenarios is the flow at the Dsc outlet. The two scenarios are now defined by the description of the remaining 4 boundaries of the supra-aortic vessels (RSA, RCA, LCA and LSA). The first scenario is referred to as the pressure-BC scenario as all remaining boundaries are prescribed as pressure boundaries. The second scenario is referred to as the flow-BC case in which all remaining boundaries except the descending outlet are flow boundaries. These two experimental setups represent two different physical cases for aortic flow.

The pressure-BC case represents a situation where pressure differentials between outlets govern the flow fraction over a cycle. Pressure measurements can be made from remote locations with respect to the region of interest and related back to locations within the region of interest either through a set of assumptions or an underlying model. Inflow conditions can be determined from estimating the stroke volume from the heart for which in practice the most common options include ultrasound and or qMRI measurements. Advantages of this approach from a data collection point of view, are that other more readily available modalities than MRI can be used to estimate the required BC data, but it is difficult to obtain sufficiently precise pressure measurements. An important outcome of simulations done using the pressure scenarios is the flow at the outlets.

The flow-BC case is more representative of the current day clinical conditions and can be used to determine the pressure distribution. Flow distribution through the

outlets is fully pre-determined however and for the current case requires flow information for all supra-aortic vessels. At the present time, flow data for these vessels requires investigation using MRI. The advantage of this approach is that the pressure at the Dsc boundary is only used as a pressure reference and therefore the results are expected to be far less sensitive to any measurements error with respect to this pressure. The resulting outcome of this approach however is only the pressure distribution between the separate vessels.

2.3.2.   Computational setup

Fig. 2.2 demonstrates the process for constructing the computational mesh.
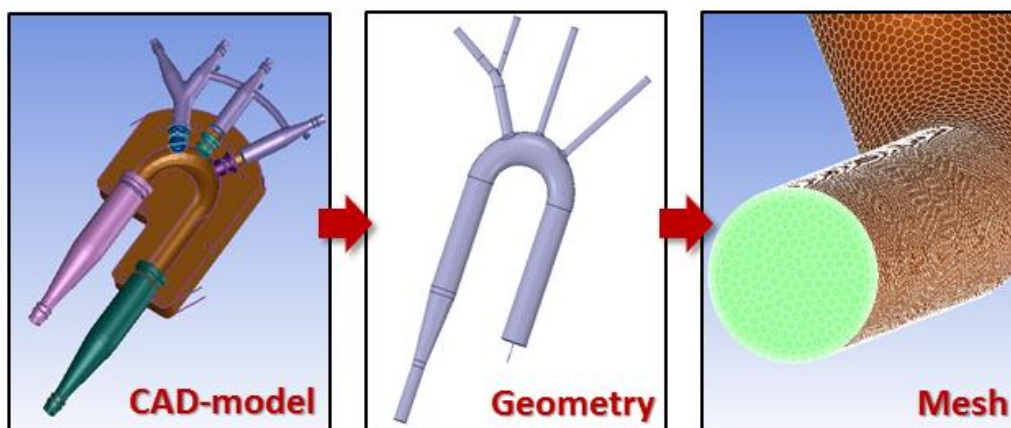
Fig. 2.2 - Polyhedral computational mesh(right), constructed from geometry(middle) derived from interior volume of CAD model(left)

A CAD-model was available from which the physical flow phantom was constructed. Construction of the geometry consists of determining the internal volume of the flow phantom which was accomplished using Spaceclaim (ANSYS Inc., Cannonsburg, Pennsylvania, US). The tapered connection at the inlet has been

retained in order to simulate the inlet effects of the experimental setup, while the outlet has been cut at the location of the luer-lok used for pressure measurements. It is assumed that the tapering at the outlet has a limited effect on the pressure and velocity profiles within the flow phantom. The computational mesh is constructed using Fluent Meshing (ANSYS Inc., Cannonsburg, Pennsylvania, US). A mesh is constructed using polygonal elements with an average diameter of approximately 1[mm] in addition to a set of 7 prism-layers near the wall. Finally, the mesh is used in a simulation using Fluent (ANSYS Inc., Cannonsburg, Pennsylvania, US). From the flow data reported in the thesis by Müller, it was estimated that the maximum flow velocity is approximately 2[m/s]. As such to satisfy a courant number of $CFL = 1[-]$ a time-step of $\Delta t = 5 \cdot 10^{-4}[s]$ is chosen. The peak Reynolds number in the wider section of the ascending aorta is estimated to be in the order of magnitude of $O(Re_D) = 10^4[-]$ necessitating the inclusion of a turbulence model for better convergence properties of the simulation. For this purpose, a large eddy simulation was performed with the Smagorinsky-Lilly subgrid-scale model. While this model is not appropriate for the conditions within the phantom, this model has the lowest requirements in terms of data and model set-up. BC profiles, regardless of the physical quantity prescribed, are prescribed as uniform scalar values over their surfaces. Therefore, it is assumed that pressure and flow can be averaged over the boundary surfaces, i.e pressure and velocity are independent of radial position.

2.4. Data pre-processing

2.4.1. Flow pre-processing

Before proceeding to simulation of both scenarios it is necessary to pre-process the acquired data. Upon closer inspection of the datasets provided by Müller, only the raw data from the flow measurements was available. Effectively, this means that flow signals over time were available from ultrasound measurements whereas raw MRI data was available for the 2D- and 3D-PC MRI derived measurements. Due to the complex nature and the expertise required for pre-processing MRI data, a choice was made to forego analysis of the MRI data and attempt simulating the experimental setup based on the ultrasound measurements. As an example, fig. 2.3 below demonstrates the flow derived for all 3 flow measurement modalities as reported in the thesis by Müller.
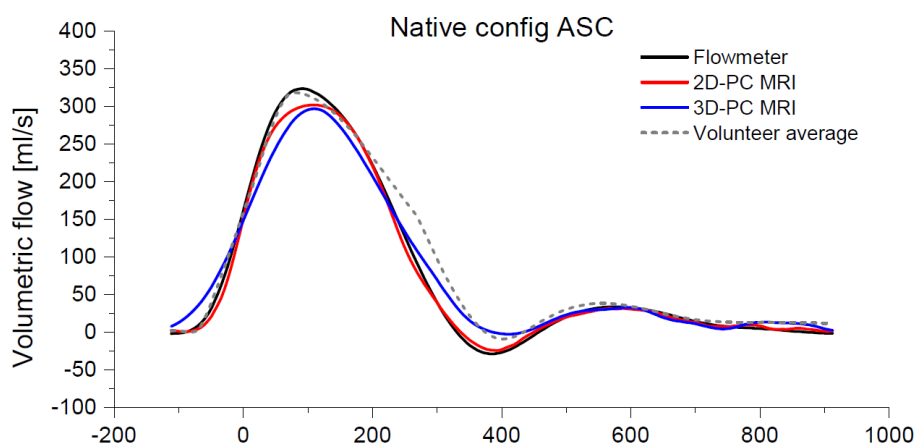
Fig. 2.3 - Ascending aortic boundary flow from Ultrasound flowmeters, 2D-PC & 3D-PC MRI (Müller [44])

A maximum difference of about 25[ml/s] exists between measurement modalities, corresponding to approximately 8% of the maximum flow. Additionally, it can be seen that the 2D-PC MRI results follow the ultrasound measurements more closely

over the full duration of the signal as compared to the 3D-PC MRI results. While no information is available on the true pressure and flow conditions, it can be argued that the flow patterns are representative of the true flow due to good agreement between different measurement methods.

Graphs were available in the thesis for all boundaries of the flow phantom, but an attempt is made to reconstruct the flow using the data provided by the raw ultrasound flow measurements.

Flow was measured using 3 ultrasound probes simultaneously. As there are 6 boundaries besides the wall itself, ultrasound flow measurements were made using effectively two separate experiments. Flow through the Asc, Rsa and Rca boundaries were simultaneously measured first after which the ultrasound probes were relocated behind the Dsc, Lsa and Lca vessels. As the ultrasound probes are an in-line component of the setup rather than a device placed over the outside of the PVC tubing, it was necessary to shut off the pump and recalibrate the setup after relocation of the ultrasound probes. Therefore, besides 3 of the 6 flow measurements not being recorded at the same time it cannot be guaranteed that the measurements were taken under identical conditions.

For the native configuration of the aortic arch approximately 70[s] of usable raw ultrasound flow data was available at a resolution of approximately 20[Hz]. A single flow cycle lasts for 1.024[s] which is dictated by the cycle duration of the

pulsatile pump. A set of data point and their measurement time was available with unequal spacing in time. These measurement points were then distributed over 50 subintervals of equal length within their cycle. As a first attempt, the subintervals for all cycles are grouped and averaged. The group averaged flow over a cycle can be seen in fig. 2.4. It can be seen that the Asc and Dsc flow measurements appear to contain noise and showcase discontinuous flow patterns between data points.
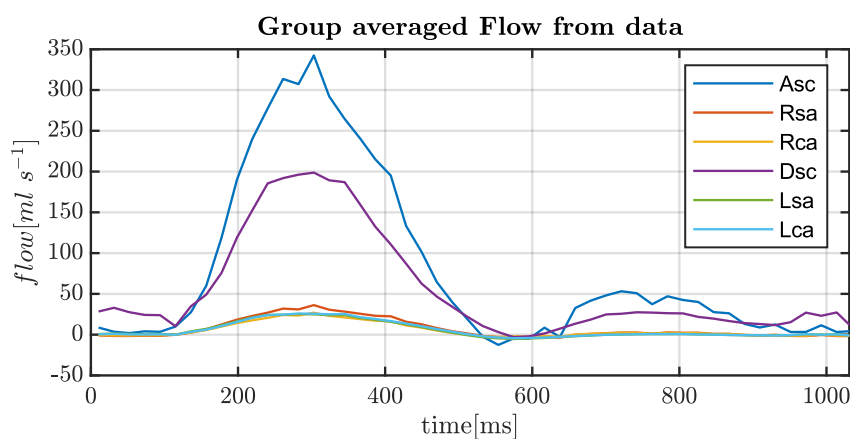
Fig. 2.4 - Group averaged flow at flow phantom boundaries from raw ultrasound measurements.

To smooth the flow over a cycle and increase the time resolution, cubic spline interpolation was used as suggested in study of Müller et al. As can be seen from fig. 2.5 however, the flow measurements retain their noise and are not representative of the measurements presented by Müller. Therefore, this approach is deemed unacceptable for re-producing flow signals suitable for numerical simulation.
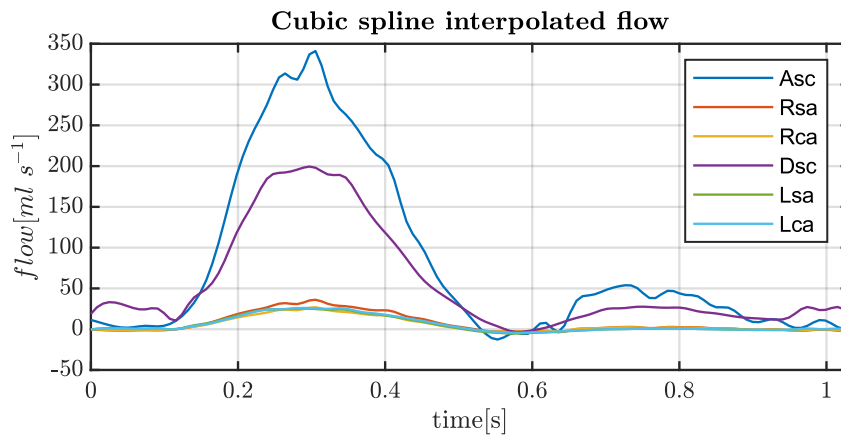
Fig. 2.5 - Cubic spline interpolation of the group averaged flow from fig 2.4.

To obtain more acceptable flow curves for numerical simulation a separate process as described in the thesis of Müller is broadly followed. This process will be partially demonstrated for the ascending aorta boundary (Asc). Firstly, a cubic spline is fitted throughout the entire dataset obtained from the continuous measurement of approximately 70[s] in duration. The resulting signal is then resampled at 128 datapoints per cycle which is equal to a frequency of 125[Hz]. Each individual cycle can be regarded as a single instance of an ensemble average. Data was available for the raw measurements indicating when one cycle ends and the next begins. However, this resulted in individual cycles of intermittent length. I.e. subsequent cycles would either contain 21 datapoints or 22 datapoints. It is likely that this is an artefact of the discrete sampling rate. Additionally, upon closer inspection it appeared that the full-length signal drifts slightly over time, indicating that the signal is slightly longer than the indicated 1.024[s]. Fig. 2.6 depicts the first 60 cycles where the drift over time has manually been corrected as well as possible in order to have a minimal spread between all signals within the dataset. A choice was made to only isolate the first 60 cycles as the remaining cycles had very

apparent data anomalies which did not describe the physical process within the flow phantom. Following this correction process, the signals were resampled for all signals to have equally spaced points over time.
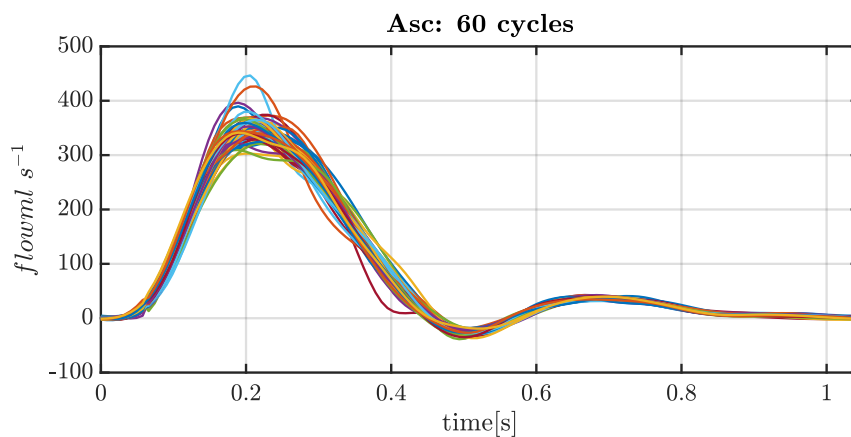
Fig. 2.6 - Ensemble of Asc flow cycles derived from ultrasound demonstrating signal variability.

Finally, the ensemble average of all cycles is taken to give flow signal representative of the conditions within the flow phantom. Fig. 2.7 depicts the ensemble average of these 60 cycles:
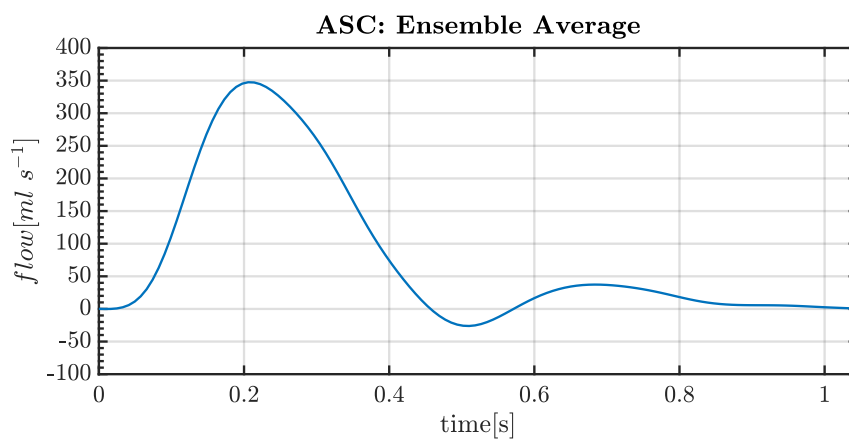
Fig. 2.7 - Ensemble average of all Asc flow cycles

In comparison to the results from the thesis by Müller, it can be remarked that both the maximum and minimum flow are marginally higher, with the maximum flow at approximately 350[ml/s] and the minimum at approximately -25[ml/s]. The maximum flow derived from fig. 2.3 from the work of Müller is approximately 325 [ml/s] while the minimum is approximately -35[ml/s]. This difference is within the order of magnitude of the difference between the different measurement modalities. Additionally, it was mentioned that the native configuration of the aortic arch was measured separately twice to study repeatability of the experiment resulting in a 4.45[%] difference in average flow. It is unclear from the text if the reported graphs belong to the first or the second measurement experiment. For the current study a choice was made to analyse the data of the second measurement experiment as the corresponding pressure measurements correspond better with the flow patterns prescribed at the inlet. Therefore, the difference might be explained by the analysis of different datasets. Lastly, only the first 60 cycles of the dataset were considered potentially changing the magnitude and average flow of the ensemble averaged signal. Besides these discrepancies, the signal is considered to be in reasonable agreement with the results from Müller.

The process above was similarly carried out for all other boundaries, matching the individual cycles. There are effectively 2 datasets for a measurement experiment. The first dataset consisting of the Asc, Rsa and Rca data while the second one consists of the Dsc, Lsa and Lca data. Signals within a dataset can be processed simultaneously. However, as the data in the two datasets has been measured

independently, they are uncorrelated in time. Information on the required time shift to correlate both datasets was available for the raw ultrasound measures. The result for all ensemble averages is provided below in Fig. 2.8:
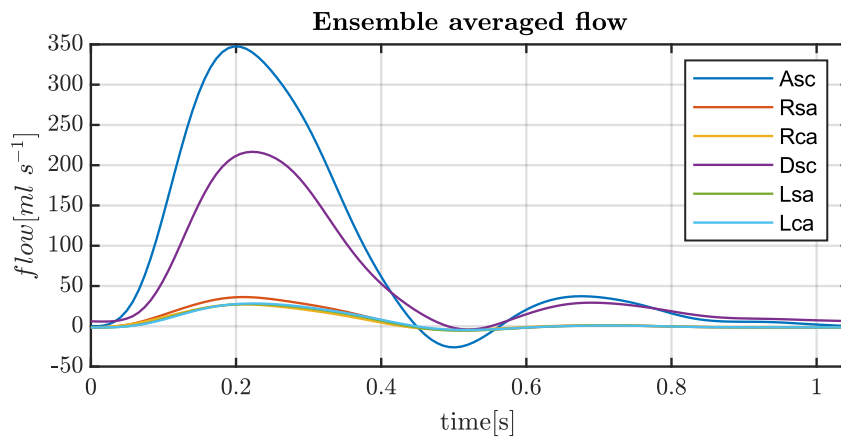
Fig. 2.8 - Ensemble averaged flow cycles for all boundaries

When compared to the graphs from Müller the graphs of the current study have similar patterns, maximum and minimum flow. However, they are not identical due to the same discrepancies mentioned for the derivation of Asc flow.

While these results seem encouraging, a number of issues still exists at this point with respect to using these flow signals for numerical simulation BCs. Most importantly, due to the rigidity of the flow phantom and the fluid being incompressible, the inflow needs to be exactly equal to the outflow to comply with the conservation of mass. Fig. 2.9 below shows the inflow through the Asc and the combined outflow of all other boundaries. For a large part of the cycle, mass is not conserved. Were mass conserved, both graphs for in- and outflow- would overlap. For the first 0.7[s] of the cycle, the outflow signals seem to have shifted with respect to time nor are the maxima and minima of the in- and outflow equal.
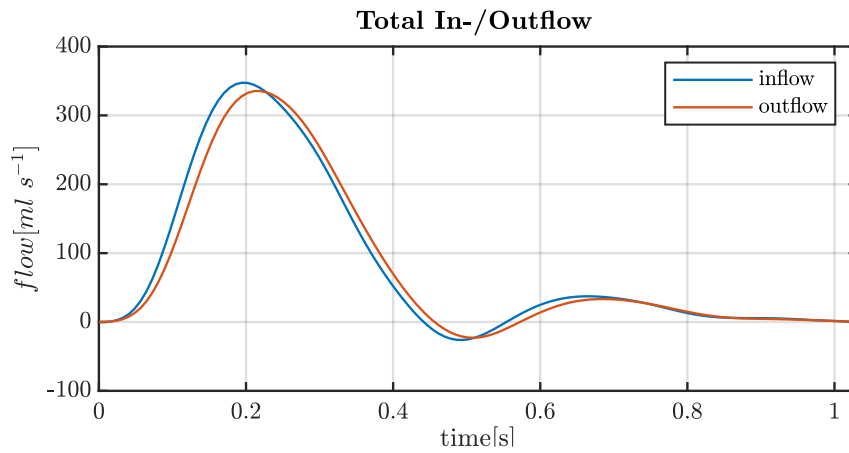
Fig. 2.9 - Inflow through the Asc and outflow through the remaining boundaries of the flow phantom showing non-conservation of mass over time.

To make the flow comply with the conservation of mass, the difference between in- and outflow, hereby referred to as the residual flow, is either added to or subtracted from the outlet boundaries. In order to determine the portion of the residual flow attributable to individual boundaries, each boundary receives a percentage of the total residual flow, according to the flow fraction of that individual outlet. For example, the Dsc has a flow fraction of approximately 68% of the total inflow and therefore receives 68% of the total residual flow for each time-step. The average flow per cycle after this correction, adhering to the conservation of mass is depicted below in fig. 2.10:
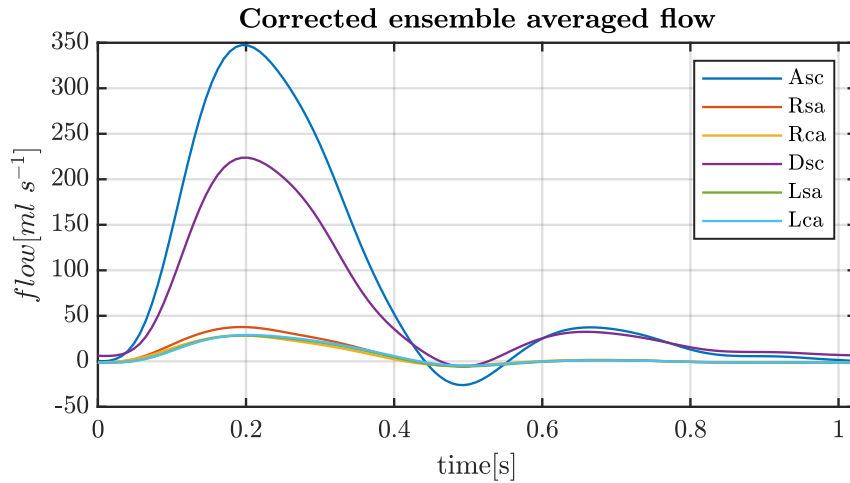
Fig. 2.10 - Ensemble averaged flow cycles corrected for conservation of mass.

Lastly, for an ensemble average for which the conditions remain unchanged, the resulting signals should be periodic. While this is not apparent from fig. 2.10, the flow cycles provided are not periodic and cause data discontinuities during simulation. Depending on which types of BCs are set for the numerical model in-silico, this might be a requirement for simulating consecutive cycles. A straight-forward way of guaranteeing continuity between cycles is to approximate these signals using a Fourier series. For this purpose, the signals have been approximated using the first 20 harmonics, and subsequently sampled at 2000[Hz] for producing 10 consecutive cycles. This sampling rate is a necessary requirement imposed by the simulation time-step size which in turn was imposed by the element size and flow velocity. The resulting flow cycles are shown for the first 5 cycles in Fig. 2.11. These are used for numerical simulation in both the pressure-BC and the flow-BC scenario. To obtain a lower discrepancy between the Fourier series approximation and the original signals, the original signals were shifted in time in order for the Asc flow to start in a local minimum at $t = 0[s]$. It should be noted that application

of a Fourier approximation after enforcing the balance of mass, breaks that enforcement. This discrepancy can be rectified by re-enforcing the balance of mass after producing the continuous signal containing multiple consecutive cycles. However, due to prescribing the Dsc as a pressure boundary, a degree of freedom exists to guarantee mass conservation and the difference with respect to the measured data is expected to be negligibly small.
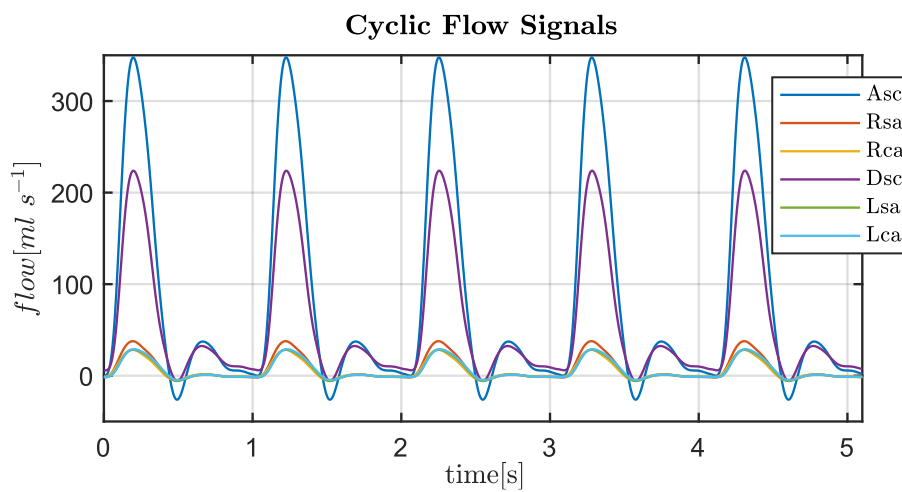
Fig. 2.11 - Ensemble averaged flow cycles after correcting for conservation of mass and enforcing periodicity used for simulation.

2.4.2. Pressure

Only one set of data was available for the pressure cycles similar to those reported in the thesis of Müller et al. Therefore, no ensemble averaging of raw data was possible. In order to obtain cyclic pressure measurements, all signals were smoothed and subsequently approximated by the 20 first harmonics of a Fourier series, sampled at 2000[Hz] producing again 10 consecutive cycles. The results of pressure signal processing for a single cycle are depicted in Fig. 2.12 below.
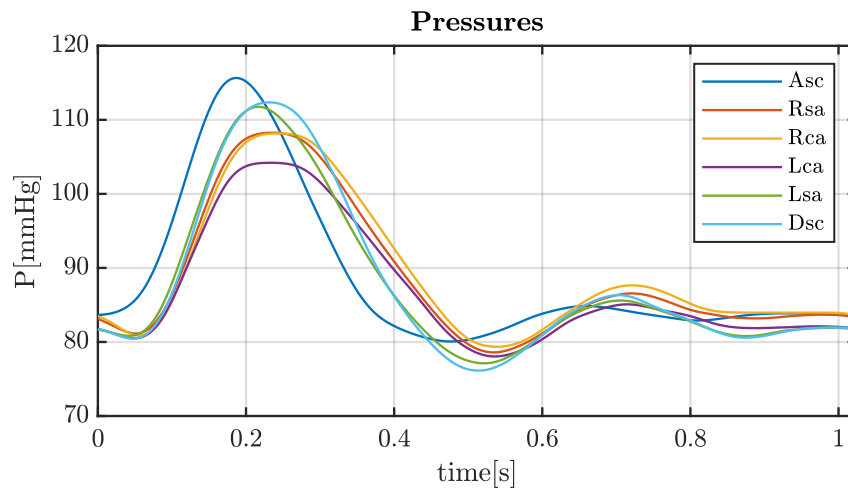
Fig. 2.12 - Pre-processed Pressure signals used for simulation

2.4.3.   *Pressure- and Flow-measurement inconsistencies*

Lastly it should be noted that pressure signals were measured during the acquisition of the MRI signals. Before the MRI measurements could be taken it was necessary to remove all ultrasound flow probes and subsequently re-calibrate the setup. As such it cannot be guaranteed that pressure signals correlate with any of the flow signals with respect to time or the overall experimental conditions. Physically however, pressure and flow are very strongly coupled. Without modelling the geometry in some form or way, it is not straightforward to match the pressure and flow signals with respect to time or magnitude, as the acceleration of flow depends on the local pressure gradients.

Some inconsistencies between pressure and flow data can be shown a priori, based on the measurement data alone. As demonstrated by the flow fraction of 68[%] towards the Dsc, it can be assumed that the main flow occurs between the Asc and Dsc. Fluid acceleration and deceleration between the Asc and Dsc, can be estimated

35

by the pressure differential between these outlets. This is a result of applying Newton's second law of motion and therefore pressure is directly proportional to acceleration. Acceleration can also be estimated from the time derivative of flow. In order to compare the patterns for acceleration derived from the pressure differential and the boundary flow, their respective signals are rescaled according to equation 2.1. This scales signals to have a range of 1 between their maximum and minimum value but retains the zero-crossings from the original signal.

$$\varphi_{scaled}(t) = \frac{\varphi(t)}{\max(\varphi(t)) - \min(\varphi(t))} \qquad \text{(Eq. 2.1)}$$

Fig. 2.13 below shows the time derivatives of the boundary flow at the Asc and Dsc in blue and red respectively, as well as the pressure differential between both boundaries shown in purple.
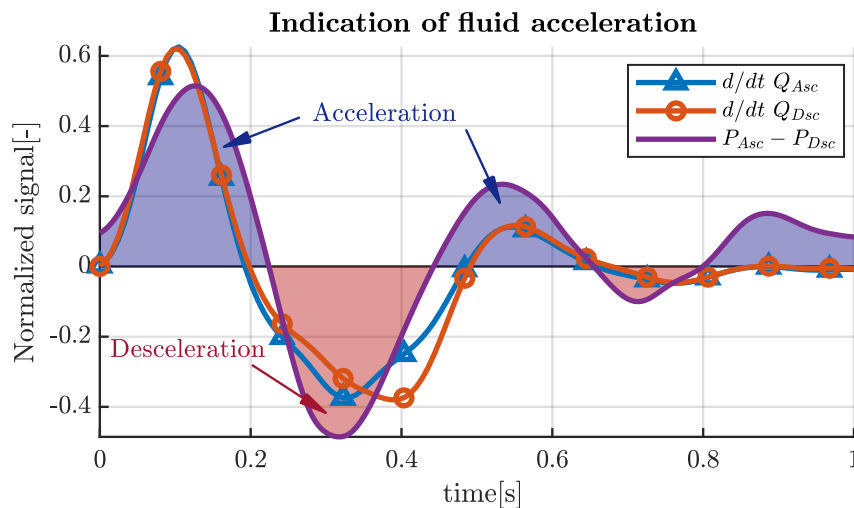
Fig. 2.13 - Accelerative/decelerative phases of the flow derived from Pressure differential between the Asc and Dsc boundaries and derived from flow measurements do not agree.

Accelerative phases according to the pressure differential have been drawn as shaded areas in purple, while decelerative phases have been drawn as areas shaded in red. It can be seen that the time derivatives of both in- and outflow signals have different accelerative and decelerative phases compared to the acceleration derived from the applied pressure differential. The initial acceleration peak for the flow derived acceleration occurs earlier compared to the pressure differential while the second accelerative phase occurs later. More importantly according to the pressure differential the first acceleration phase starts at 0.8[s] of the previous cycle and does not end untill approximately 0.25[s] of the current cycle corresponding to a duration of 0.45[s]. For the flow derived acceleration the duration of the first accelerative phase is only 0.2[s]. Additionally, a clear difference exists even between the in- and outlet flow with respect to the first decelerative phase which seems unlikely to occur, given that the flow phantom is rigid, has no compliant parts and the fluid being incompressible. As mentioned before, It is unclear how to preprocess the pressure signals to satisfy the balance of momentum without modelling the physics involved one way or another. Therefore, as BCs for the numerical simulations, the signals from Fig. 2.11 and 2.12 above have been utilised. It is expected that these descrepancies can be compensated to an extent due to the posed BCs of the numerical simulations but will result in different results compared to the measurement data.

2.4.4.   Fluid density

The fluid flowing through the mock aortic circuit is described as a blood analogous fluid with a reported viscosity. Numerical simulation of the flow phantom requires a measurement or an estimate of the density of this mixture which is unreported. The fluid consists of a mixture of water and glycerine which at 23°[C] results in a dynamic viscosity of $\mu = 4.4[cP]$. It is mentioned that the mixture is 40[%] glycerine and 60[%] water by volume. A density model by Volk and Kahler [45] is used, which is fitted to within an error margin of 0.07[%] with respect to measured densities from literature. Therefore, it is estimated that the density of the fluid used in the mock aortic circuit was approximately $\rho = 1112.7\ [Kg\ m^{-3}]$.

2.5. Simulation Results

2.5.1.   Pressure-BC scenario

Pressure and flow are only shown for boundaries where that specific quantity was not used as a BC. Therefore, inlet Asc pressure and the flow on all other boundaries are the outcomes of the simulation. Before proceeding to the pressure results it should be noted that this simulation diverges during the 2nd cycle for reasons that will become clear further on. Therefore, this strategy was not suitable for simulating this setting.

Pressure curves for the pressure-BC case are shown below in the top graph of fig. 2.14. for the first simulation cycle.
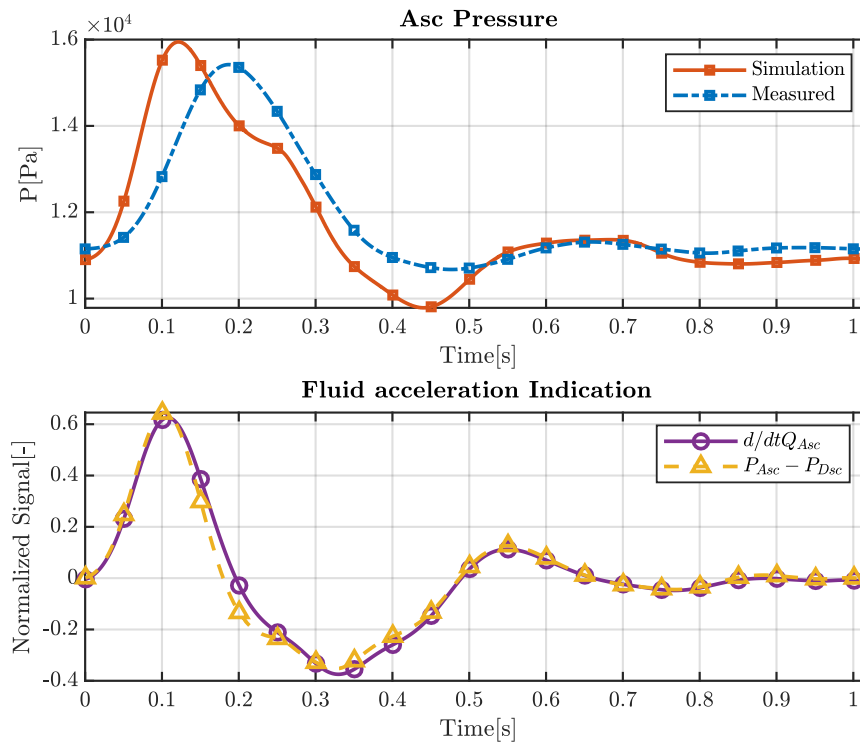
Fig. 2.14 - (top) pressure curves from simulation showing the discrepancies with respect to measurements. (bottom) Accelerative/decelerative phases derived from simulation pressure and flow measurements in good agreement.

The ascending aortic pressure is of the same order of magnitude as the measured data but displays a different pattern with respect to the first half of the cycle. The maximum pressure peak from simulation occurs earlier but is larger in magnitude after which the pressure is lower for most of the remainder cycle. The bottom graph of fig. 2.14 shows fluid acceleration indicators analogous to fig. 2.13 above but including the pressure data derived from simulation instead of measurements. The pattern for fluid acceleration derived from the flow results agrees well with that of the pressure differential between the Asc and Dsc boundary. This implies that the pressure differential between these 2 boundaries is mainly governed by the inlet

Chapter 2

flow rather than the imposed pressures. It is not possible to arrive at a simulated inlet pressure similar to the measured pressure given the imposed pressure conditions at the remaining outlets downstream. Additionally, no indication is provided to which measurements are coherent with each other. Under the assumption that the used modelling conditions represents the physical experiment, it can only be inferred that an incoherence between measurements exist. Therefore, regarding the measurements, it can only be concluded that the measured pressure differential between the Asc and Dsc boundaries is incoherent with the measured flow at the Asc.

The flow signals can be used to explain the non-convergence of the simulation. Fig. 2.15 below displays the flow through all outlets for the first cycle.
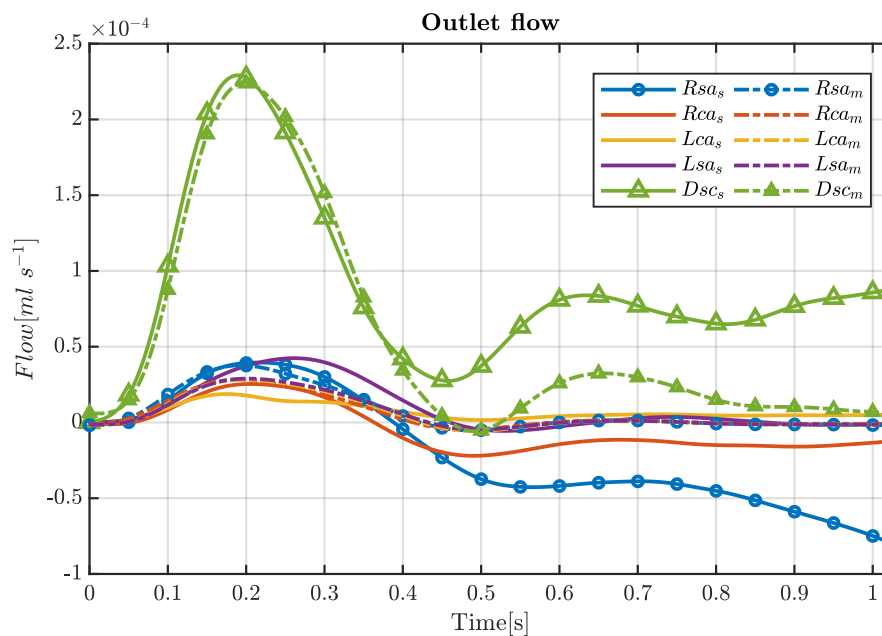
Fig. 2.15 - Flow comparison between simulation (solid lines) and measurements (dashed lines) indicating big discrepancies for all boundaries.

Positive flow indicates flow out of the domain. Simulation data is denoted by a subscripted 's' and depicted using solid line, while measurement data is denoted by a subscripted 'm' and depicted by dashed lines. Flows from measurement are periodic by design and approach zero for all supra-aortic branches. However, the flow from simulation is not periodic and at the end of the cycle, flow enters the domain from the Lsa vessel and leaves the domain from the Dsc vessel downstream even when no flow is provided at the Asc inlet.

A cross-section of the 3D velocity field is shown in fig. 2.16.
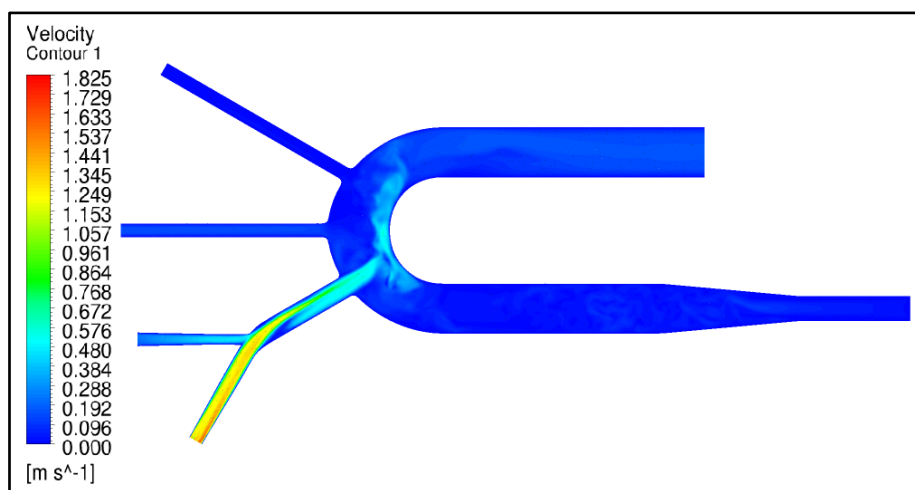
Fig. 2.16 - A fluid jet enters domain through Lsa boundary in absence of inlet

flow

At $t = 1.024[s]$ a strong jet is visible, directed back into the flow phantom domain eventually impacting the wall of the aortic arch. The pressures imposed at the outlets cause a net acceleration of fluid along the path between the Lsa and the Dsc over a single cycle. For this to happen in the physical setup, fluid from the outlets would have to flow back into the flow phantom without any driving force. In this

41

case, the pump is the only driving force which cannot drive the flow between the Lsa and Dsc vessel. Hence, these signals cannot be coherent with the physics within the mock aortic circuit.

As the imposed BC signals are periodic, it is expected that the flow is increased more over subsequent cycles. It was indeed observed that during the 2nd cycle the simulation diverges as the flow between the Lsa and Dsc grows exponentially. Before diverging around 0.6[s] into the 2nd cycle, the velocity through the Lsa boundary is approximately 1.8[m/s] into the interior of the domain, which corresponds to a Reynolds number of approximately Re=4000[-]. For clarity of the graphs the 2nd cycle of pressure and flow have been omitted.

2.5.2.   Flow-BC scenario

This simulation strategy lead to a successful convergence and simulation was stopped after the 2nd cycle due to periodicity of the result. Due to imposing flow BCs on all boundaries except the Dsc, the flow at the Dsc boundary is fully pre-determined. A figure has been omitted as the inlet and outlet flow graphically overlap. The RMS-difference between simulation and measurements for the Dsc flow is $RMS = 9.86 \cdot 10^{-7} [m^3 \cdot s^{-1}]$ with a normalized RMS of $NRMS = 0.43[\%]$. Although minor, This discrepancy was caused by not re-enforcing balance of mass for the measurements after making a Fourier approximation for periodicity.

Fig. 2.17 below displays the pressure at the boundaries from simulation on the left and the measured pressures as reference on the right.
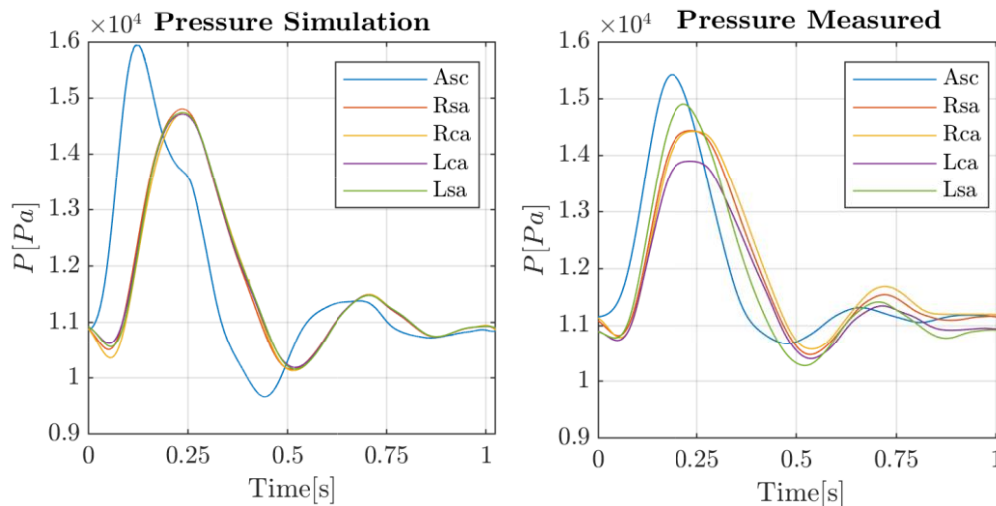
Fig. 2.17 - Pressure from simulation(left) and from measurements(right). Little spread exists between the simulated pressures while the inlet pressure is higher and earlier compared to measurements.

The most remarkable difference between the simulation and measured results, is the spread between the pressures of the individual boundaries. For the simulation, the mean over time of the maximum pressure difference between any 2 outlet boundaries, is approximately 141[Pa]. This includes the Dsc boundary not displayed in the graphs below. For the measurements, this mean value amounts to approximately 487[Pa]. This is especially apparent when comparing the peak pressures excluding the Dsc boundary. The difference between the Lsa and Lca boundary is approximately 1000[Pa] for the measured data. For the simulated data the maximum peak pressure difference occurs between the Rsa and Lca boundaries and is approximately 90[Pa] which is an order of magnitude smaller.

These results imply that, given the provided boundary flow signals, the measured pressures do not correspond with the physics present within the flow phantom. As an example, consider the Lca and Lsa vessels again. It seems unlikely that peak pressure differentials of order of magnitude $O(\Delta p)=1000$[Pa] would exist between te Lca and Lsa boundary. The Lca and Lsa vessel are of equal length, have equally long paths back to the pump and connect to the aorta at sites with approximately only 1[cm] distance between them, making them geographically very close. It can be seen from the measured flow graphs in Fig. 2.15 above, that the flow through the Lca and Lsa vessels is very similar. This implies that either there should be no pressure differential between both vessels or significant amounts of flow should appear between the Lca and Lsa vessels. As was considered before, the latter case is highly unlikely due to the fact that the only driving force in the system is the pump at the inlet. Furthermore, the pressure differential between these 2 geographically close vessels has the same order of magnitude as the one between the inlet and all other outlets. It is thus very likely that the pressure was measured with a significant error.

An important result of the preceding exercise, is that failing to reproduce measurement results using numerical simulation, or failing to produce any simulation results at all, does not automatically imply that the applied modelling approach is wrong. Numerical simulation of experimental setups or patient specific measurements can provide an additional tool to either validate measurements or

highlight data inconsistencies that should not be physically possible. Therefore it remains important to quantify the quality of measurement data and apply corrections where necessary besides investigating the appropriateness and accuracy of the numerical model.

2.6. Discussion

Comparing the pressure-BC and flow-BC case, it is perhaps unsurprising that the pressure-BC strategy is unsuccessful. The case being simulated is a rigid flow phantom with only one means of storing energy, namely through kinetic energy. Kinetic energy is fully determined by the velocity associated to a certain mass. Therefore velocity or flow would be the only state variable were this model to be reduced to a state-space description. For the flow-BC case, the velocity is fully predetermined and all BCs are periodic in nature. Hence at the end of a cycle, the initial state of kinetic energy is reached and therefore the initial state of the entire system. The only new information this system provides is the pressures at the inlet and supraaortic vessels which can almost be considered as a post-processing exercise.

For the pressure-BC case, pressure differentials exist between outlets which indirectly prescribe the acceleration of fluid between outlets. The acceleration caused by local pressure gradients, cause a change in the local fluid velocity and thus a change in kinetic energy. This means that, unless the energy added and subtracted to the system is periodic over time, it can not be guaranteed that pressure

and flow are periodic over time. In other words, a strong coupling exists between the pressure and flow in a system. The coherence between pressure and flow signals can be observed by considering the energy flux attached to them. It is however not straightforward to correct measurement results a priori based on these observations. Even if a correct estimate of the energy flux over a boundary is known, should it be the pressure or the flow measurements that are corrected? Additionally, a precise estimate of viscous losses needs to be available to impose the balance of energy. A better approach seems to be to optimise the coherence between pressure and flow at the moment of data-collection.

It was noted previously that a turbulence model was chosen which is inappropriate for the current setting. The Smagorinsky-lilly model was shown in numerous studies to perform well for homogeneous isotropic turbulence [46, 47] for which the constant $C_s = 0.17$ was determined by Smagorinsky [48]. This is not the case for cardiovascular flows as often transitional flow regimes are encountered. Additionally, in laminar regions of the flow, as potentially in the supra-aortic vessels or flow near the vessel wall, this model is overly dissipative. However these consideration seems unlikely to explain the magnitude of the differences observed from simulation with respect to the focus of the study. The overly dissipative effect of the simulation more likely has a stabilizing effect on the simulation, giving the analysis the best possible chance at attaining stability. A full analysis of turbulence models for cardiovascular simulations is out of the scope of the current project.

Additionally, it should be noted that patient-specific flow simulations need to include one additional level of complexity, namely vessel compliance. By including vessel compliance, local pressure becomes an additional state variable. Besides kinetic energy, potential energy can be stored due to elasticity of the wall and it no longer holds that the flow-BC strategy fully determines the energy contained by the system. Hence, it becomes important to know the pressures applied over the domain to determine the change in energy within the domain. Guaranteeing conservation of energy over a cycle, necessitates coherence of pressure and flow over the boundaries of the domain.

Due to the uncertainty in measurements and often the unknown link between different signals measured under different conditions or at different times, it is challenging to directly prescribe pressure and flow for simulations from measurements in a correct manner. The uncertainty of measurment signals can only be augmented by improving measurement accuracy. However, the signal coherence problem can also be overcome by modelling the conditions upstream and downstream of the region of interest, which is to be adressed in chapter 3. Data aqcuisition for these types of boundary models, should then focus on obtaining data usable for fitting the parameters used for these models. Boundary conditions posed in this manner are less susceptible to measurement errors over time and signal incoherence.

Chapter 3

3. Windkessel Boundary conditions for Fluent

3.1. Introduction

The chapter is intended to introduce the concept of using physical models as BCs as opposed to the direct measurement data usage strategies explored in chapter 2. Making use of BC models addresses some of the coherence issues between pressure and flow at boundaries, described in chapter 2. The use of additional physical models is part of the multi-scale modelling approach which will be further explored in Chapter 4. As such the goal of this chapter is to provide tools for the following chapters as well as provide a numerical analysis regarding the conditions under which this model should be used.

For the current chapter, the computational aspects for the Windkessel (WK)-model are described as part of the integration within Fluent (ANSYS, Canonsburg, Pennsylvania, US). For the remainder of the thesis, this model is used as the BC model for distal boundary termination. After introduction of the model, a description is given of the implementation within Fluent. This is followed by verification of the model including time-convergence studies for pulsatile flow characteristic of arterial flow. An extensive review regarding the practice of validation and verification for computational fluid dynamics is available Oberkampf and Trucano [49] for the interested reader.

Lastly it should be noted that the WK-model was released as a ready-to-use ACT extension for fluent. It was distributed as a free open-source add on the ANSYS App store.

3.2. Windkessel models

Windkessel models are often used to impose downstream boundary conditions representing the distal vasculature. Historically the name of these types of models derives from a pressure storage vessel used in fire engines at the time. This class of lumped-parameter models can be constructed from 0D-components which will be discussed below. Otto Frank [50] proposed the original 2-element WK-model consisting of a compliance element and a peripheral resistance (Fig. 1a) to model the afterload of the heart. As such it can be used to account for the compliance and resistance in the entire cardiovascular system using only 2 parameters. Improvements of this model led towards the 3- and later the 4-element WK-models in which the additional effects of impedance and fluid inertia were added in different configurations.

A comprehensive review on 0D-models for cardiovascular models, including the windkessel models can be found in Westerhof et al. [51], while the article by Shi et al. [52] provides a more detailed review regarding 0D and 1D-modelling.A choice was made to implement the 2- and 3-element WK-models, depicted in fig. 3.1, due to their relatively simple structures:
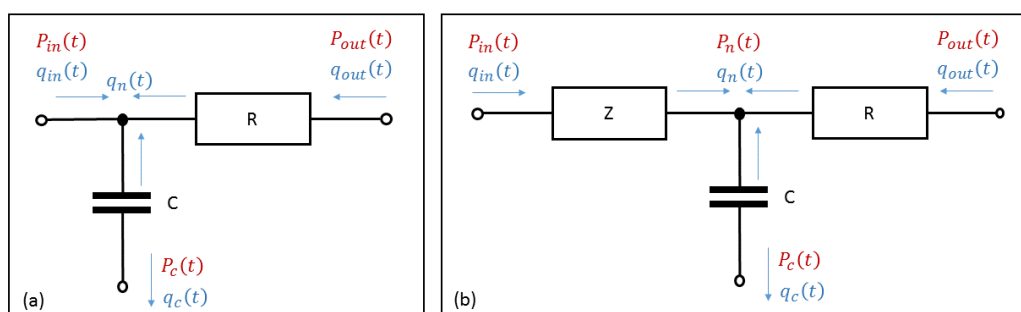
Fig. 3.1 - (a) 2-element WK-element, (b) 3-element WK-element.

More detailed and accurate models exist capable of describing the pressure and flow in parts of the cardiovascular system. However, the loss in detail within these compartments of the model is acceptable as the primary goal is to provide realistic boundary conditions to the upstream vessel in the form of either pressure or flow. Additionally, a large advantage of these WK-models is that only 2 or 3 parameters need to be estimated from clinical data while retaining low computational cost for model evaluation. To obtain the 3-element windkessel model from the 2-element windkessel model, an impedance element, Z, is added. This resistance has been introduced to match the input impedance to that of the connecting vessel upstream.

Differential equations for the 2- and 3-element WK models are given in eqs. 3.1-3.2 respectively. The different variables are denoted as the inlet flow Q_{in}, the pressures at the inlet, compliance and outlet denoted by P_{in}, P_c and P_{out} respectively, the compliance C, the peripheral resistance R_p and the vascular impedance Z. An impedance element was added to the 2-element WK-model to provide impedance matching at the interface between models. The 2-element WK-model can therefore easily be derived from the 3-element WK-model, by setting the impedance to zero. For the remainder of the discussion, all derivations are based on the 3-element WK-model.
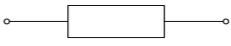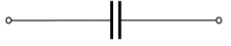
$$Q_{in} = C\frac{d(P_{in} - P_c)}{dt} + \frac{P_{in} - P_{out}}{R} \qquad \text{(Eq. 3.1)}$$

$$Q_{in} = C\frac{d(P_{in} - Q_{in}Z - P_c)}{dt} + \frac{P_{in} - Q_{in}Z - P_{out}}{R} \qquad \text{(Eq. 3.2)}$$

3.3. 0D-Components

The WK-model equations can be represented as a set of 0D-element equations. Modelling the cardiovascular system using 0D-methods, requires representation of the main characteristics of the full 3D-model. These characteristics are the viscous losses in the system, the fluid inertia of the transported blood and the blood vessel compliance. Viscous losses can be represented using a resistance element, dissipating energy. Examples of this kind of dissipatory effects are wall friction or turbulent effects. Mainly, in larger blood vessels inertial energy is stored or released due to accelerating or decelerating a mass of fluid and is represented by an inertance element. Additionally, Blood vessels can expand and contract, storing or releasing potential energy in the form of a driving pressure. This effect is called vessel compliance and is accounted for by compliance elements.

Element	Equation	
Resistance/Impedance	$\Delta p(t) = q(t)R$	(Eq. 3.3)
Inertance	$\Delta p(t) = L\dfrac{\partial q}{\partial t}(t)$	(Eq. 3.4)
Compliance	$q(t) = C\dfrac{\partial}{\partial t}(\Delta p)(t)$	(Eq. 3.5)

Table 3.1 - 0D-modelling components and their mathematical description as a function of pressure, Δp and flow q.

The previously described characteristics can be translated to 0D-elements relating pressure over an element Δp and flow through an element q. Table 3.1 presents the equations from which to build most 0D-models.

R represents the resistance, L represents the fluid inertance and C represents the vessel compliance. If the resistance is frequency dependent R is referred to as an impedance. For ease of notation, the pressure differential Δp will simply be denoted as p throughout the remainder of the thesis unless noted otherwise. It is possible to derive eqs. 3.3-3.5 from a 1D-description of the Navier-Stokes equation which has been omitted for the current discussion.

3.4. Numerical Implementation

Numerical implementation of 0D-boundary conditions presents a set of challenges. Firstly, multiple temporal discretisation schemes exist under fluent which need to be available for the 0D model and computable in a parallel computing environment. Secondly, multiple choices exist for coupling pressure and flow at the interface between 3D and 0D models and need to be implemented but which are independent of the choices available within Fluent. And lastly, the model needs to be made accessible through graphical and text-based user interfaces (GUI and TUI respectively) to be of value to the scientific community.

3.4.1.   Temporal Discretisation

An expression of temporal derivative terms in the WK equations (eqs. 3.1-3.2) needs to be found in terms of pressure and flow at discrete points in time. Often an

exact description of these terms does not exist and must be approximated. Taylor expansions can be used to approximate derivative terms using the definition of a derivative known from elementary calculus. A Taylor expansion of a function $f(x)$ of order n is defined as:

$$f(x) = \sum_{i=0}^{n} \frac{f^{(i)}(a)}{1!}(x-a)^i + O\big((x-a)^{i+1}\big) \qquad \text{(Eq. 3.6)}$$

In which $f^{(i)}(a)$ implies the ith-derivative of $f(a)$ while the last term on the right-hand side represents the truncation error. Depending on the way the Taylor-series is approximated, backward, forward and central difference expressions can be derived for various derivative terms. For consistency, the temporal derivative schemes within Fluent are maintained within the windkessel model. The used derivative schemes are a first and second order backward difference scheme (BDF1 and BDF2 respectively) which are the most commonly used schemes for these types of models:

BDF1
$$\frac{df(t)}{dt} = \frac{f(t) - f(t-h)}{h} + O(h) \qquad \text{(Eq. 3.7)}$$

BDF2
$$\frac{df(t)}{dt} = \frac{3f(t) - 4f(t-h) + f(t-2h)}{2h} + O(h^2) \qquad \text{(Eq. 3.8)}$$

The derivative approximations in eqs. 3.7-3.8 depend only on values at preceding timesteps allowing them to be solved. Both equations can be represented by a general equation and picking appropriate values for the α-coefficients:

BDF $\qquad \dfrac{df(t)}{dt} \cong \dfrac{\alpha_0 f(t) + \alpha_1 f(t-h) + \alpha_2 f(t-2h)}{h}$ (Eq. 3.9)

The general discretised equation for the windkessel model implemented under Fluent can be derived by substituting eq. 3.9 into eq. 3.2:

$$
\begin{aligned}
Q_{in}(t) = \left(\frac{C\alpha_0}{\Delta t} - \frac{1}{R}\right)\left(P_{in}(t) - Q_{in}(t)Z\right) \\
+ \left(\frac{C\alpha_1}{\Delta t}\right)\left(P_{in}(t-\Delta t) - Q_{in}(t-\Delta t)Z\right. \\
+ P_c(t-\Delta t)) \\
+ \left(\frac{C\alpha_2}{\Delta t}\right)\left(P_{in}(t-2\Delta t) - Q_{in}(t-2\Delta t)Z\right. \\
+ P_c(t-2\Delta t)) + \left(\frac{C\alpha_0}{\Delta t}\right)P_c(t) + \frac{P_{out}(t)}{R}
\end{aligned}
$$

(Eq. 3.10)

To re-iterate, the 2-element windkessel model can be derived by setting Z=0. The BDF1 discretisation is obtained by setting $\alpha_0 = 1, \alpha_1 = -1$ and $\alpha_2 = 0$. The BDF2 discretisation is obtained by setting $\alpha_0 = \frac{3}{2}, \alpha_1 = -2$ and $\alpha_2 = \frac{1}{2}$.

3.4.2. Coupling

Coupling pressure and flow between models, is most commonly done explicitly or semi-implicitly, depending on the time during model calculation when information is exchanged. Explicit coupling at the boundary considers variables at the connecting boundary to be evaluated at the previous time step given by:

$$q_{3D}(t,i) = p_{wk}(t-1, i_{end})$$ (Eq. 3.11)

$$p_{wk}(t,i) = q_{3D}(t-1, i_{end})$$ (Eq. 3.12)

i indicating the iteration number and i_{end} indicating the final iteration. i_{end} Has been used to reflect the fact that the solver for the 3D geometry can be considered iterative despite the coupling being non-iterative at the boundary. The semi-implicit coupling can be written similarly as:

$$q_{3D}(t,i) = p_{wk}(t,i) \qquad \text{(Eq. 3.13)}$$

$$p_{wk}(t,i) = q_{3D}(t,i-1) \qquad \text{(Eq. 3.14)}$$

The windkessel pressure is determined at beginning of an iteration step using the flow from the previous iteration step. Within an iteration loop there is an explicit dependence of the windkessel pressure with respect to the 3D flow which is the reason for referring to this scheme as semi-implicit. A fully implicit coupling would require the equations of the both the 3D-model and WK-model to be solved simultaneously or the computation of an infinite iteration loop, which is not possible using a segregated solver approach.

At any point in time, the windkessel pressure needs to be prescribed as a static pressure. However, at backflow through a pressure outlet, Fluent (at the time of writing) is only capable of prescribing the total pressure instead of the static pressure at a BC. This means that at backflow the pressure at the boundary is prescribed as the static pressure produced by the windkessel model, plus the dynamic pressure determined by the inflow over the boundary from either the previous time-step or the previous iteration.

3.4.3. *Software Implementation*

The 2- and 3- element windkessel models have been implemented as an extension to Fluent using the ANSYS Application Customization Toolkit (ACT). Three processes are necessary for this extension to function: model evaluation, a user interface and a communication interface between the both.

Model evaluation has been implemented as a user defined function (UDF). UDFs are compilable scripts of computer code written in C and/or C++, capable of adding custom functionality not readily available in Fluent. The UDF consists of a set of functions to compute the flow through a boundary and subsequently prescribe a pressure boundary corresponding to the WK-model previously described. Additionally, effort was spent making these functions applicable in a parallel computing environment. While the model itself is not computationally expensive this parallelisation is required for the parallel functionality of simulations under Fluent.

A graphical user interface, displayed in fig. 3.2, has been created using the scheme programming language and is interpreted by the fluent environment:
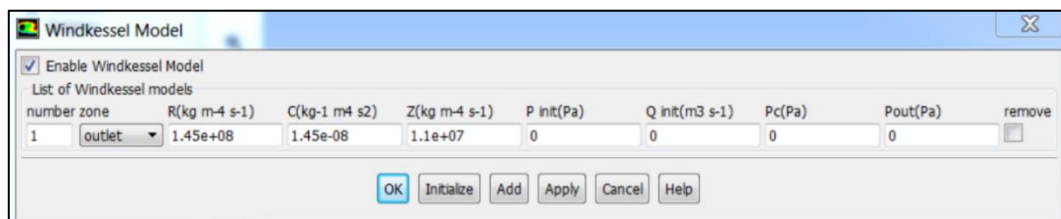
Fig. 3.2 - Depiction of the graphical user interface for a single outlet.

It allows for definition and initialisation of the windkessel models as well as selection of the coupling-scheme. Additionally, a text-based user interface is available that can be used when it is required to automate simulations using Fluent journal scripts, manage additional settings and to communicate values and messages back to the user. The interface as a complete package automates the correct communication between the UDF and the Fluent front end, the definition of the WK models and initialisation.

Communication of variables and parameters between the interface and the UDF is accomplished using RP variables. RP variables can be transmitted from the scheme environment to the UDF environment and vice versa.

3.5. Analytical Model

An analytical model is used for the verification of the iterative model in Fluent. Verification is important as it is the process required to guarantee that a model works as intended. Additionally, validation is often required to assure that the model correctly represents the required physical behavior. Model validation is only possible in the presence of validation data from the system being modelled. For example, from medical data or in-vitro laboratory set-ups.

An analytical relation between the pressure and flow of the windkessel model can be derived via the frequency domain and under the assumption that the input signal

can be represented by a finite Fourier series. Derivation of the inlet pressure function is demonstrated below for a simple harmonic input function Q_{in}:

$$Q_{in} = a_n \cos(\omega_0 t) + b_n \sin(\omega_0 t) \qquad \text{(Eq. 3.15)}$$

With a_n and b_n some arbitrary coefficients, angular frequency ω_0 and time t. Firstly, the Fourier transform from eq. 3.16 below can be used to derive a transfer function from eq. 3.2 given in eq. 3.17. Secondly, the input flow can be transformed to the frequency domain to complete the pressure description of all components in the frequency domain:

$$F(\omega) = \text{F}\{f(t)\} = \int_{-\infty}^{\infty} f(t)e^{-i\omega t}dt \qquad \text{(Eq. 3.16)}$$

$$\frac{P_{in}(\omega)}{Q_{in}(\omega)} = H_{wk3}(\omega) = \frac{R - i\omega CR^2}{1 + (\omega CR)^2} + Z \qquad \text{(Eq. 3.17)}$$

$$Q_{in}(\omega) = \pi\left(a_n\big(\delta(\omega - \omega_0) + \delta(\omega + \omega_0)\big)\right)$$
$$+ \pi\left(\frac{b_n}{i}\big(\delta(\omega - \omega_0) - \delta(\omega + \omega_0)\big)\right) \qquad \text{(Eq. 3.18)}$$

Where $\delta(t)$ is the dirac-delta function. The windkessel transfer functions describe the characteristic impedance. Combining eqs. 3.17-3.18 and subsequently using the inverse Fourier transform defined in eq. 3.19, the time domain solution for the inlet pressure of the 3-element windkessel can be derived, given in eq. 3.20:

$$f(t) = \text{F}^{-1}\{F(\omega)\} = \frac{1}{2\pi} \int_{-\infty}^{\infty} f(t)e^{i\omega t}d\omega \qquad \text{(Eq. 3.19)}$$

$$P_{in}(t, \omega_0) = \frac{a_n}{k_3} (k_1 \cos(\omega_0 t) + k_2 \sin(\omega_0 t))$$

$$+ \frac{b_n}{k_3} (k_1 \sin(\omega_0 t) - k_2 \cos(\omega_0 t))$$

(Eq. 3.20)

$$k_1 = R + k_3 Z; \quad k_2 = \omega C R^2; \quad k_3 = 1 + (\omega C R)^2;$$

Arbitrary functions can be approximated as a Fourier series according to:

$$f(t) = \frac{a_0}{2} + \sum_{n=1}^{\infty} a_n \cos\left(\frac{2\pi n t}{T}\right) + \sum_{n=1}^{\infty} b_n \sin\left(\frac{2\pi n t}{T}\right) \quad \text{(Eq. 3.21)}$$

Note that this is a linear combination of the harmonic inflow function from the starting point. Therefore, a general result is obtainable for the pressure at the windkessel outlet from a linear combination of the pressure solution given by eq. 3.20:

$$P_{wk}(t) = \frac{a_0(R + Z)}{2} + \sum_{n=1}^{\infty} P_{in}\left(t, \frac{2\pi n}{T}\right) \quad \text{(Eq. 3.22)}$$

3.6. Verification

The Fluent implementation is verified against the analytical model at various time-step sizes to determine the modelling error due to the implementation of the WK model. Conditions for the verification experiment are taken to be similar to those in a small section of the aorta. Therefore, an inviscid fluid through a small section of axisymmetric pipe of length $l = 5[cm]$ and radius $R = 1[cm]$ is assumed. BCs include a volume flow BC at inlet, a windkessel pressure BC at outlet and a no-slip condition at the vessel wall. Fluid density equals $\rho = 1056[kg \cdot m^{-3}]$. The

60

windkessel model represents a lumped model of the entire circulation and can be tuned from a general assumption of the average blood pressure, average flow and time constant of the system, leading to:

$R[Kg \cdot m^{-4} \cdot s^{-1}]$	$Z[Kg \cdot m^{-4} \cdot s^{-1}]$	$C[Kg^{-1} \cdot m^4 \cdot s^2]$
$1.414 \cdot 10^8$	$1.414 \cdot 10^7$	$1.286 \cdot 10^{-8}$

Table 3.2: windkessel parameters used for verification

The procedure for the analytical model is implemented under MATLAB but does not contain the description of the pipe. Due to the absence of viscosity the pipe segment can be separately modelled as an inductor with inductance $L = \frac{l\rho}{\pi R^2} = 1.681 \cdot 10^5 [Kg \cdot m^{-4} \cdot s^{-2}]$. The pressure drop over the inductance is only a function of the flow through it and can be calculated a-posteriori according to:

$$\Delta p_I = L\left(\frac{2\pi n}{T}\right)\left(\sum_{n=1}^{\infty} b_n \cos\left(\frac{2\pi nt}{T}\right) - \sum_{n=1}^{\infty} a_n \sin\left(\frac{2\pi nt}{T}\right)\right) \quad \text{(Eq. 3.23)}$$

While different variations of the described time-scheme and solvers were tested, the results below were performed using the BDF2-scheme and the SIMPLE solver. Shown in figure 3.3 is the outlet pressure for both the analytical model and the simulation data, given a sinusoidal inflow with an amplitude of $5 \cdot 10^{-5} [m^3 \cdot s^{-1}]$ at a time-step size $\Delta t = 10^{-2}[s]$. While the results from the implicitly coupled model simulation closely follow the analytical model, the explicitly coupled model experiences a time-delay equal to the simulation time-step size. This is expected as the flow BC for the windkessel model, originating from the outlet of the pipe,

experiences the same time-delay. However, this does introduce a simulation error as will be shown below.
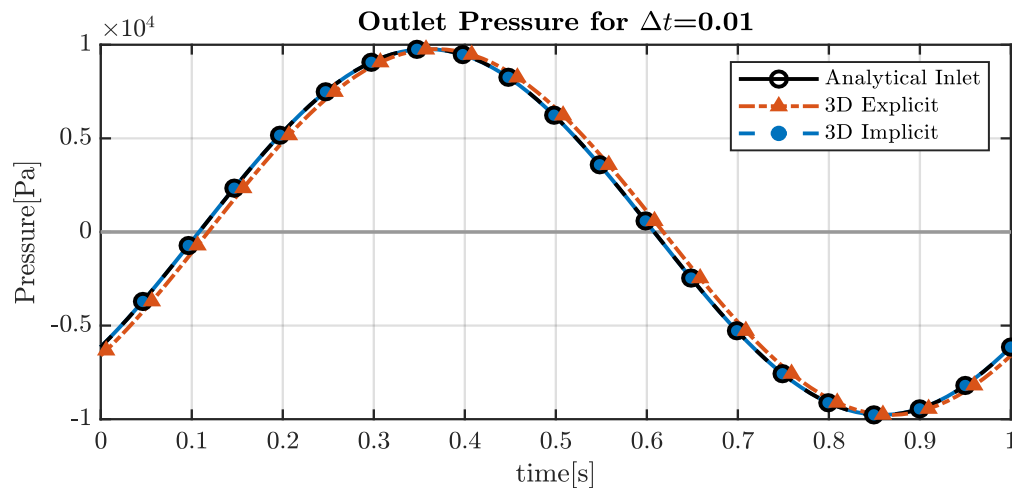
Fig. 3.3 - Time-delay of the explicitly coupled model simulation(red) with respect to the analytical model(black) and implicitly coupled model(blue).

Shown in fig. 3.4 is the normalised maximum error for several time-step sizes with respect to the analytical model. On the left of fig. 3.4, the error is normalised with respect to the root-mean square (RMS) value of the analytical model pressure. At a time-step of $\Delta t = 10^{-3}[s]$ the error of the explicitly coupled model becomes smaller than the 1% threshold while the implicitly coupled model is below this threshold regardless of the time-step size in this range. The error produced solely by the windkessel model can be obtained by correcting the explicitly coupled model results for the time-delay. It can then be seen that the error resulting from the windkessel model alone is comparable with the error from implicit coupling.
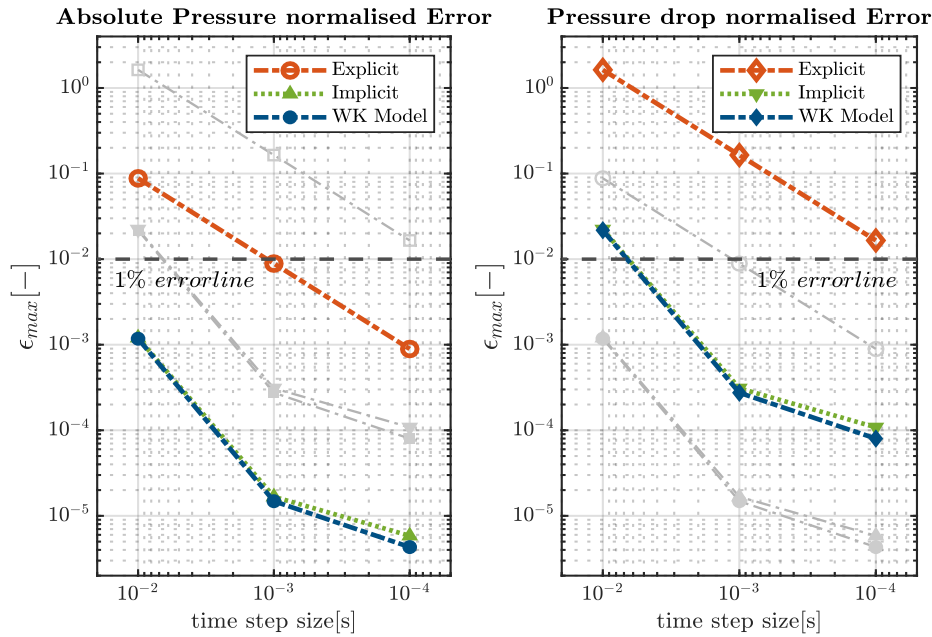
Fig. 3.4 - Pressure error compared to the analytical model, normalised to RMS of pressure(left), normalised to RMS of 3D pressure drop (right). WK-model indicates results of explicit simulation corrected for time-delay.

Additionally, it appears that the error for the implicit coupling method might converge to a minimum value. Upon closer inspection it was found that the limiting factor for the decrease in error in this case was the convergence norm for the residuals of the 3D simulation, which was set at $10^{-5}[-]$. From these results it could wrongfully be concluded that a time-step size of $\Delta t = 10^{-3}[s]$ is sufficient, regardless of the used coupling method. The problem in determining the time-step size using the previous results, lies in the choice of pressure reference. Reporting the error in terms of the absolute pressure scale of the problem is a common practice. However, this choice of pressure reference is arbitrary and does not properly reflect the scale of the driving forces within the 3D geometry of the problem. Therefore, for the simple pipe problem presented, a better reference is the

pressure differential over the length of the pipe. Shown on the right of fig. 3.4 is the simulation error normalised to the RMS value of the pressure differential over the pipe. It demonstrates for the explicit coupling, that even at a time-step of $\Delta t = 10^{-3}[s]$ an error of 20% can result and none of the considered time-steps satisfy the 1% threshold. While for this specific case the velocity in the 3D geometry is unaffected, this error can become significant when multiple pressure outlets are present, possibly affecting the flow distribution between outlets.

The same analysis process has been repeated for a pulsatile flow profile to arrive at a more relevant conclusion for real-world applications and is shown in fig. 3.5. Note that the pressure differential between the in- and outlet is of order of magnitude $O(10^2)$ while the average pressure is of the order $O(10^4)$.
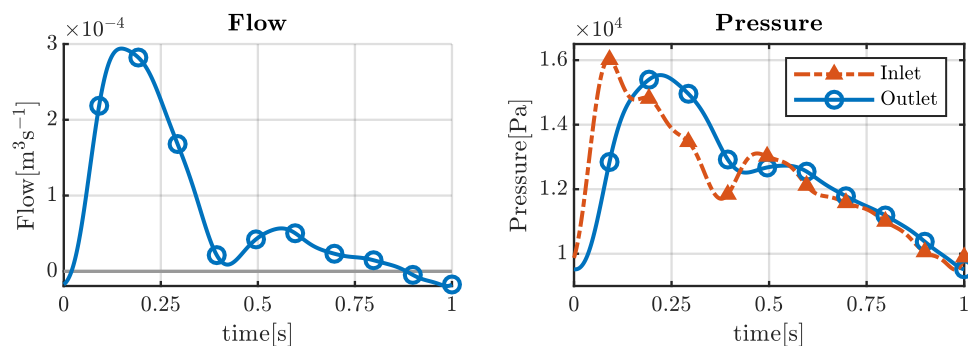
Fig. 3.5 - Analytical model results for pulsatile flow (left) and corresponding in-, outlet pressure(right).

Comparing the error of the pulsatile inflow to that of the sine inflow, fig. 3.6, demonstrates the relevance of the pressure reference choice more clearly.
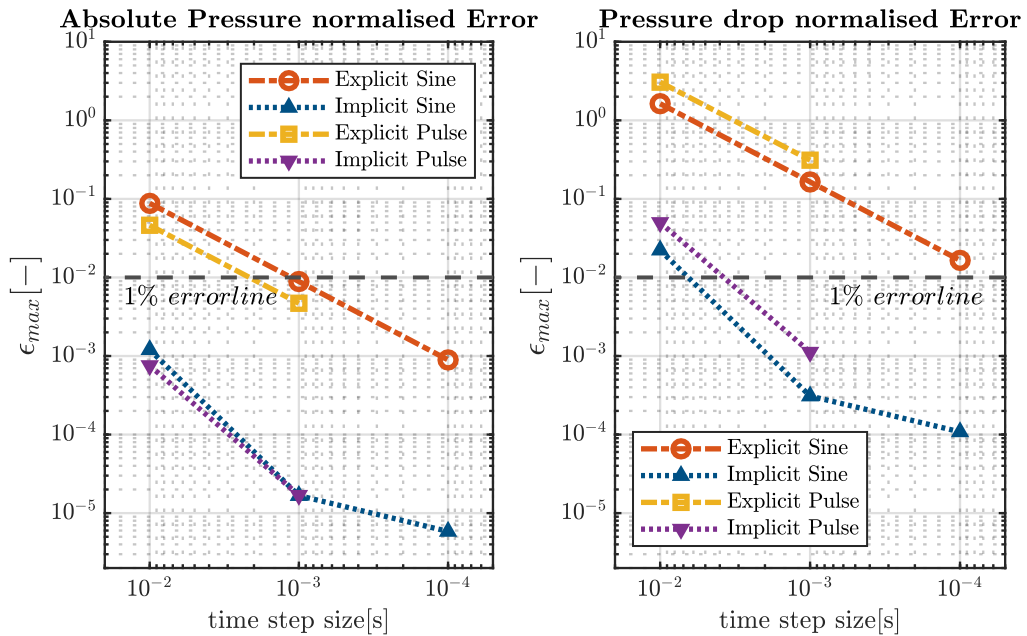
Fig. 3.6 - Pressure error compared to the analytical model, displayed for sine and pulsatile inflow

BCs. normalised to RMS of pressure(left), normalised to RMS of 3D pressure drop (right).

The error for the pulsatile flow appears smaller than that of the sine profile, when taking the RMS of the pressure as a reference and comparing equal coupling schemes (fig 3.6, left). However, the inverse is true, when taking the RMS of the pressure differential as a reference (fig. 3.6, right). This is due to the average pressure of the pulsatile flow being higher, yet the RMS value of the pressure differential driving the flow, is smaller. Aside from these differences, the results for this relatively short pipe segment are comparable between the sine- and pulsatile-inflow cases. The idea of using pressure differentials as reference is extensible to the multiple-outlet case. As an example, the reference pressure can be the minimum pressure differential, taken pairwise between all flow and pressure boundaries. This ensures that a maximum error between all boundary conditions can be guaranteed.

3.7. Simulation periodicity

It should be noted that the results shown above are from the final cycles of simulations with a total simulation time of $\sim 10[s]$. This relatively long simulation time is necessary to arrive at periodicity of the pressure curves for each consecutive cycle but can be avoided by prescribing appropriate initial conditions.

At the start of the simulation, the compliance present in the system needs to be charged to an appropriate average value. Initial values for pressure and flow were estimated, at in- and outlet from the analytical model implementation for the current time-step, previous time-step and the before previous timestep t_0, $t_0 - 1$ and $t_0 - 2$ respectively. These values were used as initial conditions at the boundaries and approximate initial pressure and flow fields were determined using Fluent's built-in hybrid initialization. Starting from any initial conditions not satisfying the conditions at the last cycle of the model, the time required to arrive at an acceptable periodicity is related to the Windkessel RC-time. Fig. 3.7 demonstrates this by plotting the equation of a charging capacitor, as the RC-predicted average in eq. 3.24, against the analytical average pressure over a $1[s]$ time frame. Both curves overlap for all practical purposes. It can be derived that the average pressure changes less than 5% after 3 RC-times and 1% after 4.62 RC-times. At a time-constant of $\sim 2[s]$ the solution is converged from the 6$^{\text{th}}$ or the 10$^{\text{th}}$ cycle respectively.

$$P_{avg}(t) = \frac{Q_{avg}}{(R + Z)} \left(1 - e^{-\frac{t}{(R+Z) \cdot C}} \right) \qquad \text{(Eq. 3.24)}$$
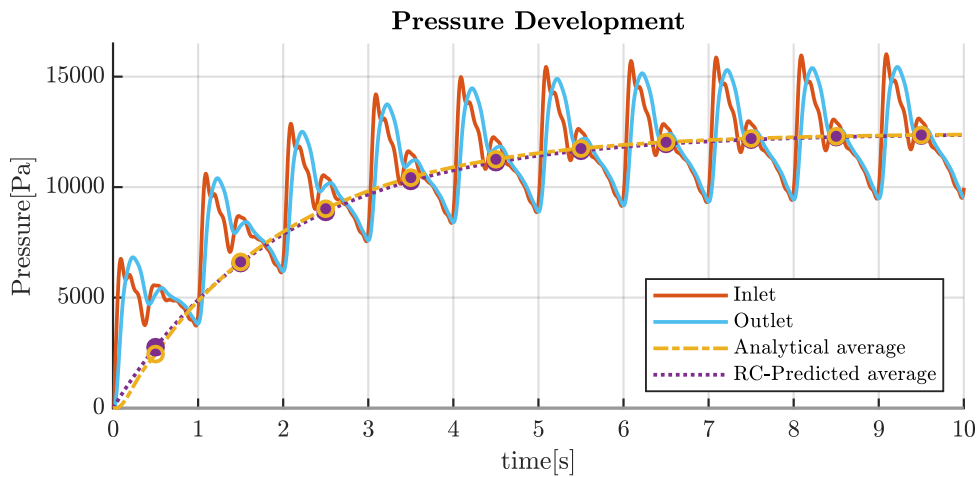
Fig. 3.7 - Average Windkessel pressure predicted from RC-model vs. derived from

analytical model (left). Zoom of Analytical Inlet and Outlet pressure of last cycle(right).

In conclusion, a time-step size of $\Delta t = 10^{-3}[s]$ is deemed sufficient to obtain an acceptable level of accuracy for the implicit coupling method. For the explicit coupling, a time-step size of $\Delta t = 10^{-4}[s]$ could be considered acceptable in practice at an error of 1.65% for the sine profile inflow.

3.8. Discussion

The 2/3-element WK models have been implemented as an ACT package under fluent, at the disposal of the scientific community. Verification of the model has demonstrated the accuracy of the windkessel model and the implemented coupling conditions including the global requirements for the numerical simulation using CFD. Additionally, a case was made to scale relative errors by the pressure differential as opposed to the absolute pressure as this provides a better reference for the scale of the problem.

Although for explicit coupling a time-step size of $\Delta t = 10^{-4}[s]$ is suggested for sufficient accuracy, sizes of this magnitude or smaller are not useful in practice, due to large mesh size requirements combined with the long total simulation time common for hemodynamical simulations. The error threshold of 1% can be considered overly stringent depending on the specific case. Lastly, due to the similarity of the results between the sine- and pulsatile-inflow cases and the reasons mentioned above, the error of the pulsatile flow was not explored at the smallest time-step size.

Chapter 4

4. Multiscale-model coupling stability

4.1. Introduction

The analysis of a simulation driven by clinically derived measurements from chapter 2 highlighted the importance of two aspects. Firstly, the importance of coherence between measured pressure and flow signals at the boundary and secondly an appropriate choice of boundary condition types. Using additional physical models to impose BCs for a simulation simplifies the enforcement of pressure and flow coherence at the boundaries and allows for more freedom regarding the choice of boundary condition type. This brings us within the domain of multiscale-models. It is well known that numerical errors and instabilities can arise for modelling approaches due to numerical discretisation, integration and differentiation schemes. However, Model-coupling can lead to similar numerical errors and instabilities. The focus of this chapter is on the numerical coupling schemes used in the coupling of multiple fluid dynamics models and the stability considerations that accompany these coupling schemes.

Numerous approaches exist to numerically combine and couple models which fall into the categories of monolithic modelling approaches and partitioned modelling approach. For cardiovascular flows, these two approaches are often addressed in FSI contexts where a structural model is coupled to a fluid model. In a monolithic approach the modelling equations of separate models are fully coupled by solving all equations simultaneously as described in [53, 54, 55]. The main advantages of this approach are their robustness and accuracy. However, a detailed understanding and consistent implementation of the equations of each model involved is required

and existing numerical code often needs to be heavily modified. Often these requirements are too restrictive in a practical setting and few commercial codes of this type exist at the current time.

In a partitioned modelling approach, models are considered separately. Models are coupled by imposing equivalence of state variable at common coupling interfaces between models [55, 56, 57]. No knowledge is required of the numerical implementation as long as the required boundary conditions are known. A partitioned approach therefore allows combining existing numerical codes, non-consistent modelling descriptions among different numerical codes and is less susceptible to implementation difficulties related to changes in the separate sub-models. Essentially, the models coupled to one-another can be considered to be black-box models. Advancements in partitioned approaches potentially have a wider range of application. Therefore, this approach is highly preferred in the current context due to the availability of advanced numerical solvers within the ANSYS software suite for different types of physics and models.

Within the context of partitioned modelling approaches for transient simulations the most commonly applied coupling conditions at coupled boundaries include explicit and implicit iterative schemes. A study by Moghadam et al. [58] investigated several coupling techniques noting the improved stability and convergence rate of (semi-)implicit coupling schemes. Similar conclusions were drawn regarding FSI couplings and the reader is referred to the review article by

Fernandez [59] (which itself refers to [60, 61]) . However, for the lumped parameter coupling of Moghadam, a more consideration of the stability is lacking.

Stability of these methods can be analysed using various techniques. The current chapter will focus on analysing the conservation of mass, momentum and energy for sets of coupled 0D models of increasing complexity in order to assess stability of the model. A study by Formaggia [62] considers stability from an energy standpoint within complete 3D and 1D domains from a theoretical point of view. The current study seeks to explore the stability following a similar path only regarding the interface conditions of 0D models and to take a closer look and some of the mechanisms involved. Model coupling principles applicable to complex models are often demonstrable on simple test models which are better suited for obtaining a qualitative understanding of the processes involved. Additionally, these models are easier to implement, less computationally expensive and sometimes analytical solutions are available.

At the start of this chapter a harmonic oscillator model is used to introduce energy conservation for 0D fluid dynamics models. As this model is a non-dissipative closed-loop model and an analytical solution can be derived, this model lends itself to studying the energy conservation properties of different numerical schemes and different coupling conditions. An analytical solution is derived which is used as validation for both a monolithical and a partitioned 0D modelling approach. The

monolithic model is used to consider the effects of numerical discretisation while the partitioned approach is used to study the effect of coupling schemes.

Thereafter a 0D model of an arterial bifurcation is utilized to explore the stability properties of more commonly encountered models in hemodynamics. This includes dissipative effects and intends to look at the stabilizing effect of dissipators in potentially unstable modelling systems.

4.2. Harmonic Oscillator Model

The concept of stability is introduced for a model problem known as an LC-Oscillator. This type of circuit is well-known in the field of electronics and can be used for harmonic signal generation or as a band-pass filter. Its name derives from the LC-circuit depicted on the right of fig. 4.1 consisting of a capacitor and an inductor.
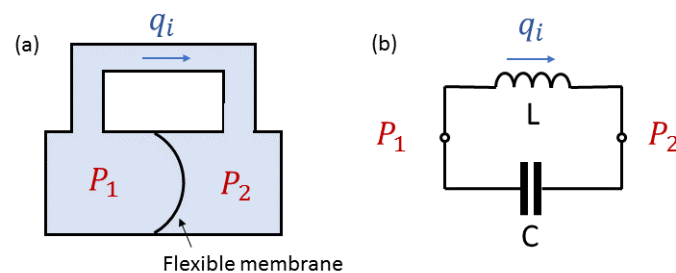
Fig 4.1 - Harmonic Oscillator for a fluid(a) consisting of elastic membrane compliance and connecting pipe modelling fluid inertia. (b) equivalent electrical analogue LC-circuit.

The equivalent harmonic oscillator in the fluid domain, can be thought of as two chambers separated by a flexible membrane but connected through a separate pipe,

73

depicted on the left of fig. 4.1. The membrane and chambers serve as a compliance in the system storing elastic energy. Depending on the direction in which this membrane is stretched, one of the chambers will hold a larger volume than the other, the membrane will exert a force on the fluid chambers and a pressure differential exists between them. This pressure differential causes fluid to flow from one chamber to the other, converting elastically stored energy into kinetic energy by moving fluid through the connecting pipe. Storing kinetic energy is the function of an inertance in this context, hence the mass of fluid flowing through the connecting pipe serves as an inertance. No viscous losses are modelled within the system and the system is therefore an ideal LC-Oscillator.

An ideal LC-oscillator has several advantageous properties as model problem for energy conservation. Firstly, as mentioned before, there are no dissipative elements and the system is otherwise isolated. Therefore, any energy stored initially on either the inertance or the compliance will remain within the system. Secondly, unless there is no initial pressure differential exists and the fluid is at rest, an LC-oscillator will have a transient behaviour for any point in time. Lastly, an analytical solution for this model exists under some assumptions for the inflow, because of the simplicity of this system. This makes it straightforward to compare numerical schemes and determine the numerical error with respect to a known solution.

The model can be constructed from the compliance and inertance elements introduced for the windkessel discussion, i.e. eqs. 3.4-3.5, and modelled

monolithically. In the context of the model coupling discussion, these elements can also be considered as separate sub-models and thus modelled as partitioned models. Both the monolithical and the partitioned modelling approach are implemented as state-space models for the current study with the states of the models and sub-models being either pressure $p(t)$ or flow $q(t)$.

In the partitioned approach, the models are coupled at pressure nodes P_1 and P_2 in fig. 4.1b. Recognising that the flow and pressure differential experienced by each element are of equal magnitude, the pressure differential and flow can be defined as $p = p_1 - p_2 \equiv p_L$ and $q = q_L$ respectively, with flow in the direction from node 1 to node 2. Kirchhoff's voltage law dictates that around a closed loop the algebraic sum of potential should be zero. Therefore, it must hold that $p_L = -p_C$. These state variables fully describe the system, with the equations and their corresponding signs given by eqs. 4.1-4.2. Note that the state-variables do not depend on themselves.

$$p(t) = L \frac{\partial q(t)}{\partial t} \qquad \text{(Eq. 4.1)}$$

$$q(t) = -C \frac{\partial p(t)}{\partial t} \qquad \text{(Eq. 4.2)}$$

4.2.1.   *Analytical model*

The equations for the LC-Oscillator, satisfy an initial value problem of 2nd-order. A derivation of the general solution is presented below. Taking the time derivative of by eqs. 4.1-4.2 and combining both equations, a set of 2nd-order differential equations with constant coefficients can be derived:

$$\frac{d^2q(t)}{dt^2} = -\frac{1}{LC}q(t) \qquad \text{(Eq. 4.3)}$$

$$\frac{d^2p(t)}{dt^2} = -\frac{1}{LC}p(t) \qquad \text{(Eq. 4.4)}$$

From differential calculus it is known a particular solution exists for this problem, presented in eq. 4.5. Substituting this result back into either eq. 4.3 or 4.4, the same characteristic equation can be derived having 2 particular solutions for λ, presented in eq. 4.6.

$$\varphi = C_i e^{\lambda t} \qquad \text{(Eq. 4.5)}$$

$$\lambda^2 C_i e^{\lambda t} = -\frac{1}{LC} C_i e^{\lambda t} \qquad \text{(Eq. 4.6)}$$

Any linear combination of the particular solutions also satisfies the set of differential equations and the general solution is then given by:

$$\lambda = \pm\sqrt{-\frac{1}{LC}} = \pm i\frac{1}{\sqrt{LC}} \qquad \text{(Eq. 4.7)}$$

$$\varphi(t) = C_1 e^{i\frac{1}{\sqrt{LC}}t} + C_2 e^{-i\frac{1}{\sqrt{LC}}t} \qquad \text{(Eq. 4.8)}$$

In which $\varphi(t)$, is the solution for either $p(t)$ or $q(t)$. This leaves the coefficients C_1 and C_2 to be determined requiring assumptions on the initial conditions. A straightforward choice for the initial conditions, is an initial pressure stored on the compliance $p_C(0) = -P_0$ and zero initial flow through the inductance, $q(0) = 0$. Starting from $\varphi(t)$ as a solution for $q(t)$, eq. 4.9 can be derived from the initial flow condition while eq. 4.10 can be derived using eq. 4.1:

$$C_1 + C_2 = 0 \qquad \text{(Eq. 4.9)}$$

$$i\sqrt{\frac{L}{C}}(C_1 - C_2) = P_0 \qquad \text{(Eq. 4.10)}$$

The unique solution satisfying these equations, indicates that C_1 and C_2 are complex conjugates and we see that eq. 4.8 is satisfied by:

$$q(t) = -\frac{P_0}{2i\sqrt{\frac{L}{C}}}\left(e^{i\frac{1}{\sqrt{LC}}t} - e^{-i\frac{1}{\sqrt{LC}}t}\right) = \frac{P_0}{\sqrt{\frac{L}{C}}}\sin\left(\frac{t}{\sqrt{LC}}\right) \qquad \text{(Eq. 4.11)}$$

Substituting this result back into equation 4.1 gives the solution for $p(t)$ completing the system. The general solution is presented in eqs. 4.12-4.13 including the phase θ. Changing the phase θ of the solution satisfies eqs 3.4-3.5, the relationships for inertance and compliance respectively, but does not directly satisfy the initial conditions posed before.

$$p(t) = P_0\cos\left(\frac{t}{\sqrt{LC}} + \theta\right) \qquad \text{(Eq. 4.12)}$$

$$q(t) = -\frac{P_0}{\sqrt{\frac{L}{C}}}\sin\left(\frac{t}{\sqrt{LC}} + \theta\right) \qquad \text{(Eq. 4.13)}$$

4.2.2. *Monolithic Numerical Model*

The numerical model is solved using a time-stepping approach for a state-space description. Starting from a known state φ_0 at time t_0, the value of a state variable φ at time t can be found by integrating the change of the state variables over time:

$$\varphi(t) = \varphi(t_0) + \int_{t_0}^{t} \frac{d\varphi(t)}{dt} dt \qquad \text{(Eq. 4.14)}$$

Numerically evaluating this equation requires discretisation of the derivative and subsequently of the integral. Additionally, eq. 4.14 holds for a vector of state-variables $\vec{\varphi}(t)$. For the model under consideration, the state-space equations are simply given by rewriting eq. 4.1-4.2 as a function of the time derivatives of the state variables.

4.2.2.1. *Numerical schemes*

A discretised expression for the derivative of a function, can be defined using the previously introduced Taylor expansion in chapter 3. This expansion can be used to derive time-discretisation schemes to help solve the state-space models.

$$f(x) = \sum_{i=0}^{n} \frac{f^{(i)}(a)}{1!} (x - a)^i + O\left((x - a)^{i+1}\right) \qquad \text{(Eq. 4.15)}$$

Along the curve of a function, the same point x is approachable from two initial positions x_0, namely from a forward point $x_0 = x - \Delta x$ or a backward point $x_0 = x + \Delta x$. To obtain 1st-order discretisation schemes, the 1st-order Taylor expansion of a function can be used. Depending on the point from which the function is approximated this expansion is given by eqs. 4.16 and 4.17 below:

$$\varphi(t_0 \pm \Delta t) \cong \varphi(t_0) + \frac{d\varphi(t_0)}{dt} (\pm \Delta t) + O(\Delta t^2) \qquad \text{(Eq. 4.16)}$$

$$\varphi(t_0) \cong \varphi(t_0 \pm \Delta t) + \frac{d\varphi(t_0 \pm \Delta t)}{dt} (\mp \Delta t) + O(\Delta t^2) \qquad \text{(Eq. 4.17)}$$

Where the last term on the right-hand side represents the truncation error. eqs 4.16-4.17 can subsequently be rewritten into its form known from elementary calculus. This leads to the forwards- and backwards-Euler derivative methods:

Forwards Euler

$$\lim_{\Delta t \to 0} \frac{\varphi(t_0 + \Delta t) - \varphi(t_0)}{\Delta t} = \frac{d\varphi(t)}{dt} \cong \frac{d\varphi(t_0)}{dt} + O(\Delta t^2) \quad \text{(Eq. 4.18)}$$

Backwards Euler

$$\lim_{\Delta t \to 0} \frac{\varphi(t_0 + \Delta t) - \varphi(t_0)}{\Delta t} = \frac{d\varphi(t)}{dt}$$

$$\cong \frac{d\varphi(t_0 + \Delta t)}{dt} + O(\Delta t^2) \quad \text{(Eq. 4.19)}$$

the forwards- and backwards-Euler are sometimes referred to as explicit and implicit derivative approximations, respectively. These derivative descriptions are effectively one-sided limits of the derivative which only exists if the left and right limit converge to the same value. A more accurate approximation of the derivative is a central difference-based technique obtained by combining eqs. 4.16 and 4.17 to approximate the limit equation for the derivative:

Central difference

$$\lim_{\Delta t \to 0} \frac{\varphi(t_0 + \Delta t) - \varphi(t_0)}{\Delta t}$$

$$= \frac{1}{2} \left(\frac{d\varphi(t_0)}{dt} + \frac{d\varphi(t_0 + \Delta t)}{dt} \right) + O(\Delta t^3) \quad \text{(Eq. 4.20)}$$

Note that the truncation error is of 3rd order due to the 2nd order terms cancelling out when the taylor expansion from eq. 4.15 is taken as the starting point. The 1st-order central-difference equation approximates the derivative from both the left sided and right sided limit, e.g. the backward- and forward-Euler approximations.

All 3 methods presented approximate $\varphi(t)$ only as function of the values at the previous and current timestep. The current analysis could be repeated for higher order schemes but this out of the scope of the current study. It will be shown in the next section that the central differencing scheme has superior properties regarding model coupling and the conservation of energy compared to the forwards and backwards Euler methods. However, before we can arrive at this step, the time-integral in eq. 4.14 needs to be evaluated for the state variables.

4.2.2.2.   Time advancement

Equation 4.14 can be solved by choosing one of the schemes presented in eqs. 4.18-4.20. Within a time interval, integrating the state-variables from time t to $t + \Delta t$, the discrete derivative is essentially constant. The derivative itself can potentially be updated iteratively within a timestep but eq. 4.14 is solved according to:

$$\varphi(t + \Delta t) = \varphi(t) + \frac{d\varphi}{dt} \int_t^{t+\Delta t} dt = \varphi(t) + \frac{d\varphi}{dt} \Delta t \qquad \text{(Eq. 4.21)}$$

For the selected state variables, the 3 numerical schemes of the system can be rewritten in general form from eqs. 4.1-4.2:

$$\frac{\partial q}{\partial t} = \frac{1}{L} \big((1 - \theta) p(t + \Delta t) + \theta p(t) \big) \qquad \text{(Eq. 4.22)}$$

$$\frac{\partial p}{\partial t} = -\frac{1}{C} \big((1 - \theta) q(t + \Delta t) + \theta q(t) \big) \qquad \text{(Eq. 4.23)}$$

Where θ is either $0, \frac{1}{2}$ or 1 for respectively backward Euler, central difference and the forward Euler schemes. In order to solve this system a state-space description approach is followed according to:

$$\frac{d\vec{x}}{dt}(t) = A\vec{x}(t) + B\vec{u}(t) \qquad \text{(Eq. 4.24)}$$

$$\vec{y}(t) = C\vec{x}(t) + D\vec{u}(t) \qquad \text{(Eq. 4.25)}$$

Where $\vec{x}(t)$ is the state vector, $\vec{u}(t)$ is the input vector, A is the system matrix, B is the input matrix, $\vec{y}(t)$ is the output vector, C is the output matrix and D is the feedforward matrix, As the state variables at the next time steps are unknown a-priori an additional step is required combing eqs. 4.22-4.23 to rewrite the derivative as a function of the previous time step only. The system of equations can be rewritten and rearranged in matrix form as follows:

$$\begin{pmatrix} 1 & -\dfrac{(1-\theta)\Delta t}{L} \\ \dfrac{(1-\theta)\Delta t}{C} & 1 \end{pmatrix} \begin{pmatrix} q(t+\Delta t) \\ p(t+\Delta t) \end{pmatrix} = \begin{pmatrix} 1 & \dfrac{\theta\Delta t}{L} \\ -\dfrac{\theta\Delta t}{C} & 1 \end{pmatrix} \begin{pmatrix} q(t) \\ p(t) \end{pmatrix} \qquad \text{(Eq. 4.26)}$$

$$M_1 \overrightarrow{\varphi(t+\Delta t)} = M_2 \overrightarrow{\varphi(t)}$$

Hence, a solution to the system exists of the form:

$$\frac{d}{dt}\overrightarrow{\varphi(t)} = \frac{\left(M_1^{-1}M_2 - I\right)}{\Delta t}\overrightarrow{\varphi(t)} = A\overrightarrow{\varphi(t)} \qquad \text{(Eq. 4.27)}$$

The system matrix $\mathbf{A}$ is then given by:

$$\mathbf{A} = \frac{1}{\Delta t^2(\theta-1)^2 + CL}\begin{pmatrix} (\theta-1)\Delta t & C \\ -L & (\theta-1)\Delta t \end{pmatrix} \qquad \text{(Eq. 4.28)}$$

It is straight forward to verify that a particular instance of matrix $\mathbf{A}$ follows the form below for the 3 numerical schemes:

Explicit

$$\mathbf{A} = \begin{pmatrix} 0 & \dfrac{1}{L} \\ \dfrac{1}{C} & 0 \end{pmatrix}$$

(Eq. 4.29)

Implicit

$$\mathbf{A} = \frac{1}{\Delta t^2 + CL} \begin{pmatrix} -\Delta t & C \\ L & -\Delta t \end{pmatrix}$$

(Eq. 4.30)

Central-

Difference

$$\mathbf{A} = \frac{1}{\dfrac{\Delta t^2}{4} + CL} \begin{pmatrix} -\dfrac{1}{2}\Delta t & C \\ -L & -\dfrac{1}{2}\Delta t \end{pmatrix}$$

(Eq. 4.31)

As the model has no inputs or useful outputs besides the state variables themselves, matrices $\boldsymbol{B}, \boldsymbol{C}$ and $\boldsymbol{D}$ are not defined. The time advancement is now simply given by fulfilling eq. 4.21 for the state vector and substituting eqs. 4.28. In short, this implies that the derivative of the state vector is computed and used in a 1st-order Taylor approximation to estimate the states at the next time step, with the end result presented in eq. 4.32.

$$\overrightarrow{\varphi(t + \Delta t)} = \overrightarrow{\varphi(t)} + \frac{\overrightarrow{d\varphi(t)}}{dt}\Delta t = (\boldsymbol{I} + \mathbf{A}\Delta t)\,\varphi(t)$$

(Eq. 4.32)

This description was chosen to adhere to the general form of ordinary differential equation solvers and allows for replacement of the presented descriptions by readily available ODE-solvers (as for example present in Matlab).

4.2.3. *Energy Conservation*

For a lumped-parameter 0D-system represented by the state variables pressure $p(t)$ and flow $q(t)$ there is no implicit notion of mass or momentum conservation within the system. These conservation laws can be re-introduced by making appropriate assumptions. However, it is more interesting to consider the conservation and flow

of energy across the system boundaries. Therefore, it is required to consider a 0D energy transport equation. As it will be shown subsequently, the dissipation and storage of energy for a system can be related to the pressure and volume flow within the system and jointly represented by the energy transported.

The change of energy of a system ΔE can be related to the work imposed on a system. It is known from thermodynamics that the change of energy of a system is equal to the mechanical work imposed on the system plus the heat added to the system over time. No heat can be added or removed for this specific case since it is assumed that all components are isothermic and no dissipation occurs. The change of energy then follows as:

$$\frac{dE}{dt} = \frac{dW}{dt} \equiv P$$
(Eq. 4.33)

Where the amount of work per unit time is defined to be the power P. In the absence of body forces, energy can only flow in over the boundaries of the sub-systems. Therefore, if the work imposed on the boundaries of a system is known, the energy change within that system is also known.

The total amount of work can be derived for a fluid traveling along a segment of pipe. Work is defined as the force F acting through a distance s and can be applied infinitesimal fluid parcels. The distance dS_{in} (eq. 4.34) a fluid parcel passes per time increment and the force acting on this fluid element dF_{in} (4.35) are equal to:

$$dS_{in} = vdt \qquad \text{(Eq. 4.34)}$$

$$dF_{in} = \frac{dp}{dz}dA \qquad \text{(Eq. 4.35)}$$

To find the work exerted on the entire pipe, the work on separate fluid parcels has to be integrated over the volume within the pipe. Following the definition of work in eq. 4.36 below, it can be shown that this volume integral can be approximated by:

$$W = \int F \cdot ds = \int \left(\iiint \frac{dp}{dz} dz dA \right) vdt$$
$$= \int (p_{in} - p_{out}) A_0 \, vdt \qquad \text{(Eq. 4.36)}$$

Therefore, the time derivative of work combined with the equality $q = vA$, simplifies to:

$$\frac{dW}{dt} = \frac{dE}{dt} = \Delta p(t) q(t) \qquad \text{(Eq. 4.37)}$$

Eq. 2.58 implies that the energy change of this type of fluid system is equal to the flow q through that system along or against a potential field Δp. A certain amount of potential energy flows in and out over the boundaries of a system and gets converted into a different form of energy or dissipated into heat.

The amount of energy stored or dissipated by a system, otherwise known as the change in total energy of that system, can be found by integrating eq. 4.37 over time. Using the equations for the 0D-components eqs. 3.3-3.5, energy dissipation and storage equations can be derived on a component level:

Resistance	$$\Delta E_r = \int_{t_0}^{t} pq\,dt = \int_{t_0}^{t} Rq^2\,dt$$	(Eq. 4.38)
Inertance	$$E_L = \frac{L}{2}q^2$$	(Eq. 4.39)
Compliance	$$E_C = \frac{C}{2}p^2$$	(Eq. 4.40)

4.2.3.1. Analytical model

At this point, analytical descriptions of pressure and flow are known from eqs. 4.12-4.13 in addition to a description of the energy storage and dissipation of our 0D components. Analytical energy equations can therefore be derived separately for the compliance and inertance components as well as the total energy of the model:

$$E_L(t) = \frac{P_0^2 C}{2}\sin^2\left(\frac{t}{\sqrt{LC}} + \theta\right) \qquad \text{(Eq. 4.41)}$$

$$E_C(t) = \frac{P_0^2 C}{2}\cos^2\left(\frac{t}{\sqrt{LC}} + \theta\right) \qquad \text{(Eq. 4.42)}$$

$$E_t = E_C + E_L = \frac{P_0^2 C}{2}\left(\sin^2\left(\frac{t}{\sqrt{LC}} + \theta\right) + \cos^2\left(\frac{t}{\sqrt{LC}} + \theta\right)\right)$$

$$E_t = \frac{P_0^2 C}{2} \qquad \text{(Eq. 4.43)}$$

In which E_L is the energy stored in the inertance, E_C is the energy stored in the compliance and E_t is the total energy contained in the LC-oscillator. Note that the energy of the total system is constant and equal to the initial energy stored on the compliance due to the choice of initial conditions. The magnitude of the energy stored on the separate components together is thus equal to the initial energy on the

compliance. However, both signals are out of phase as when the capacitor is fully

charged no energy is stored on the inertance and vice versa.

4.2.3.2. *Numerical model*

For the analytical solution of the system, the conservation of energy was analyzed

by considering the energy stored by each separate component. In a more complex

coupled 3D-nD model it is more challenging to determine each separate element of

energy storage or dissipation and detailed knowledge about the system is required.

Another method of analyzing the storage of energy is to consider the flow of energy

across the boundaries of the system. As the solution of the system is already

calculated, deriving the energy contained in the system is purely a post-processing

step. However, the conservation of energy should follow the same integral

presented in Eq. 4.14, substituting φ by E.

$$E(t) = E(t_0) + \int_{t_0}^{t} \frac{dE(t)}{dt} dt \qquad \text{(Eq. 4.43)}$$

The energy derivative in eq. 4.43 can be rewritten as a function of pressure and flow

using equation 4.37. Utilizing the chain rule for differentiation, eq. 4.43 becomes:

$$E(t) = E(t_0) + \int_{t_0}^{t} \left(q(t) \frac{dp(t)}{dt} + p(t) \frac{dq(t)}{dt} \right) dt \qquad \text{(Eq. 4.44)}$$

It is important to recognise that due to discretisation of the system of differential

equations, a number of variables will be constant during one time-step. By solving

the problem as a system of equations, this qualitative understanding is somewhat

obscured. As an example, eq. 3.4 describes the differential equation of the inductor in which an expression is found for the flow derivative through this component. Regardless of the discretisation used for this component, numerically advancing from one time point to the next, the pressure and thus the flow derivative, remains constant within a time-step. However, the flow does not remain constant during the time step as the fluid is accelerated or decelerated from one time-step to another. Therefore, the flow changes linearly between the beginning and end of the time-step. This is a result of integrating using eq. 4.21 Under this assumption it can be demonstrated that the energy at time t for the discretised inductor using an explicit approach becomes:

$$E_L(t_n) = E_L(t_0) + \int_{t_0}^{t_n} \left(q(t) \frac{dp(t_0)}{dt} + p(t) \frac{dq(t)}{dt} \right) dt$$

Explicit
$$= E_L(t_0) + \sum_{i=0}^{n} p(t_i) \int_{t_i}^{t_{i+1}} \frac{dq(t)}{dt} dt \qquad \text{(Eq. 4.45)}$$

$$= E_L(t_0) + \sum_{i=0}^{n} p(t_i) \frac{\left(q(t_{i+1}) + q(t_i) \right)}{2} (t_{i+1} - t_i)$$

As the pressure is constant during a time-step, the pressure derivative is equal to zero in the numerical solution, eliminating the first term of the integral in the 1st equation. Consecutively, the pressure is evaluated explicitly, hence at the lower limit of the integral. Lastly, the flow integral over a time-step can be calculated exactly using the trapezium rule as the flow increases linearly over the time step. Hence, the change in energy is a function of the average flow over the time interval, times the initial pressure at time t_0.

Similarly, for the implicit approximation, the change in energy is the average flow over the interval times the pressure at time t. Both descriptions are inconsistent with the definition for continuous functions provided in equation 4.37. However, the central difference approach dictates that the change in energy is given by an average of the flow over the interval times the average of the pressure over the same interval. Even though the pressure and flow curves might approximate the differential equations, the central difference description is mathematically consistent and conservative with respect to the energy in the system.

Implicit

$$E_L(t_n) = E_L(t_0) + \sum_{i=0}^{n} p(t_{i+1}) \frac{\left(q(t_{i+1}) + q(t_i)\right)}{2} (t_{i+1} - t_i) \qquad \text{(Eq. 4.46)}$$

Central difference

$$E_L(t_n) = E_L(t_0) + \sum_{i=0}^{n} \frac{\left(p(t_{i+1}) + p(t_i)\right)}{2} \frac{\left(q(t_{i+1}) + q(t_i)\right)}{2} (t_{i+1} - t_i) \qquad \text{(Eq. 4.47)}$$

For the compliance, similar considerations hold with the end results presented in eqs 4.48-4.50.

Explicit

$$E_C(t_n) = E_C(t_0) + \sum_{i=0}^{n} q(t_i) \frac{\left(p(t_{i+1}) + p(t_i)\right)}{2} (t_{i+1} - t_i) \qquad \text{(Eq. 4.48)}$$

Implicit

$$E_C(t_n) = E_C(t_0) + \sum_{i=0}^{n} q(t_{i+1}) \frac{\left(p(t_{i+1}) + p(t_i)\right)}{2} (t_{i+1} - t_i) \qquad \text{(Eq. 4.49)}$$

Central difference

$$E_C(t_n) = E_C(t_0) + \sum_{i=0}^{n} \frac{\left(p(t_{i+1}) + p(t_i)\right)}{2} \frac{\left(q(t_{i+1}) + q(t_i)\right)}{2} (t_{i+1} - t_i) \qquad \text{(Eq. 4.50)}$$

4.2.4. *Monolithic Simulation & Results*

For the type of 0D systems described, only resistors, compliances and inertances are present. In addition, the flow and pressure for every component is known. It is preferable in this case, to analyse the balance of energy directly from the state variables. An LC-oscillator is simulated with a compliance of $C = 1.5915 \cdot 10^{-9}[Kg^{-1} \cdot m^4 \cdot s^2]$ and an inertance $L = 1.5915 \cdot 10^7[Kg \cdot m^{-4} \cdot s^{-2}]$. These values have been chosen to get pressure and flow at similar order of magnitude as in the large arteries while having an oscillation frequency of $1[Hz]$. The time-step size is chosen to be $\Delta t = 10^{-2}[s]$ with a total simulation time of $t = 5[s]$ in order to generate enough numerical error for the effects to be visible. The number of iterations for the implicit and central-difference methods was set at $N = 10[-]$.

Fig. 4.2 depicts the pressure and flow over time for each numerical method used. For the forward-euler method, both pressure and flow are amplified over time. Given an initial excitation of the model, by providing an initial pressure on the compliance, the state variables will continue to increase indefinitely over time. For the backward-euler method, both pressure and flow diminish in magnitude over time and eventually all signals dampen out. The central-difference method curves overlap with those of the analytical model. However, pressure and flow diverge with respect to the analytical solution over time but with an order of magnitude $O(100)$ times smaller compared to the forward-Euler method. Considering the timescales involved, the relatively coarse time step and the required accuracy, the error between the analytical model and the central difference scheme is negligible for all practical purposes.

Numerical Scheme comparison for Pressure and Flow
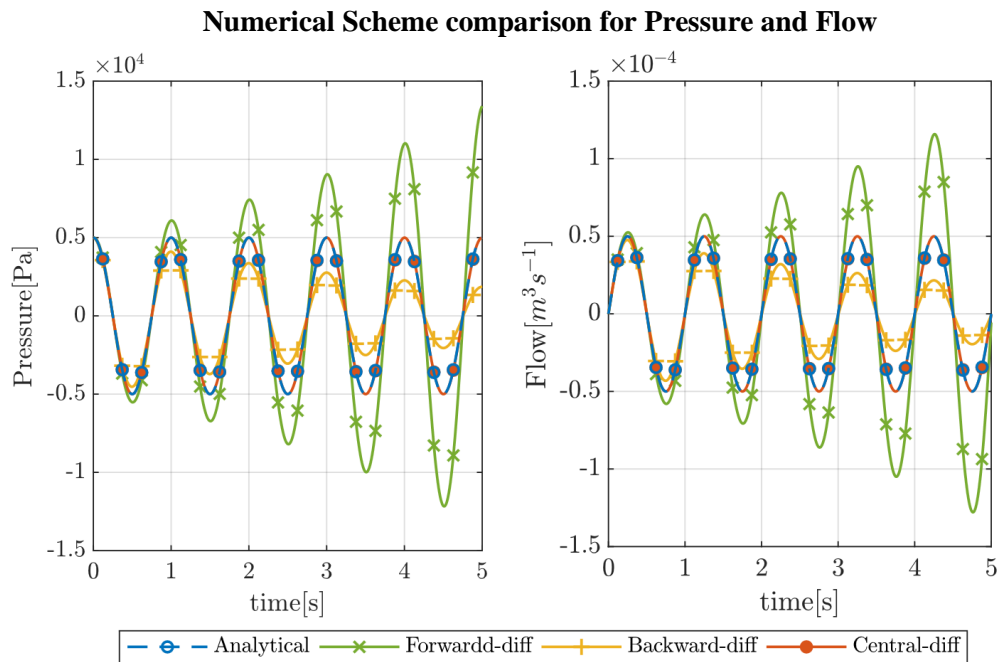
Fig. 4.2 - LC-Oscillator pressure(left) and flow(right) demonstrating

increase/decrease over time.

Additionally for this system to be periodic, as predicted by the analytical system, the state variables have to return to their initial conditions once every period. Fig 4.3 left shows the trajectories through state-space, better demonstrating that only the central difference scheme satisfies a return to the initial conditions.

It could be concluded from the pressure and flow curves that the forward-Euler method is non-conservative and therefore unstable, the backward euler method is non-conservative and stable and only the central difference scheme is both stable and conservative.
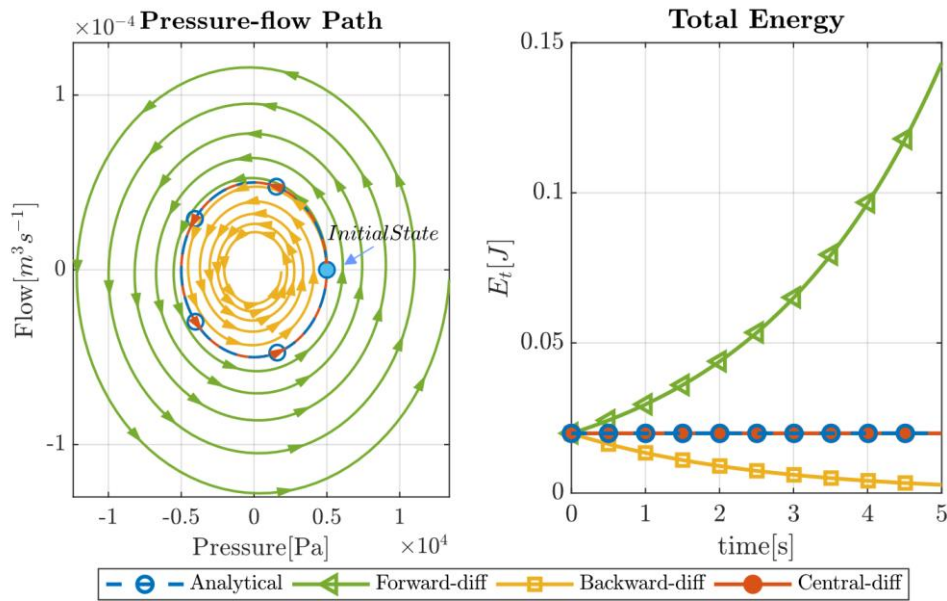
Fig. 4.3 - (Left)Trajectories of Pressure vs. flow, time direction indicated by arrows. (Right) System's Total energy stored, demonstrating energy conservation and model stability for numerical schemes.

Intuitively, this concept is more apparent from the state-space trajectories. However, visualisation of this space is only possible because this space is 2-dimensional and analysing pressure and flow curves by eye is impractical for larger systems.

A less ambiguous measure to analyse the stability of the system is therefore the total energy of the system and its time derivatives. The right graph of fig. 4.3 shows the total energy of the LC-oscillator for the different numerical schemes. Energy is generated by the backward-Euler method, is approximately conserved for the central difference method and is dissipated by the forward-Euler method. Note that the change in energy in itself does not permit conclusions about the stability of

arbitrary systems as energy can be introduced externally or dissipated by any resistances present. However, no energy should be generated autonomously upon perturbation of a system from steady-state. Since this system is isolated and non-dissipative, no energy should be generated without external introduction of energy, in order for the system to be stable.

Lastly, the equivalence of state descriptions in eqs. 4.39-4.40 was compared against the time integral description of eqs. 4.45-4.50. The error normalised to the initial energy $E_t(t_0)$ is of order of magnitude $O(10^{-13})[\%]$ which is effectively negligible. This equivalence might not seem surprising as the state description of energy for each component was derived from the time integral equation. However, it shows that the energy transfer of the components cannot simply be calculated from integrating the change of energy from eq. 4.37. The two components in this model, the compliance and inertance, share the same state-variables. Therefore, if the energy transfer during a time-step is calculated from eq. 4.37, the flow from one component to the other is always exactly equal and there is no change in total energy. This in turn means that no energy can be lost or gained over any boundary during a time-step which is untrue due to numerical discretisation. Therefore, the numerical energy transfer across a boundary is dependent on the type of boundary.

4.2.5.   *Partitioned Model Coupling*

The same reasoning can be applied to coupling separate sub-models. For this purpose, the LC-oscillator is subdivided into the two smallest possible sub-models.

One compliance model and one inertance model. Each sub-model then receives boundary conditions from the other sub-model at each iteration or each time-step. Due to this coupling the partitioned models only depend on source inputs from the other model and not on the states themselves. The state-variables are redefined as the compliance pressure $P_C(t)$ and the inertance flow $q_L(t)$ with the models still following eqs. 4.1-4.2, although they are now evaluated in isolation. This makes it straight-forward to calculate the energy of each sub-model directly from their state-variables and makes it possible to retain the differential equations previously introduced.

4.2.5.1. *Coupling Schemes*

Compartmentalisation of parts and connecting them at their respective coupling interfaces, is an artificial operation. Using a partitioned solver approach, compartments exchange information at their coupling interface. Different coupling schemes are considered in this chapter in order to pose boundary conditions for the coupled sub-models. For continuous functions the most intuitive choice at time t are boundary conditions that satisfy the exact solution at time t. However, for discrete models using an iterative approach requires integration over time of the form presented in eq. 4.14, reiterated below:

$$\varphi(t) = \varphi(t_0) + \int_{t_0}^{t} \frac{d\varphi(t)}{dt} dt \qquad \text{(Eq. 4.14)}$$

Similarly, to the considerations presented for the numerical schemes discussion, the choice of coupling scheme affects the approximation of the integral and thus the

conservation of energy. The coupling schemes considered in this chapter can be classified as explicit, implicit and central-differenced schemes.

To introduce the coupling schemes, consider two models, arbitrarily assigned model 1 and 2. Pressure and flow need to be defined at the coupling interface of both models. Model 1 provides pressure BCs for model 2, while model 2 provides flow BCs for model 1. It is important to recognise that these BCs are coupled since they need to be consistent with both models, simultaneously. However, at the interface, the state variables are not known a priori and need to be approximated. Shown in fig. 4.4 are the two explicit coupling methods considered, which are referred to as fully explicit and a semi-explicit and the coupling between models.
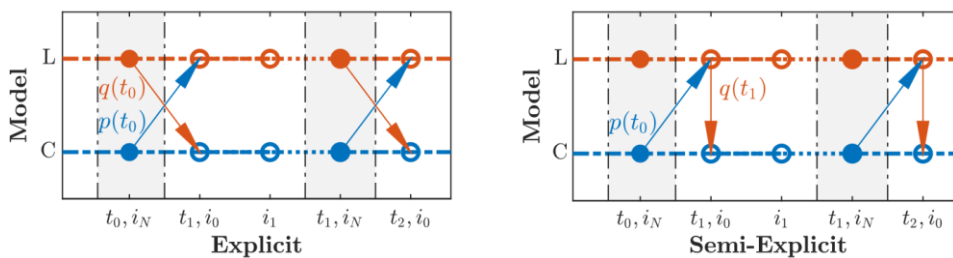
Fig. 4.4 - (Left) fully explicit BCs derived from previous time-step, (right) Semi-explicit, One BC derived from previous one BC derived from estimate at current time step.

For the fully explicit coupling, All BCs for the current time-step, are derived from values at the previous time-step (eq. 4.51). During the iterations within a time-step the solutions of both models are therefore uncoupled. For the semi-explicit coupling (eq. 4.52), one of the models approximates a solution for the current time step using a BC from the previous time-step.

$$\text{Explicit} \qquad \begin{aligned} p_j(t,i) &= f(q_k(t - \Delta t, i_N)) \\ q_k(t,i) &= g(p_j(t - \Delta t, i_N)) \end{aligned} \qquad \text{(Eq. 4.51)}$$

$$\text{Semi-Explicit} \qquad \begin{aligned} p_j(t,i) &= f(q_k(t - \Delta t, i_N)) \\ q_k(t,i) &= g(p_j(t, i_0)) \end{aligned} \qquad \text{(Eq. 4.52)}$$

This solution at the current time-step is used to pose a BC for the connected model at the current time-step which can be considered as an implicit BC. Combining an explicit and an implicit BC, leads to a stronger coupling which is the reason for referring to this model as semi-explicit. Both coupling methods only update the BCs at the first iteration of each time-step. It is assumed that both models can be iterative in nature, with i indicating the iteration number irrespective of the BCs being updated iteratively or not.

The change in total energy over time will be demonstrated after introducing the remaining coupling schemes considered. Weakly-implicit and strongly-implicit coupling can be defined for the implicit coupling methods again with the coupling shown in fig. 4.5.:
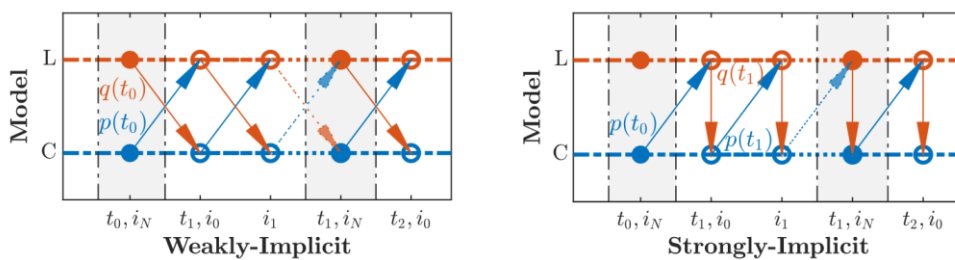
Fig. 4.5 - (Left) weakly-Implicit coupling derived from previous iteration, (right) Strongly-Implicit coupling, One BC derived from previous iteration while one BC derived from current iteration.

Compared to the explicit coupling, the boundary conditions are updated at each iterative step instead of just at the beginning of each time-step. The weakly-implicit coupling utilises the solution information from the previous iteration or time-step for both boundary conditions. For strongly-implicit coupling, a leapfrogging pattern like that of the explicit coupling exists. Each iteration, one model has a BC posed from values at the previous iteration, the solution of this model is updated. The other model then receives boundary conditions at the current iteration from this updated solution. Both coupling methods are expressed in eqs. 4.53-4.54. Note that the order depends on which model is evaluated first each time step, but that the effect of the order on the end solution should be negligible.

Weakly-
Implicit
$$p_j(t, i) = f(q_k(t, i - 1))$$
$$q_k(t, i) = g(p_j(t, i - 1))$$
(Eq. 4.53)

Strongly-
Implicit
$$p_j(t, i) = f(q_k(t, i - 1)))$$
$$q_k(t, i) = g(p_j(t, i))$$
(Eq. 4.54)

Finally, two central-difference(CD) coupling schemes were considered, again classified as weakly and strongly coupled. Shown in Fig 4.6 is the coupling between the models for both schemes.
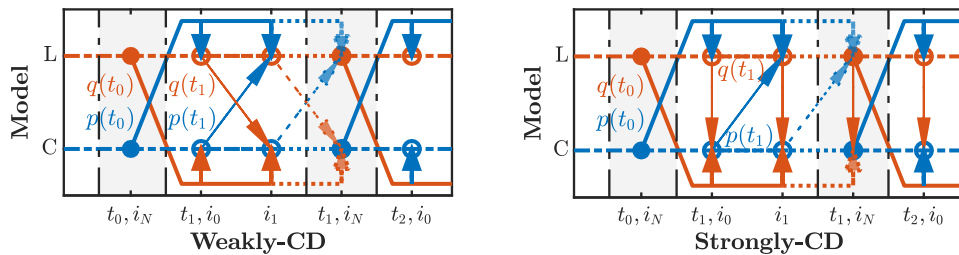
Fig. 4.6 - (Left) fully explicit BCs derived from previous time-step, (right) Semi-explicit, One BC derived from previous one BC derived from estimate at current time step.

The boundary conditions are now a central-differenced average of both the solution at the previous and the current time step. Identical to the implicit methods, the difference between the weakly and strongly coupled methods is the evaluation of the pressure at the current time step. Both Central-differenced coupling methods are expressed in eqs. 4.55-4.56.

Weakly-CD
$$p_j(t,i) = f\left(\frac{q_k(t-\Delta t, i_N) + q_k(t, i-1)}{2}\right)$$
$$q_k(t,i) = g\left(\frac{p_j(t-\Delta t, i_N) + p_j(t, i-1)}{2}\right)$$
(Eq. 4.55)

Strongly-CD
$$p_j(t,i) = f\left(\frac{q_k(t-\Delta t, i_N) + q_k(t, i-1)}{2}\right)$$
$$q_k(t,i) = g\left(\frac{p_j(t-\Delta t, i_N) + p_j(t, i)}{2}\right)$$
(Eq. 4.56)

In summary, if we consider the last iteration of a model solution to be the most accurate approximation at the current time step, A coupling constant κ can be introduced similarly to the numerical scheme constant θ. The coupling for the source terms then becomes as give in eq. 2.57 with $\kappa = 0$ implying implicit coupling, $\kappa = 1$ implying implicit coupling and $\kappa = 1/2$ meaning central-differenced coupling. Note that in the event of semi-explicit coupling, one model will follow and implicit-coupling approach while the other will follow an explicit coupling approach.

$$\vec{u}^*(t) = (1 - \kappa)\vec{u}(t + \Delta t) + \kappa\vec{u}(t) \qquad \text{(Eq. 4.57)}$$

4.2.5.2. Energy Conservation

It was discussed previously, that the change of energy of an isolated model, can be calculated from the flow of work over its boundaries. The conservation of energy due to coupling schemes will be demonstrated for the fully explicit coupling using the same principle. It is assumed that no energy is generated or dissipated internally in the sub-models. The BCs are taken as the pressure and flow at the previous time step, which implies treating the derivatives of the model explicitly according to eqs. 4.22-4.23. Returning to the integral in eq. 4.14, note that the boundary conditions are constants during a time-step and the integral is effectively approximated by:

$$\int_t^{t+\Delta t} \frac{d\varphi(t')}{dt'} dt' \cong \left.\frac{d\varphi(t')}{dt'}\right|_{t'=t} \Delta t \qquad \text{(Eq. 4.58)}$$

However, during a time-step the pressure and flow of the continuous systems change, which is neglected by this approximation. Returning to the LC-circuit under consideration, it can be shown that the energy change during a time-step is not arbitrarily zero. The energy change of the inertance model, the compliance model and the total coupled system are given as:

$$\frac{dE_L}{dt} \cong \frac{\Delta E_L}{\Delta t} = p(t)\frac{\left(q(t + \Delta t) + q(t)\right)}{2} \qquad \text{(Eq. 4.59)}$$

$$\frac{dE_C}{dt} \cong \frac{\Delta E_C}{\Delta t} = -q(t)\frac{\left(p(t + \Delta t) + p(t)\right)}{2} \qquad \text{(Eq. 4.60)}$$

$$\frac{\Delta E_T}{\Delta t} = \frac{\Delta E_L}{\Delta t} + \frac{\Delta E_C}{\Delta t} = \frac{p(t)q(t + \Delta t) - q(t)p(t + \Delta t)}{2} \quad \text{(Eq. 4.61)}$$

As the change of energy for this isolated system is none-zero, energy can be generated or dissipated during a time-step. This is not a property of the systems considered but rather of the way in which boundary conditions are posed and is equally true for imposed time-profiles. For the central-differenced coupling schemes, the integral in eq. 4.14 is approximated as:

$$\int_t^{t + \Delta t} \frac{d\varphi(t')}{dt'} dt' \cong \left(\frac{\frac{d\varphi(t)}{dt} + \frac{d\varphi(t + \Delta t)}{dt}}{2} \right) \Delta t \quad \text{(Eq. 4.62)}$$

If the underlying system changes linearly from one time-step to the next, eq. 4.62 becomes an exact evaluation of the integral. The change in energy for the inertance, compliance and the total system can now be evaluated analogously, and the results of this process are reported in table 4.1 below. It is assumed that the inertance model is the first model to be evaluated at each time-step and all values are taken at the final iteration of a time-step. For ease of notation, the current time-step is denoted simply as t_1 while the previous time-step is denoted as t_0.

	$\dfrac{\Delta E_L}{\Delta t}$	$\dfrac{\Delta E_C}{\Delta t}$	$\dfrac{\Delta E_T}{\Delta t}$
Explicit	$p(t_0)\dfrac{(q(t_1) + q(t_0))}{2}$	$-q(t_0)\dfrac{(p(t_1) + p(t_0))}{2}$	$\dfrac{p(t_0)q(t_1) - q(t_0)p(t_1)}{2}$
Semi-Explicit	$p(t_0)\dfrac{(q(t_1) + q(t_0))}{2}$	$-q(t_1)\dfrac{(p(t_1) + p(t_0))}{2}$	$\dfrac{p(t_0)q(t_0) - q(t_1)p(t_1)}{2}$
Implicit	$p(t_1)\dfrac{(q(t_1) + q(t_0))}{2}$	$-q(t_1)\dfrac{(p(t_1) + p(t_0))}{2}$	$-\dfrac{p(t_0)q(t_1) - q(t_0)p(t_1)}{2}$

Central-Difference	$\dfrac{\left(p(t_1)+p(t_0)\right)}{2}\dfrac{\left(q(t_1)+q(t_0)\right)}{2}$	$-\dfrac{\left(p(t_1)+p(t_0)\right)}{2}\dfrac{\left(q(t_1)+q(t_0)\right)}{2}$	0

Table 4.1 - Energy change per time-step for Inertance $\Delta E_L/\Delta t$, Compliance $\Delta E_C/\Delta t$

and total system $\Delta E_T/\Delta t$.

There are several noteworthy things about these relations. Firstly, note that values at the current time-step are independent of the calculation method, e.g iterative or non-iterative. Only the final value at the end of an iterative loop influences the energy balance per time step. Therefore, both implicit methods have the same change in energy per time step, which also holds for both central-differenced methods. Secondly, note that the change in total energy of the system for the fully explicit and the implicit coupling schemes are equal in magnitude but opposite in sign. Hence if energy is generated during a time-step for one scheme, it is dissipated for the other. Thirdly, the only arbitrarily conservative coupling scheme is the central-differenced coupling in which the change of total energy per time-step is zero. Lastly, for the semi-explicit coupling method, the generation or dissipation is proportional to the difference in energy flow between the current and the previous time step.

4.2.5.3. Simulation Results

The LC-oscillator is simulated under the same conditions as before, with a compliance of $C = 1.5915 \cdot 10^{-9}[Kg^{-1} \cdot m^4 \cdot s^2]$, an inertance $L = 1.5915 \cdot 10^7[Kg \cdot m^{-4} \cdot s^{-2}]$, a time-step size of $\Delta t = 10^{-2}[s]$ with a total simulation time of $t = 5[s]$. Additionally, the number of iterations per time-step was set at 15. At

this number of iterations, the difference in energy change derived from the state variables as compared to the energy change derived from energy flow approached machine precision for all methods involved.

Fig. 4.7 demonstrates the cumulative change in total energy using the relations from table 4.1.:
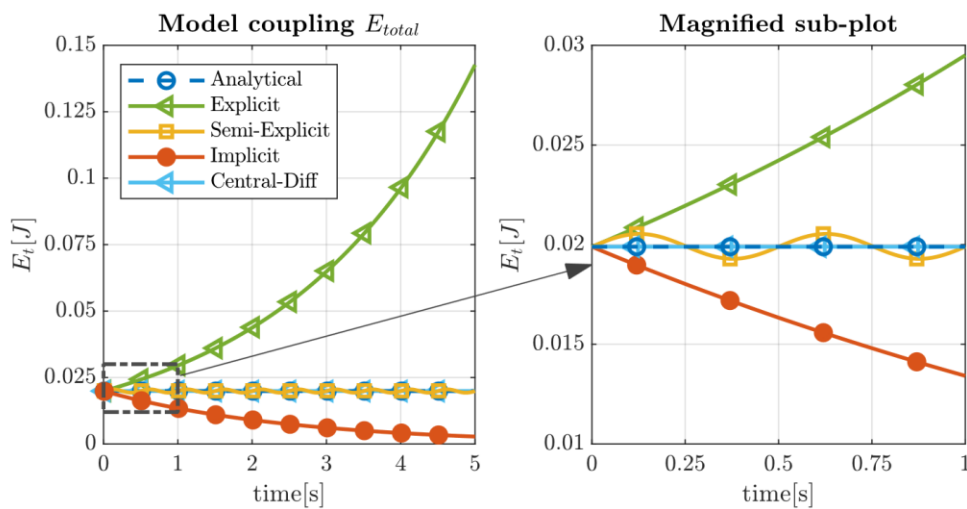
Fig. 4.7 - (Left) Total energy change due to partitioned model coupling for various schemes, (right) Plot magnification demonstrates cyclic energy conservation of semi-explicit scheme for periodic signals.

The maximum error, normalised to the initial energy $E_t(t_0)$, between the state-derived total energy and the cumulative total energy was again of order of magnitude $O(10^{-13})[\%]$ for all coupling methods. Therefore, the state-derived and cumulative methods are considered equivalent. For the central differenced scheme, the total energy is plotted using the state-derived method. This allows considering any numerical errors which is not possible using the term from table 4.1 being zero.

Only the central-differenced scheme fully conserves energy. As was noted before, this is a result of the linear time-integration between points. The fully explicit coupling scheme generates energy which in turn leads to additional energy being generated next time step and is therefore unstable. The inverse is true for the implicit coupling scheme which dissipates energy, approaching zero total energy as time increases.

For the semi-explicit method, energy is conserved over one cycle of the system. This can be explained by the periodicity of the flow and pressure and the symmetry of the total energy change term $\Delta E_T / \Delta t$. For every time-step where the flow and pressure change a certain amount, a time-step exists where flow and pressure change an opposite amount. Hence, any erroneous addition of energy gets compensated by an equal dissipation of energy elsewhere in the cycle.

4.3. Vascular Bifurcation Model

Stability of a system can now be related to the energy balance over time of that system. In the harmonic oscillator system, no energy can be physically dissipated as there are no resistances present. However, the vascular system is more complex containing sources and sinks of energy. Energy is added to the system by the heart, by generating pressure causing blood to flow into the large blood vessels. The large blood vessels are distensible, and flow is assumed to be inertia dominated. Here, Blood coming from the heart is stored as potential and kinetic energy in the form of pressure and flow respectively while viscous dissipation is minimal. Eventually, the blood is transported to the microvasculature where the average flow is lower,

the vessel diameters are smaller, but the total wall surface of all vessels combined is large. Most viscous dissipation occurs in the microvasculature causing a pressure drop before the blood returns to the heart via the venous system.

As has been shown in the previous section, partitioned evaluation of models can cause energy to be generated or dissipated at the coupling interface. In a system containing resistances, this coupling energy can be compensated for but requires the introduction of dissipation into our systems. As an example, A 0D-model of a simplified vascular bifurcation is used shown below in figure 4.8.
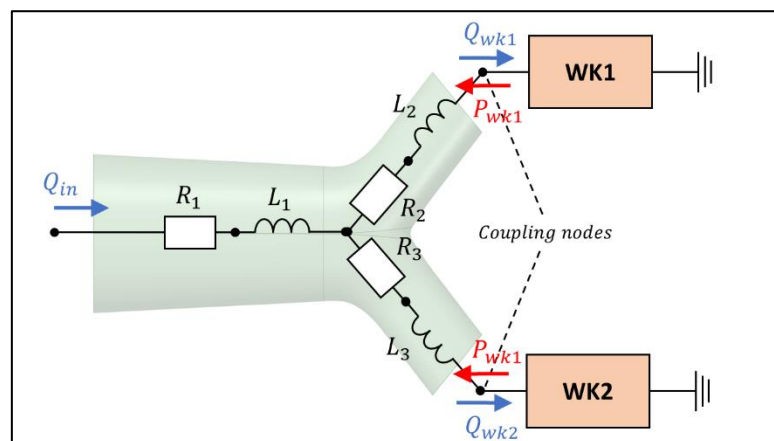
Fig. 4.8 - 0D-bifurcation model consisting of 3 vessels each consisting of a resistance and inertance coupled to 2 windkessel models.

This model has similar dimensions to those experienced in large blood vessels like the aorta and is subjected to similar flows. The inertance L_i' and resistance R_i' per unit length of tube, under the assumption of simple laminar flow are given below and for simplification no compliances are present within the geometry. Lastly at the bifurcation, all vessels are simply coupled together without compensating for the

complex 3D behaviour occurring at the bifurcation. While these assumptions are not representative for the physical conditions, they are sufficient to demonstrate the concepts. More complex relationships for resistance, inertia and compliances can be substituted in at relatively little loss of generality.

$$L'_i = \frac{\rho}{\pi r_i^2} \qquad \text{(Eq. 4.63)}$$

$$R'_i = \frac{8\eta}{\pi r_i^4} \qquad \text{(Eq. 4.64)}$$

4.3.1. *Numerical Model*

The bifurcation itself consists of 3 vessels each consisting of a resistance and an inertance and is again modelled using a state-space description as was done for the harmonic oscillator:

$$\frac{d\vec{x}}{dt} = \boldsymbol{A}\vec{x} + \boldsymbol{B}\vec{u} \qquad \text{(Eq. 4.65)}$$

$$\vec{y} = \boldsymbol{C}\vec{x} + \boldsymbol{D}\vec{u} \qquad \text{(Eq. 4.66)}$$

The states of the model consist of the flow through the inertances Q_{L1}, Q_{L2} and Q_{L3} while the inputs of the model are the windkessel pressures P_{wk1}, P_{wk2} and the time-derivative of the input flow:

$$\vec{x} = \begin{pmatrix} Q_{in} \\ Q_{wk1} \\ Q_{wk2} \end{pmatrix}, \quad \vec{u} = \begin{pmatrix} P_{wk1} \\ P_{wk2} \\ \dfrac{dQ_{in}}{dt} \end{pmatrix} \qquad \text{(Eq. 4.67)}$$

With system- and input- matrices given by:

$$A = \frac{1}{(L_2 + L_3) + (1 - \theta)(R_2 + R_3)\Delta t} \begin{pmatrix} 0 & 0 & 0 \\ 0 & -R_2 & R_3 \\ 0 & R_2 & -R_3 \end{pmatrix} \quad \text{(Eq. 4.68)}$$

$$B = \begin{pmatrix} 0 & 0 & (L_2 + L_3) + (1 - \theta)(R_2 + R_3)\Delta t \\ -1 & 1 & L_3 + (1 - \theta)R_3\Delta t \\ 1 & -1 & L_2 + (1 - \theta)R_2\Delta t \end{pmatrix} \quad \text{(Eq. 4.69)}$$

This is sufficient to calculate the change of states of the bifurcation model and additionally provide inlet flows for the windkessel models. Therefore, the output vector, output matrix and feedforward matrix are given by:

$$\vec{y} = \begin{pmatrix} Q_{wk1} \\ Q_{wk2} \end{pmatrix} \quad C = \begin{pmatrix} 0 & 1 & 0 \\ 0 & 0 & 1 \end{pmatrix} \quad D = \begin{pmatrix} 0 & 0 & 0 \\ 0 & 0 & 0 \end{pmatrix} \quad \text{(Eq. 4.70)}$$

The windkessel model can be written as a state-space description given eq. 3.1 and 3.2 with a single state P_{ci}, an input Q_{wki} and output P_{wk1} :

$$\vec{x} = P_{ci}, \vec{u} = Q_{wki} \quad A = \frac{-1}{R_i C_i + (1 - \theta)\Delta t} \quad B = \frac{R_i}{R_i C_i + (1 - \theta)\Delta t} \quad \text{(Eq. 4.71)}$$
$$\vec{y} = P_{wk1} \quad\quad\quad C = 1 \quad\quad\quad D = Z_i$$

Where, R_i, Z_i and C_i are the windkessel's peripheral resistance, impedance and compliance respectively.

4.3.2. *Energy sources and dissipation*

To calculate the inflow of energy at the inlet, the pressure at inlet is required. Similarly, to the considerations in the harmonic oscillator circuit, it is important to note that during a time-step, all inertances experience a constant pressure while the flow changes from $q_i(t)$ to $q_i(t + \Delta t)$. Therefore, over a timestep an average flow is experienced at the outlet boundaries and the inlet pressure is given in eqs. 4.72-4.73. Note that the pressure contributed by the resistances of the bifurcation itself

are taken at time t . This is due to consistency of the pressure-flow relationship for resistances (eq. 3.3) since pressure and flow from the model are an approximation of the continuous system.:

$$P_{in}(t) = P_{mid}(t) + L_1 \frac{dQ_{in}}{dt}(t) + R_1 Q_{in}(t) \qquad \text{(Eq. 4.72)}$$

$$P_{mid}(t) = (1 - \kappa)\frac{P_{WK}(t + \Delta t)}{2} + \kappa \frac{P_{WK}(t)}{2} + \frac{Q_{DWK}}{2}(t)$$
$$P_{WK}(t) = \left(p_{wk1}(t) + P_{wk2}(t)\right) + \left(R_2 Q_{wk1}(t) + R_3 Q_{wk2}(t)\right) \quad \text{(Eq. 4.73)}$$
$$Q_{DWK}(t) = L_2 \frac{dQ_{wk2}}{dt}(t) + L_3 \frac{dQ_{wk2}}{dt}(t)$$

In the bifurcation model, pressure is constant while flow changes. Energy inflow over the boundary each time-step is therefore equal to:

$$\Delta E_{in}(t) = P_{in}(t)\frac{\left(q_{in}(t + \Delta t) + q_{in}(t)\right)}{2}\Delta t \qquad \text{(Eq. 4.74)}$$

Lastly, Resistances and impedances dissipate energy depending on the path they are included in as the other connected elements can change the pressure and flow on individual paths. Therefore, dissipation has to be considered separately for every dissipator in the system. All dissipators included those in the bifurcation model are in paths with changing flow but constant pressure. Hence their energy dissipation is equal to eq. 4.75. Dissipators present in the windkessel experience constant flow at their boundaries while the compliance changes the pressure at the centre and inlet nodes leading to the dissipation term in eq. 4.76.

$$\text{Bifurcation} \qquad \Delta E_R(t) = P_R(t)\frac{\left(q_R(t + \Delta t) + q_R(t)\right)}{2}\Delta t \qquad \text{(Eq. 4.75)}$$

Windkessel $\qquad \Delta E_R(t) = q_R(t) \dfrac{\left(p_R(t + \Delta t) + p_R(t)\right)}{2} \Delta t \qquad$ (Eq. 4.76)

4.3.3. Model parameters

An initial base system is used to demonstrate the instability consisting of 3 vessels as depicted in Fig. 4.8 above. The main assumptions include that the compliance of the bifurcation is captured within the windkessel compliances. This is consistent with rigid vessel assumptions for 3D hemodynamics simulations. Additionally, it is assumed that the pressure drop of the vascular system is mainly attributed to the windkessel resistance and impedance. Hence, the total windkessel resistance is equal to the ratio of average pressure to average flow.

The inlet vessel has a length of 30[cm], with both outlet vessels after the bifurcation having a length of 10[cm]. The radius of the inlet vessel is chosen to be 1[cm] while both outlet vessels have a 0.77[cm] radius. Fluid density was set to $\rho = 1056[Kg \cdot m^{-3}]$ and kinematic viscosity $\eta = 3.5 \cdot 10^{-3}[m^2 s^{-1}]$. These parameters are in the same order of magnitude as those encountered in the aorta up till the bifurcation of the iliac arteries. Windkessel total resistance was estimated from assuming an average pressure of 12.5[kPa] at a stroke volume of 80[ml $\cdot s^{-1}$] . A very rough estimate of input impedance Z_i is 10% of the value of peripheral resistance R_i. The Compliance was then estimated from assuming an RC constant of 2[s]. To create an asymmetry between the 2 outlets, the total resistance of Windkessel model 1 is decreased by 20% while that in the windkessel model 2 was increased by 20%. Without this asymmetry the flow fraction to each outlet vessel is equal and no

pressure differential exist between them. The only determinant of the flow through the bifurcation in that case is the inlet flow which is predetermined and leads to identical solutions irrespective of the chosen coupling method. Compliance is equal in both windkessel models. A summary of the resulting parameters can be found below in table 4.1.

Parameter (Bifurcation)	*value*	Parameter (Bifurcation)	*value*
$L_1[kg \cdot m^{-4}]$	$1.0084 \cdot 10^6$	$R_1[kg \cdot m^{-4}s^{-1}]$	$2.6738 \cdot 10^5$
$L_2[kg \cdot m^{-4}]$	$1.6807 \cdot 10^6$	$R_2[kg \cdot m^{-4}s^{-1}]$	$7.4272 \cdot 10^5$
$L_3[kg \cdot m^{-4}]$	$1.6807 \cdot 10^6$	$R_3[kg \cdot m^{-4}s^{-1}]$	$7.4272 \cdot 10^5$
Parameter (Windkessel)	*value*	Parameter (Windkessel)	*value*
$Z_1[kg \cdot m^{-4}s^{-1}]$	$2.1818 \cdot 10^7$	$Z_2[kg \cdot m^{-4}s^{-1}]$	$2.2728 \cdot 10^7$
$R_{p1}[kg \cdot m^{-4}s^{-1}]$	$2.1818 \cdot 10^8$	$R_{p2}[kg \cdot m^{-4}s^{-1}]$	$2.2728 \cdot 10^8$
$C_1[kg \cdot m^{-4}s^{-1}]$	$6.6667 \cdot 10^{-9}$	$C_2[kg \cdot m^{-4}s^{-1}]$	$6.6667 \cdot 10^{-9}$

Table 4.1 - Model parameters of the bifurcation and the coupled windkessel models.

The model is partitioned into a model containing the bifurcation and one model containing both windkessel models. Input flow of the model is equivalent to the realistic flow pulse described in Fig. 3.5 for the windkessel chapter. Time-step size is set at $\Delta t = 10^{-2}[s]$ and a Central-difference approach is utilised for the numerical scheme of both partitioned models implying $\theta = 0.5[-]$. This minimizes the energy losses due to the numerical evaluation at each time-step allowing an analysis in which the only energy losses are due to dissipation and the chosen coupling method.

4.3.4.   *Coupling Instabilities*

In real-world systems, any net energy that flows into the system is either dissipated by dissipators like resistances and impedances or is stored onto compliances and inertances as potential and kinetic energy respectively. The numerical system has additional energy sources and at the boundaries due to coupling making the effective pressure and flow at these boundaries appear higher or lower to the system. Both the implicit and explicit coupling can therefore become unstable for similar reasons, namely the accumulation of numerical energy. However, the energy introduced through explicit coupling accumulates over time, whereas the energy within implicit coupling can accumulate within an iteration cycle. Instabilities for both methods will be demonstrated below.

4.3.4.1.   *Explicit coupling instability*

In order for the coupling energy to accumulate over time, the energy generated at each time-step should be higher than the energy that is dissipated at each time-step. Briefly revisiting the harmonic oscillator model, it is important to remember that energy is used in this context as an accounting tool. In the numerical system, the boundary condition either introduces an excess pressure onto the inertance or an excess flow onto the capacitance. Indirectly this increases the amount of mass passing through the inertance and increases the amount of fluid stored on the compliance, effectively increasing both the mass and pressure within the system. Each time-step the energy associated with this pressure and flow travels in a single path without being dissipated, namely the LC-loop. Any energy that was previously generated by the coupling, in turn generates more energy at the next time-step.

An equivalent harmonic oscillator circuit can be recreated from the bifurcation model. In order to do so the system needs to be isolated at its boundaries. This can be done by specifying zero flow at inlet while letting resistance values R_{pi} approach infinity. A closed path is created between the two compliances of the windkessel models. If the impedance and resistances within the bifurcation are set to zero, the energy within this closed path is able to accumulate over time. This last condition is sufficient but not required and as will be shown, all that is required is that the energy that gets generated is not sufficiently dissipated leading to a net energy accumulation. It can be demonstrated that even more realistic cases can become unstable.

If the impedance of the windkessel model is set below a certain threshold, eventually the amount of energy generated by model coupling will surpass the energy dissipated over all dissipators in the system. To demonstrate this, the outlets of the model are shortened to half the original length and the value of the windkessel impedances is set to zero. This creates a shorter path, halving the inertance and resistance between both windkessel models but doesn't change the characteristics of the shortened geometry. The input flow is changed to be a single pulse inflow of $q(t) = 1 \cdot 10^{-4} [m^3 s^{-1}]$ at $t = 0.1[s]$ which is an equivalent volume of fluid of $1[ml]$. After the initial impulse the inflow is 0.

Fig. 4.9 below shows the pressure differential across both outlets and the flow between both outlets for the implicit, explicit and central-differenced coupling methods.
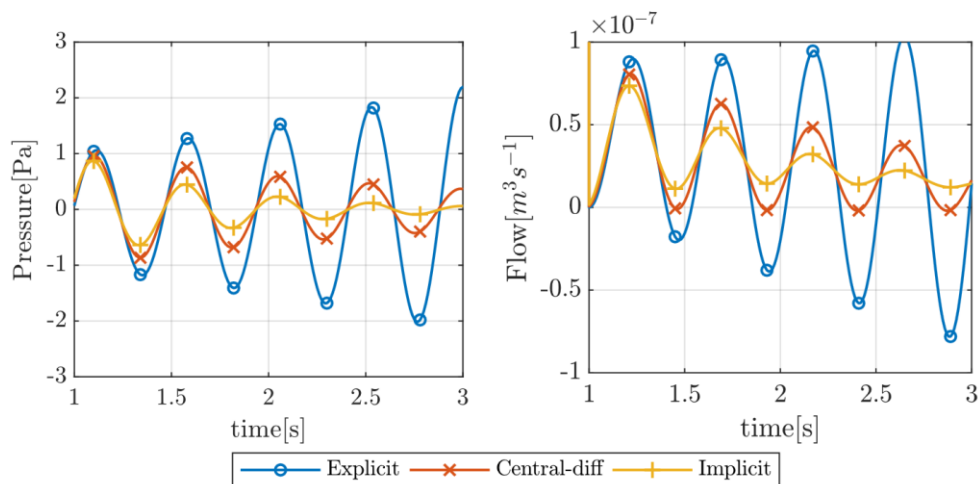
Fig. 4.9 - Pressure(left) and flow(right) for the bifurcation model for different coupling methods. Pressure and flow are generated or dissipated for the explicit and implicit methods respectively.

Since there are no sources present except for the inlet flow, fluid should leave the model via the peripheral resistances at the windkessel outlets until pressure is no longer stored on the resistances, i.e. p=0[Pa]. The pressure and flow magnitude increase with each cycle for the explicit method while they decrease for the remaining coupling methods. However, the implicit coupling method diminishes pressure and flow faster than the central-differenced method. An additional numerical wave of energy exists, a source for the explicit method and a sink for the implicit method, as was seen for the harmonic oscillator

Fig. 4.10 below depicts the difference between the energy generated by the coupling method and the energy dissipated by all dissipators in the system, on the left side of the figure. Both the implicit and central difference method diminish in total energy over time, implying that the dissipation of energy is larger than the generated coupling energy. The difference between the central-difference and implicit coupling is obscured by the scale of the graph which is mainly relevant to difference in accuracy between coupling methods and not for the stability. Furthermore, a change in total energy of the system is not purely due to the additional coupling energy. The right side of fig. 4.10 depicts the difference in total dissipated energy between the explicit and central-difference coupling and between the implicit and central-difference coupling. The explicit method dissipates less energy up until approximately the first 2.25[s] of the simulation after which both the implicit and explicit method dissipate more energy than the central-difference method. This is because a change in flow or pressure through a path including dissipators, also changes the total dissipation. Furthermore, the implicitly coupled system is effectively half a time-step ahead of the central-difference coupled system while the explicitly coupled system is half a time-step behind.
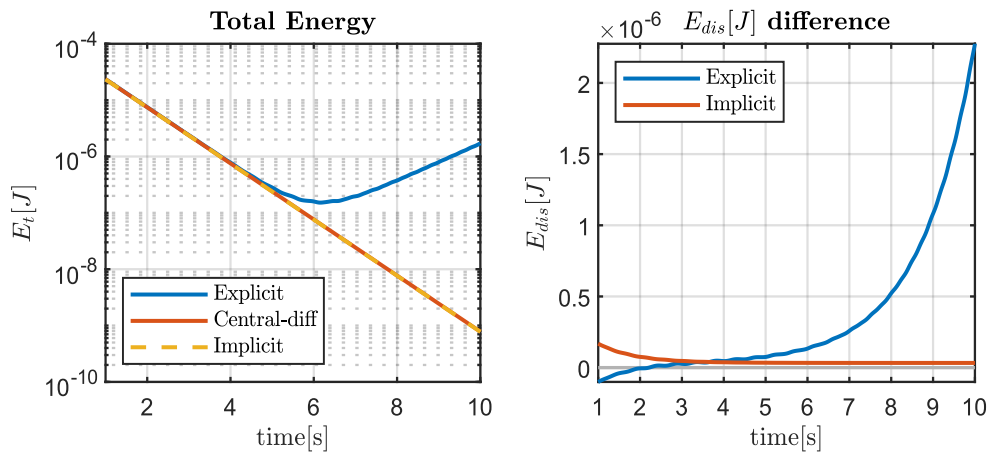
Fig. 4.10 - (left) Total energy of the system demonstrating the energy generation of the explicitly coupled models, (right) Total energy dissipated for explicit/implicit coupling compared to central-difference coupling, demonstrating coupling influence on dissipation.

After having considered the zero-impedance model it can be shown that the bifurcation model can become unstable for none-zero values of the impedance. For this the impedance is multiplied with a factor f_z, an impedance ratio with a range between 0 and 1. For the arterial system the RC time is approximately 2[s] or smaller. Since there is no input flow, the system should reach an equilibrium after 6[s] and therefore a simulation time of 10[s] should be sufficient. . This assumption also approximately holds for human physiological pulse signals as long as the pulse is cyclic. Fig. 4.11 demonstrates the difference in stability depending on the value of Z_i. The approximate smallest value in this graph for the impedance for which the model is still stable is a value of $f_z = 0.025$.

$$Z_i^* = f_z Z_{i,initial}$$
(Eq. 4.77)

113
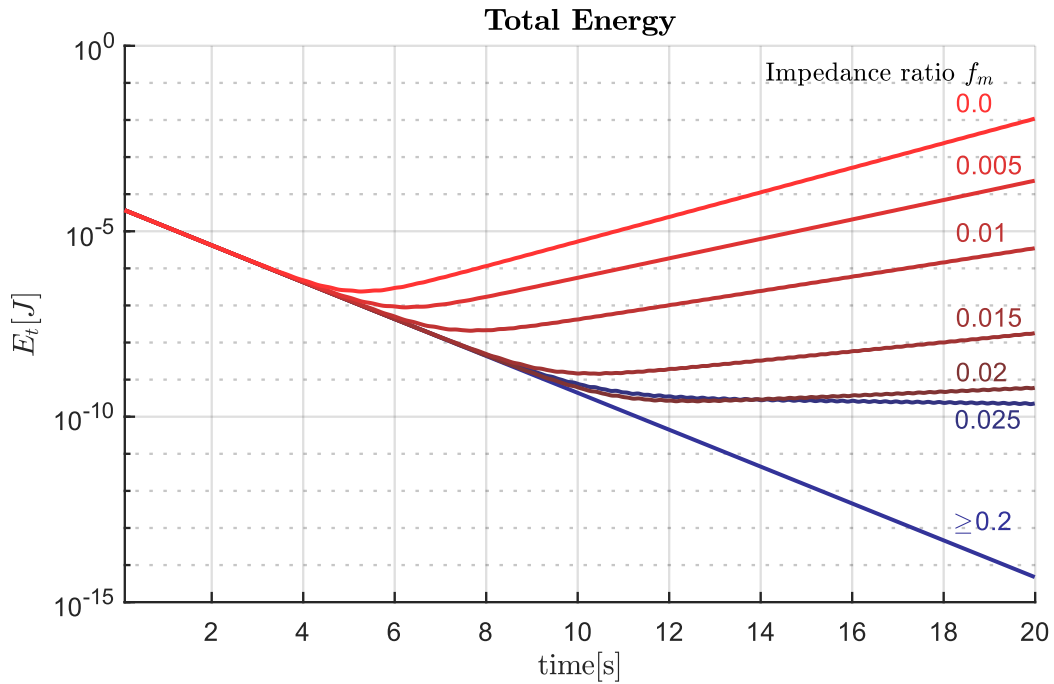
Fig. 4.11 - Total energy as a function of time. Separate curves indicate different impedance values with red curves indicating unstable models, blue curves indicating stable models.

A more precise value of this cut-off was estimated manually to be $f_z = 0.0237$. At this value the total resistance between the two capacitors is equal to approximately $R_{cc} = 2.035 \cdot 10^6 [kg \cdot m^{-4} s^{-1}]$. This value is an order of magnitude smaller than the impedance, implying that this resistance threshold can never be reached solely by changing the value of the resistances in the bifurcation itself. This threshold can only be reached for $f_z \leq 0.037$ for having 0 resistance inside the bifurcation.

To test the assumption that the resistance in the path between the two capacitors needs to be below this threshold, another experiment is performed in which f_z assumes 2 values namely $f_z = \{ 0.03, 0.04 \}$. The inertances remain unchanged. For the higher value of $f_z = 0.04$, zero resistance inside of the bifurcation should not

lead to instability. For the lower value of $f_z = 0.03$, a factor f_r is introduced to set the resistances inside of the bifurcation to a fraction of the initial resistance value:

$$R_i^* = f_r R_{i,initial} \qquad \text{(Eq. 4.78)}$$

The threshold resistance R_{cc} is reached for $f_r = 0.268$. Fig. 4.12 below demonstrates that indeed the threshold for stability is passed for $f_r = 0.268$ at $f_z = 0.03$.
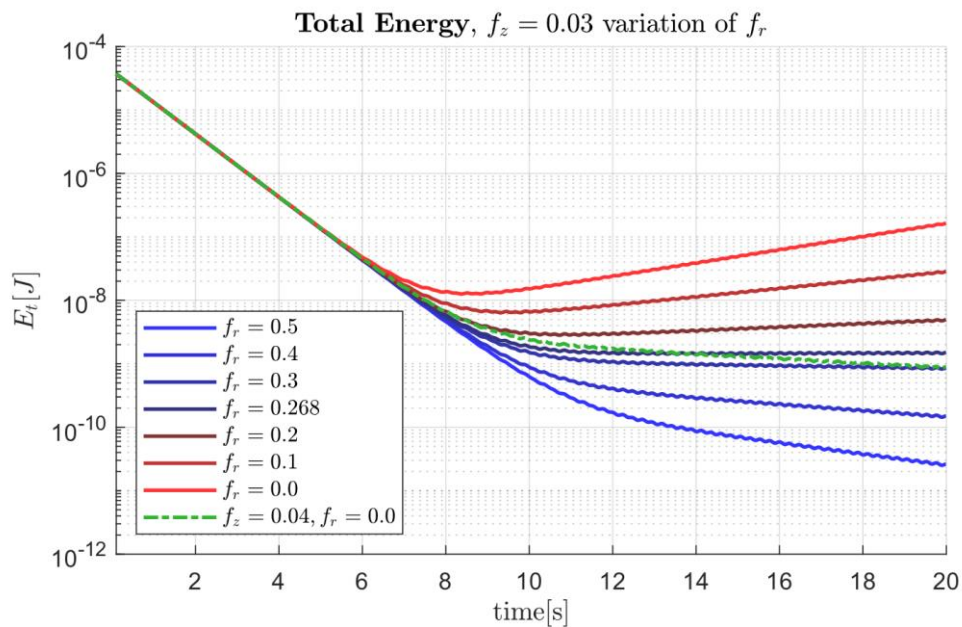
Fig. 4.12 - Total energy as a function of time for $f_z = 0.03$. Separate curves indicate

different values, red curves indicating unstable models, blue curves for stable models.

Green line depicts stability at $f_z = 0.03$ and zero resistance in bifurcation domain.

A range of other values of f_r is provided to show the stability properties for higher and lower values of resistance. The green dashed line provides demonstrates the simulation is stable regardless of the resistance inside of the bifurcation model at $f_z = 0.04$. Lastly it should be noted that the total energy does not approach 0 at the

end time. This means that some residual energy will exist in the model although this energy is negligible for all practical purposes.

This result indicates that any combination of resistances and impedances leading to an R_{cc} resistance below the threshold will lead to an instability. It is expected that this value is related to the peripheral resistance of the windkessel element, but more work is required to establish a general condition utilizing all model parameters. Peripheral resistance influences how much fluid can flow onto the compliance for flow into the windkessel model and also determine how much fluid flows back into bifurcation at windkessel backflow, including numerically generated energy.

The stability condition for this particular model is given in eq. 4.79. This instability does not consider the accuracy of the model nor the implications of the instability. Energy added over time, might not be noticeable with respects to the simulation results and depend on the total duration of the simulation and the time-step used. For the current simulation a set time step of $\Delta t = 10^{-2}[s]$ was used. A smaller time-step reduces the coupling energy generation or dissipation and thus makes the model more stable. This is in-line with expectations regarding the convergence behavior regarding explicit couplings.

$$R_{cc}[kg \cdot m^{-4}s^{-1}] = R_2 + R_3 + Z_1 + Z_2 \begin{cases} R_{cc} \geq 2.035 \cdot 10^6 & Stable \\ R_{cc} < 2.035 \cdot 10^6 & Unstable \end{cases} \qquad \text{(Eq. 4.79)}$$

This study explains a number of practical observations often encountered in 3D simulations of the vascular system. The most prominent assumption is that the impedance reduces wave reflections and therefore aids in the stability of the model.

This is partially true, since waves reflected back across coupling borders aid in either the numerical generation and dissipation of energy for the explicit and implicit coupling respectively. However, in addition a numerical wave is created just by the coupling conditions itself. Under the right conditions in a 3D setting, a model can be perfectly stable given a certain windkessel impedance but might become unstable for failing to include viscous resistance or even dissipation from turbulence.

A condition that was examined but not described is that a reduction in compliance aids in creating instability. The principal reason for this, is that a larger compliance dampens the flow that comes in by storing more fluid flow at a lower pressure. A lower pressure means that generated or dissipated coupling energy is lower than it would have been otherwise and vice versa. Additionally, a smaller compliance increases the frequency of the flow wave travelling between 2 windkessel terminations. Similarly, relationship exists for inertances whereby a larger inertance has a destabilizing on the full model due to coupling conditions. However, more work is required to establish formal relationships.

4.3.4.2.   *Implicit coupling instability*

It is often established that implicit evaluation of a model is unconditionally stable. This is not the case regarding partitioned model coupling. As was mentioned before, energy can accumulate within the full partitioned model within an iteration cycle during a single time-step. To see this, a different narrative will be used compared to the energy narrative used so far. Instead each model will be rewritten as a single

equation to return the outputs as function of the inputs simultaneously. Additionally, for simplification of the procedures a fully implicit scheme is used for both the numerical scheme of the partitioned models as well as the coupling conditions.

The starting point of this discussion is the model consisting of the outlet vessels only with a possible flow inlet source at the centre. This simplification is made because the flow through the inlet vessel is fully determined a priori. Equations for all three partitioned models, the bifurcation and the two windkessel models, can be rewritten such that terms which are constant during a time-step and those that are allowed to vary during a time-step, are separated. For the 2 outlet vessels in the bifurcation, the continuous function for pressure from the windkessel model up until the inlet node can be written as:

$$P_{in}(t) - P_{wki}(t) = q_i(t) \sum_i R_i + \frac{dq_i(t)}{dt} \sum_i L_i \qquad \text{(Eq. 4.80)}$$

In the bifurcation model each outlet only contains a single resistor and inertance making it possible to drop the summation signs. Pressure at the outlets is prescribed by the windkessel models and are therefore a source term for this model. After discretisation using backward-euler discretisation from eq. 4.19 for the derivative term, eq. 4.80 results in an expression for the flow.

$$q_i(t + \Delta t) = K_{1i}\big(P_{in}(t + \Delta t) - P_{wki}(t + \Delta t)\big) + K_{2i}q_i(t)$$
$$K_{1i} = \frac{\Delta t}{R_i \Delta t + L_i}, \quad K_{2i} = \frac{L_i}{R_i \Delta t + L_i} \qquad \text{(Eq. 4.81)}$$

For reading clarity it is assumed that all functions are evaluated at the next time-step $t + \Delta t$ unless indicated otherwise for the remainder of the discussion. Using the conservation of flow at the inlet node, the pressure at the inlet can be written as a function of the inlet flow, pressure at the outlets and the flow at the inlets:

$$p_{in} = \frac{q_{in} + \Sigma_i\big(K_{1i}P_{wki} - K_{2i}q_i(t)\big)}{\Sigma_j K_{1j}} \qquad \text{(Eq. 4.82)}$$

This expression can be substituted back into eq. 4.81 to obtain an equation of the partial flows from which the inlet pressure has been eliminated:

$$q_i = K_{3i}\left(q_{in} + \sum_j K_{1j}\big(P_{wkj} - P_{wki}\big)\right) + C_{1i} + C_{2i} \qquad \text{(Eq. 4.83)}$$

$$K_{3i} = \frac{K_{1i}}{\Sigma_j K_{1j}}, \quad C_{1i} = -K_{3i}\sum_j K_{1j}q_j(t), \quad C_{2i} = K_{2i}q_i(t) \qquad \text{(Eq. 4.84)}$$

Note that q_{in} is fully predetermined and that C_{1i} and C_{2i} only depend on the flow at the previous time-step. As such these values do not change during a time step and can be grouped in a single constant C_{3D}. If only the 2-outlet case is considered, the K-constants that remain for the pressure can be grouped into a single K constant K_{3D}, leading to:

$$q_i(t + \Delta t) = K_{3D}\big(P_{wkj}(t + \Delta t) - P_{wki}(t + \Delta t)\big) + C_{3D,i} \qquad \text{(Eq. 4.85)}$$

$$K_{3D} = \frac{K_{11}K_{12}}{K_{11} + K_{12}} \quad C_{3D,i} = K_{3i}q_{in}(t + \Delta t) + C_{1i} + C_{2i} \qquad \text{(Eq. 4.86)}$$

Eq. 4.86 can be used to provide flow boundary conditions for the windkessel model but is a function of the windkessel pressure at the next time-step $t + \Delta t$ which is unknown a priori. A similar procedure can be followed for the windkessel model of which the derivation is omitted, and the result given by:

$$p_{wki}(t + \Delta t) = K_{wk,i}q_i(t + \Delta t) + K_{wk1,i}C_{wk1} + K_{wk2,i}C_{wk2}$$
$$= K_{wk,i}q_i(t + \Delta t) + C_{wki}$$

(Eq. 4.87)

$$K_{wk,i} = \frac{\Delta t(R_{p,i} + Z_i) + R_{p,i}C_iZ_i}{\Delta t + R_{p,i}C_i}$$
$$K_{wk1,i} = \frac{R_{p,i}C_i}{\Delta t + R_{p,i}C_i}, \quad K_{wk2,i} = \frac{-R_{p,i}C_iZ_i}{\Delta t + R_{p,i}C_i}$$
$$C_{wk1} = p_{wki}(t), \quad C_{wk2} = q_i(t)$$

(Eq. 4.88)

In order to couple these equations, the strongly-implicit coupling scheme from Eq. 4.54 is used. While the starting order of the models is relatively unimportant, assume for bookkeeping purposes that a single iteration consists of first evaluating the 3D model, obtaining an estimate of the windkessel flow at time $t + \Delta t$ after which an estimate of the windkessel pressure is found at the current time-step. Assuming the pressure and flow at the next iteration are better estimates of the correct pressure and flow, the difference between iterations of these quantities can be regarded as the error at that iteration. This eliminates all C-constants from the system as they do not depend on the iteration number. Therefore, subtracting eq. 4.85 and 4.87 at subsequent iterations and substituting these equations into one another results in:

$$q_i(t + \Delta t, n) - q_i(t + \Delta t, n - 1) = \varepsilon_{q,i}(t + \Delta t, n)$$

$$= K_{3D}\left(K_{wk,j}\varepsilon_{q,j}(t + \Delta t, n - 1) - K_{wk,i}\varepsilon_{q,i}(t + \Delta t, n - 1)\right)$$

(Eq. 4.89)

$$p_i(t + \Delta t, n) - p_i(t + \Delta t, n - 1) = \varepsilon_{p,j}(t + \Delta t, n)$$

$$= K_{wk,i}K_{3D}\left(\varepsilon_{p,j}(t + \Delta t, n - 1) - \varepsilon_{p,i}(t + \Delta t, n - 1)\right)$$

(Eq. 4.90)

This implies that the error at the current time-step of any quantity is dependent on the introduced K-constants and the error of those quantities at the previous iteration. Omitting the indication of the time-step and considering the 2-outlet case, this can be written in system form as:

$$\begin{pmatrix} \varepsilon_{q,1}(n) \\ \varepsilon_{q,2}(n) \end{pmatrix} = K_{3D}\begin{pmatrix} -K_{wk,i} & K_{wk,j} \\ K_{wk,i} & -K_{wk,j} \end{pmatrix}\begin{pmatrix} \varepsilon_{q,1}(n - 1) \\ \varepsilon_{q,2}(n - 1) \end{pmatrix}$$

(Eq. 4.91)

$$= \boldsymbol{A}_{\varepsilon q}\overrightarrow{\varepsilon_q}(n - 1)$$

$$\begin{pmatrix} \varepsilon_{p,1}(n) \\ \varepsilon_{p,2}(n) \end{pmatrix} = K_{3D}\begin{pmatrix} K_{wk,i} & -K_{wk,i} \\ -K_{wk,j} & K_{wk,j} \end{pmatrix}\begin{pmatrix} \varepsilon_{q,1}(n - 1) \\ \varepsilon_{q,2}(n - 1) \end{pmatrix}$$

(Eq. 4.92)

$$= \boldsymbol{A}_{\varepsilon p}\overrightarrow{\varepsilon_p}(n - 1)$$

Note that $\boldsymbol{A}_{\varepsilon p} = -\left(\boldsymbol{A}_{\varepsilon q}\right)^{\boldsymbol{T}}$. This system is stable within an iteration loop, if the solution approaches a finite value for $\lim\limits_{n\to\infty}$ implying that $\varepsilon_{\varphi,j}$ approaches zero. For the flow error this can be rewritten in system form as:

$$\lim_{n\to\infty}\overrightarrow{\varepsilon_q}(n - k) = \lim_{n\to\infty}\left(\boldsymbol{A}_{\varepsilon q}\right)^{\boldsymbol{n}}\overrightarrow{\varepsilon_q}(k)$$

(Eq. 4.92)

It can be shown that the matrix in eq. 4.92 can be rewritten in limit form as a function of the matrix $\boldsymbol{A}_{\varepsilon q}$:

$$\lim_{n \to \infty} \left(\boldsymbol{A}_{\varepsilon q} \right)^{\boldsymbol{n}} = \lim_{n \to \infty} (-1)^{n-1} \left(K_{3D} \left(K_{wk,i} + K_{wk,j} \right) \right)^{n-1} \boldsymbol{A}_{\varepsilon q}$$

$$= \lim_{n \to \infty} (-1)^{n-1} K_s^{\ n-1} \boldsymbol{A}_{\varepsilon q}$$

(Eq. 4.93)

Derivation has been omitted as this involves a lengthy manipulation of equations. It should be noted that for real systems, all parameters are positive and that the values in $\boldsymbol{A}_{\varepsilon q}$ are finite and constant within a time-step. In order for the limit in eq. 4.93 tot be finite the K_s-term has to be smaller than 1. In other words, K_s takes the roll of an amplification factor which must be smaller than 1 for the value of all quantities to converge to a stable value. In the case where $K_s = 1$, the model can be considered unstable for practical purposes as none of the quantities will converge to a stable value. Due to the anti-symmetry of $\boldsymbol{A}_{\varepsilon p}$ and $\boldsymbol{A}_{\varepsilon q}$ the exact same result can be obtained for pressure.

Also note that the change of a quantity, $\varepsilon_{\varphi,j}$ for either pressure or flow, changes sign with every iteration step due to the factor $(-1)^{n-1}$. If the system is stable, the quantity will therefore experience a diminishing oscillation around the final value while an unstable system will experience an amplifying oscillation around that same value. The stability criterion for the 2-outlet case can be summarised as:

$$K_s = K_{3D} \left(K_{wk,i} + K_{wk,j} \right) \begin{cases} K_s > 1 & Unstable \\ K_s = 1 & Stable\ Oscillation \\ K_s < 1 & stable \end{cases}$$

(Eq. 4.94)

Lastly, it is possible to generalise this system from a bifurcation to a k-way junction. This can become relevant in practical cases as 3-way junctions or approximations

thereof can occur in the human vascular system. The process for arriving at a resulting set of equations is completely analogous to that presented for the bifurcation but requires modifications to eqs. 4.85, 4.86, 4.89 and 4.90, presented below:

$$q_i(t + \Delta t) = \sum_j K_{3D,ij} \left(P_{wkj}(t + \Delta t) - P_{wki}(t + \Delta t) \right) + C_{3D} \qquad \text{(Eq. 4.95)}$$

$$K_{3D,ij} = \frac{K_{1i}K_{1j}}{\sum_j K_{1j}} \qquad \text{(Eq. 4.96)}$$

$$\varepsilon_{q,i}(t + \Delta t, n) = \sum_j K_{3D,ij} \left(K_{wk,j}\varepsilon_{q,j}(t + \Delta t, n - 1) - K_{wk,i}\varepsilon_{q,i}(t + \Delta t, n - 1) \right) \qquad \text{(Eq. 4.97)}$$

$$\varepsilon_{p,j}(t + \Delta t, n) = K_{wk,i} \sum_j \left(K_{3D,ij} \left(\varepsilon_{p,j}(t + \Delta t, n - 1) - \varepsilon_{p,i}(t + \Delta t, n - 1) \right) \right) \qquad \text{(Eq. 4.98)}$$

For the windkessel pressure equation no changes are necessary. The resulting equations can be reassembled into a system according to $\vec{\varepsilon_q}(n) = \boldsymbol{A}_{\varepsilon q} \vec{\varepsilon_q}(n - 1)$. However, it is not straight-forward to find a general amplification factor as was done for the bifurcation case as interaction effects between boundaries exist. No general analytical amplification factor was found during this study. Some interactions can dissipate numerical energy while others can generate energy leaving the sign of the conservation of energy undetermined. It is possible to assess the stability of this system numerically because $\boldsymbol{A}_{\varepsilon q}$ from eq. 4.93 is constant during a time-step and only relies on the physical parameters of the model. For the limit of $n \to \infty$, all entries of $\left(\boldsymbol{A}_{\varepsilon q} \right)^{\boldsymbol{n}}$ should remain finite in order for the system to be stable.

Lastly, a resemblance can be seen between the terms in the summation of eqs. 4.97-4.98 for k-boundaries and eqs. 4.89-4.90 for just 2 boundaries. This resemblance indicates that the total error amplification can be imagined to be a sum of the errors between pairwise paths. The K factors are constant within a time-step hence the error can grow along certain paths within the geometry while along others it can only diminish. Therefore, the stability can potentially be analysed from a standpoint of an error amplification of the energy passing along sections of the geometry. However, this would require an analysis from an energy point of view which has not been carried out for the current study.

4.4. Discussion

This chapter started-off examining the conservation behaviour of a conservative ideal LC-model with respect to its numerical discretisation demonstrating the well-known stability behaviour of backward and forward difference methods. Consecutively for this 2-element model it was shown that partitioned coupling approaches between both elements result in stability behaviour that is very similar to the behaviour seen for numerical discretisation choices. Various coupling schemes were analysed, and a central-difference based scheme was introduced resulting in an energy conservative coupling.

Although, the used modelling approach is a 0D approach and thus inherently different from a final volume-based method, the coupling conditions and iterations schemes used can be applied in any partitioned approach. As such it is expected

that the same stability behaviour would hold for coupling between 3D geometries and 0D lumped parameter boundaries.

Subsequently, a more realistic 0D geometry of a bifurcation was considered to introduce physical dissipation within the model and additionally to introduce the concept of an open-loop system in which energy can be added or removed. For this model it was ultimately demonstrated that the model is stable for an explicit coupling when the numerical energy generation is smaller than the physical energy dissipation. The numerical energy generation rate is dependent on the time-step and the physical values for compliance and inertance while energy dissipation is only dependent on the resistances and impedances in the system. However, the exact relation for energy generation rate as a function of these parameters has not been established in the current study.

It should be noted that even if the entire model is dissipative in nature overall, it is not implied that this model is accurate. In order for the model to be accurate the discrepancy in energy flows between compartments needs to be rectified by enforcing a numerically conservative coupling which is dependent on the used time-integration scheme of the solvers. Simply adding additional dissipation or removing energy through the posed boundary conditions does not rectify a non-conservative coupling.

Translation of these analyses to 3D methodologies requires additional attention. For inviscid flows in 3D geometries, the stability can be examined solely by considering

the numerical energy generation at the boundaries. However, for flows containing internal physical dissipation, as in viscous dissipation at walls or turbulent effects, the preceding analysis is less straightforward as those dissipators need to be included in the analysis adding to the computational cost. In this case considering the numerical energy generation only at the boundaries can however still provide information on the probability of encountering an instability. If the net effect at the boundaries is a dissipative effect the model is unable to become unstable.

Lastly, an alternative stability analysis approach was taken to demonstrate the possibility of an implicit coupling instability, by analysing an error amplification factor. Within a timestep energy can be dissipated through physical effects but this effect is limited from iteration to iteration. Additionally, a smaller time-step further limits the physical dissipation. For a lumped-parameter bifurcation, it is possible to analytically determine an amplification factor.

While this might be more complicated for a 3D geometry it is to be expected that a reasonable stability estimate could still be derived by constructing a reduced order 0D or 1D model of the geometry for this purpose. For a K-outlet geometry this amplification factor cannot be derived analytically but numerical approximation using 0D approximations would not lead to significant computational cost as the number of vessels connecting to a single junction in the cardiovascular system generally remains low.

Additional work is required to assess the validity and practicality of this approach for 3D techniques. Additionally, the stability analysis of the implicit coupling utilized the analysis of an amplification factor a more elegant approach would be to consider the energy amplification between iterations as a summary measure. However, the main recommendation of the current chapter is to invest more effort to develop conservative couplings given a time integration scheme in future.

Chapter 5

5. Simplified Wave-Propagation

5.1. Introduction

Up till this point a number of conclusions can be drawn from previous chapters. Chapter 2 addressed the data requirements and simulation strategies for directly prescribing flow and pressure from patient-specific data. It was shown that this is generally an unsuccessful strategy. The windkessel model from chapter 3, being one of the simplest and most commonly used models in hemodynamics, was used as an example for providing boundary conditions for 3D geometries using a multiscale approach. Numerical energy generation or dissipation were then considered due to the coupling between a 0D representation of a section of the vascular system, a vascular bifurcation, and a set of windkessel models in chapter 4. Additionally, this chapter provides a rational for the results from chapter 2. The data from measurements was not consistent with different physical effects encountered and no effort was made to make the data posed at the boundaries energy conservative.

By representing the vascular bifurcation in chapter 4 as a lower dimensional 0D representation some of the physical 3D characteristics of the system get misrepresented. Misrepresentation of these effects did not affect the analysis of coupling energy as it has been shown that gain or loss of energy in a model with minimal numerical losses can be attributed solely to the coupling conditions regardless of the actual model. Additionally, the bifurcation geometry was assumed to be rigid, containing only inertances and resistances.

Failing to include these physical characteristics affects the accuracy of the model with regards to the real-world physical system. One of the biggest and most common simplifications made, is to assume a rigid 3D-geometry. In chapter 2 this was achieved by having no compliances in the bifurcation model and as a result lump all system compliance into the windkessel models. The disadvantage of this approach is that the wave-propagation inside of the 3D-geometry is effectively infinite meaning that any flow or pressure change anywhere in the domain immediately effects all other locations in the domain as was discussed in the introductory chapter. In the case of aortic arch simulations this completely foregoes the main function of the vessel, namely, to store blood volume at a certain pressure in order to gradually transport and distribute it elsewhere in the body.

A significant part of the function of the large arteries stems from the distensibility of these vessels which gives them compliance. In order to integrate compliance into 3D Fluid dynamics simulations, it is necessary to incorporate movement of the vessel wall. When considering a single blood vessel, the blood exerts forces on the wall, either through static pressure or dynamic pressure caused by the movement of fluid. These forces drive the expansion of the wall and until the wall is exerting an equal and opposite amount of force on the fluid. By doing so the vessel stores elastic energy within the vessel wall material. Additionally, by expanding the wall, that vessel accommodates an additional amount of fluid. When a pressure differential exists with respect to neighbouring parts of vascular system, i.e. the pressure in the

vessel is higher than the pressure downstream, fluid stored in the blood vessel can flow out of the vessel again.

Numerically this requires another coupling between multiple models known as fluid-structure interaction (FSI). Required are at least two models, namely a fluid dynamics model for blood flow and a solid mechanics model for the wall. The study by Reymond et al. [63] discusses the importance of including FSI effects and compares Compliant 3D models vs. rigid 3D models vs. 1D models, concluding significant differences in hemodynamical indicators like wall-shear stress. Historically, the compliance in the windkessel model or other lumped parameter models has often been used to compensate for not representing FSI effects [64, 65] but this approach can still be found in some more recent studies [66, 67, 68]. This lumps all compliance effects onto the distal vasculature foregoing the pressure and flow wave propagation present in vasculature. This approach is warranted for smaller diameter vessels where compliance effects are less influential on the clinical outcome as in the simulation of FFR for instance [69, 68].

Potentially more model interactions can be added i.e. boundary conditions models or rheological models introducing more interaction effects. Interaction effects due to coupling are a bigger concern in a partitioned modelling approach as compared to a monolithic modelling approach where all model components are evaluated simultaneously. Each model coupling potentially generates or dissipates its own numerical energy, potentially destabilising the model at best leading no accuracy

errors between the model and the real system. An example is the added mass effect in FSI where partitioned model coupling introduces numerical instabilities [70, 71]. In partitioned modelling approaches with implicit couplings, iterations are required to calculate approximate solutions of pressure and flow at the next time-step for each model. These estimates are then used to compute similar solutions in the coupled models which again serve as boundary conditions for other models. Hence every interaction effect potentially increases the number of iterations required during a time-step due to coupling. This makes partitioned modelling of fluid-structure interaction computationally increasingly expensive depending on the complexity of the model and potentially unstable. Additionally, due to the complex behaviour it is cumbersome to automate this procedure.

An alternative to modelling the full fluid structure interaction system was introduced in the thesis work by Brown [72]. The general concept is to model the propagation of pressure and flow waves by having a compressible fluid instead of distensible walls. The storage of mass now occurs through compression of the fluid instead of increasing the volume. Elasticity of the wall is now captured in the elasticity of the fluid by having a constitutive equation relating density to fluid pressure. Because of this it is possible to handle all computations by a single solver, in the case of this study ANSYS Fluent. A big advantage of this approach includes a static mesh, making this method more robust in practice and making it easier to guarantee the accuracy of the solution. Additionally, this removes the need for a coupling infrastructure between partitioned solvers. Designing appropriate physical

132

coupling conditions is often more straightforward than the implementation of said methods. As an example, Fluid dynamics solvers are often designed within a Eulerian frame of reference, i.e. all quantities are described with respect to their position in space. Solid mechanics solvers are often written from a Lagrangian standpoint, i.e. a frame of reference that follows the material being deformed. Therefore, methods are required to map the solution from the fluid dynamics solver onto the domain of the structural mechanics solver and vice versa. This imposes requirements on the mesh of both solvers near the coupling boundary and communication of quantities between both solvers which might use completely different file storage methods or not be available to the level of detail required.

Designing software coupling interfaces for solvers that are not written for that specific purpose is a non-trivial procedure making a single solver approach more attractive. Rather than developing a monolithic solver from the ground up, a straightforward way of having a single solver approach is to include additional physics within a pre-existing solver. The compressible fluid method explored by Brown [72] could potentially provide this functionality. However, discrepancies in terms of results were observable between the compressible method and a full 3D 2-way FSI approach. This chapter focusses on characterising the wave propagation behaviour of both models and a third 1D model in order to suggest improvements to the compressible fluid model.

5.2. Wave propagation comparison

In the study of Brown [72], a compressible fluid model was used to add the effect of wave propagation In this part of the study, part of their analyses will be revisited. Analysis of the model comprised of two parts. The first part was verification that the compressible fluid model had the desired modeling effect compared to the physical system, results from the numerical 3D compressible fluid model were compared to an analytical 1D wave propagation model. For this analysis, a straight distensible tube of 20[cm] in length was modelled, coupled to a single windkessel model. Two important outcomes arose from the first part of this analysis. It was firstly remarked that using the 2-element windkessel as opposed to the 3-element windkessel could give rise to significant oscillations in the solution for both the numerical as well as the analytical model. When these oscillations were only apparent in the numerical solution, viscosity was increased at the start of the simulation to dampen spurious oscillations due to start-up effects after which it was gradually reduced until equal to average blood viscosity. After dampening a discrepancy remains which was attributed to the fact that the models are functionally different due to the 3D model containing viscosity while the 1D model is effectively inviscid.

In the current study it is argued that the discrepancy is due to functional differences between these models which excludes viscosity. For this purpose, the experiment is repeated after giving the details of both the 1D model implementation and the compressible fluid-based model.

5.3. 1D Wave-propagation

5.3.1. 1D-Fluid Theory

The aim of this section is to arrive at a 1D description of fluid flow through a straight compliant vessel after which this 1D vessel will be coupled to outlet windkessel conditions. Deriving the equations for a 1D tube requires simplification of the 3D characteristics of the flow and a number of assumptions. The fluid dynamics are governed by the Navier-Stokes equations which describe the conservation of mass and momentum. Additionally, other conservation laws can be added as for instance the law of energy conservation depending on the level of detail and accuracy required to model a system of interest. The Navier-Stokes equations in vector notation for Newtonian incompressible flow are given by:

$$\rho\left(\frac{\partial \vec{v}}{\partial t} + (\vec{v} \cdot \nabla)\vec{v}\right) = -\nabla p + \mu\nabla^2\vec{v} + \vec{f} \qquad \text{(Eq. 5.1)}$$

$$\nabla \cdot \vec{v} = 0 \qquad \text{(Eq. 5.2)}$$

In which ρ is the fluid density, $\vec{v}$ is the fluid velocity, p is the pressure, μ is the dynamic viscosity and $\vec{f}$ are additional volume forces, for instance gravity. A derivation of the Naiver-Stokes equations can be found in most introductory textbooks on fluid dynamics. Both mass and momentum are transportable quantities and as such their balance equations can be derived using Reynolds transport theorem over an arbitrary control volume:

$$\frac{d}{dt}\iiint_V \varepsilon dV = \iiint_V \frac{\partial \varepsilon}{\partial t}dV + \iint_\Gamma \varepsilon \vec{v} \cdot \vec{n}d\Gamma \qquad \text{(Eq. 5.3)}$$

This theorem says that the change of any transportable quantity ε in a volume V, is equal to the change of that quantity in the volume due to sources or sinks and the influx of that quantity over the border. Since the Reynolds transport theorem should hold for an arbitrary control volume it should also hold for an infinitesimal volume leading to eq. 5.1-5.2. After derivation of the 3D Navier-Stokes equations it is possible to derive a 1D version by making several assumptions including negligible circumferential flow and axisymmetric geometries as was done by Barnard et al. [73] .However, Hughes&Lubliner [74], formed the 1D balance equations for mass and momentum for axial flow along a pipe shaped control volume. This analysis foregoes the assumption of axisymmetry and some of the results here will be re-stated for clarity. The resulting 1D Reynolds transport theorem, for an arbitrary control length of tube, is re-stated below for the control volume depicted in fig. 5.1:

$$\frac{\partial}{\partial t}(S\bar{\varepsilon}) + \frac{\partial}{\partial z}\left(S(\overline{\varepsilon v_z})\right) = \int_S \dot{\varepsilon}da + \oint_C \varepsilon w_n dl \qquad \text{(Eq. 5.4)}$$

In which, S is the surface of the cross-section of the tube, C is the bounding curve of S on the outer-surface of the pipe, w_n is the velocity of the pipe relative to the fluid and any quantity with an overline indicates the average of a quantity with respect to cross-section S. It was assumed that fluid can flow over the luminal surface of the vessel. It will be assumed for the remainder of the text that the luminal

136

surface is impermeable, and no fluid can flow across it making $w_n = 0$. Additionally, $\dot{\varepsilon}$ is the material derivative given by:

$$\dot{\varepsilon} = \frac{\partial \varepsilon}{\partial t} + \vec{v} \cdot \nabla \varepsilon \qquad \text{(Eq. 5.5)}$$
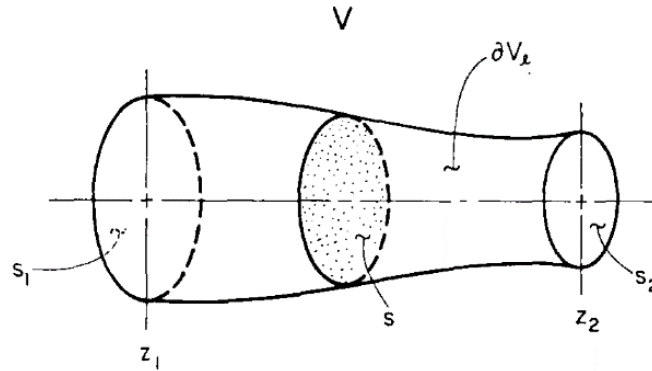
Fig. 5.1: Control volume adapted from Hughes& Lubliner [74]

The conservation of mass can be given by substituting $\varepsilon = \rho$, with ρ the density of the fluid. For incompressible flow this reduces the equation of mass to:

$$\rho \left(\frac{\partial S}{\partial t} + \frac{\partial S \bar{v}_z}{\partial z} \right) = 0 \qquad \text{(Eq. 5.6)}$$

Or in words, the change in cross-sectional area is equal to the net inflow of fluid at either section of the pipe. Similarly, the momentum equation can be derived for this setting by substituting $\varepsilon = v_z$. If it is assumed that transverse flow, or radial flow in the axisymmetric case, and external body forces are negligible, the 1D momentum equation reduces to:

$$\dot{\bar{v}}_z + \frac{1}{S} \frac{\partial}{\partial t} \left(S \left(\overline{v_z^2} - \bar{v}_z^2 \right) \right) = -\frac{1}{\rho} \frac{\partial p}{\partial z} + \frac{1}{S} \oint_C \frac{\mu}{\rho} \frac{\partial v_z}{\partial m} dl \qquad \text{(Eq. 5.7)}$$

With $\frac{\partial()}{\partial m}$ the directional derivative with respect to the outward wall normal. It can be shown using dimensional analysis for pulsatile flow through large arteries that viscous forces are negligible and that the flow is inertia dominated. For frictionless flow and neglecting the no-slip condition at the wall, flow $\bar{v}_z = v_z$ and eq. 5.7 reduces simply to:

$$\dot{\bar{v}}_z = -\frac{1}{\rho}\frac{\partial p}{\partial z} \qquad \text{(Eq. 5.8)}$$

Both equations 5.6 and 5.8 can be rewritten in terms of flow q and pressure p resulting in the following system of equations:

$$\frac{\partial S}{\partial p}\frac{\partial p}{\partial t} + \frac{\partial q}{\partial z} = 0 \qquad \text{(Eq. 5.9)}$$

$$\rho\frac{\partial q}{\partial t} + S\frac{\partial p}{\partial z} = 0 \qquad \text{(Eq. 5.10)}$$

Eqs. 5.9-5.10 are the 1D equations for the propagation of flow and pressure. Often for the ease of solving the system the equations are linearized by assuming small deformations for which $\frac{\partial S}{\partial p} = C_0$ is the compliance of the vessel and S= S_0 with both approximately constant. Compliance C_0 is a relationship between the pressure and the cross-sectional area of the tube and depends primarily on the material properties and geometry of the vessel wall. What the exact functional relationship for the compliance should be, will be left unaddressed until after the full model development.

5.3.2.   *Analytical model*

An analytical model of eqs. 5.9-5.10 can be found using a transformation to Fourier space. By combining eqs. 5.9-5.10 both equations can be rewritten in terms of only one of the quantities, either pressure or flow. As an example, this can be done by taking the derivative with respect to time of eq. 5.9 and the derivative with respect to axial coordinate z of eq. 5.10 and combining the resulting equations to eliminate the flow. This results in a 2nd-order equation for pressure eq. 5.11. A similar procedure can be performed to eliminate the pressure instead resulting in eq. 5.12.

$$L_0 C_0 \frac{\partial^2 p}{\partial t^2} = \frac{\partial^2 p}{\partial x^2} \qquad \text{(Eq. 5.11)}$$

$$C_0 L_0 \frac{\partial^2 q}{\partial t^2} = \frac{\partial^2 q}{\partial x^2} \qquad \text{(Eq. 5.12)}$$

In which $L_0 = \frac{A_0}{\rho}$ and $C_0 = \frac{\partial S}{\partial p}$, the inertance and compliance per unit length in axial direction. The model represented by these two equations is well known in the field of electronics and is called a transmission line model. An infinitesimal segment of a lossless transmission line model can effectively be modelled by an inertance and a compliance as given in fig. 5.2. Both equations 5.11 and 5.12 can be recognised to be in the form of 1D wave equations.
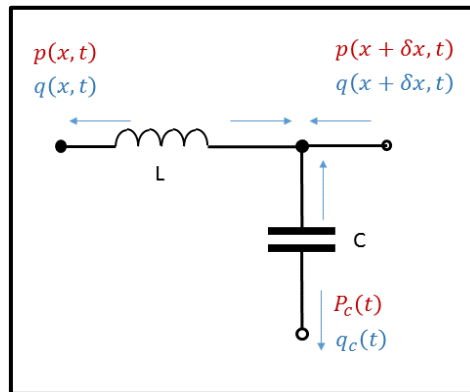
Fig. 5.2 - Lumped parameter model for infinitesimal 1D-segment of transmission line model

A solution to 1D wave equations of this form was described for vibration of a string by d'Alembert [75]. It states that the general solution is a function of a superposition of a set of forward and backward traveling waves. Hence for pressure and flow this gives:

$$p(z,t) = p^+(z - ct) + p^-(z + ct) \qquad \text{(Eq. 5.13)}$$

$$q(z,t) = q^+(z - ct) + q^-(z + ct) \qquad \text{(Eq. 5.14)}$$

In which the positive superscripts for pressure and flow indicate forward traveling waves, negative superscripts indicate backward traveling waves, z is the axial position along the domain and c is the wave velocity. Initial conditions have been neglected for the current formulation. Recall from chapter 3, the possibility to represent any signal by a Fourier decomposition of infinite order as was done using eq. 3.21. This implies that any signal can be represented as a superposition of sine and cosine functions. Using eqs. 5.13-5.14 it is possible to come to a numerical solution of pressure and flow, which will be demonstrated for a single harmonic denoted by $P_\omega(z,t)$ and $Q_\omega(z,t)$ respectively. Employing a convenient scaling for

the axial and temporal coordinates z and t respectively the forward pressure and

flow waves can be written as:

$$p^+(z - ct) = P_{c,+}cos(kz - \omega t) + P_{s,+}cos(kz - \omega t) \quad \text{(Eq. 5.15)}$$

$$q^+(z - ct) = Q_{c,+}cos(kz - \omega t) + Q_{s,+}cos(kz - \omega t) \quad \text{(Eq. 5.16)}$$

In which $\omega = 2\pi f\,[-]$ is the angular frequency in time and $k = \omega/c\,[-]$

representing the angular frequency in space. A similar decomposition can be made

for the backwards traveling wave and combined with eqs. 5.13-5.14. However, an

additional relationship exists between pressure and flow governed by the

characteristic impedance. For a lossless transmission line, this relationship reduces

to:

$$Z_0 = \sqrt{\frac{L_0}{C_0}} = \frac{p^+}{q^+} = -\frac{p^-}{q^-} \quad \text{(Eq. 5.17)}$$

This allows for rewriting the Fourier coefficients in the pressure equation p^+ as a

function of those in the flow equation q^+:

$$P_\omega(z,t) = \sqrt{\frac{L'}{C'}}(\{Q_{\omega,1}cos(kz - \omega t) + Q_{\omega,2}sin(kz - \omega t)\,\} \quad \text{(Eq. 5.18)}$$

$$- \{Q_{\omega,3}cos(kz + \omega t) + Q_{\omega,4}sin(kz + \omega t)\,\})$$

$$Q_\omega(z,t) = \{Q_{\omega,1}cos(kz - \omega t) + Q_{\omega,2}sin(kz - \omega t)\,\}$$

$$+ \{Q_{\omega,3}cos(kz + \omega t) + Q_{\omega,4}sin(kz + \omega t)\,\} \quad \text{(Eq. 5.19)}$$

This is a system of 2-equations with 4 unknowns, namely the Fourier coefficients

for flow. It is possible to obtain 4 equations by employing the proper boundary

conditions similar to those in the 3D case. At inlet, flow boundary conditions are prescribed similarly according to a Fourier description:

$$Q_\omega(0, t) = Q_0(t) = Q_{0c}\cos(\omega t) + Q_{0s}\sin(\omega t) \qquad \text{(Eq. 5.20)}$$

For this to hold with respect to eq. 5.19 and through the symmetry relations for sine and cosine functions, it can be shown that this implies that:

$$Q_{0c} = Q_{\omega,1} + Q_{\omega,3} \qquad \text{(Eq. 5.21)}$$

$$Q_{0s} = Q_{\omega,4} - Q_{\omega,2} \qquad \text{(Eq. 5.22)}$$

At the end of the tube at axial position L, a windkessel model is connected under an assumption that the flow can be represented by a similar decomposition as eq. 5.20:

$$Q_\omega(L, t) = Q_L(t) = Q_{Lc}\cos(\omega t) + Q_{Ls}\sin(\omega t) \qquad \text{(Eq. 5.23)}$$

Under this condition it is possible to use the result of chapter3, eq. 3.20 as an outlet boundary condition for pressure. It can be seen that eq. 3.20 can be recast in similar form to the flow boundary condition of eq. 3.20:

$$P_\omega(L, t) = P_{lc}\cos(\omega t) + P_{Ls}\sin(\omega t) \qquad \text{(Eq. 5.24)}$$

Similar to the flow boundary condition, eq. 5.24 can be combined with eq. 5.18 and the symmetry relations for sine and cosine resulting in another set of two equations which have been omitted. This system of 4 equations with 4 unknowns can be written in matrix form as:

$$(\boldsymbol{H} - \boldsymbol{K}^{-1}\boldsymbol{G}\boldsymbol{F}\,)\underline{\boldsymbol{Q}} = \underline{0} \quad \underline{\boldsymbol{Q}} = \begin{pmatrix} Q_{\omega,1} \\ Q_{\omega,2} \\ Q_{\omega,3} \\ Q_{\omega,4} \end{pmatrix} \qquad \text{(Eq. 5.25)}$$

$$\boldsymbol{H} = \sqrt{\frac{L'}{C'}} \begin{pmatrix} \cos(kL) & \sin(kL) & -\cos(kL) & -\sin(kL) \\ \sin(kL) & -\cos(kL) & \sin(kL) & -\cos(kL) \end{pmatrix} \qquad \text{(Eq. 5.26)}$$

$$\boldsymbol{F} = \begin{pmatrix} \cos(kL) & \sin(kL) & \cos(kL) & \sin(kL) \\ \sin(kL) & -\cos(kL) & -\sin(kL) & \cos(kL) \end{pmatrix} \qquad \text{(Eq. 5.27)}$$

$$\boldsymbol{K}^{-1} = \frac{R}{1 + (RC\omega)^2} \begin{pmatrix} 1 & -RC\omega \\ RC\omega & 1 \end{pmatrix} \qquad \text{(Eq. 5.28)}$$

$$\boldsymbol{G} = \begin{pmatrix} 1 + \dfrac{Z}{R} & ZC\omega \\ -ZC\omega & 1 + \dfrac{Z}{R} \end{pmatrix} \qquad \text{(Eq. 5.29)}$$

The general solution can then be recovered by a superposition of the solution for different harmonics according to an infinite Fourier series. This solution is referred to as the analytical due to the fact that it provides an exact solution to the wave equations presented, given that the boundary conditions can be described exactly using a Fourier series. In practice for this to hold in a numerical system this means that the inflow signal has to be representable by a finite Fourier series. This is the reasoning behind choosing a pure sine function as the inflow boundary condition for verification of the windkessel model. It should be noted that the system does not provide an analytical solution of the hemodynamical system being modelled by the wave equations. Several simplifications have been made which do not hold in practice which will be shown further on.

In summary, a 1D model provides a description of pressure and flow by eq. 5.18-5.19 provided that the angular frequency ω and wave velocity c are given. The Fourier coefficients can then be computed at every instance in time for every angular frequency using eqs. 5.25-5.29. And lastly a general solution can then be found by superposition of the solution for all harmonics according to the Fourier series presented in eq. 3.21. The angular frequencies to consider can simply be chosen to be the first n-harmonics of a function. This implies that the base harmonic for biological signals is of the order of the period of a single heartbeat or $O(\omega) = 2\pi[-]$. Several choices can be made for the wave velocity which depends on the system including both the fluid dynamics as well as the solid mechanics model. However, the choice for both the compliance as the wave velocity is only relevant for creating an equivalence between the compressible and the distensible system represented by a conventional FSI simulation.

5.4. Compressible fluid model

As mentioned before the compressible fluid model stores and releases mass based on the density of the fluid as opposed to storing or releasing fluid by expanding or contracting the vessel, i.e. displacing the vessel wall. As such it can be noted that the distensible system and the compressible have the following relationships for linear elasticity and small deformations:

	Cross-sectional Area	Density
Distensible	$A(z,t) = A_0 + \dfrac{\partial A}{\partial \bar{p}} d\bar{p}(z,t)$	$\bar{\rho}(z,t) = \rho_0$
compressible	$A(z,t) = A_0$	$\bar{\rho}(z,t) = \rho_0 + \dfrac{\partial \bar{\rho}}{\partial \bar{p}} d\bar{p}(z,t)$

In which an overbar indicates the average of that quantity over the cross-sectional area and $d\bar{p}(z,t)$ is the change from the reference pressure p_0. By assuming small deformations, the compliance of the systems is approximately constant and not dependent on the pressure itself. In order to have equivalent mass in both systems, it can be recognized that it must hold that:

$$\frac{1}{A_0}\frac{\partial A}{\partial \bar{p}} = \frac{1}{\rho_0}\frac{\partial \bar{\rho}}{\partial \bar{p}}$$

<div align="right">(Eq. 5.30)</div>

It can be derived using the definition of linear momentum and Newton's second law of motion that the speed of sound in an isotropic material is equal to equation 5.31 in which K is the bulk modulus. It should be noted that the equality on the right, follows from the definition of the bulk modulus as being the derivative of pressure with respect to volume for a material:

$$c = \sqrt{\frac{K}{\rho}} = \sqrt{\frac{\partial p}{\partial \rho}}$$

<div align="right">(Eq. 5.31)</div>

If this equation is substituted back into the equations for the density of the compressible system and the area of the distensible system, we find that:

compressible

$$\bar{\rho}(z,t) - \rho_0 = \frac{1}{c^2}(p(z,t) - p_0) \qquad \text{(Eq. 5.32)}$$

distensible

$$A(z,t) - A_0 = \left(\frac{A_0}{\rho_0}\frac{1}{c^2}\right)(p(z,t) - p_0) \qquad \text{(Eq. 5.33)}$$

In other words, the wave velocity of the compressible system can be related to the compliance of the distensible system according to:

$$c = \sqrt{\frac{A_0}{\rho_0 C_0}} = \sqrt{\frac{1}{L_0 C_0}} \qquad \text{(Eq. 5.34)}$$

These equations are straightforward to implement under ANSYS fluent as UDF. However, these relationships only hold under the assumption that the compliance and thus the wave velocity, is effectively constant. The UDF consists of specification of the density of a fluid, as a function of the reference density ρ_0 at the reference pressure p_0 given the current pressure at a location. This is fully governed by eq. 5.32 and 5.34 but in order to try to create an equivalence between both systems an expression for the compliance is required. Note that the method used here differs slightly in the equation of state compared to Brown's implementation [72]. The method used by Brown utilizes an ideal gas obeying the ideal gas law, specifying the temperature and molar mass of the gas and necessitating incorporation of the energy equation within the solver. In the current study the equation of state is determined from the wave-velocity and pressure directly without calculating the temperature field as it is not a variable of interest. The compressibility of the fluid is an artificial addition to the behaviour of a fluid that should in fact be incompressible in reality.

A modification of the windkessel model was required for operation under fluent with a compressible gas model. This is due to the fact that mass- and volume-flow are no longer equivalent in the compressible gas model. The windkessel model works under the assumption that flow is defined to be volumetric flow and therefore the mass flow over the outlet boundary has to be converted to an equivalent volume flow:

$$q_{wk} = \frac{\rho}{\rho_0} q_{3d} \qquad \text{(Eq. 5.34)}$$

5.4.1. Structural model

All vessel wall mechanics are assumed to follow pure linear elasticity. The main wave effect being modelled is a transversal wave as opposed to a longitudinal wave. Considered below in fig. 5.3 is an infinitesimal wall segment under a thin walled assumption under plane strain. This implies that the radial stress σ_{rr} is negligible. Additionally, it is assumed that the wall is axially constrained according to $\varepsilon_{zz} = 0$, i.e. no deformation in axial direction
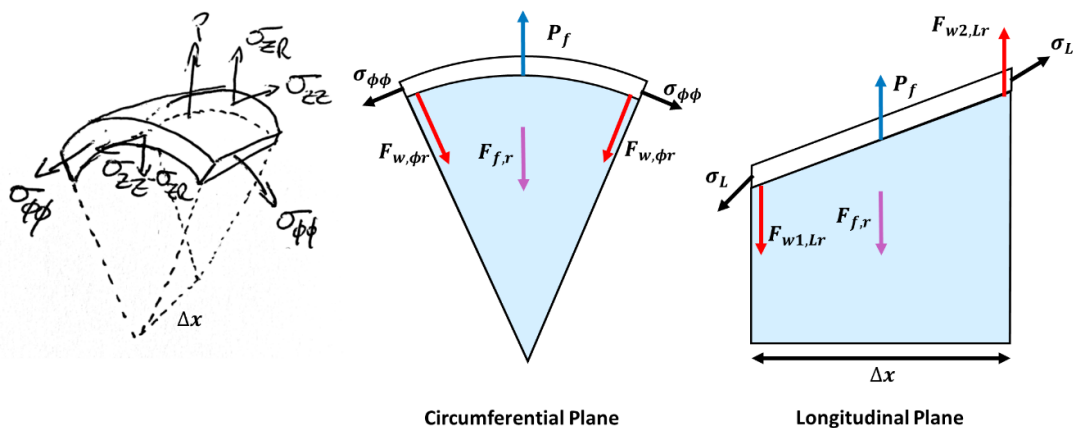
Fig. 5.3 - Infinitesimal vessel section and forces acting upon it.

The radial acceleration of an infinitesimal wall section can be determined as a function of the corresponding radial displacement. In order to do so, a balance of force can be considered combined with Newton's second law stating $m\ddot{u}_r = \sum F_i$, with m the mass, $\ddot{u}_r$ the acceleration in radial direction and $\sum F_i$ the sum of all forces acting on the wall section. Therefore, as an approximation, each infinitesimal wall section is considered to be a separate mass with an average acceleration. In the longitudinal/axial direction, the transverse wave behavior without any sources can be modelled using the following wave equation [76]:

$$\frac{\partial^2 u_r}{\partial t^2} = c_t^2 \frac{\partial^2 u_r}{\partial z^2} \qquad\qquad \text{(Eq. 5.37)}$$

With u_r the radial displacement and c_t the transversal wave speed. This is under the assumption that this thin-walled membrane follows isotropic linear elastic wave propagation neglecting angular momentum and the added mass effect. The added-mass effect is caused by the effect of the acceleration of the wall onto the fluid itself. A pressure is exerted on the wall by the fluid but in order for the wall to be able to move in radial direction an amount of fluid near the wall needs to move with the wall. Hence the pressure on the wall accelerates both the wall and an additional mass of fluid, which will be neglected for now. Referring to fig. 5.3, the total force on the wall consist of the pressure exerted by the fluid p_f combined with shear forces at point 1 and 2, $F_{w1,Lr}$ and $F_{w2,Lr}$ respectively. It can be shown that the shear stresses in a point are proportional to the shear modulus and shear strain according to:

$$\tau_{zr} = G\gamma_{zr} = G\frac{\partial u_r}{\partial z} \qquad \text{(Eq. 5.38)}$$

With, τ_{zr} the longitudinal shear stress in radial direction, G the shear modulus and γ_{zr} the corresponding shear strain. Hence the sum of all forces on the wall considered so far can be summarized as

$$(\rho_s rd\phi hdz)\frac{\partial^2 u_r}{\partial t^2} = p_f rd\phi dz + G\frac{\partial u_r}{\partial z}\Big|_{z_2} rd\phi h - G\frac{\partial u_r}{\partial z}\Big|_{z_1} rd\phi h \qquad \text{(Eq. 5.39)}$$

It is important to remember that r is a reference radius to which a small deformation occurs. This remains approximately valid for larger deformations by allowing this reference radius r, to change over time. Since eq 5.39 should hold for an infinitesimal volume, dividing by the volume of the wall and the wall density results in:

$$\frac{\partial^2 u_r}{\partial t^2} = \frac{p_f}{\rho_s h} + \frac{G}{\rho_s}\frac{\partial^2 u_r}{\partial z^2} \qquad \text{(Eq. 5.40)}$$

Hence, for purely plane strain the transversal wave speed in absence of the pressure source is governed by eq. 5.37 as:

$$c_t = \sqrt{\frac{G}{\rho_s}} \qquad \text{(Eq. 5.41)}$$

However, as mentioned this neglected the forces in circumferential direction as well as the added mass effect. In circumferential direction, a similar analysis can be performed to find $\sigma_{\phi\phi}$. For a linear elastic material, the strain in longitudinal direction is given by:

$$\varepsilon_{zz} = 0 = \frac{1}{E}\left(\sigma_{zz} - v(\sigma_{\phi\phi} + \sigma_{rr})\right) \rightarrow \sigma_{zz} = \vartheta\sigma_{\phi\phi} \qquad \text{(Eq. 5.42)}$$

In which E is the young's modulus of the wall material and ϑ the poisson ratio. Similarly, the strain in circumferential direction can be derived resulting in a relationship between circumferential stress and strain according to:

$$\varepsilon_{\phi\phi} = \frac{(r + u_r)d\phi - rd\phi}{r_0 d\phi} = \frac{u_r}{r_0} = \frac{1}{E}(1 - \vartheta^2)\sigma_{\phi\phi} \qquad \text{(Eq. 5.43)}$$

Part of the circumferential stress acts in radial direction on the wall element. Therefore, the force in radial direction as a result of the circumferential stress is approximately equal to:

$$F_{w,\phi r} = -\sigma_{\phi\phi}\sin\left(\frac{d\phi}{2}\right)hdz \approx = -\sigma_{\phi\phi}\frac{d\phi}{2}hdz \qquad \text{(Eq. 5.44)}$$

Combining equations 5.44 and 5.43, adding this additional force on both sides of the wall element, to the momentum eq. 3.39 and dividing again by the wall volume a general equation for the wall displacement can be found. For completeness, the added mass is added as an additional inertia term with a factor M_a. Often, as in the work of Causin [70] , the Timoshenko factor is used for correction of the shear strain in the wave equation with the result given below in eq. 5.45

$$(\rho_s h + M_a)\frac{\partial^2 u_r}{\partial t^2} - k_T hG \frac{\partial^2 u_r}{\partial z^2} = \left(p_f - \frac{Eh}{r^2_0(1 - \vartheta^2)}u_r\right) \qquad \text{(Eq. 5.45)}$$

Using this formulation, the wall displacement is described fully by the solid model, in which the effect of fluid movement has been modelled as an augmented mass onto the solid. Eq 5.45 has the same form as a 1D-wave equation with a forcing

term on the right-hand side but has not considered the added mass. The added mass will be considered further on in the text. For linear elasticity the shear modulus is related to the Poisson ratio and the Young's modulus according to:

$$G = \frac{E}{2(1 - \vartheta)}$$ (Eq. 5.46)

If the effects of inertia, added mass and longitudinal shear forces are neglected eq. 3.45 can be rewritten as the quasi static relationship between pressure and radial wall displacement. This effectively results in the radial displacement given a static pressure. With the relationship that $u_r = \sqrt{A/\pi} - \sqrt{A_0/\pi}$, eq. 5.45 can be rewritten as

$$A = \pi \left(p_f \frac{r_0{}^2(1 - \vartheta^2)}{Eh} + r_0 \right)^2 \approx A_0 + 2\pi r_0 u_r$$ (Eq. 5.47)

In order to provide a wave velocity for the compressible fluid approach and a compliance for the 1D model, an expression is required for the derivative of the area with respect to the pressure. This derivative is given in eq. 5.48. The zeroth-order approximation of eq. 5.48, in which the pressure dependent term is neglected, leads to a compliance that is consistent with the Moens-Korteweg equation.

$$C = \frac{\partial A}{\partial p} = 2\pi \left(p_f \left(\frac{r_0{}^2(1 - \vartheta^2)}{Eh} \right)^2 + \frac{r_0{}^3(1 - \vartheta^2)}{Eh} \right)$$ (Eq. 5.48)

$$\approx \frac{2\pi r_0{}^3(1 - \vartheta^2)}{Eh}$$

For the experimental results that follow, the approximate compliance of Eq. 3.48 has been used and the wave velocity associated with this is simply given by:

$$c = \sqrt{\frac{Eh}{2\rho_0 a_0^1(1-v^2)}}$$

<div align="right">(Eq. 5.49)</div>

5.4.2. Simulation & results

To compare the 3D compressible fluid method and the 1D wave propagation method a marginally longer pipe is taken as in Brown in order to amplify some of the differences. The methods from Brown and the current study were first verified against each other to ensure they provide similar results. For this the parameters of the test cases were set identical to those by Brown, shown in Table 5.2:

Tube parameters		Windkessel Parameters	
Initial Radius	$a_0 = 10^{-2}[m]$	Impedance	$Z = 1.1 \cdot 10^7 [kg\ m^{-4}\ s^{-1}]$
Domain length	$L = 2 \cdot 10^{-1}[m]$	Compliance	$C = 1.45 \cdot 10^{-8}[kg^{-1}\ m^4\ s^2]$
Material Properties		Resistance	$R = 1.45 \cdot 10^8 [kg\ m^{-4}\ s^{-1}]$
Vesselwall thickness	$h = 8 \cdot 10^{-4}[m]$	**Derived parameters**	
Young's modulus	$E = 10^6[Pa]$	Wave Speed	$c = 7.06[m/s]$
poison ratio	$v = 0.49[-]$	Inertance per unit length	$L' = 3.34 \cdot 10^6 [kg\ m^{-5}]$
Fluid density	$\rho = 1.05 \cdot 10^3\ [kg\ m^{-3}]$	Compliance per unit length	$C' = 5.97 \cdot 10^{-9}[kg^{-1}\ m^3\ s^2]$

Table 5.1 - Base Simulation settings for the fluid structure interaction simulations

At the inlet of the tube a sinusoidal inflow is used of amplitude $5 \cdot 10^{-4}[m^3 s^{-1}]$:

$$Q_{in}(t)[m^3 \ s^{-1}] = 5 \cdot 10^{-4} sin \ (2\pi t) \qquad \text{(Eq. 5.50)}$$

Both the 3-element and the 2-element methods were compared approximately by overlaying the pressure graphs from both studies. Fig. 5.4 below demonstrates the pressure for both studies for the 3-element windkessel as the 2-element windkessel is no longer discussed in the remainder of the study. Results from both implementations are considered equivalent on the basis of these graphs.
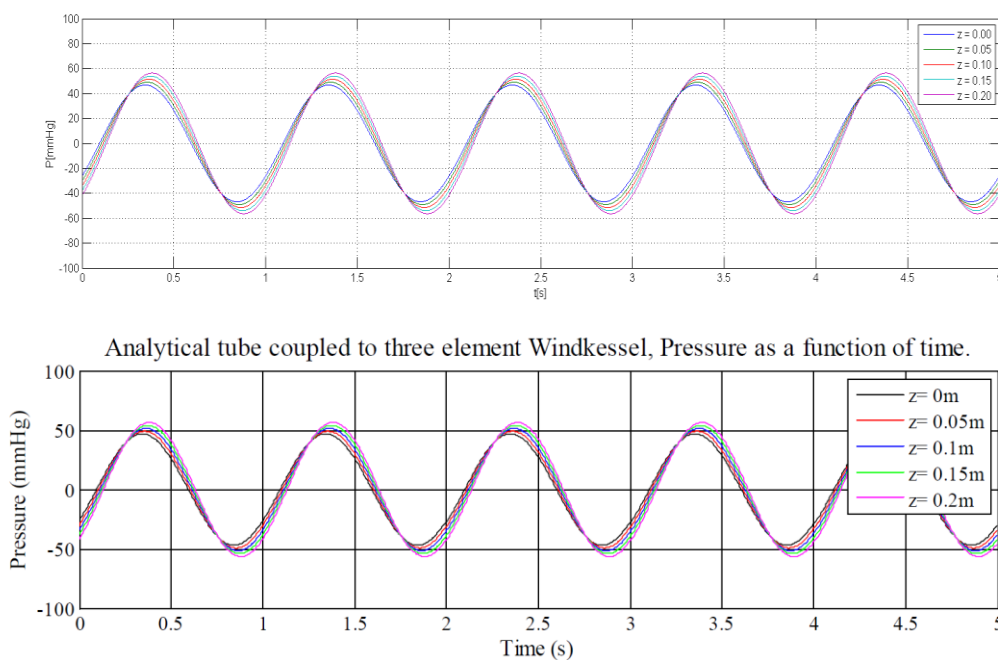
Fig. 5.4 - Analytical 1D-model solutions, (Top) Pressure at 5 positions for the current study and (bottom) as adapted from Brown, demonstrating both implementations produce equal results.

For the comparison between the 3D compressible fluid and the 1D model it was concluded by Brown that most discrepancies between the methods were attributable to the viscosity included in the 3D model as opposed to the inviscid assumption in

the 1D model leading to a maximum error of 3.55% normalised to the maximum pressure. It was concluded that therefore both methods were in good agreement

The numerical experiment is repeated but with a tube length of 30[cm]. This is still a reasonable length to perform 3D numerical simulation but is slightly better suited to distinguish wave propagation effects from numerical or methodical errors. As the geometry becomes longer, wave propagation effects between one end of the tube and another become more apparent due to the time it takes waves to travel. All other parameters have remained equal.

Depending on the initial conditions of the model, start-up effects are to be expected due to the windkessel model that's coupled as an outlet BC. This was discussed in chapter 2. For the 3D model these start-up effects can be avoided, if the velocity and pressure are described exactly equal to the periodic signal solution. An estimate can be provided based on the average pressure and flow, but this does not change the time required to reach periodicity of the solution. Due to the frequency-based solution method for the 1D analytical model, this model is only capable of representing periodic signals, as demonstrated in fig. 5.4. An obvious choice is to run the 3D simulation until periodicity and then compare the final cycle of the 1D and 3D models. However, it should be noted, that it is possible introduce start-up effects from starting at 0 initial pressure and flow in the 1D model. Simply by pre- and appending the inflow signal $Q_{in}(t)$ by $Q_{in} = 0$,for a sufficient length of time. A choice has been made to prescribe it as:

$$Q_{in}(t) = \begin{cases} 0 & 0 \leq t < 10[s] \\ 5 \cdot 10^{-4} sin\,(2\pi t) & 10 \leq t < 20[s] \\ 0 & 20 \leq t < 30[s] \end{cases} \qquad \text{(Eq. 5.51)}$$

This choice makes the inflow signal periodic and allows the system a time of 20[s] in total for the windkessel model to return to the 0 pressure and flow conditions after the sinusoidal period of the flow has stopped. By having this sudden start at 10[s] of the sinusoidal flow signal, high frequencies are introduced into the system. As the computational cost of the 1D model is limited, the number of harmonics was arbitrarily limited to the first 500 harmonics of the signal. The inflow signal that results from this procedure was then also used as the Inlet boundary condition for the 3D model. The 3D model assumes an inviscid flow in order to eliminate any functional differences between the 1D and the 3D model due to viscosity. Additionally, a semi-explicit coupling between the 3D compressible region and the windkessel model was utilized.

Fig. 5.5 below demonstrates pressure resulting from the 1D-model and the start-up effects similar to that seen in the windkessel discussion. During the influx of the first cycle, the average flow is none-zero which charges the windkessel compliance. Periodicity is then reached from approximately the 7th cycle at t=17[s]. The maximum amplitude of the pressure appears higher at the outlet of the tube compared to the inlet. While this seems counter-intuitive, it is important to note that the only the pressure gradient drives the acceleration and deceleration of the fluid
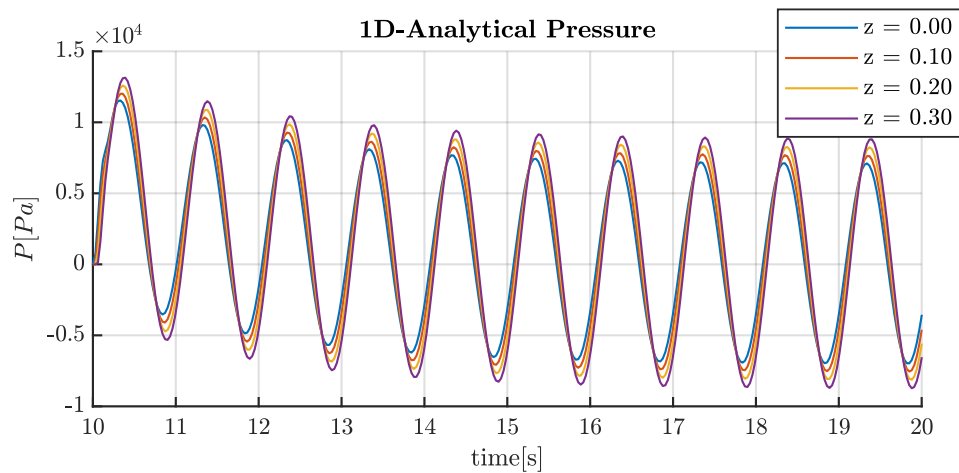
Fig. 5.5 - 1D-analytical pressure from initial conditions p=0, q=0. Pressure at 4 locations in axial direction.

and that the outlet pressure of the tube is fully determined by the flow through the windkessel model. At the outlet the flow can still be accelerating while at the beginning of the tube the flow has already started decelerating and so the pressure of the windkessel model can still increase while that of the outlet is decreasing. For reference the pressure of the 3D and the 1D model at inlet and outlet are provided in fig. 5.6:
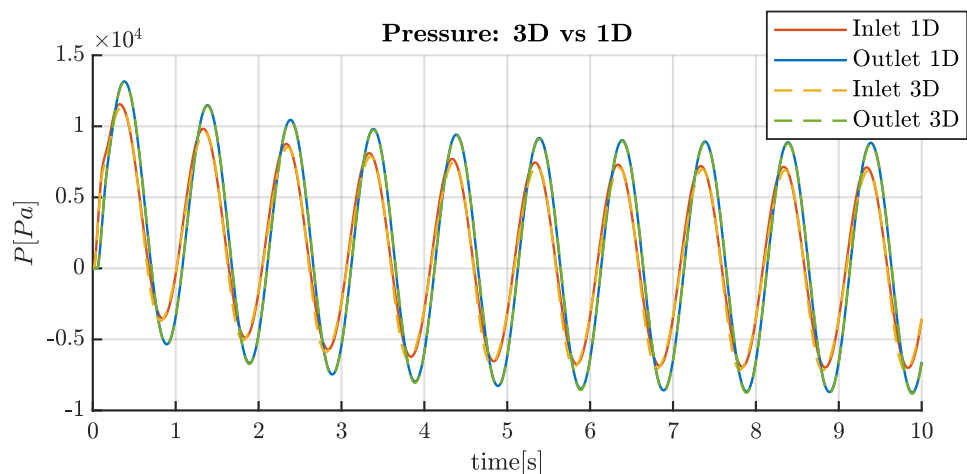
Fig. 5.6 - 3D/1D pressure from initial conditions p=0, q=0. Pressure at inlet and outlet

At first glance these pressures are in good agreement, hence start-up effects can be included in the 1D-analytical model. However, a similar argument as in chapter 2 can be made that the scale of the pressure, dictated by the windkessel model, can obscure the notable characteristics of the system.

The left graph of fig. 5.7 depicts the absolute pressure at in- and outlet for both the 1D-analytical and 3D-compressible methods.
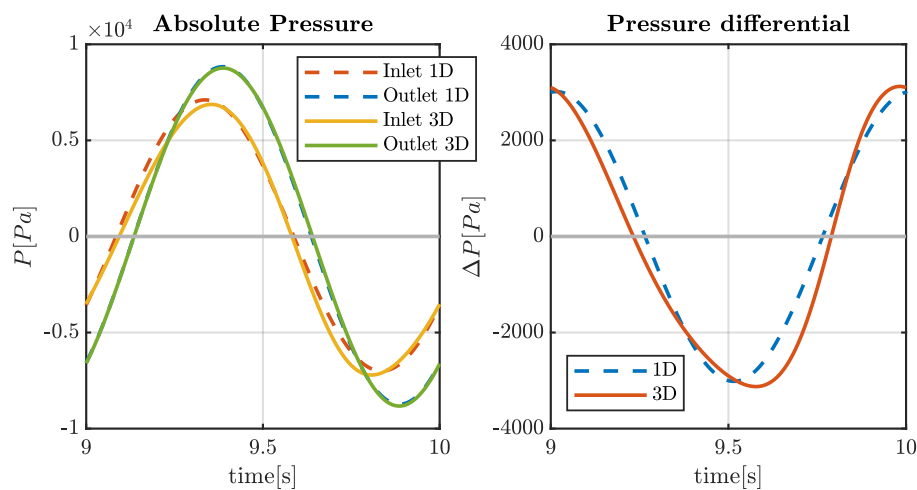
Fig. 5.7 - (Left) Absolute pressure of 1D and 3D-compressible methods for the final cycle, (right) Pressure differential over full length of tube for both methods.

First, the difference with respect to the maximum pressure during the final cycle is calculated, according to the method by Brown [72]. For the inlet the maximum difference was calculated to be approximately 11.44[%] whereas at outlet it was 1.91[%]. It was noted during analysis that this difference was susceptible to the coupling method employed but the extent was not quantitatively assessed. The right graph of fig. 3.6 represents the pressure differential over the full length of the tube

for both methods by subtracting the outlet pressure. Pressure differentials are responsible for acceleration and deceleration of flow or deformation of vessel walls and are therefore more indicative of the pressure scale of the problem. The maximum difference between the 1D and 3D methods with respect to the maximum pressure differential of the 1D case is 31.72[%] occurring at approximately 9.7[s]. Even if the absolute pressure is similar to that of real-world cases this is a significant difference. However, this error is mainly caused due to the difference in time characteristics of the signal rather than the magnitude of the signal.

It can be seen that the pressure differential of the 3D-compressible case is much more asymmetric than that of the 1D-model which can be explained qualitatively. Initially, when fluid is flowing in through the outlet, the pressure in the 3D-compressible case is lower. Fluid close to the inlet is compressed and accelerates. The compressibility dampens the imposed pressure during influx. Locally, this means that a mass of fluid starts travelling along the tube with a higher density and thus a larger inertia. Eq. 5.34 indicates that because of this the wave speed decreases locally. In fig. 5.7 it can be seen that the absolute pressure at inlet of the 3D method lags behind because of this. Eventually, the decelerative phase of the cycle is reached and the inverse process happens. The mass of fluid that was previously accelerated needs to be decelerated. Due to the inertia fluid near the outlet is not immediately decelerated and can still flow into the windkessel model. At the inlet, the flow is fully predetermined and the density decreases, reducing the inertia locally and increasing the wave velocity. This type of non-linearity is difficult to

model by taking a frequency-based approach to the solution of the 1D wave-equations. However, this is considered to be an effect due to functional differences between models, instead of numerical errors as indicated by Brown. [72]

Lastly, it should be noted that even a maximum difference or error around but below 5% can be considered significant. To exemplify this, the pressure is depicted in fig. 5.8 below for the compliant 1D case and the rigid 1D case. The rigid 1D case has been created by setting the Young's modulus of the wall above $E = 1.805 \cdot 10^9 [Pa]$. At this Young's modulus and a time resolution of $\Delta t = 10^{-3} [s]$, the wave speed increases to $c = 300 [m/s]$ and any pressure or flow waves traverse the domain instantly within the time-resolution time-step. As a safety margin the Young's modulus was taken to be $E = 10^{12} [Pa]$. Fig. 5.8 displays the absolute pressure and pressure differential for the compliant system considered and the rigid equivalent. In absolute sense, the maximum difference with respect to the rigid system for absolute pressure is 19.35[%] at inlet while for the pressure differential this difference is 8.53[%]. Firstly, this implies that the effect of adding FSI is approximately only 4 times bigger than a 5[%] error while keeping all other parameters equal. Hence, while it might be concluded that the absolute pressure agrees reasonably well between models, the magnitude of the effect is not that large. Secondly, the difference in pressure differential between the compliant 1D model and the rigid 1D model is a lot smaller than the difference between the 3D compressible model and the 1D-compliant model.
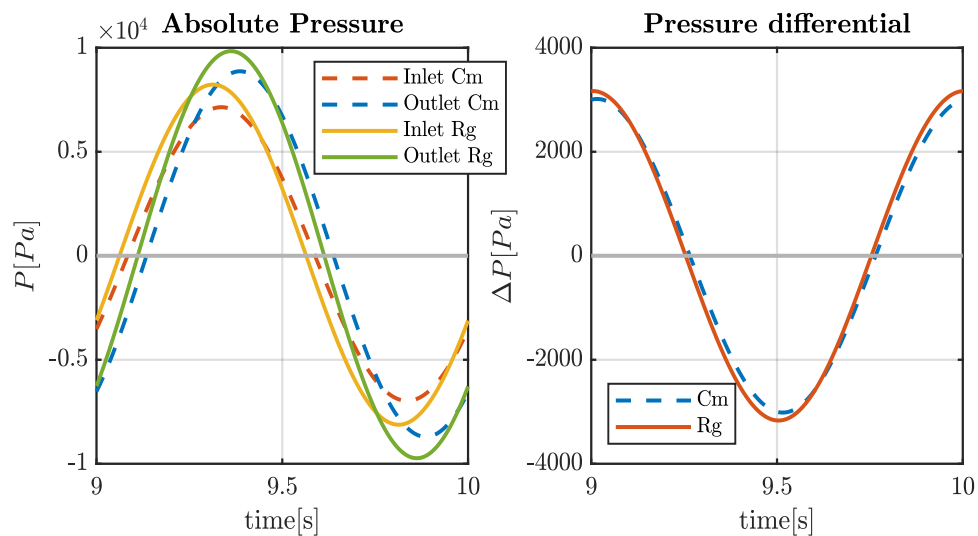
Fig. 5.8 - 1D-analytical absolute pressure(left) and pressure differential along the tube(right) for compliant walled (Cm) and rigid walled tube (Rg) indicating functional difference for including FSI. Pressure differential for the Rigid case is symmetric over period.

How does this sit within the context of human physiology and pathophysiology? Stage 1 hypertension is defined to be a systolic blood pressure between 130-139[mmHg] whereas a normal systolic blood pressure is around 120[mmHg]. This is approximately an 8% to 16% difference in pressure implying that a 5% error in pressure estimates can be relevant to some clinical applications. Stage 2 hypertension is defined to be at a systolic blood pressure upwards of 140[mmHg].

 The inflow for this case is not realistic and therefore the experiment is repeated one last time with an inflow with a more realistic pulsatile inflow. The average flow has been normalized to 80[ml/s] corresponding to an average human stroke volume. At P=0[Pa], the compliance of the entire artery modelled by the 1D domain is equal to $C_{1D} = 1.737 \cdot 10^{-9} [kg^{-1} \, m^4 \, s^2]$. The compliance of the windkessel is reduced by this amount to keep the total compliance of the system constant. Additionally, the

impedance of the Windkessel is set to that of the characteristic impedance of the vessel to minimize wave reflections (taken from Brown, eq. 3-29) $Z = 1.1 \cdot 10^7 [kg\ m^{-4}\ s^{-1}]$. Pressure and flow waveforms under these conditions are depicted in Fig. 5.9.
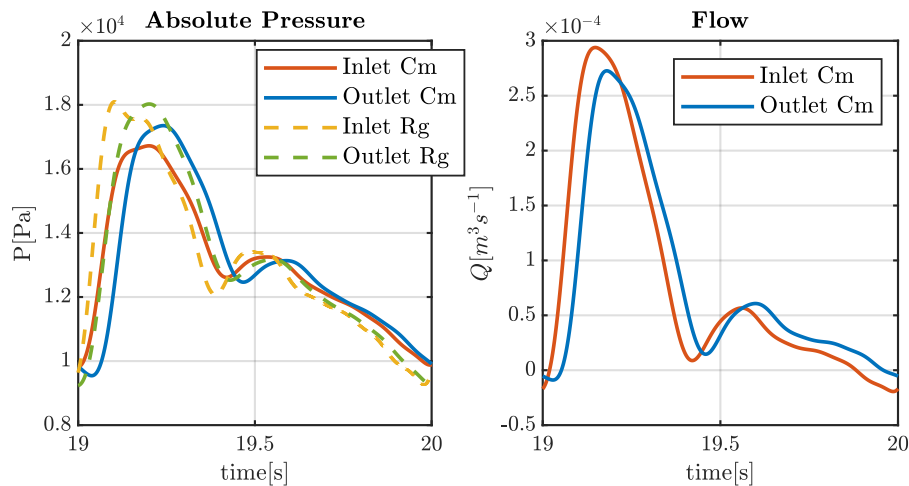
Fig. 5.9 - 1D model Pressure(left) and flow(right), comparing a rigid walled blood vessel to a compliant blood vessel. Average pressures are lower for the compliant system and outlet flow is delayed

For the rigid walled vessel, inflow and outflow are equal to the prescribed inflow and therefore these curves have been omitted from fig. 5.9. The maximum difference in pressure between the rigid and the compliant 1D model is 19.55[%] at outlet during peak systole. This percentual elevation in pressure due to neglecting vessel compliance would be comparable to the elevation seen in stage 2 hypertension. Lastly, fig. 5.10 depicts the volume change of the vessel which is calculated by integrating the sum of the inflow and outflow over time per cycle. It can be seen that, approximately 13[ml] of fluid is stored within the 3D region which is released into the windkessel model at a slower rate compared to the rigid walled

case. This is approximately 16% of the stroke volume imposed while the compliance of the 1D region is around 11% of the total system compliance.
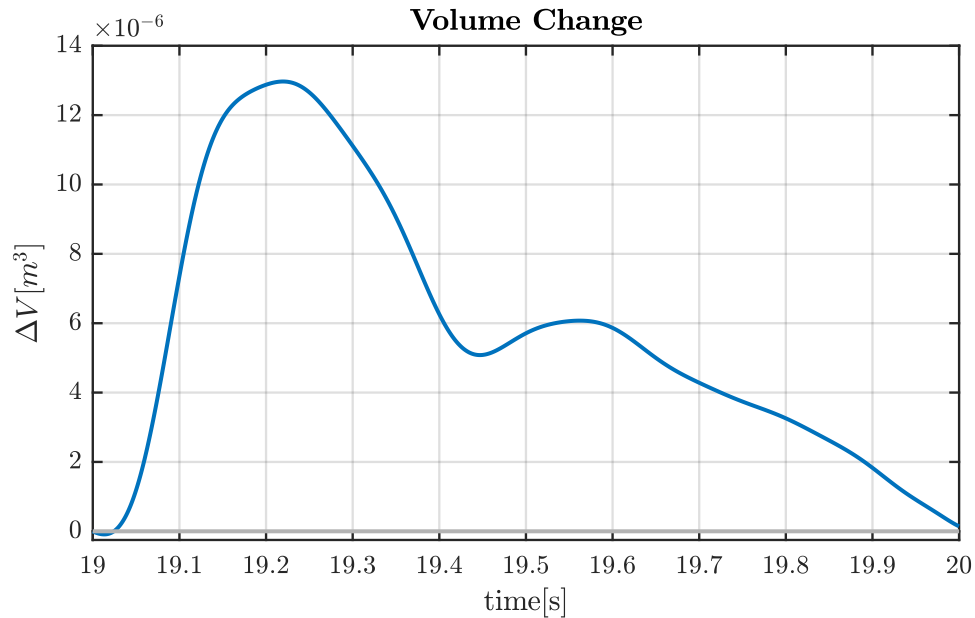
Fig. 5.10 - Volume change of the 1D region of the 1D Model. Volume increases up till 0.23[s] implying 13[ml] fluid storage after which the stored volume is gradually released over the rest of the cycle.

5.5. Conventional FSI

The previous section has introduced methods to introduce compliance into a fluid dynamics system using a compressible fluid without necessitating full modelling and coupling of a wall structure. In the preceding study by Brown [72], the 1D model was used to verify the functionality of this 3D compressible fluid model. However, both methods function under different assumptions with the 1D model not being capable of representing the non-linearities involved. Additionally, the compressible fluid model assumed a constant wave velocity disregarding local

changes in compliance and inertance. In order to better characterize the error of the model with respect to the real-world scenario, data would have to be available. Instead the accuracy will be compared to a conventional FSI standard which will be referred to as the 2-way FSI due its 2-way coupling between the structural model and the fluid dynamics model. This model is used as a golden standard after which the compressible model would have to be modelled to provide the same functionality.

5.5.1. 2-Way FSI

In order to understand which model, the 1D model or the compressible fluid model, is closer to the real behavior it would be necessary to compare both models to experimental data of wave propagation through tubes. In order to quantify the pressure and flow fields at different locations this would require a complex set-up of sensors along the length of the tube as was done in the work of Bessems et al. [77] and Giannopapa et al. [78] . In the current study, the approach is taken to compare both models to a 3D 2-way FSI model of a long tube. This allows for examining pressure and flow in every point where needed and can be considered the gold standard towards comparing FSI within the ANSYS software collection.

Both monolithic and partitioned FSI approaches exist under ANSYS. However, at the time of writing the partitioned approach offers more versatility compared to the monolithic approach. In partitioned FSI involving solid and fluid mechanics, a fluid dynamics solver and a structural mechanics solver are coupled with each solver being referred to as a participant. Following this approach, a dedicated solver can

be used for the fluid and the solid structure, which often implies that many more models are available to describe different types of physics. In this case ANSYS Fluent is used for the fluid dynamics part of the solver whereas ANSYS mechanical is used to compute the transient structural mechanics. Fluent uses a finite volume approach written from a Eulerian point of view, whereas Mechanical utilizes a finite element approach written from a Lagrangian point of view. More effort is required to write monolithically coupled systems of equations and a monolithic approach often comes at a higher computational cost. Commercially, an incentive to build a monolithic solver might be required which means these solvers tend to be either limited in scope or non-existent making it more interesting to improve on existing techniques.

In order to couple models, it is necessary to specify coupling conditions at the interface between both models. In the case of blood vessels this interface is where the blood comes in contact with the vessel wall. At the coupling interface, the movement of the fluid should be equal to that of the wall while the forces exerted by the fluid should be equal to those exerted by the wall. Since the flow is inviscid, only the normal stress with respect to the wall is important. These are known as the kinematic and dynamic conditions and for an inviscid fluid in radial coordinates are given by:

$$\vec{u} \cdot \vec{n} = \frac{\partial u_r}{\partial t} \qquad \text{(Eq. 5.52)}$$

$$p_f = f_s \qquad \text{(Eq. 5.53)}$$
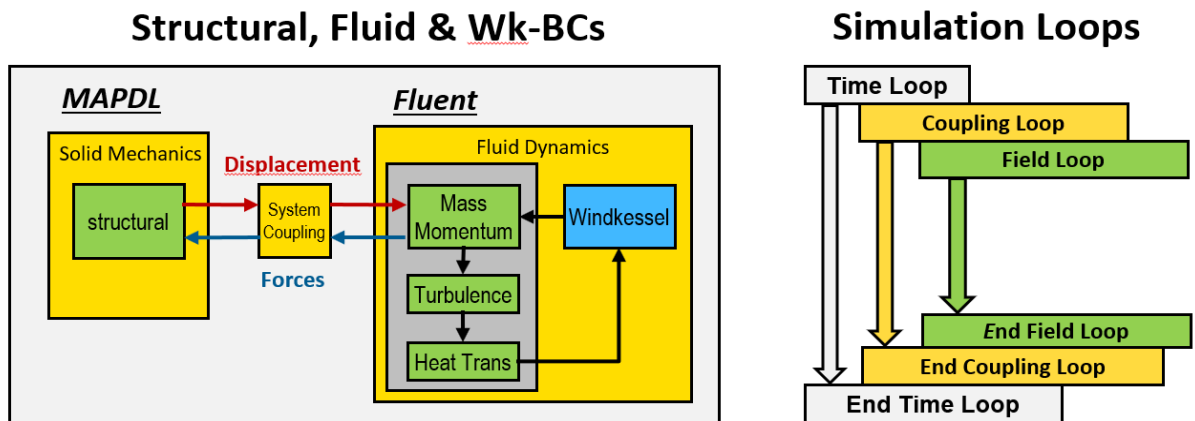
Fig. 5.11 - (left) coupling schematic of different coupling participants involved, (right) Different loops involved in simulation with yellow colour indicating processes managed by system coupling box and green processes handled by partitioned solvers.

Fig. 5.11 depicts the 3-way model coupling. Coupling the Fluent fluid dynamics and Mechanical structural mechanics model is done using the system coupling box software. The system coupling box manages the transfer of data between models by mapping forces from the fluid model onto the structural model while mapping the structural displacement onto the mesh movement of the fluid model. System coupling box also handles the coupling iteration loop between models whereas the separate partitioned models find iterative solutions to their pressure, deformation and flow fields as normal. Similarly, to the windkessel discussion, model coupling can be classified as explicit, semi-explicit, weakly implicit and strongly implicit. The system coupling box has no option at the present time to perform central differenced coupling. Lastly, the windkessel model is coupled through Fluent which adds another coupling interaction within the model.

For this study, models were evaluated using a computational cluster using Univa Grid Engine as a cluster manager. Due to a bug in the system coupling box at the time, only a certain number of maximum iterations of the full model could be run after which the system coupling box would produce an error making it impossible to continue the simulation. When a GUI is available a work around exists in which the simulation can be stopped and restarted from that point. For automated execution on a cluster using a GUI is impractical and it was necessary to write a set of scripts to reserve the necessary computational resources and manage automation of the stop-restart mechanism. Besides this stop-restart mechanism a restart mechanism was implemented in order to automatically restart simulations from the last saved point in case of other unforeseen errors during simulation.

5.5.2.   *Computational model setup*

5.5.2.1.   *Structural & Fluid mechanical Models*

A schematic overview of the simulation set-up is provided in fig. 5.12 below, depicting the boundary conditions and conditions expressed in eqs. 5.52-5.53:
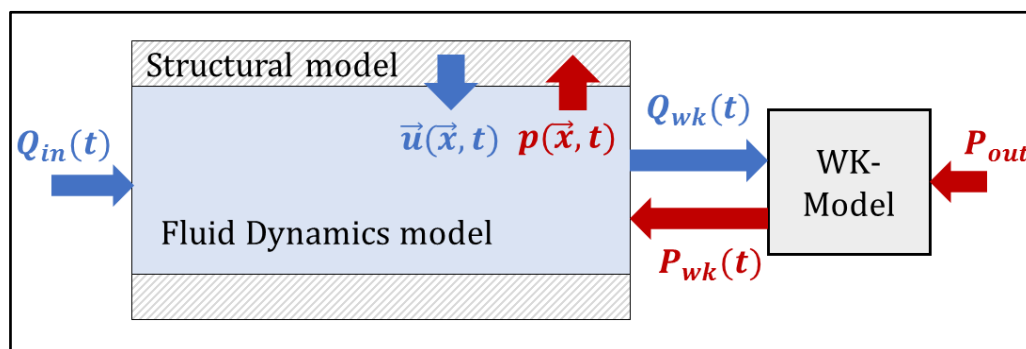
Fig. 5.12 - Schematic overview of coupling between the structural, 3D fluid dynamics and windkessel model.

The kinematic condition determines the mesh deformation of the fluid dynamics model via wall displacement $\vec{u}(\vec{x}, t)$. As such it provides the geometrical BCs for the FSI simulation. Displacement is depicted in blue as it imposes a velocity on the fluid near the wall. In turn, the dynamic condition prescribes a wall force via the pressure exerted by the fluid.

For all elements of the structural model displacement was constrained in longitudinal and circumferential direction. This means that the structural model can only displace in radial direction and shear imposed by the fluid can therefore be neglected. At in- and outlet a symmetry condition is applied in order to enforce the longitudinal constraint. Additionally, the stabilization feature in ANSYS mechanical is turned off as the case is stabilized in Fluent.

To conform with the geometrical constraints the Fluent model is set up with a deforming boundary at in- and outlet in which deformation can only occur in-plane of the in- and outlet. This allows the boundaries to deform in radial direction but enforce a longitudinal constraint. The wall boundary is prescribed as displacement by setting it up as a system coupling boundary. Additionally, the internal mesh deformation is fully elastic using the diffusion-based method for smoothing in fluent specifying a factor of 0. This means that any deformation of the wall is imposed equally to the elements along the radial direction of the pipe. This was necessary to prevent computational anomalies where elements near the wall could be displaced through cells close to the center of the pipe. The fluid is assumed to be

inviscid as the setting describes a large artery flow that is mainly inertia dominated. As mentioned before this does not affect the wall displacement as shear forces are not relevant due to the geometrical constraints.

Simulation conditions have been taken such that they are identical with the parameters depicted in table 5.2. This includes all geometrical and windkessel parameter to have coherence with the previous simulations. The inflow at inlet was set by setting velocity as the sinusoidal signal described by eq. 5.50.

The windkessel model was coupled explicitly as defined in chapter 4, eq. 4.52. An explicit coupling was chosen due to implicit coupling leading to instabilities which were difficult to trouble-shoot. When the work for the current chapter was carried out, the work for chapter 4 did not exist yet. A central-difference based coupling is suggested for future work. Lastly to aid in the stability of the coupling conditions between the structural and fluid dynamics models, the coefficient-based solution stabilization feature in fluent was used specifying a factor of 4.5.

5.5.2.2.   *Model Coupling Instabilities*

Upon attempting to compute a fluid-structure interaction simulation using system coupling box and parameters suggested by the accompanying documentation it was quickly discovered that the simulation would result in coupling instabilities. In order to illustrate this, fig. 5.13 provides a lumped parameter representation of the electrical equivalent circuit of the model:
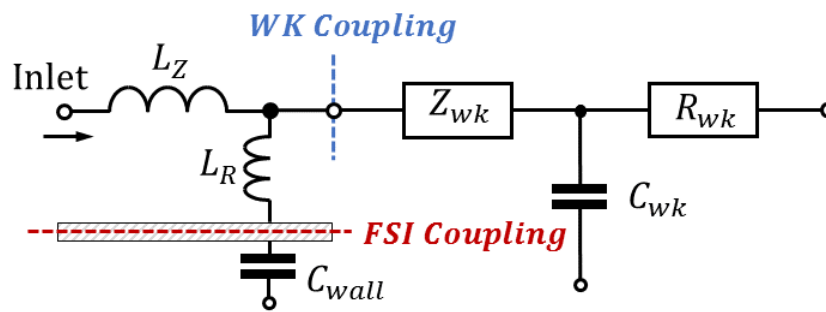
Fig. 5.13 - Electrical equivalent lumped parameter model of fig. 5.12

C_{wall} represents the elastic force exerted by the wall, while L_Z and L_R represent the inertia in longitudinal and radial direction. The inertia in radial direction is added to represent the added mass effect. This description is not fully correct as the fluid flowing towards the wall is not a separate flow as depicted. However, it does exemplify that this situation is similar to that presented for the harmonic oscillator and bifurcation model in chapter 4. A partitioned coupling can be recognised, in which a set of inertances in the fluid dynamics model, is coupled to 2 boundary models containing compliances. As such, an LC-oscillator can be created under the correct conditions leading to the same instability mechanisms described in Chapter 4. The only dissipators and outlet for fluid to exit the geometry are located in the windkessel model and are therefore the only physically stabilizing components of the system.

As mentioned before however, the consideration within chapter 4 were not known to the author when the work was carried out and other guidelines were used for simulation. For the coupling between models a strongly implicit coupling is used.

This implies that coupling iterations are used for each time-step in which for each iteration force and displacement are exchanged between models. It is mentioned in Causin [70] that for an implicit coupling of the Dirichlet-Neumann type, in which the fluid experiences displacement boundary conditions while the structure experiences force boundary conditions, an analytical relaxation factor can be calculated for which the model coupling is stable. It is mentioned By Brown [72] that an underrelaxation factor was used of 0.5 in which 7 coupling iterations are required for convergence between both models. It is possible to specify under relaxation factors within the system coupling box, however a choice was made to use the ramping of solutions instead. This functions according to:

$$\varphi_{ramped} = \varphi_i + \frac{i}{N_{max}}(\varphi_{i+1} - \varphi_i) \qquad \text{(Eq. 5.54)}$$

In which φ_{ramped} is the solution provided to the coupling participant. The solution was ramped with $N_{max} = 5$ and a total number of 10 coupling iterations per time-step. This has the advantage that after 5 iterations the relaxation factor returns to 1 but that instabilities for the 5 first iterations are still effectively dampened. These settings lead to a convergent simulation at all time-steps after a trial and error process to determine any remaining parameters.

5.5.2.3.   *Computational Meshes*

The mesh structures used are depicted in figure 5.14. A single layer of hexagonal elements was used for the structural model in mechanical as it is expected that the radial stress and displacement is negligible while the radial stress and strain are not

considered in the model derivation. For the fluid model mesh, a prism layer of 3 elements was initially included to increase the accuracy of the solutions if viscosity were to be included later. Additionally, even if the magnitude of radial flow is much lower than that of longitudinal flow, due to the added mass effect instabilities it is important to correctly model pressure and flow near the wall making it beneficial to add a prism layer. The thickness of the prism layer was chosen to be 1[mm] which was estimated to be the thickness of a stokes layer for the given setting if viscosity were to be included.

The core of the tube is modeled using a swept tetrahedral mesh. It is not required to have a conformal mesh between the structural and fluid dynamics mesh. However, due to the simplicity of the tube, the elements at the coupling interface have been chosen conformally to minimize the mapping error from one model to the other.
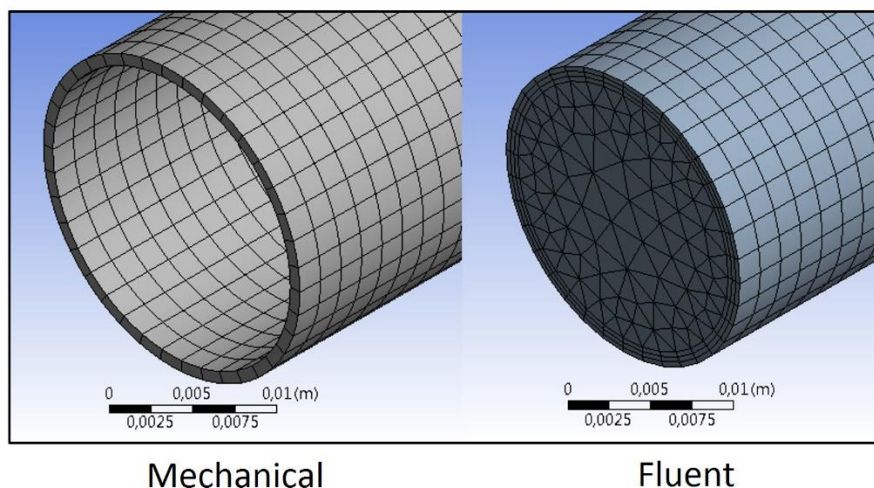
Fig. 5.14 - (left) Mechanical computational mesh, (right) Fluent computational mesh

5.5.3. *Wave-propagation dependencies on mesh- and time-step size*

Time-step and mesh-size dependency were analyzed for the compressible fluid. These types of dependency studies are not uncommon for both the fields of structural and fluid mechanics. However different requirements exist for the coupled system due to the introduction of wave-propagation.

It was first determined by an investigative analysis that the simulation was most sensitive with regards to mesh size in axial direction. Variations of mesh size in radial direction had almost no effect. It was established that even a single tetrahedral element spanning from the center of the vessel up to the wall was capable of giving similar results to the fluid mesh represented in fig. 5.14. This is perhaps unremarkable as for inviscid flow through a straight tube no velocity gradients should exist in radial direction. As such the time-step and mesh-size in axial direction are varied simultaneously to analyze the convergence behavior. The values are given below:

$$\Delta t = \{0.04, 0.01, 0.004, 0.001, 0.0004\}$$

$$\Delta z = \{0.01, 0.005, 0.0025, 0.001\}$$

The root mean square difference is pairwise compared for each parameter value to a value that is assumed to give more accurate results. This means for example for the pressure at a time-step of $\Delta t = 0.01$, the rms-difference is compared to the pressure a time-step of $\Delta t = 0.004$. This provides an idea of the residual change with respect to the time-step or mesh-size.

$$rms(\varphi) = \sqrt{\frac{\sum_i^N \big(\varphi(t)_j - \varphi(t)_{j+1}\big)^2}{N}}$$

(Eq. 5.55)

The results for pressure differential, assuming the same simulation settings as before, are shown below in fig. 5.15:
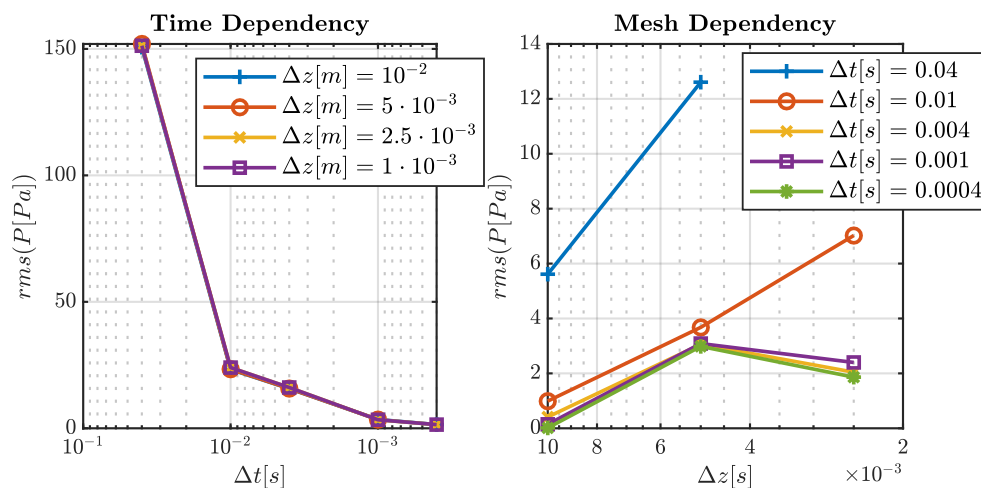
Fig. 5.15 - Compressible fluid pressure mesh-size and time-step dependency

It can be seen from the Time dependency graph, that the main result of a reduction in time-step size leads to very similar reduction in RMS value regardless of mesh-size. At a time-step of $\Delta t = 0.001[s]$ the difference is approximately 3[Pa]. On a pressure differential scale of $O(3 \cdot 10^3)[Pa]$ of the solution, this is considered sufficient to pick a time-step of $\Delta t = 0.001[s]$. Moving on to the mesh dependency graph, it can be seen that the effect of mesh size is smaller than the effect of the time-step by approximately a factor 10. Above a time-step of $\Delta t = 0.004[s]$ the RMS increases with regards to diminishing mesh size. However, it was difficult to obtain non-divergent results during simulation given these time-step sizes in general. Below that time-step size, the difference in rms for different mesh sizes is

very similar amongst different time-steps. for a mesh size in longitudinal direction below 0.005[m] the change in RMS is considered sufficient.

Similar results can be obtained for the differential in flow between inlet and outlet, which would normally be a measure of the change of volume of the pipe (Fig. 5.16). This indicates that the considered time-step and mesh-size considerations are considered sufficient.
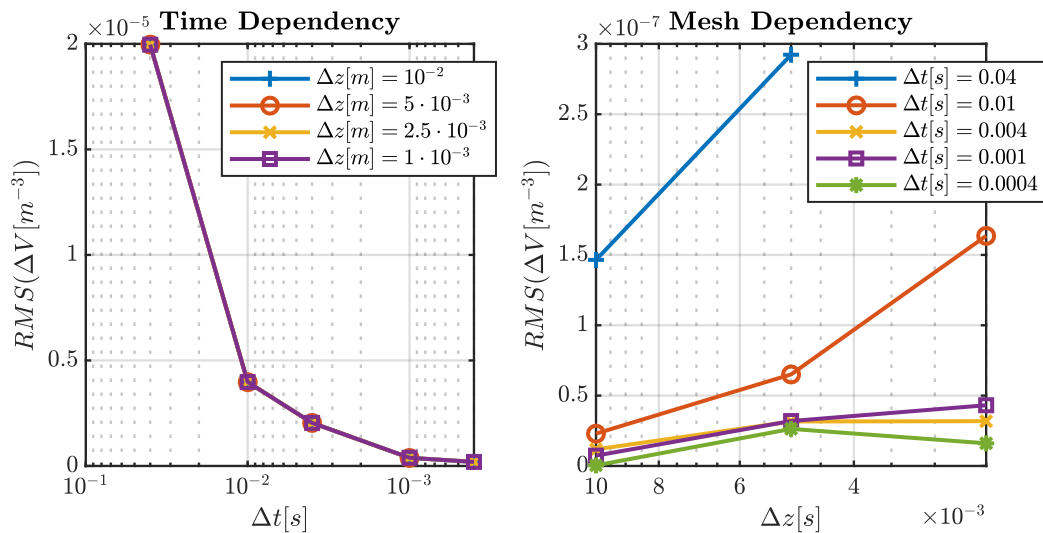
Fig. 5.16 - Compressible fluid pressure mesh-size and time-step dependency

To perform this same procedure for the 2-way FSI simulations is computationally expensive and therefore could not be performed exhaustively. A choice was made to investigate the mesh-size dependency only and to accept a time-step of $\Delta t = 0.001[s]$. A larger time-step leads to poor convergence behavior even in the case where no vessel compliance is being considered, on the basis of the time signals for pressure and flow considered as well as the behavior of the coupled windkessel model. A smaller time-step of the order $O(10^{-4})$ is very prohibitive for simulations.

As mentioned before, 10 coupling iterations are employed which means that the effective number of time-steps being calculated is 10 times bigger than for the uncoupled models. In Brown's thesis work [72], computation of a realistic aortic geometry took approximately 6 days at a time step of just $\Delta t = 0.005[s]$, 50 times larger than the smallest time-step previously considered. Mesh-size dependence however will be tested at a time-step of $\Delta t = 0.001[s]$ for which the parameters are again taken to be:

$$\Delta z = \{0.01, 0.005, 0.0025, 0.001\}$$

Results of this variation are shown below in fig. 5.17:
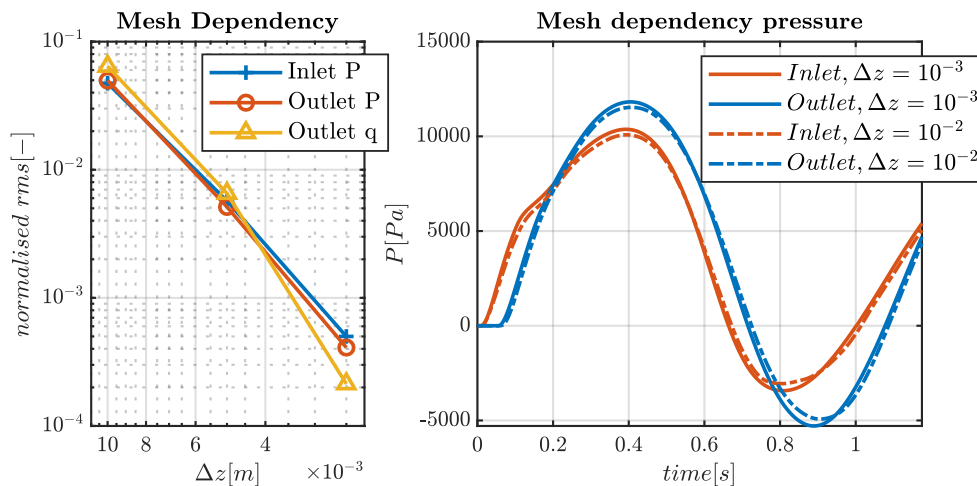
Fig. 5.17 - (left) Normalized RMS difference, (right) Difference between pressure curves using different element sizes

On the left is the rms difference for pressure and flow as before but normalized to the rms value of the pressure and flow signals. This has been done to be able to display the pressure and flow rms in the same graph. It can be seen that the rms

changes less than 1[%] for $\Delta z \leq 0.005[m]$ hence for the 2-way FSI model, a mesh size in longitudinal direction of $\Delta z = 0.005[m]$ is deemed sufficient.

Pressure is displayed on the right of fig. 5.17 for the biggest and smallest element sizes showing the discrepancy in pressure between them. The graphs for the other 2 mesh sizes have been omitted as they visually coincide with the results for $\Delta z = 0.001[m]$. This can be explained by the mesh size requirements of the physics. The problem considered has effectively 3 timescales, namely that of the structure, the fluid and that of the coupled problem. For the structure, the timescale is equal to the wave speed were the structure to be uncoupled from all other systems. Using Eq. 5.41 it can derived that the wave speed of the wall material if it were a 2D plate, is approximately $c_t = 30 \ [m \cdot s^{-1}]$. Since the fluid is incompressible the wave speed of the fluid is effectively infinite and does not factor into considerations for determining mesh size. However, the fluid velocity is in the order of $v_z = O(1) \ [m \cdot s^{-1}]$ for large artery flow, which is the characteristic velocity of this part of the problem. The timescale of the combined problem is governed approximately by the Moens-Korteweg wave speed and is approximately $c_{coupled} = 7 \ [m \cdot s^{-1}]$. Different mesh-size requirements exist depending on the gradients of quantities and the velocities involved. As an example, for fluid dynamics, it is advised that the CFL number, in this case $C = v_z \Delta t / \Delta z$, should be smaller than 1. This guarantees that during a time-step fluid flowing from a cell, can only flow into neighbouring cells. For a time-step of $\Delta t = 0.001[s]$ the acoustic courant number, utilizing the

wave propagation velocity of the coupled problem restricts the maximum size of elements in the direction of wave propagation:

$$\Delta z \leq c_{coupled} \Delta t = 7 \cdot 10^{-3} [m]$$ (Eq. 5.56)

If the element size Δz exceeds this length, the effective wave velocity is higher as the smallest possible wave velocity in this system is dictated by the length of the element. For example, if the element had only 1 element in longitudinal direction, any change in flow at the inlet would immediately be sensed at the outlet. The CFL number for the fluid limits the minimum size approximately $\Delta z \geq 1 \cdot 10^{-3} [m]$. Failing to adhere to this guideline would mean that the fluid can effectively travel across elements in a single time-step. Hence the length of the element is forced to be:

$$v_{z,max} \Delta t \leq \Delta z \leq c_{coupled} \Delta t$$ (Eq. 5.57)

On this scale, the time dynamics of the fluid, fully govern the time dynamics of the system. In order for the wall to expand, fluid has to flow into a section and towards the wall. The wall itself can propagate force and displacement information at the transversal wave speed but is unable to move without movement of the fluid. This also implies the wave speed cannot be lower than the flow velocity of the system as in this case the minimum element size surpasses the maximum element size and will be unable to represent either the wave propagation or the fluid flow phenomenon correctly.

5.5.4.   FSI Model Comparison: 1D, Compressible, 2-way

Functional differences between all 3 models have not been addressed up to this point. It is assumed that the 2-way FSI model is most capable of representing the correct physics and is therefore the benchmark case. In order for the 1D and compressible fluid models to be accurate they need to be able to represent the same pressure and flow behavior as the 2-way FSI model. Fig. 5.18 shows the absolute pressure for all 3 methods at in- and outlet.
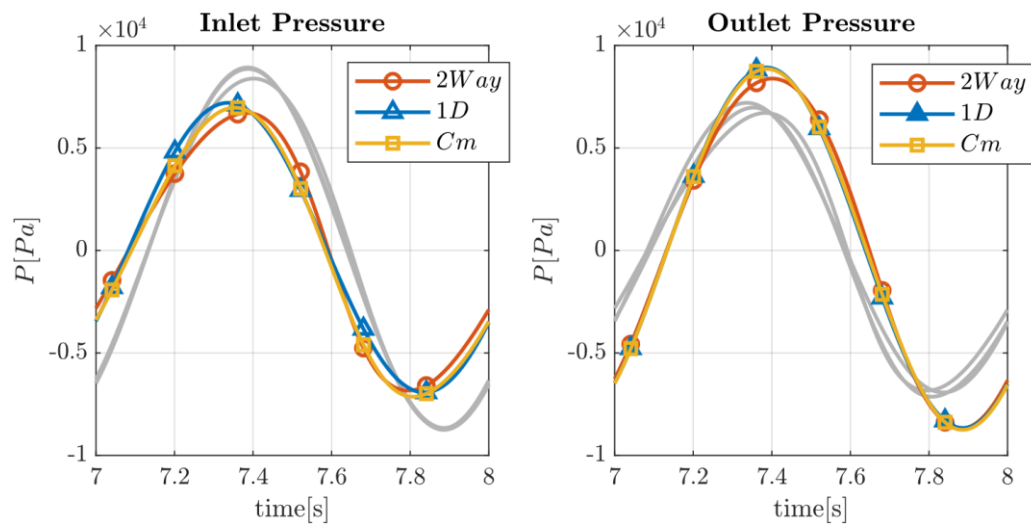
Fig. 5.18 - (left) Pressure comparison between FSI methods for inlet, (right) and for outlet demonstrating that the biggest differences regard the inlet pressures.

The most noteworthy aspect is that the pressure extrema, i.e. the minimum and maximum pressures, are lower for the 2-way FSI method compared to the other 2 methods. During the inflow phase, which is roughly the first half of the cycle, the delay between the maximum pressure at in- and outlet is smaller than with the other methods while also arriving later in the cycle. This indicates that the effective compliance is higher in the 2-way FSI case and the wave-propagation speed is lower

compared to the other 2 methods. Towards the outflow phase, the pressure at outlet is similar between the 2-way and the compressible methods while the minimum pressure is reached earlier in the cycle compared to the 1D model. This was already mentioned during the comparison of the 1D and compressible model above. However, what was not mentioned before is that the pressure at the outlet is similar for both the 1D and compressible model. Since the pressure is fully determined by the flow through the windkessel model they experience similar flows. This in turn implies that the flow wave propagation between both models is similar even though the pressure diverges at inlet during the inflow phase.

The main function of arteries is to transport blood while maintaining the cardiovascular system in good enough condition to function over the lifetime of a person. Therefore, pressure and stress information are useful to determine the condition of the blood vessels themselves but do not address the transport function.

The flow and volume change of the vessel, depicted in Fig. 5.19, show a clear difference between different methods regarding the storage and flow of blood. The time-axis has been shifted to match the start of net-inflow to more clearly distinguish the inflow from the outflow phase.
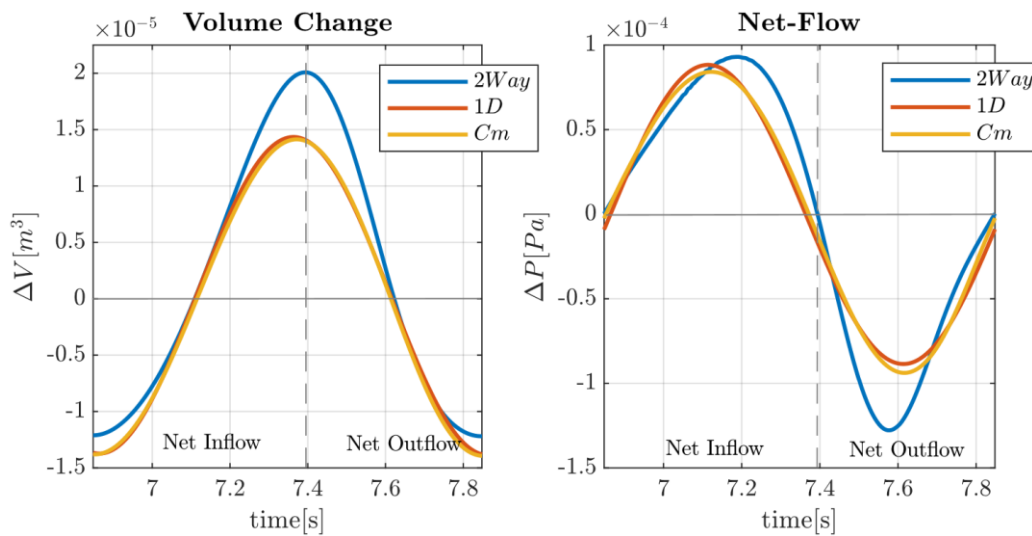
Fig. 5.19 - (left) volume change of entire geometry per method over time, (right) Net inflow into the domain as a function of time.

It is apparent from both graphs of the 2-way FSI method, that an asymmetry exists between the behavior during the inflow phase and that of the outflow phase. Whereas the inflow phase and outflow phase last roughly equally long for the 1D and compressible methods, the inflow phase lasts longer for the 2-way FSI method. As can be seen from the volume change graph, more than 40[%] more fluid accumulates inside the tube for the 2-way method compared to the other methods. This demonstrates that the flow wave is transmitted faster using the 1D and compressible fluid methods and that fluid is stored longer inside the tube for the 2-way method. Even if during the outflow phase, the volume contained internally doesn't reach the minimum of the 1D and compressible methods, the difference between the maximum and the minimum volume is higher for the 2-way FSI method. On the right of fig. 5.19 it can be seen that vessel distension starts off more gradually but continues for a longer period. During the outflow phase the opposite

effect is seen, where most of the outflow of the 2-way FSI method occurs sooner than for the other two methods. Going back to the left graph, during the outflow phase, the tube moves towards a similar volume for all 3 methods. In other words, the additional volume stored in the tube using the 2-way FSI method, is expelled faster.

It should be kept in mind that the imposed reverse flow action is a very unnatural situation in the human body. While some backflow might occur, it is never present on this scale. Additionally, in a natural situation the backflow is caused by a negative pressure differential as opposed to prescribing a reverse volume or mass flow. In the current situation, once the windkessel compliance has lost all its charge, flow is completely reversed through the windkessel outlet. The flow is not restricted physically and can freely flow in from an infinite reservoir. However, this test case is still valid to consider conditions more extreme than encountered in the human body while at the same time still being valid for physiological flows.

5.5.5. *Characterization of effects*

5.5.5.1. *1D data collection*

Up till this point all analyses have been made based on the flow at in- and outlet which has provided no information about the origin of the discrepancy between FSI models. As the fluid is modelled in 3D for the compressible model few simplifications are made regarding the fluid dynamics involved. Most of the simplifying assumptions are made with respect of the structural model. In order to get a clearer understanding of which effects are relevant to representing the

structural physics it is necessary to consider the local interaction of forces and effects. The strategy for doing so is to collect data regarding fluid pressure, fluid flow and wall displacement and fitting this data to the models presented before. It was found for the mesh size dependency that the number of elements in radial direction did not have a great effect on the accuracy of the simulation results. This is coherent with the assumptions justifying a 1D model representation to the 3D FSI case. As a result, the data collection will follow the same 1D approach which makes it possible to calculate the terms in the structural model of eq. 5.45.

As a 3D geometry is simulated additional steps are required to reduce the dimensionality to 1D. The primary step is to determine a centerline of the vessel which functions as the 1D coordinate. Determining a centerline and the accompanying radius is not straightforward and various methods exist to determine both the centerline and radius [79].After having determined a centerline and radius, the volume and boundary elements of the computational mesh need to be attributed to a location along the centerline in order to compute the average pressure, velocity and wall distension at that location.

This classification problem is complicated for general cases but considerably more straightforward for the straight vessel under consideration. The centerline is simply the straight axis along the vessel and the radius for the undeformed vessel is pre-defined as an initial radius r_0. Due to the mechanical constraints prescribing that only radial displacement can occur, the position along the centerline of an element

is fixed. Were this position not fixed, it could still be argued that due to the relatively small displacements during a cycle it would be unlikely for elements to be attributed to a different location on the centerline. Hence classification can be performed on the initial mesh and kept throughout the duration of the calculation.

In order to implement the previous considerations, a UDF was created for fluent to classify elements according to their position along the centerline, collect data from these elements at every time step and save values of pressure, flow and radius of the vessel. Instead of utilizing a continuous centerline, the centerline is discretized into n equidistant sections, with n=50 for the current study. Each surface and volume element is then attributed an identification number corresponding to a point on the centerline leading to the classification in fig. 5.20 below:
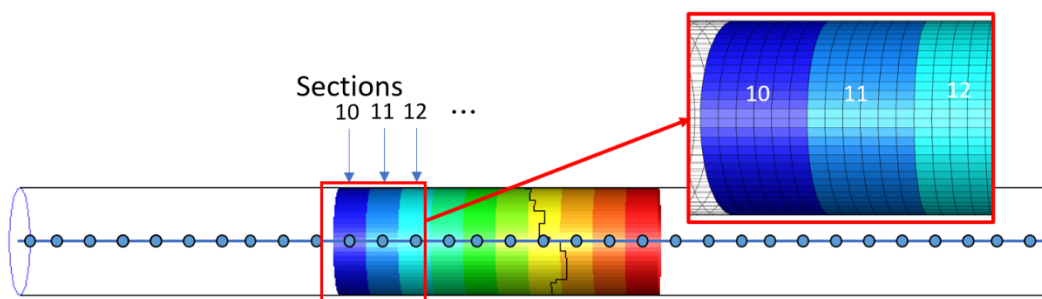
Fig. 5.20 - Cell grouping to correspond with a position along the centerline. Each point along the centerline corresponds to a disk of elements with 6 elements in longitudinal directions.

Without element grouping the results become susceptible to numerical inaccuracies of individual elements. Additionally, the averaging in longitudinal direction over a short distance should not negatively influence the continuity of the results along the

centerline. The distance between 2 centerline point was chosen to be $\Delta L = 6[mm]$ which is smaller than the traversable distance dictated by the wave velocity. Wave velocity in this pipe was determined to be approximately $7[m \cdot s^{-1}]$ or $7[mm]$ per timestep $\Delta t = 10^{-3}[s]$. Therefore, it is expected that the variability for any quantities averaged within a section is minimal.

5.5.5.2. *Determining Structural Model terms*

5 terms are present in the structural model presented in eq. 5.45 if the added mass effect is considered independently. Using dimensional analysis, it is expected that the dominant term of this equation is the term on the right-hand side. Therefore, a simplified description of eq. 5.45 can be written as:

$$0 = \left(p_f - p_{ext}\right) - \frac{Eh}{r^2(1-\vartheta^2)}u_r \qquad \text{(Eq. 5.58)}$$

In which p_{ext} is a lumped parameter description of the remaining minor terms. Often p_{ext} is assumed to be negligible and used to describe quasi-static wall deformation. All inertia terms are dropped as well as the shear stress induced term resulting in eq. 5.46 below. This assumption is made for both the 1D and compressible fluid methods presented before. In the 3D 2-way FSI scenario these terms are fully represented including the longitudinal shear wave in the structural model. Therefore, the model eq. 5.45 is modified to include the additional pressure term:

$$(\rho_s h + M_a)\frac{\partial^2 u_r}{\partial t^2} - k_T hG \frac{\partial^2 u_r}{\partial z^2}$$

$$= \left(p_f - p_{ext}\right) - \frac{Eh}{r^2(1 - \vartheta^2)}u_r$$

(Eq. 5.59)

Subsequently, the data from the 3D 2-way FSI is used to assess the order of magnitude of the terms in model above. Any pressure that is unexplained for will then be attributed to the lumped parameter term p_{ext}. The term on the far right-hand side, is responsible for the force caused by elastic deformation of the wall and will not explicitly be considered as it is known that this term is relevant. If p_{ext} is positive, pressure is used to do some other form of work besides local deformation of the wall. If p_{ext} is negative some yet to be determined pressure source is present. For this exercise the inertial terms due to wall inertia and added mass will be grouped under a single term.

Using the discrete data from simulation to determine the 2nd order derivatives occurring in eq. 5.59, discretization is required. Using the Taylor expansion from eq. 3.6 of order 2, a central difference approximation of the 2nd order derivative can be found to be:

$$\frac{d^2\psi}{dx_i} \cong \lim_{h \to 0} \frac{\psi(x_i + h) - \psi(x_i) + \psi(x_i - h)}{h^2}$$

(Eq. 5.60)

After determining all terms in eq. 5.59, the order of magnitude of the terms is compared using an RMS-value similar to eq. 5.55. this allows calculation of a single metric with respect to time for each location on the centerline.

$$rms(\varphi(x_i)) = \sqrt{\frac{\sum_j^N \left(\varphi(x_i, t_j)\right)^2}{N}}$$

(Eq. 5.61)

5.5.5.3. Results

The RMS-values along the length of the tube are displayed in fig. 5.21 below. Depicted in blue is the longitudinal term describing the longitudinal shear term. The most noteworthy outcome is that the external pressure is at least 5 orders of magnitude larger than both the longitudinal term and the wall inertia term when end-effects are ignored. On the basis of this remark, both the longitudinal and wall inertia can be neglected in eq. 3.45. Near the in- and outlet the longitudinal term has a larger effect than at the center of the tube. This effect is caused by the boundary conditions imposed at the in- and outlet. Additionally, the longitudinal effects are more important than the wall inertia effects which includes the added mass term.
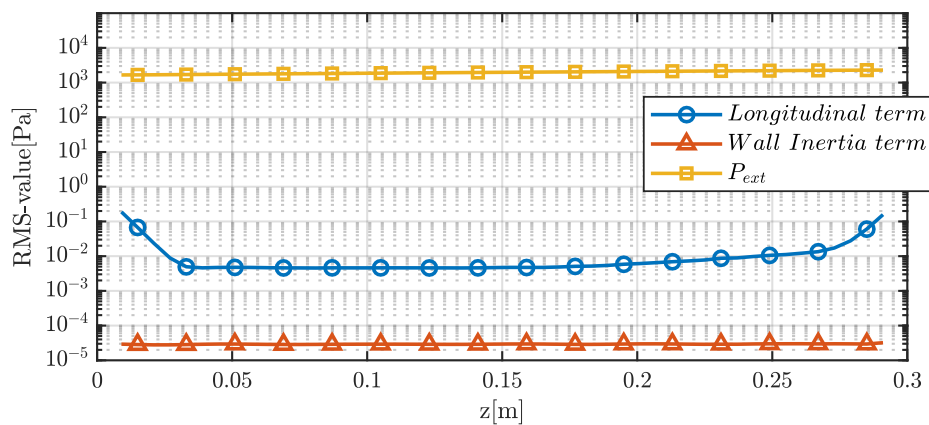
Fig. 5.21 - Order of magnitude of terms of structural model along the tube demonstrating that the inertial and longitudinal shear terms of the structural model have negligible influence.

186

5.6. model correction

The results from the characterization of effects for the 2-way FSI simulations have demonstrated that the discrepancies between the 3 FSI models, the 1D FSI model, the compressible fluid model and the 3D 2-way FSI model are not explained by the simplifications introduced into the structural mechanics model. This discussion starts of by attempting to provide a correction to the 1D FSI model. The structural model in the 1D description is represented by the balance of mass equation, eq. 5.9. Therefore, in order to improve the 1D FSI model. the momentum equation is revisited in an attempt to arrive at a more realistic description for pressure a flow. The balance of momentum in integral form for the current case is given according to:

$$\sum \vec{F} = \frac{d}{dt} \iiint_{CV} \rho \vec{v} \, dV + \oiint_{CS} \rho \vec{v} (\vec{v} \cdot \vec{n}) dS \qquad \text{(Eq. 5.62)}$$

All 3 terms will be derived in longitudinal direction for the case of an axisymmetric geometry and inviscid fluid flow. For this purpose, the control volume under consideration is presented in fig. 5.22:
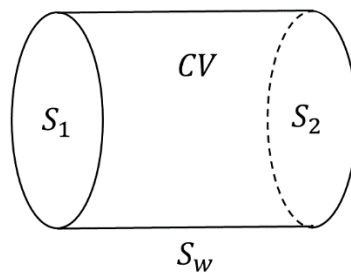
Fig. 5.22 - Axisymmetric control volume used for momentum equation derivation

In which CV is the control volume with volume ΔV and CS is the control surface set consisting of the wall surface S_w and the axial surfaces S_1 and S_2. The force balance in longitudinal direction is comprised of the normal forces on S_1 and S_2 plus the wall shear stress on S_w. As the flow is inviscid the shear force can be neglected, and it holds that:

$$\sum F_z = F_{1,z} + F_{2,z} = A_1 P_1 - A_2 P_2 \qquad \text{(Eq. 5.63)}$$

In which A_1 and A_2 are equal to the surface area of surfaces S_1 and S_2 and P_1 and P_2 their corresponding pressure. Under the assumption that the control volume is much smaller than the wavelength considered for wave-propagation, $A_1 \cong A_2$ .The first term of eq. 5.62 can then be rewritten as:

$$\sum F_z = -\Delta V \frac{dP}{dz} \qquad \text{(Eq. 5.64)}$$

The first term on the right-hand side of eq. 5.62 can be evaluated assuming velocity varies linearly along the length of the control volume:

$$\iiint_{CV} \rho \, v_z dV = \int_0^{2\pi} \int_z^{z+\Delta z} \int_0^{R(t)} \rho v_z \, r dr dz d\theta$$

$$\cong \frac{\Delta V \rho}{2} \left(v_{z,1} + v_{z,2} \right) \qquad \text{(Eq. 5.65)}$$

Rewriting this equation as a function of flow and taking the derivative with respect to time results in:

$$\frac{d}{dt} \iiint_{CV} \rho \, dV = \frac{d}{dt}\left(\frac{V\rho}{2A}(q_1 + q_2)\right) = \frac{\Delta V \rho}{A}\frac{d}{dt}\frac{(q_1 + q_2)}{2} \qquad \text{(Eq. 5.66)}$$

The last term in eq. 5.66 can be interpreted as the average flow within the control volume. Hence if the 1D momentum equation would be considered at this point and divided by the infinitesimal volume ΔV, eq. 5.10 would be recovered:

$$\frac{\rho}{A}\frac{\partial \bar{q}}{\partial t} + \frac{\partial p}{\partial z} = 0 \qquad \text{(Eq. 5.67)}$$

The main difference in notation is that it is specified that the flow is the average flow over all boundaries in a discretized space, whereas eq. 5.10 holds for a continuous space. Otherwise, the two equations are functionally equal.

The second term on the right-hand side has not been considered at this point demonstrating its absence in the previous 1D model. This term represents the in- and outflow of momentum over the boundary. Evaluating the integral assuming that the velocities at S_1 and S_2 are known results in:

$$\oiint_{CS} \rho \vec{v}(\vec{v} \cdot \vec{n})dS = \rho(-v_{z1} \cdot v_{z1} + v_{z2} \cdot v_{z2})A$$
$$= \Delta V \rho \frac{v_{z,2}^2 - v_{z,2}^2}{\Delta z} = \Delta V \rho \frac{d}{dz}(v_z^2) = \Delta V \rho \frac{d}{dz}\left(\frac{q}{A}\right)^2 \qquad \text{(Eq. 5.68)}$$

All terms of eq. 5.62 are known and the system of 1D equations becomes:

$$\frac{\partial A}{\partial p}\frac{\partial p}{\partial t} + \frac{\partial q}{\partial z} = 0 \qquad \text{(Eq. 5.69)}$$

$$\frac{\rho}{A}\frac{d\bar{q}}{dt} + \frac{dP}{dz} + \rho \frac{d}{dz}\left(\frac{q}{A}\right)^2 = 0 \qquad \text{(Eq. 5.70)}$$

189

This term is similar to 1D models as in for example Bessems et al. but is unaccounted for in the 1D wave equation model considered by Brown. The additional term creates a non-linearity that is difficult to solve in the frequency domain using the method from Brown [72].

Lastly, this system above can be rewritten in terms of mass flow and an effective pressure:

$$q_m = \rho q_v \qquad \text{(Eq. 5.71)}$$

$$p_{eff} = p_S + \rho \left(\frac{q}{A}\right)^2 = p_S + \rho v_z^2 \qquad \text{(Eq. 5.72)}$$

With q_m the mass flow and p_{eff} the effective pressure. Up to this point it was assumed that $q = q_v$ and that $p = p_S$. The effective pressure is similar to the total pressure in which the dynamic pressure is doubled. The continuity equation as a function of mass flow can be found by multiplying eq. 5.69 by the density and rewriting the derivative of the area with respect to the effective pressure:

$$\rho \frac{\partial A}{\partial p_{eff}} \frac{\partial p_{eff}}{\partial t} + \frac{\partial q_m}{\partial z} = 0 \qquad \text{(Eq. 5.73)}$$

For the momentum equation it should be noted that density is constant in our application and the density can be grouped within both the time and spatial derivative. Subsequently the two derivative terms can be combined resulting in:

$$\frac{1}{A} \frac{d(\overline{q_m})}{dt} + \frac{dp_{eff}}{dz} = 0 \qquad \text{(Eq. 5.74)}$$

A similar derivation using a control volume can be performed for the compressible system which is omitted. It can be shown that both the compressible and the compliant system can be represented by a single set of equations:

$$\frac{\partial(\rho A)}{\partial t} + \frac{\partial(\rho q)}{\partial z} = 0 \qquad \text{(Eq. 5.75)}$$

$$\frac{1}{A}\frac{d(\rho \bar{q})}{dt} + \frac{dP}{dz} + \frac{d}{dz}\left(\rho \left(\frac{q}{A}\right)^2\right) = 0 \qquad \text{(Eq. 5.76)}$$

5.7. Time-Domain 1D models

5.7.1. Reduced Complexity method

The equations presented in eqs. 5.75-5.76 are not easily solvable in the frequency domain using the approach from section 5.3. Instead, a time-domain based approach is taken to simulate the 1D model that includes the convective term for the momentum equation. The method is based on the work of Kroon et al. [80] which proposes a method of reduced complexity for evaluation of 0D and 1D networks. The approach of the method is division of the domain into a set of discrete elements which can be described by a pressure-flow relationship in which full system is of the form:

$$\boldsymbol{K}\vec{p}^{t+\Delta t} = \vec{q}^{t+\Delta t} + \vec{f} \qquad \text{(Eq. 5.77)}$$

$\vec{p}^{t+\Delta t}$ and $\vec{q}^{t+\Delta t}$ contain the pressure and flow respectively at all nodes of the network, $\boldsymbol{K}$ is a stiffness matrix and $\vec{f}$ is a vector containing any terms evaluated at the previous time-step and any source terms. The key idea of the method is that flows are defined to be directed towards the nodes making all internal flows equal to 0 and therefore known. The only unknown flows occur at pressure boundary

nodes while the pressure is unknown only at nodes where the flow is known. Hence the result is a system with as many unknowns as equations.

Eqs. 5.6-5.7 can also be found in the work of Kroon et al. [80], albeit modified to include viscous forces and to account for pulsatile flows. The reader is referred to this work for details regarding the implementation of the framework. For the current study, only the terms occurring in eqs. 5.69-5.70 have been included for the 1D elements as well as the set of 0D-elements required to describe the WK model, hence viscous forces are neglected. The convective momentum term is linearized and added as a source term in the vector $\vec{f}$.

Additionally, the model has been modified to include the partitioned model coupling as described in chapter 3. Subsequently, the model coupling was set to an explicit coupling as was done in the FSI-simulations. The pipe domain and the windkessel model are modelled using separate models using the methods from Kroon et al. but are linked by a central-difference coupling.

Kroon et al. uses a constitutive equation for compliance which is taken from Langewouters et al. [81] . For the current purpose, a compliance function has been fitted from the 3D 2-way FSI simulations to guarantee identical compliance behaviour for the purpose of comparing the two methods.

Data was available for pressure and radius along the centreline at every time-step of the simulation. However, characterising the compliance by evaluating dA/dp at every time step is not a successful strategy due to the reversal of the pressure differential and the accompanying zero-crossings. Instead the cross-sectional area is first modelled as a function of pressure. The cross-sectional area was therefore calculated for each point along the centreline and each pair of points was plotted as a scatterplot:
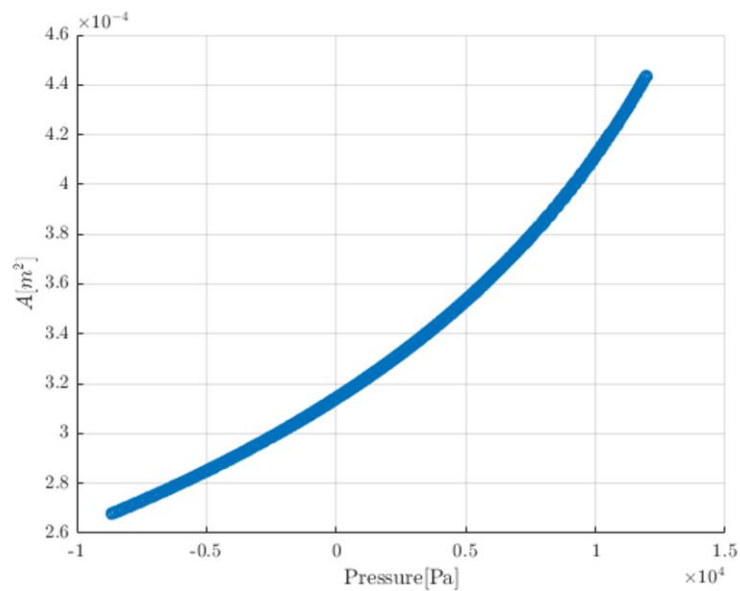
Fig. 5.22 - Plot of all pairs of cross-sectional area and pressure derived from 2-way FSI simulation shows clear relationship between them.

The relationship between them, implies that the area is independent of the time history of the system and can be modelled as a function of the pressure only. The area was fitted to a general exponential fit model of the form:

$$A(p) = ae^{bp} + ce^{dp}$$
(Eq. 5.78)

The fit coefficients where determined to be $a = 3.018 \cdot 10^{-4}$, $b = 1.514 \cdot 10^{-5}$, $c = 1.25e - 05$ and $d = 1.547 \cdot 10^{-4}$ using matlab's curve fitting toolbox at a coefficient of determination $R^2 > 0.99$. The advantage of this fit model is that the derivative of A(p) with respect to pressure is easily determined to be:

$$\frac{dA(p)}{dp} = abe^{bp} + cbe^{dp} \qquad \text{(Eq. 5.79)}$$

This relation is used as the constitutive equation for representing the 3D 2-way FSI simulations as a 1D model. All simulation parameters with respect to geometry and properties not mentioned till this point of the system have been kept equal to those in table 5.2 and eq. 5.50. Additionally, for the temporal discretisation the 1st-order backwards difference scheme was used. The number of elements in longitudinal direction was set to 150 elements as no increase in accuracy of the results was observed for smaller element lengths.

5.7.2. Results

Firstly, the original scenario is simulated in which the 1D equations are equal to eqs. 5.9-5.10. This is relevant to determine the agreement between the 1D modelling method by Brown and the method utilized by Kroon [80]. Results for this comparison are shown below in fig. 5.23:
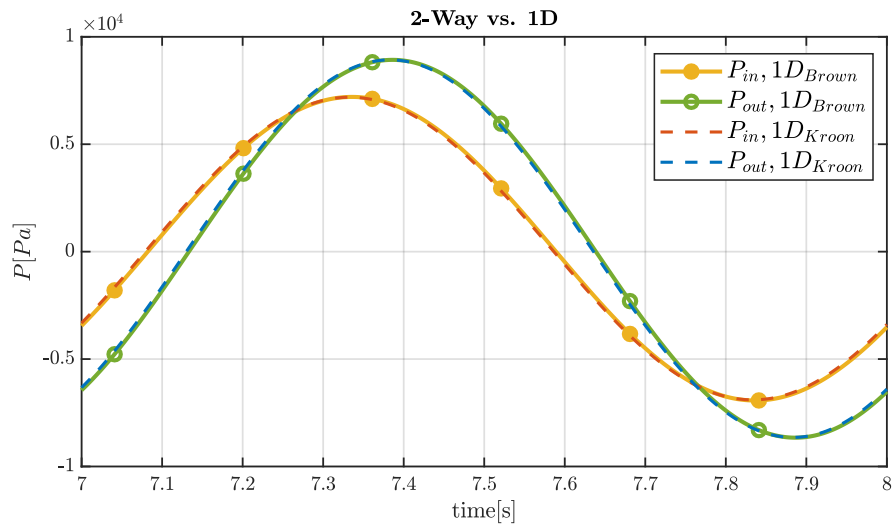
Fig. 5.23 - 1D Method comparison between Brown's wave equation based solver and Kroon's time-iterative solver are in good agreement.

Both methods are within good agreement. Upon closer inspection a short time lag can be observed for Kroon's method. This time lag is the result of enforcing a partitioned modelling approach using an explicit model coupling. Both descriptions are considered equivalent as the time lag exactly explains the discrepancy according to the methodology used in chapter 3.

Lastly the simulation including the convective momentum term is carried out. Results for this simulation are shown below in fig. 5.24 in which the 1D time-iterative method from Kroon, the compressible fluid method and the 3D 2-way FSI methods are compared:
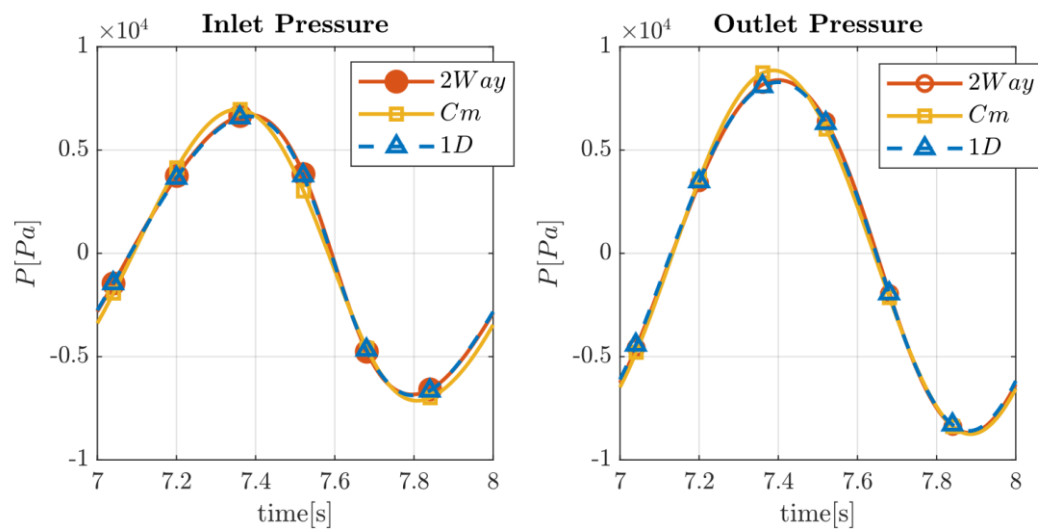
Fig. 5.24 - Time-iterative 1D, Compressible (C_m) and 3D 2-way FSI methods are compared, showing good agreement between the 1D and 3D 2-way methods.

Results for pressure between the 1D method including the convective momentum term and the 3D 2-way FSI are within good agreement. The maximum difference at the final simulation cycle is approximately 1.2% for both the outlet and inlet pressure. For the compressible model this maximum difference was noted to be approximately 9.6% at inlet. Therefore, the 1D method including a convective momentum term performs significantly better for the purpose of wave-propagation of pressure and flow compared to the compressible method.

5.7.3.   *Quasi 1D Modelling*

Lastly an attempt was made to reduce the computational cost of the 3D 2-way FSI method for the purpose of wave-propagation for this specific case. It was noted for the mesh- and time-step size dependency of the model that the variation of the number of elements in radial direction had little effect on the accuracy of the results. This concept can be taken up to the point where only 1 element spans the entire

diameter of the pipe under the assumption of axisymmetry. Additionally, discretizing the domain using only a single element is similar to assuming a 1D description in which all values in 3D space are reduced to points along a centreline. The key differences

To explore the accuracy of this approach, the geometry is represented as only a 5° section in circumferential direction of the original pipe geometry. The resulting mesh for the structural model and fluid dynamics model are shown below:
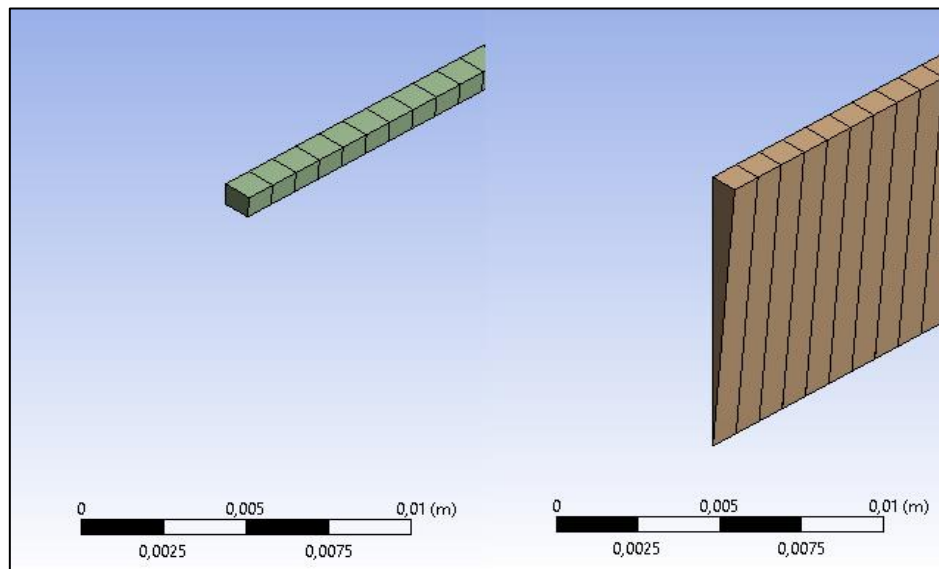
Fig. 5.25 - (left) Structural model mesh, (right) Fluid dynamics model mesh, both comprised of only a single element in radial direction

Simulation of a wedge-shaped element is necessary due to the deformation imposed on the structural model. If this model were simulated as a 2D in-plane geometry no circumferential stress would be generated in the structural model and it would be able to freely move through space. For the fluid dynamics a symmetry condition is

applied on both side-surfaces of the wedge enforcing axisymmetry. 300 elements were chosen in longitudinal direction and all parameters used for previous simulations in this chapter were retained. Therefore, the total model consists of 300 elements in the structural model and 300 elements in the fluid dynamics model. The simulation was otherwise simulated following the identical steps as described for the 3D 2-way FSI case for which the results for the first 3 simulation cycles are shown below:
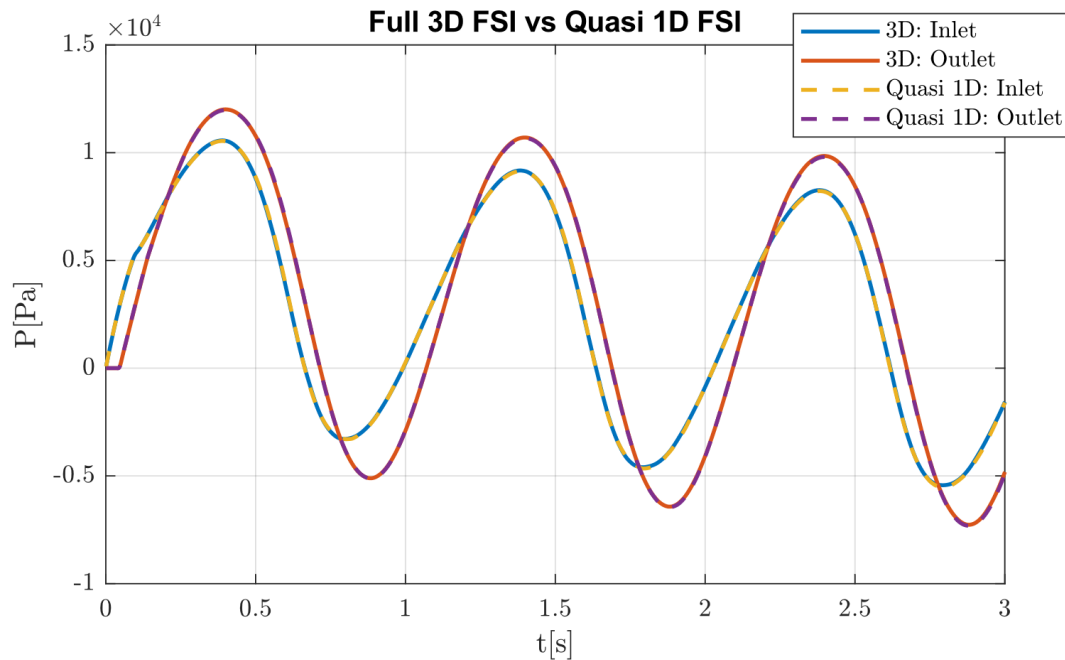
Fig. 5.26 - Pressure results for the 3D 2-way FSI and the Quasi 1D FSI approximation in good agreement.

Both methods agree with each other with a maximum difference of below approximately 1%. This difference is similar as that found between the 2-way FSI and the full time-iterative solver from Kroon et al. [80]

5.8. Discussion

This chapter has sought to explore the differences between three different methodologies incorporating FSI. The motivation behind this approach was to suggest improvements to a compressible fluid model which is far less computationally expensive as a full 2-way FSI but is still capable of representing part of the 3D flow features. This was deemed necessary as the error reported by Brown [72] was deemed significant with respect to the magnitude of the effect of incorporating FSI.

The wave-propagation models presented by Brown [72] have been recreated for the current study using ANSYS Fluent, Mechanical, System-coupling box for the 3D methods and Mathworks Matlab for the 1D wave propagation model. In order to establish if non-accounted terms in the structural model were the cause of the discrepancy between the 1D and full 2-way FSI model a more detailed equation for the thin walled vascular wall was derived. This model included the added mass effect and a longitudinal wave propagation term of the structure.

It is noted in section 5.5.2.2 that the FSI model has very similar coupling characteristics compared to the models considered in chapter 4. As such there is good reason to believe that the stability considerations for an implicit coupling mechanism translate directly to instability effects seen in for instance the added-mass instability (as discussed by Causin [70]). A partitioned FSI simulation could therefore significantly benefit from a central-differenced coupling. At the time of

execution of the work however these considerations were not known to the author and the fully implicit coupling mechanism provided with ANSYS System coupling box were used. Future work, in order to improve model stability, should include a central-difference based model coupling.

Higher order terms could have been included for the structural model but have often been disregarded in literature due to their relative magnitude compared to the other terms. This assumption was further confirmed by the negligible effect of the added-mass effect and the longitudinal term with respect to explaining the noted model discrepancies.

As this analysis left the discrepancies unexplained for, an alternative route was taken to consider the balance of momentum to derive a 1D differential equation. It can be concluded that the 1D equation in the Fourier approach fails to consider the convective influx of momentum. As this influx is difficult to model using a strictly Fourier based approach, a choice was made to simulate this equation using an iterative time-domain based method. The resulting 1D model was in good agreement with the Full 2-way FSI model indicating that the missing term almost fully explains the model discrepancy.

While this remark invalidates the strictly Fourier based 1D method, it should be noted that this term can potentially be incorporated within the compressible fluid model. As the compressible fluid model only requires a constitutive equation of the density as a function of simulation pressure. However, more work is required to

implement the suggested correction due to the fact that the wave propagation behaviour needs to conform to that of eqs. 5.73-5.74 requiring a different calculation of the wave velocity c at every timestep as well as additional step for calculating p_{eff}.

Additional future work includes making the parameters for the compressible fluid model dependent on local geometry and material properties. In the current study results, the wave velocity was maintained constant. However, an explorative study of a 50% constriction of a vessel revealed a potential shortcoming of the compressible fluid approach. As the fluid approaches the constriction, its velocity increases where ultimately at the throat the velocity approaches the wave velocity and thus reaches Mach 1. At these velocities, the fluid can no longer accelerate and a shockwave exists at the throat. In a real-world scenario this is not feasible as the fluid is incompressible in reality, hence the wave velocity needs to change locally to accommodate the requirement of the Mach number remaining below 0.3 in order model incompressible flow.

Making adaptations to the local vessel compliance and inertance might ameliorate the shortcoming of the model to represent big changes in circumferential area. However, many questions regarding the applicability of this technique to represent the 3D flow features present in the real-world case, remain unanswered in the current work. One significant benefit of the compressible fluid model over a 1D modelling approach is to incorporate some of these 3D flow features. However,

some effects are impossible to carry over as for instance for the constriction case. The compressibility of the fluid is only a function of the local static pressure. However, it is clear that the forces experienced at the throat of the constriction are partly dependent on the flow direction near the wall. This is an inherent local change of the shape of the geometry, i.e. the vessel wall, due to inertial effects of the fluid with respect to the structure. It is expected to play an equal role in flows around sharp bends. It was noted by Morbiduci [41] that a change in input velocity profile had a marked effect on the flow features downstream. Changes in geometry due to FSI effects can be expected to have similar effects. However, as the impact of these effects has not been characterised in the current study, a thorough characterisation remains as future work.

Lastly a quasi 1D method was suggested as an approximation of the full 2-way FSI for which results are within good agreement. Advantages of using the quasi 1D method include a significant reduction of numerical elements within the model while still being able to perform the simulation using commercial 3D solvers. Therefore, no additional models need to be built, validated and subsequently verified for their respective software environments. Additionally, the fluid behaviour due to 3D effects, as for instance flow in a curved tube, are not neglected as they are in a 1D or 0D approach. Simulating a wedge for this purpose is not recommended due to the asymmetry of the flow, but the idea could be extended by using circular axisymmetric pipe segments instead with a minimal number of elements in radial direction, preferably one element. This would allow for inclusion

of vessel curvature and some degree of flow and pressure asymmetry. However, more work would be required to explore this idea fully and design methods to handle bifurcations of vessels for this idea to be useful in practice. For now, the wedge model has its uses for studying wave propagation in straight pipes for a partitioned modelling approach at minimal computational cost.

Chapter 6

6. Transient Reduced Order Modelling

6.1. Introduction

Reduced order modelling comprises the set of all techniques that can be used to reduce the dimensionality of a model while still obtaining acceptably similar results. As such the class of 0D models and approaches utilized in previous chapters also fall under the class of reduced order modelling. Fluid and structural models often containing millions of elements get reduced to a set of hundreds to thousands of elements. A pressure and flow can be obtained from these models that approaches that of the Full order model (FOM) at a fraction of the computational costs. As was seen previously, this classical form of model order reduction has been successfully applied in 0D-, 1D- and at times 2D- models. Although 2D models often rely on simulations in which axisymmetry applies

The previously described method for model order reduction is heavily reliant on the knowledge of the underlying system. Without knowledge of the physical equations being approximated in the reduced order model (ROM) approximation, it is not possible to derive 0D,1D or 2D models representations. This also implies that often a different software implementation or environment is used for each separate application. The many different models in scientific literature are a testimony of this.

The class of reduced order modelling that will be discussed falls under the category of proper orthogonal decomposition (POD). A primer on the POD concept can be found in Chinesta et al. [82]. POD can be used to derive an optimal basis describing

the variation within a dataset and is known under different names including the Karhunen-Loève transform [83], principal component analysis [84] and the singular value decomposition(SVD) [85] depending on the scientific field. While the description of the techniques might differ slightly, the underlying principles are the same. One of the first applications within the field of fluid mechanics of POD was first suggested by Lumley et al. [86] for the identification of large coherent structures. POD based techniques regarding reduced order modelling for different fields of mechanics however, have historically mainly found their way into applications using finite element modelling [87, 88]. These can be considered to be intrusive methods as in this context the reduced basis derived from the POD is used in solving a set of differential equations that are related to or equal to the governing equations of the physics involved. A review regarding turbulent flows can be found in Berkooz [89].

A non-intrusive POD based approach is used at the present time within ANSYS. Non-intrusive techniques do not interact with the differential equations of the problem and are therefore solver independent. As such, they are more easily made suitable to a wider class of problems and solution methods. The full process of a study can be depicted as in fig. 6.1 below and will be used to describe the approach:
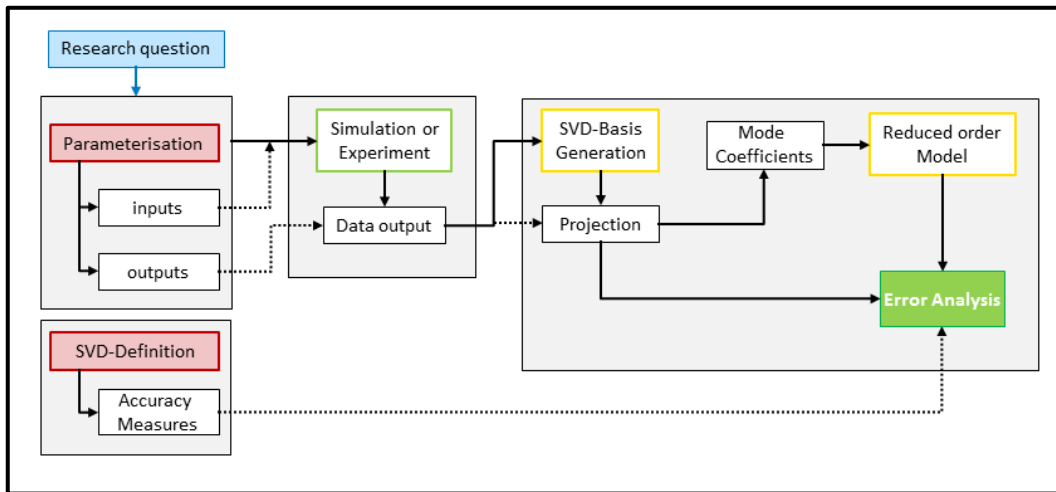
Fig. 6.1 - Overview of processes involved in reduced order modelling

The first 3 blocks on the right-hand side of fig. 6.1 are steps that are related to general simulation steps. Depicted on the left-hand side is a block describing the additional processes involved for creating the reduced order model. A reduced order model is of the general form:

$$\overrightarrow{Y'}(t, \vec{k}) = f(t, \vec{k}, \boldsymbol{U}) \cong \vec{Y}(t, \vec{k}) \qquad \text{(Eq. 6.1)}$$

In which vector $\overrightarrow{Y'}$ is the ROM approximation of an output field $\vec{Y}$ from the FOM. $\vec{k}$ describes a set of input parameters grouped in vector format while $\boldsymbol{U}$ is a matrix containing the basis vectors spanning the output space for $\overrightarrow{Y'}$. Then, $f(t, \vec{k}, \boldsymbol{U})$ is some to be determined function that relates the input parameters at time t to the basis vectors for that particular model. The model order reduction stems from representing the FOM solution space as a limited set of basis vectors. In the FOM a set of equations needs to be solved for every element in the simulation. For the ROM only one set of equations needs to be solved per basis vector involved.

Determining the basis in U to be used in the reduced order model is done using the SVD.

Generating the SVD and ROM both rely on data from the FOM. The data that gets returned from the FOM can be grouped in a 1D vector which is referred to as a snapshot. A key point of the current ROM strategy is that its outputs are always a linear combination of the basis provided in U. As such, any information or behaviour that is not represented in the basis but occurs in the FOM cannot be reproduced by the ROM. This puts requirements on the snapshots provided by full order model. Firstly, the main requirement is that the simulation to be set up answering the research question is parameterizable in order to satisfy eq. 6.1. Secondly the snapshots generated by the FOM should contain the necessary information to describe the full output space with respect to the range of the input parameters.

The nature of the modelling function $f(t, \vec{k}, U)$ is determined by ROM builder (ANSYS, Cannonsburg, Pennsylvania, US). However, within the context of the current study there is no control or detailed knowledge about the model itself as it is proprietary information. As such the part that is controllable for the full reduced order modelling process, is generation of the SVD basis to be used for the ROM. There are two research questions of interest with respect to the quality of this basis:

- How much training data is required for constructing an SVD basis with acceptable accuracy?
- How can a basis be constructed containing the necessary features to describe a problem?

In order to answer these questions, a set of accuracy measures needs to be defined for the current problem.

Firstly, in this chapter an introduction will be given regarding the subjects of singular value decomposition and reduced order modelling in the current context. Subsequently, using a steady-state example, the behaviour of SVD results is demonstrated. The remainder of this chapter will focus on a transient example as this study is mainly concerned with techniques applicable to large artery flows. These types of flows are inherently transient in nature due to the pulsatile flow characteristics and bring with it a separate set of challenges regarding SVD basis creation. Lastly, generation of a reduced order model will briefly be discussed.

6.2. Reduced order Basis generation

POD is used to produce a reduced order basis providing an acceptable approximation for all possible reachable solutions of a model. The problem can be reformulated as an optimization problem to minimize the difference between the original and approximated data for all solutions within the working range of a model. However, a method to determine such a basis that does not require an optimisation algorithm is the singular value decomposition. The singular value decomposition can be seen as a generalized method for matrix diagonalization of the form:

$$X = U\Sigma V^*$$
(Eq. 6.2)

In which X is the snapshot matrix, U is referred to as the matrix of left singular vectors (along its columns), Σ is a diagonal matrix containing the singular values along its diagonal and V^* is referred to as the conjugate transpose of the right singular vectors. For the remainder of the text however, it will be assumed that real valued matrices are being considered. Therefore V^* will be considered to be simply its transpose V^T. Snapshot matrix X contains the simulation data rearranged as column vectors, known as snapshots. The left singular vectors constitute a basis for the column vectors in X which will be referred to as the modes of the system, while the matrix resulting from the product ΣV^T constitute the mode coefficients. The mode coefficients can therefore be seen as coordinate vectors in the new basis, corresponding to each snapshot in snapshot matrix X.

For the real valued case considered, this decomposition exists and calculating the required matrices can be done using the following approach. The example given below is used to demonstrate the properties of the SVD decomposition. It can be shown that it is possible to diagonalize any symmetric matrix according to:

$$B = PDP^{-1} = PDP^T \qquad \text{(Eq. 6.3)}$$

In which D is the diagonal matrix containing the eigenvalues of B and P the orthogonal matrix of eigenvectors of B along its columns. The last equivalence in eq. 6.3 is due to P being an orthogonal matrix for which it holds that:

$$P^{-1} = P^T \qquad \text{(Eq. 6.4)}$$

For any matrix A, the products $B = A^T A$ and $B = A A^T$ result in a symmetric matrix B as $B = B^T$. Therefore B is always diagonizable. Starting from the diagonalization of $X^T X$, it can be shown that matrix U can be eliminated and the following holds:

$$
\begin{aligned}
X^T X &= PDP^T \\
&= (U\Sigma V^T)^T (U\Sigma V^T) \\
&= (V\Sigma U^T)(U\Sigma V^T) \\
&= V\Sigma^2 V^T
\end{aligned}
$$

(Eq. 6.5)

The same process can be performed for eliminating V. Therefore, for this to hold both matrices U and V must be orthogonal, which is consistent with eq. 6.3. Thus U forms an orthonormal basis for snapshot matrix X. The problem presented in eq. 6.5 is essentially an eigenvalue problem. Matrix Σ can be calculated by determining the eigenvalues of $X^T X$ such that:

$$
\Sigma = diag\left(\sqrt{\lambda_1}, \sqrt{\lambda_2}, \cdots, \sqrt{\lambda_n}\right) = diag(\sigma_1, \sigma_2, \cdots, \sigma_n)
$$
$$
\lambda_1 \geq \lambda_2 \geq \cdots \geq \lambda_n \geq 0
$$

(Eq. 6.6)

Matrix V consist of the corresponding columns of eigenvectors of $X^T X$ as is the case for common matrix diagonalization. Additionally, if complex conjugates were to be considered as in eq. 6.2, both U and V would be unitary instead of orthogonal matrices. As mentioned before it is possible to construct matrix U using the preceding approach. However, a more straightforward computational approach is to determine U simply by:

$$
U = X\Sigma^{-1}V
$$

(Eq. 6.7)

In practice more efficient computational algorithms are used but discussion of these is out of the scope of the current project and not interesting for the current application.

A basis formed by the SVD has a number of useful properties. SVD produces an orthonormal set of basis vectors in U for snapshots in $X.$ The singular values σ_i can be interpreted as the relative importance of each basis vector regarding the entire set of snapshots. Lastly, the right singular values in V can then be regarded as the normalized mode coefficients demonstrating how the modes should be combined to construct the individual snapshots. Effectively, the vectors in V form a basis for the row space of snapshot matrix X.

Lastly, A lower-rank approximation of snapshot matrix X can be constructed by truncating the number of modes that are considered in the analysis [90]. This is the goal of the reduced order modelling process by instead only having a number of functions n equal to the rank of the basis describing the output. Truncation can be achieved by setting the singular values of the higher order modes,i.e. the modes corresponding to the smaller singular values, to zero. If the lower-rank approximation of the snapshot matrix is indicated by X', the singular value decomposition minimizes the distance between the original snapshot matrix X and the truncated approximation X' with respect to the Frobenius norm. This norm is interpretable as a scalar L2 norm for matrices and is represented in eq. 6.8:

$$\|\mathbf{A}\|_2 = \sqrt{\sum_i^n \sum_j^m a_{i,j}^2} \equiv \|\mathbf{A}\|_F \qquad \text{(Eq. 6.8)}$$

This result was elegantly shown by Eckart and Young [91] in which it was also demonstrated through a scalar inner product for matrices that pre- or post-multiplication of matrices by orthogonal matrices does not contribute a change to the Frobenius norm. This simplifies the calculation of the Frobenius norm of the singular value decomposition of the snapshot matrix to:

$$\|\mathbf{X}\|_F = \|\mathbf{U}\mathbf{\Sigma}\mathbf{V}^*\|_F = \|\mathbf{\Sigma}\|_F = \sum_i^n \sigma_i^2 \qquad \text{(Eq. 6.9)}$$

The singular value decomposition minimizes the distance $\|\mathbf{X} - \mathbf{X}'\|_F$ and provides a set of basis vectors ordered with respect to their importance for describing the variation between snapshots. This basis is considered as an optimal basis according to that description.

6.3. Reduced order modelling

The second step in the reduced order modelling process is to construct the model description relating the input parameters at time t, to an output vector. A more detailed description of the form of the ROM is presented in eq. 6.10:

$$\vec{y}(\vec{x}, k_1, k_2, \cdots, k_m) = \sum_i^n a_i(k_1, k_2, \cdots, k_m)\vec{\varphi}(\vec{x}) \qquad \text{(Eq. 6.10)}$$

In which $\vec{y}$ can be any set of output scalars or field data, $\vec{x}$ is the geometrical position in space, k_i the set of remaining input parameters, a_i the mode coefficients and $\vec{\varphi}$

the modes. This is a separation of variables in which the dependence on the position is captured in a set of pre-computable modes. Once a set of modes has been chosen, the model itself consists of finding a description of the mode coefficients a_i as a function of the input parameters.

While the approach for deriving the modes is always the singular value decomposition, different approaches are used within ANSYS to derive the mode coefficients. The most important distinction is made between steady-state and transient simulations. For the steady-state setting use is made of Static ROM Builder.

Static ROM builder utilizes the algorithms present within ANSYS Design explorer to build response surfaces for each mode coefficient a_i. A genetic aggregation algorithm is used to construct a response surface by cross-referencing a set of response surfaces generated using interpolation methods including Kriging, moving least squares and non-parametric regression amongst others [92].

For the transient case use is made of Dynamic ROM builder. The reduced order model is functionally the same as in eq. 6.10 with the exception that one of the parameters is time for the transient model. However, whereas the other parameters of a system generally describe independent states, time describes the progression of one state to another and is not a state variable itself. Therefore, these states are highly interdependent. As mentioned previously, for various applications this

problem has been handled instead by solving a set of differential equations of reduced order, rather than fitting a function to represent the data. Dynamic ROM builder uses a set of proprietary techniques based on machine learning methods to determine an underlying model for the mode coefficients for all input parameters with respect to time.

Lastly, the purpose of a reduced order model however is not to predict the values of known outcomes, but to predict the outcomes for new simulation cases not contained in the training set. As such the accuracy of the model should be tested on validation data which is different from the training data. However, the training data should be from a location of the parameter space in which it is expected for the reduced order model to hold. This means that while the reduced order model might be capable of providing satisfactory results it should not be used for extrapolation of results without precaution.

6.4. Steady State SVD

6.4.1.   *Aneurysm model*

In order to demonstrate some of the properties regarding SVD, the procedure is first carried out for an idealised aneurysm model as shown in fig. 6.2. This case has been setup with dimensions and parameters which are representative of conditions within the internal carotid artery [93, 94]. A slight curvature and tapering have been added to the model to make the flow and pressure field more interesting. The inlet diameter is chosen as the characteristic diameter and set to $D_{in} = 4[mm]$ while the

fluid is considered to have a dynamic viscosity $\vartheta = 3.3 \cdot 10^{-6} [m^2\, s^{-1}]$ and a density of $\rho = 1056 [kg\, m^{-3}]$.
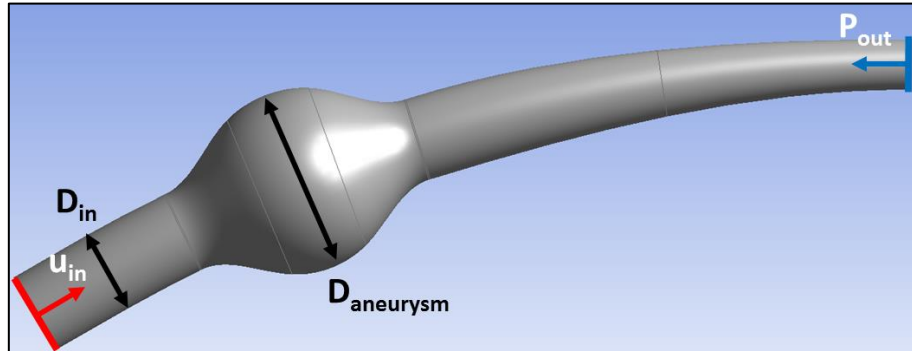
Fig. 6.2 - Aneurysm geometry used for steady-state simulation and SVD generation

As BCs for the simulation within Fluent, a constant velocity u_{in} is imposed at the inlet and a zero-pressure boundary p_{out} is imposed at the outlet. The case is parameterised using a single input parameter namely the Reynolds number at the inlet. This is defined as:

$$Re_{D,in} = \frac{u_{in} D_{in}}{\nu} \tag{Eq. 6.11}$$

This choice was made due to the different fluid dynamics phenomena at different Reynolds number for many applications. By nondimensionalizing the momentum equation an equation can be derived as a function of the Reynolds number given by:

$$(\vec{v} \cdot \vec{\nabla})\vec{v} = -\vec{\nabla}\frac{p}{\rho} + \frac{1}{Re_D}\nabla^2\vec{v} \tag{Eq. 6.12}$$

Eq. 6.12 describes the relative importance of different terms, and thus different patterns in the flow as a function of the Reynolds number. At high Reynolds numbers, the viscous term, the 2nd term on the right-hand side is expected to be

negligible while for very low Reynolds number flow it is expected to be the dominant term. At intermediate Reynolds number it is expected that all terms are of equal importance.

While the Reynolds number in the internal carotid artery is of order $O(Re_D) = 50[-]$, the simulation Reynolds number is varied between $0.1 \leq Re_{D,in} \leq 1000$ in order to include the different fluid dynamics conditions. As an example, pressure and velocity are plotted on a cross-section of the vessel for $Re_{D,in} = 10$ and 1000 in fig. 6.3.
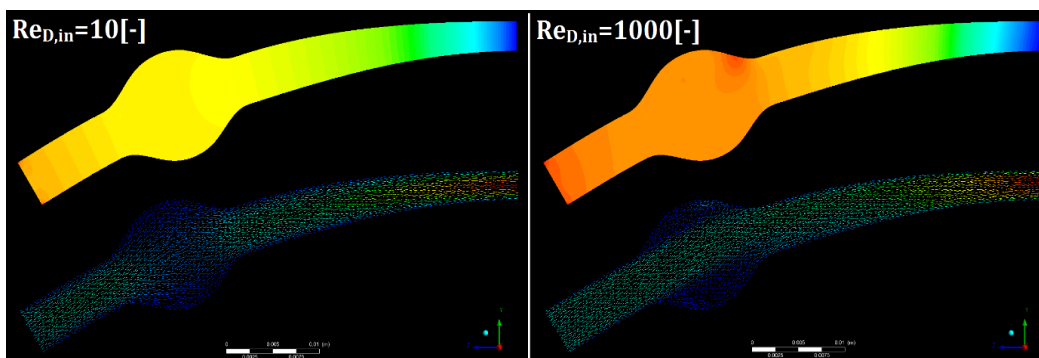
Fig. 6.3 - (left) Fluid and pressure patterns mainly governed by viscous effect (right) Flow and pressure governed by inertial effect resulting in main fluid stream and high-pressure region at the Aneurysm.

At the lower Reynolds numbers, the pressure is relatively homogeneous along the radial direction. The velocity demonstrates axisymmetry showing the relatively low importance of the steady inertial term. At the higher Reynolds number, a high-pressure region and main velocity stream can be seen inside of the aneurysm region. This high-pressure region is a result of the main velocity stream hitting the wall due

to the curvature of the vessel. Additionally, it can be seen that large coherent structures have appeared, i.e. a vortex near the high-pressure region. This supports the notion that the steady-inertial term is of much higher importance than the viscous term at this Reynolds number.

The discrete set of Reynolds numbers was chosen on a logarithmic scale within the range, resulting in 37 simulations, 9 simulations per logarithmic decade displayed on the x-axis of fig. 6.4. The output of the model is defined as the pressure field within the vessel. In order to generate an SVD basis, the 3D pressure fields from every simulation were stored as a 1D vector snapshot

6.4.2. SVD Basis Characterisation

An SVD basis was generated of order 37 of the pressure field. As the basis contains the same number of modes as the rank of the original snapshot matrix, all information of the original data is present. However, it should be noted that the modes are vectors representing the principal directions of the data and are not necessarily recognisable as the individual data snapshots. To reconstruct the original snapshots, it is necessary to determine the mode coefficients by projecting the snapshots back onto the SVD basis. As the basis is orthonormal by design, the mode coefficients are easily calculated by taking the inner product of the snapshots with the basis vectors represented by:

$$\vec{a_i} = [a_{i1} \quad a_{i2} \quad \cdots \quad a_{in}]^T = \boldsymbol{U}^T \vec{y_i} \qquad \text{(Eq. 6.13)}$$

Fig. 6.4 below shows the mode coefficients as a function of the Reynolds number. The mode coefficients have been normalised for each individual simulation snapshot $\vec{y_i}$.
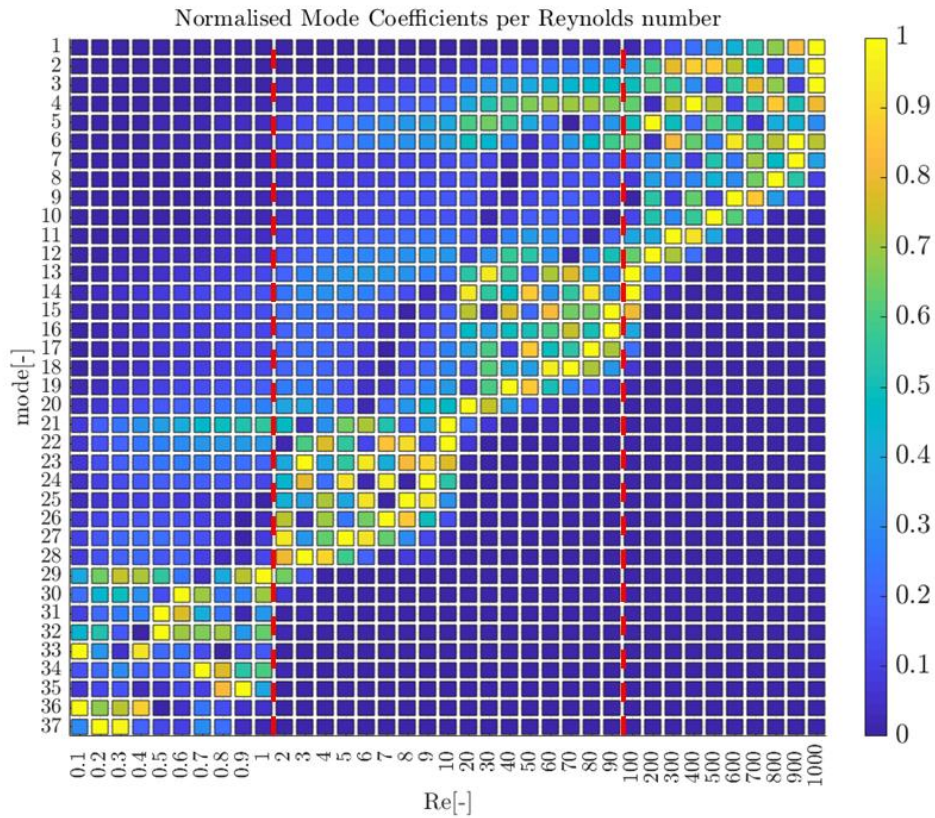
Fig. 6.4 - Modes coefficient normalized with respect to each other for every simulation showing the relative use of each mode with respect to the Reynolds number.

The most energetic mode of the SVD basis is always mode 1 and represents the average field of all snapshots considered. For reconstructing the individual snapshots, it becomes apparent that mode 1 is contributing the most to the solution of the highest Reynolds number simulations. This is a result of the average magnitude of the values in the field as the average pressure is higher for the higher

Reynolds number simulations. This implies that the higher Reynolds number simulations therefore contribute more to the SVD basis then the lower Reynolds number situations. This trend continues when regarding the higher order modes as the first 10 modes contribute most to the 10 simulations with the highest Reynolds numbers. Additionally, for different regions of the Reynolds number, different clusters of modes seem to be used to represent each snapshot. This is due to the different flow patterns experienced at different Reynolds numbers as discussed before. Different snapshot patterns are required between different ranges of the Reynolds numbers in order to correctly describe the pressure and flow fields.

Depending on the requirements of the reduced order model this can be a problem. If for example the basis would be truncated to the first 10 modes it would be capable of reproducing the pressure field for the higher Reynolds numbers within good agreement. However, it would perform more poorly at the lower Reynolds numbers. This hypothesis was explored using a subset of the original Reynolds range. As the working range of the model is supposed to be in the order of $O(Re_{D,in}) = 50[-]$, All Reynolds number simulations above $Re_{D,in} = 100[-]$ were removed and a set of bases of decreasing dimension was constructed for the remaining set. Subsequently the simulation data was projected back onto the basis. The relative projection error was then used to assess the performance of the SVD basis for representing each individual simulation according to:

$$\epsilon_{rel} = \frac{\|\overrightarrow{\varphi_{svd}}(t) - \overrightarrow{\varphi_{sim}}(t)\|}{\|\overrightarrow{\varphi_{sim}}(t)\|} \qquad \text{(Eq. 6.14)}$$

In which the vector $\overrightarrow{\varphi_{svd}}$ is the snapshot vector resulting from SVD projection, $\overrightarrow{\varphi_{sim}}$ is the original snapshot vector and $\|\cdot\|$ indicates the L_2-vector norm.

projection errors for different basis sizes shown in fig. 6.5 support the notion that for this particular case the lowest order modes are more representative of the higher Reynolds number simulations.
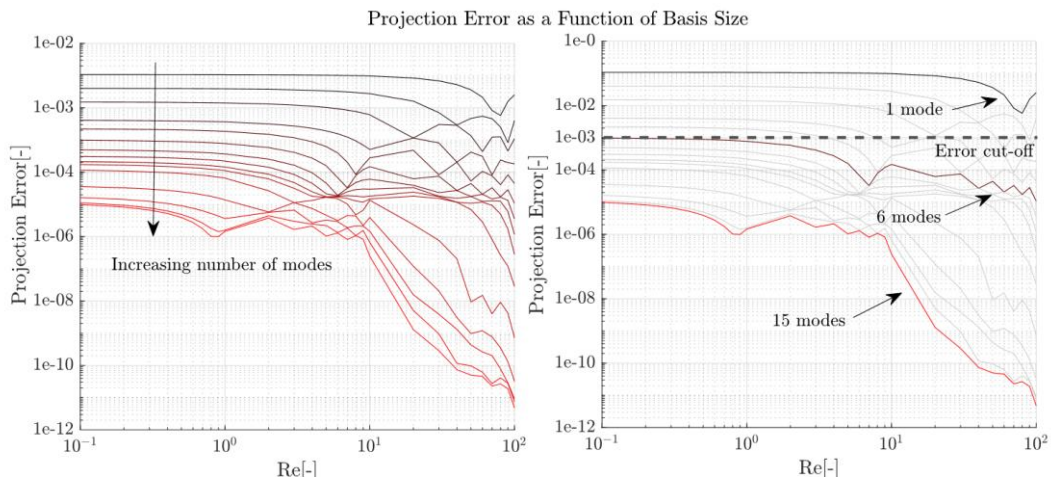
Fig. 6.5 - Projection error as a function of Reynolds number depicting the decrease in error due to incorporating more mode and the higher accuracy observed at higher Reynolds numbers.

The relative projection error is highest for the low Reynolds numbers. Increasing the basis size reduces the error over the entire range of Reynolds numbers but for most bases performs best at the higher Reynolds number ranges. At a cut-off of 0.1%, 6 modes are sufficient to reconstruct all snapshots at this level of accuracy. Considering mode 1 it can be seen that the projection error for $Re_{D,in} = 80[-]$ is the lowest, hence this mode is most similar to the solution at this Reynolds number.

The remarked behaviour of the SVD derived basis results from the properties of the SVD. Modes are constructed and ordered to describe the largest variation within the data. Due to the different pressure scales for each simulation the high Reynolds simulations contribute higher absolute values and thus are over-represented in the basis. In summary, the previous example demonstrates that different modes are representative of different patterns in pressure and flow fields that can occur. The remainder of the chapter will consider transient simulations which is closer to the intended purpose of reduced order modelling.

6.5. Transient SVD

As mentioned previously, for the application of reduced order models in hemodynamics it is often important to include the transient behavior of the flow. This is especially true for the large arteries where pulsatile flow patterns exist, and the Reynolds numbers can be of much higher magnitude. The steady-state example has demonstrated however, that different flow and pressure patterns exist at different Reynolds number. During a transient simulation of pulsatile flow, a range of Reynolds numbers is passed during each cycle. An attempt is made to derive an acceptable basis for the transient case.

 A different geometry is chosen for the transient case. The steady-state aneurysm case used previously can be seen as a localized expansion. It was found that for this case the vortices that develop are contained within the aneurysm and there is therefore minimal transport of any coherent structure. Due to pressure and wave propagation in the human vasculature it is possible to have some transport of

coherent structures. For the transient case therefore, a geometry is chosen that does exhibit this transient transport phenomenon. A well-known example that exhibits this behavior is flow through a sudden expansion, i.e. a backwards step, in which a mainstream of fluid or a generated vortex can essentially continue down the geometry unhindered. Therefore, a sudden expansion is taken as the geometry for the transient ROM analysis.

6.5.1.   Sudden Expansion setup

For the transient case, an axisymmetric sudden expansion is considered with an inlet diameter D_1 and an outlet diameter D_2. This geometry is then subjected to a pulsatile flow. The geometry of this case is presented on the left of fig. 6.6 while the pulsatile inflow pattern is depicted on the right.
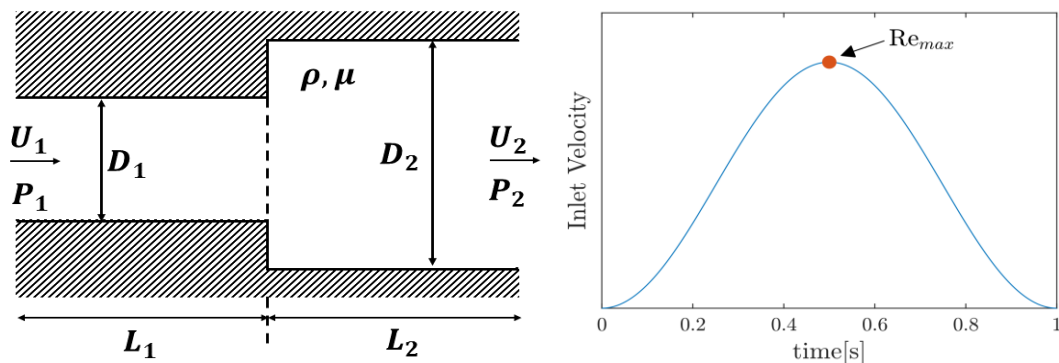
Fig. 6.6 - (left)sudden expansion geometry used for transient simulation example, (right) average velocity prescribed as a function of time at the inlet

Advantages of this model are its relative simplicity and the ability to generate large coherent structures. A small well-defined subset of parameters is capable of describing the entire range of possible models with the same topology. Additionally, due to its simplicity the requirements for computational resources can

be kept low allowing for an easy design exploration and thus the generation of training and validation sets for the purpose.

Boundary conditions for this case consist of a pulse inflow U_1 over time uniformly prescribed at the inlet surface and a zero-pressure boundary condition P_2 at the outlet. The dimensions for this case have been chosen to be representative of the dimensions of large artery vascular flow at $D_1 = 0.5$[cm], $D_2 = 1.0$[cm], $L_1 = 2.5$[cm], $L_2 = 15$[cm]. A Newtonian fluid is used to represent blood flow through this expansion with a density of $\rho = 1056[kg\ m^3]$ and dynamic viscosity $v = 3.5 \cdot 10^{-3}[Pa \cdot s]$.

The input parameter for the reduced order model is the maximum inlet velocity represented by the maximum Reynolds number in eq. 6.15. This maximum velocity occurs at the point indicated by a red dot in the right graph of fig. 6.6.

$$Re_{max} = \frac{U_{max}D_1}{v}$$
(Eq. 6.15)

The Reynolds number over time imposed at the inlet is then chosen as:

$$Re(t) = Re_{1,max} \cdot sin^2(\pi t)$$
(Eq. 6.16)

For this explorative study the maximum Reynolds number range is chosen to be $10[-] \leq Re_{max} \leq 100[-]$ as the working range of the reduced order model. In part this is done to limit the possible different types of coherent structures and keep

the basis dimensions relatively small. The coherent structures generated at $Re_{max} = 1000[-]$ might be dissimilar from the structures generated at $Re_{max} = 100[-]$ and are potentially susceptible to turbulence effects. Excluding the higher Reynolds range additionally prevents turbulence effects from occurring and thus the necessity of a turbulence model. While this limits the accuracy with which the real-world case would be modelled it does not diminish the validity of the approach for the reduced order model. At low Reynolds numbers $(Re_{max} < 10[-])$ the model produces laminar flow without any coherent structures and this range is usually not relevant for large artery flow.

At intermediate Reynolds numbers $(10 \leq Re_{max} \leq 100)$ a coherent structure is produced at the onset of the expansion, shown in fig. 6.7 below, at a Reynolds number of $Re_{max} = 100[-]$.
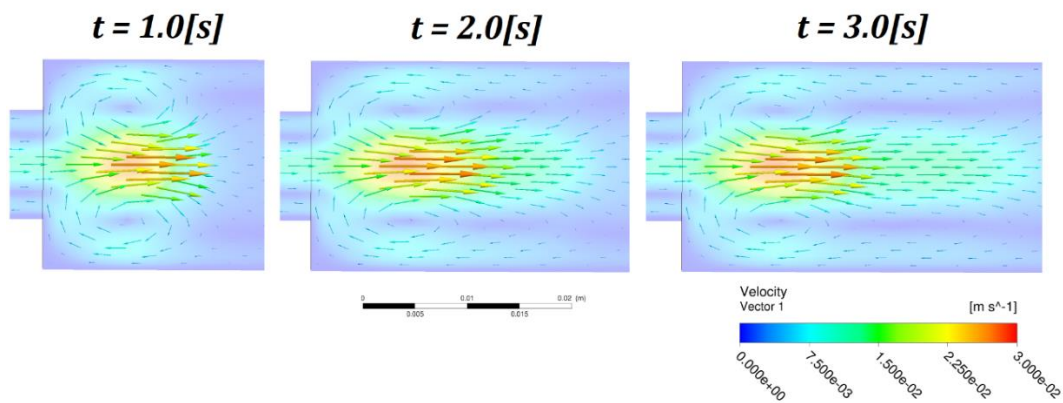
Fig. 6.7 - Depicted from left to right, the velocity vectors at the end of consecutive cycles. The vessel is truncated only for the purpose of visualization.

A vortex is created at the expansion during the 1st cycle by a traveling mass of fluid down the center. During the 2nd cycle, this mass of fluid has not fully dispersed and

another mass of fluid follows the first. This causes the vortex at the wall to elongate with subsequent cycles causing reversed flow further along the tube. As a result of this transport phenomenon, the flow pattern changes over time.

The main focus of this explorative study is on modelling the effect of a transiently transported coherent structure.

6.5.2. *Design of experiments & simulation*

Before being able to derive a reduced order model the question to be addressed is: What constitutes an optimal basis? In other words, an appropriate basis size needs to be determined and requirements regarding the training data used to construct the SVD basis need to be considered. In order to answer these questions, the design requirements of the reduced order model need to be considered.

The range $10[-] \leq Re_{max} \leq 100[-]$ was divided into increments of 10 resulting in 10 simulations. For each simulation a total simulation time of 2[s] was chosen comprising 2 flow cycles. A snapshot of pressure was then stored for the full domain every 10[ms]. This results in 200 snapshots generated per simulation which is considered to be the snapshot set for that simulation. For this purpose, a set of UDFs was utilized to save the pressure data originating from the solver in the appropriate vector format for snapshots.

For the current reduced order modelling approach 3 different scenarios were conceived to study the characteristics of the bases generated using either 2, 3 or 4 snapshot sets. The simulations chosen to train the data for each scenario are depicted in fig. 6.8 below:
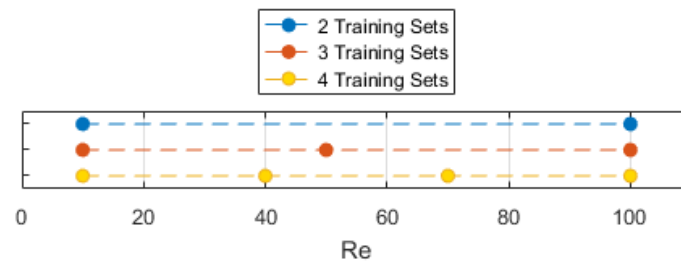
Fig. 6.8 - Datasets used for training indicated by colored dots for each training scenario

For the 2-training sets scenario, only the outermost points of the Re_{max} range are used for training and it is therefore assumed that these points will be best represented. For the remaining sets more points are picked in the interior of the chosen range to enrich the information contained in the SVD bases. The remainder of simulations for each scenario was then formally chosen as validation sets. However, as the goal is to study the behavior on the goal within the chosen range of Re_{max}, validation was carried out on all 10 datasets from simulation.

All 10 simulations were simulated and the pressure for all simulations is depicted below in fig. 6.9 to give an indication of the pressure scale of the simulations.
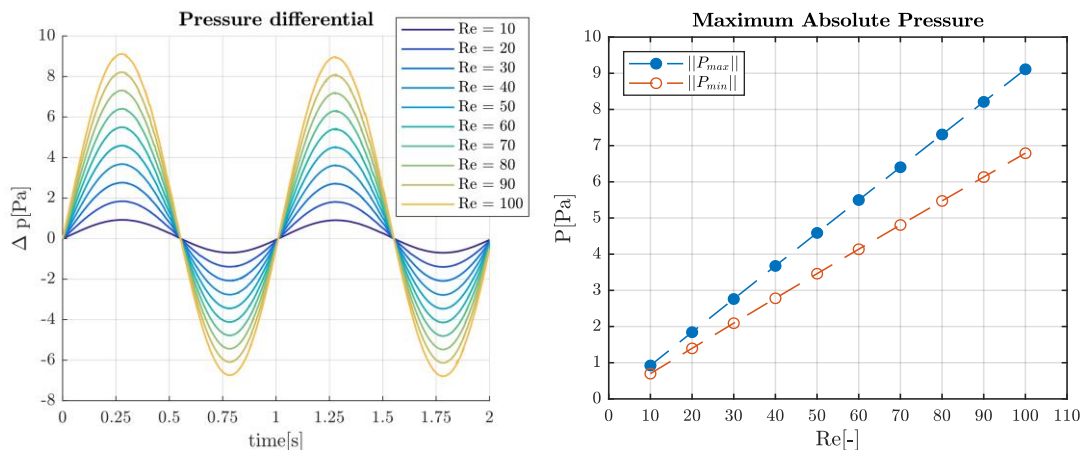
Fig. 6.9 - (left)Pressure differential for all simulations over time, (right)

Maximum pressure.

Due to the pulsatile behavior of the flow, the pressure differential from inlet to outlet is negative during the second half of a cycle to decelerate the flow. This means that there is a zero crossing with respect to pressure. Additionally, the absolute value of the maximum and minimum peak pressure was plotted against the Reynolds number demonstrating a linear relationship between them. This is a fair indicator that for this specific case the flow behavior at the lowest and highest Reynolds number is similar.

6.5.3. SVD basis characterisation

An SVD basis was generated for each of the 3 training scenarios and to assess the initial accuracy of the bases generated the Frobenius norm was calculated according to eq. 6.9. This norm describes the information present in the total dataset, that is not captured by a truncated SVD basis and as such can be used as an error estimate. The Frobenius norm is plotted below as a function of the basis size in fig. 6.10:
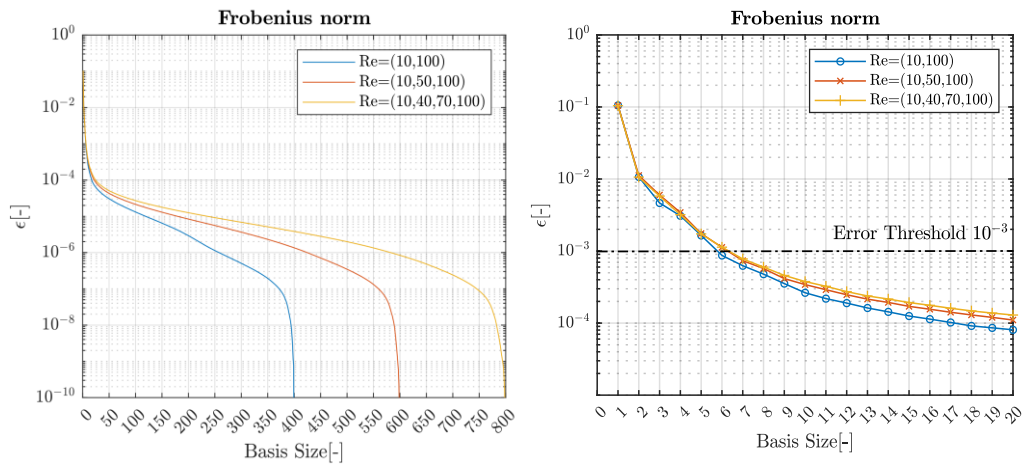
Fig. 6.10 - (left) Frobenius norm as a function of basis size up to the dimensionality of the training set, (right) Close-up view of Frobenius norm for basis size up to 20 modes

The basis size is described as the total number of modes considered, starting from mode 1 and ending at the maximum number of modes considerable for a training set. This maximum is equal to the rank of the snapshot matrix and therefore as large as the total number of snapshots constructed during simulation. On the left of figure 6.10 it can be noted that the information not captured by the SVD basis decreases rapidly as a function of basis size, up to approximately a basis size of 20 modes for all training scenarios. At this basis size the diminishment of the Frobenius norm resulting from increasing the basis size is minor. In other words, the higher order modes beyond mode 20 add relatively little information to the SVD basis and in effect either describe more detailed patterns in the pressure field for individual snapshots or simulation noise.

Furthermore, at a first eye's glance, the error appears to diminish faster for scenarios with fewer training sets. Although this seems counterintuitive, it is important to remember that the error norm compares the error with respect to information

content of the entire training set. On the right of figure 6.10 the error for a basis size below 20, diminishes in a similar pattern for all training sets. At a threshold of $\epsilon = 10^{-3}[-]$ it can be seen that 6 modes would be indicative of representing the scenario with 2 training sets acceptably, whereas 7 modes would be indicative for the other 2 scenarios.

The previous comparison between scenarios suffers from the difference in training set size of each scenario. In figure 6.11 the x-axis has been rescaled to represent the mode proportion which is defined as the basis size divided by the maximum basis size, i.e. the number of training snapshot available.
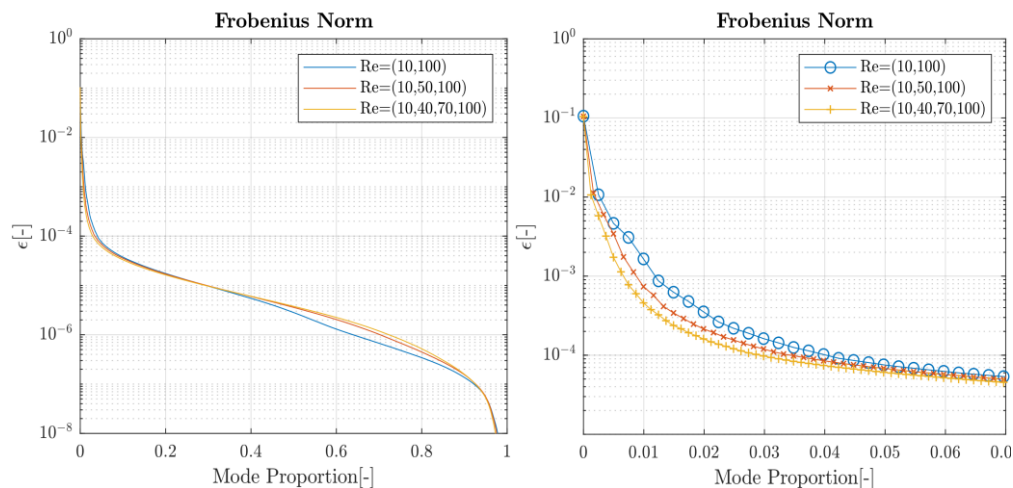
Fig. 6.11 - (left) Frobenius norm vs. mode proportion, defined as truncated basis size divided by number of training snapshots available. (right) close-up of first 7% of mode proportion

Show in the left of fig. 6.11, is that the error as a function of the mode proportion is not significantly different from one scenario to another for practical purposes. At the higher mode proportions above 0.5, the scenario with 2 learning set has a

marginally lower error at the log scale. This difference is negligible at an order of magnitude of $O(10^{-5})$. Additionally, it is expected that the number of modes required to represent the simulations within the Reynolds range is $O(10)$ which corresponds to a mode proportion of approximately 0.02 which is far below the 0.5 mode proportion.

In the right of fig. 6.11 it can be seen that the error decreases faster if the scenario contains more training sets. More modes are required to derive an SVD basis when there is more training data present. There is more variation in the pressure fields and part of this variation ends up inside of the base. After a basis has been derived however, a smaller proportion of modes is required to reach the same information content in the basis. This would indicate that relevant data is being added but additionally more data is added that is already similar to the basis.

Deriving the potential error in terms of the Frobenius norm is only relevant to the training set. In order to determine an error that's representative of new cases encountered in practice the projection error is determined for all simulated cases. In a real-life setting this step should be applied only to the validation cases. However, for our current application it is relevant to consider which cases are best represented by an SVD basis which includes the training cases. The two main methods of considering the projection error that are already implemented within the ROM builder environment are the absolute and the relative projection error.

The absolute projection error is simply the error in the quantity itself whereas the relative error was already defined in eq. 6.14. These 2 error measures are stated below:

$$\epsilon_{abs} = \|\overrightarrow{\varphi_{svd}}(t) - \overrightarrow{\varphi_{sim}}(t)\| \qquad \text{(Eq. 6.17)}$$

$$\epsilon_{rel} = \frac{\|\overrightarrow{\varphi_{svd}}(t) - \overrightarrow{\varphi_{sim}}(t)\|}{\|\overrightarrow{\varphi_{sim}}(t)\|} \qquad \text{(Eq. 6.18)}$$

Where $\overrightarrow{\varphi_{svd}}$ is the snapshot vector resulting from svd projection, $\overrightarrow{\varphi_{sim}}$ is the simulation data snapshot and $\|\cdot\|$ denotes the L$_2$ norm. As a more stringent measure the maximum absolute error with respect to time was also calculated for each point in time according to:

$$\epsilon_{max} = \max_{\vec{x}} \left(\overrightarrow{\varphi_\iota}(t) - \overrightarrow{\varphi_{\iota,p}}(t)\right) \qquad \text{(Eq. 6.19)}$$

This makes it possible to guarantee the maximum error for a case. However, the location and relevance of the maximum error in the domain is case dependent. For a basis comprising 6 modes the maximum absolute and relative error are presented below in fig. 6.12 for the scenario with 2-training sets available:
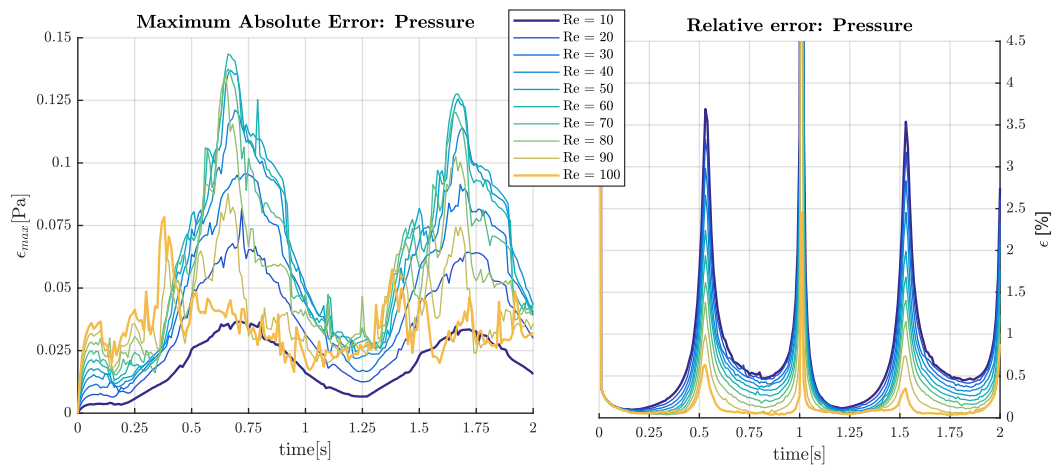
Fig. 6.12 - (left) Absolute error shows training sets exhibit lowest error compared to the validation sets. (right) Relative error shows higher accuracy for higher Reynolds number simulations

Most curves exhibit a maximum absolute error in pressure around 0.7[s]. This coincides with the time around which the flow decelerates the fastest. Additionally, at a maximum Reynolds number of $Re_{ma} = 10[-]$ and $Re_{max} = 100[-]$ the absolute error is amongst the lowest around this maximum in time. This indicates that the basis performs better for the training cases than for the validation cases as was expected.

However, the scale of the values of these 2 training sets is different as shown by the relative error implying that the relative accuracy is higher for the higher Reynolds cases. The training set $Re_{max} = 100[-]$ has the lowest relative error over time whereas the training set for $Re_{max} = 10[-]$ has the highest relative error. It can be seen that the relative error diminishes overall for increasing Reynolds numbers, indicating that the basis is in fact better at representing the higher Reynolds number

flows. An obvious shortcoming in the relative error representation of the pressure field are the error spikes around and just after $t = \{0.5, 1.0, 1.5, 2.0\}[s]$. When referring back to the pressure differential graph of fig. 6.9, it can be seen that these points coincide with the zero crossings of the signal. Therefore, the denominator of the relative error measure gets divided by a value approaching 0. A zero crossing is an often-occurring situation in biomedical settings as many phenomena are periodic. To accelerate and decelerate fluid flows, positive and negative pressure differentials are required respectively, and it is possible for backflow to occur in the vascular system. A different reference scale is chosen for each simulation equal to maximum pressure differential in absolute terms. All values are then divided by this reference, resulting in the scaled absolute error:

$$\epsilon_{sabs} = \frac{\max_{\vec{x}} \left(\overrightarrow{\varphi_i}(t) - \overrightarrow{\varphi_{i,p}}(t) \right)}{max(abs(P_{in} - P_{out}))} \qquad \text{(Eq. 6.17)}$$

In which P_{in} and P_{out} are the pressure at in- and outlet averaged over their respective boundaries. Fig. 6.13 demonstrates both the scaled absolute error for pressure as well as the average of the maximum absolute error as function of the Reynolds number. The scaled absolute error shows again that the accuracy of the simulations increases with increasing maximum Reynolds number without any anomalous spikes. The average of the maximum absolute error over time is shown on the right of figure 6.13 further exemplifying that in fact the case for $Re_{max} = 100[-]$ has a higher accuracy than some of the lower Reynolds number simulations even in the absolute sense.

However, when comparing the scaled absolute error with the relative error there is a significant percentual difference in magnitude. This was found to be due to the inlet flow which is prescribed as a plug flow with uniform velocity. This velocity creates a high-pressure gradient near the wall almost 4 times larger than values elsewhere in the flow. The pressure differential is a reference on a global scale instead of a local scale and does not take into account local deviations and anomalies in the flow. However, the maximum error is a local measure. Therefore, it is potentially better to consider the range of the pressure over time at the local level for each cell. Due to this anomaly the scaled absolute error defined in eq. 6.17 above, is disregarded for most of the remainder of this chapter. Additionally, the scale of the relative error is sufficiently small to effectively use as an error measure
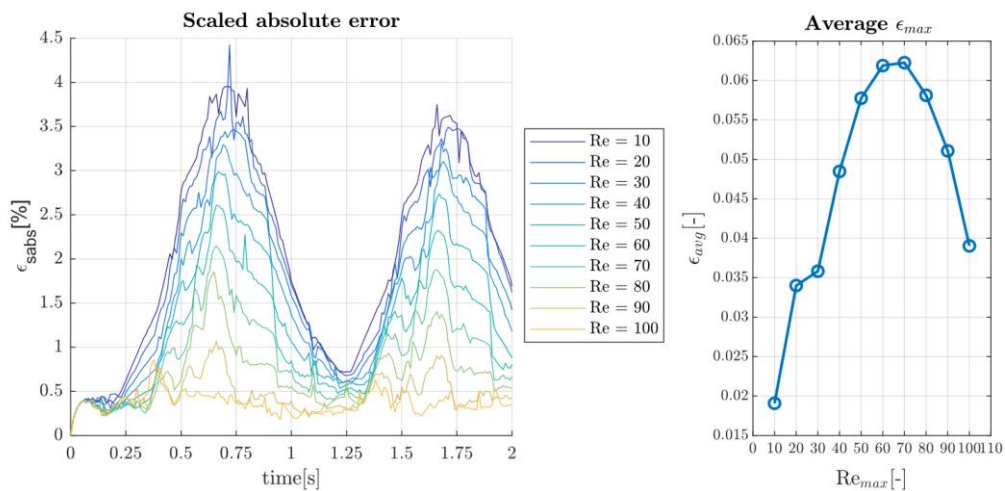
Fig. 6.13 - (left) Absolute error scaled to pressure reference of the flow showing the higher accuracy for higher Reynolds numbers, (right) average over time of maximum absolute error.

However, the message of this exercise is that a reference that relies on a global measure results in a normalised error that does not suffer from zero crossings in the data. A potential disadvantage of this approach is that the reference value needs to be manually chosen for every variable and is dependent on the purpose of the simulation. As an example, for velocity this reference can be the maximum absolute velocity.

This provides a means for examining the error for pressure projection back onto an SVD basis mitigating the effect of zero-crossings.

However, the previous discussion does not aid in the selection of a basis size or deciding criteria for training-set size. To consider basis size the error for the projection of the entire set is to be considered. Up to this point it was assumed that a choice of basis size 6 was sufficient.

6.5.4.   *Modal representation of basis*

After having gone through the SVD process a basis is derived. This basis can be visualized as each mode is a set of values that can be projected back on the original computational mesh. These basis images are shown below in fig. 6.14 for the scenario containing 3-training sets:
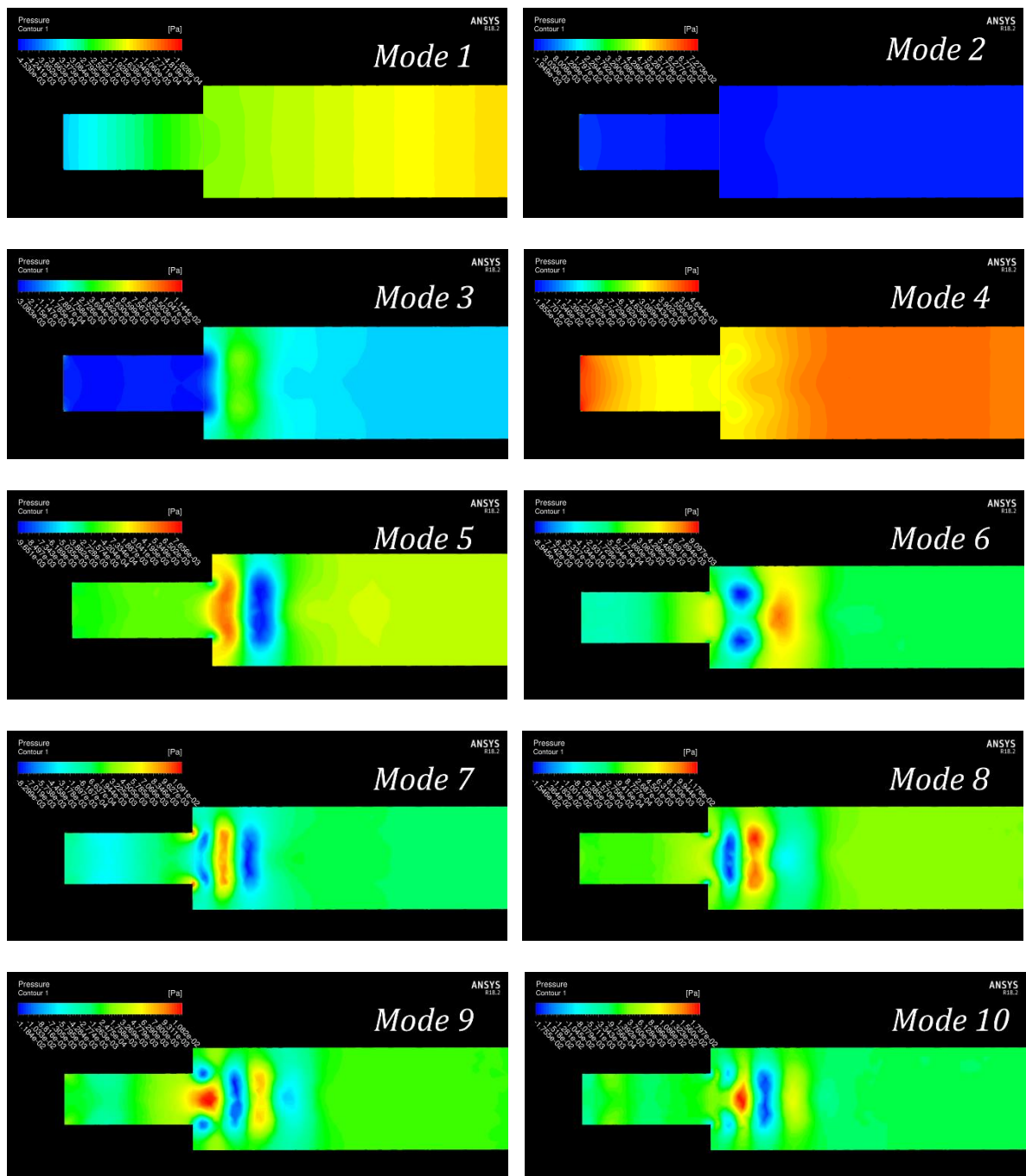
Fig. 6.14 - The first 10 modes of the pressure field for the sudden expansion from the 3-training set scenario demonstrating their distribution in the geometry.

As the mode numbers correspond to the ordering of their singular values, they are ordered with respect to the amount of variation they account for within the model.

Mode 1 can be associated with the mean pressure in the domain whereas other higher order modes can often not be attributed to have specific characteristics. Mode 2 appears to account for relatively little variation within the model besides a slight pressure drop around the expansion. However, upon closer inspection it can be seen that the highest values for this mode occur at a small area near the wall of the inlet. As mentioned before, the pressure near the wall at the inlet is approximately much higher than elsewhere in the flow, at approximately 4 times the magnitude. As a result, the variability in this small portion of all cells gets a high importance attributed by the SVD process and is heavily present in modes 2, 3 and 4.

When regarding the higher modes of the system there are many interesting features contained within the pressure field. The most apparent features are the appearance of nodules of increasingly smaller dimensions. These features are used to describe increasingly smaller details of the flow in those areas. As seen in fig. 6.7 the strongest flow effects occur around the expansion itself but over time more features are required downstream of the expansion as the flow gets transported. The vortex that is generated at the expansion itself remains the primary feature as it returns in every flow cycle. A similar pattern occurs in other decompositions as for instance in a Fourier description. Higher order modes in a Fourier decomposition imply higher wave numbers and therefore contribute to smaller patterns in a spatial field. As demonstrated below, the strength of modes derived through SVD is that they

represent patterns present in the flow itself and might therefore require far fewer modes.

6.5.5. Vector normalization

As observed in the previous sections, applying an SVD to a set of snapshots with different characteristic scales, results in a basis that favors snapshots with higher characteristic scales. For the pressure field of the sudden expansion that implies that the simulation snapshots for $Re_{max} = 100[-]$ are favored in the singular value decomposition. In many situations the SVD is useful because of this characteristic as it provides a ranking of importance of the snapshots by their corresponding singular values. While in the current setting it allows compression of the output space it also leads to a reduction in the relative accuracy of the solution at the lower Reynolds numbers. These simulations are independent from each other and it can be argued that the results at lower Reynolds numbers should be just as accurate as those at higher Reynolds numbers. If the results are bad at the low Reynolds number why should they be included in the working range of the model?

As an attempt to remedy this scale dependent accuracy the snapshots used in training the SVD basis are normalized beforehand. This removes the scale difference between snapshots and leads to the principal directions of the data being determined by local field patterns. As the snapshots are 1D vectors, they can be normalized by dividing them by their L$_2$ norm:

$$\boldsymbol{X}_{norm} = \boldsymbol{XF} = \boldsymbol{X}diag\left(\frac{1}{\|X_1\|}, \frac{1}{\|X_2\|}, \cdots, \frac{1}{\|X_n\|}\right) \qquad \text{(Eq. 6.18)}$$

With $\boldsymbol{X}_{norm}$ being the normalised snapshot matrix, $\boldsymbol{X}$ the original snapshot matrix and $\boldsymbol{F}$ the normalization matrix. Snapshot matrix $\boldsymbol{X}$ can also be represented by the full rank SVD decomposition leading to:

$$\boldsymbol{X}_{norm} = \boldsymbol{X}\boldsymbol{F} = (\boldsymbol{U}\boldsymbol{\Sigma}\boldsymbol{V}^*)\boldsymbol{F} = \boldsymbol{U}\boldsymbol{\Sigma}(\boldsymbol{V}^*\boldsymbol{F}) \qquad \text{(Eq. 6.19)}$$

Therefore, a basis for $\boldsymbol{X}$ is also a valid basis for $\boldsymbol{X}_{norm}$ and vice versa. Fig. 6.15 below shows the comparison between the information captured in the SVD bases for both the regular snapshots and the normalised snapshots as a function of basis size. As the training sets are of equal size for both scenarios it is not necessary to consider the Frobenius norm as a function of mode proportion. A training-set size of 3 was used comprising the Reynolds range $Re_{max} = \{10,50,100\}[-]$.
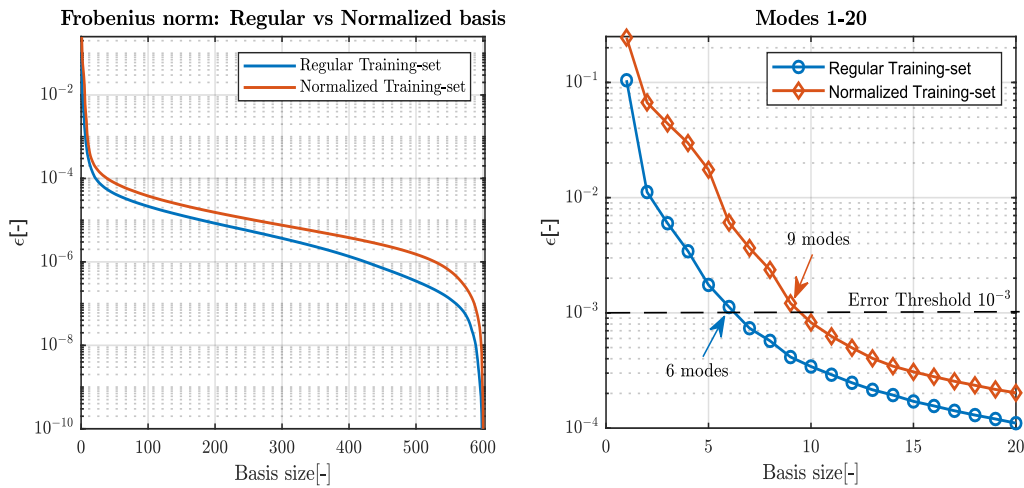
Fig. 6.15: Frobenius norm depicted for the full basis(left) and for the first 20 modes(right).

For the normalized training set scenario, the error as measured by the Frobenius norm converges slower as the number of modes considered increases. A higher

error at equal basis size would indicate that a basis derived from a set of normalized vector performs worse than using the regular vectors. However, referring back to the definition of the Frobenius norm in eq. 6.9 it can be seen that the higher error means that the differences between singular values has become smaller. As the full rank bases for both methods contain the same amount of information this indicates that the information in the normalized training-sets scenario has been distributed over more modes compared to the regular training-sets scenario. At an error threshold of $10^{-3}[-]$ it can be seen that 6 modes would need to be considered for the regular training set scenario, whereas 9 modes would have to be considered for the normalized training sets. In order to determine how the basis performs for both the training and validation data a projection of the data on the SVD basis is performed. This is shown below in Fig. 6.16 for a basis containing 6 modes.
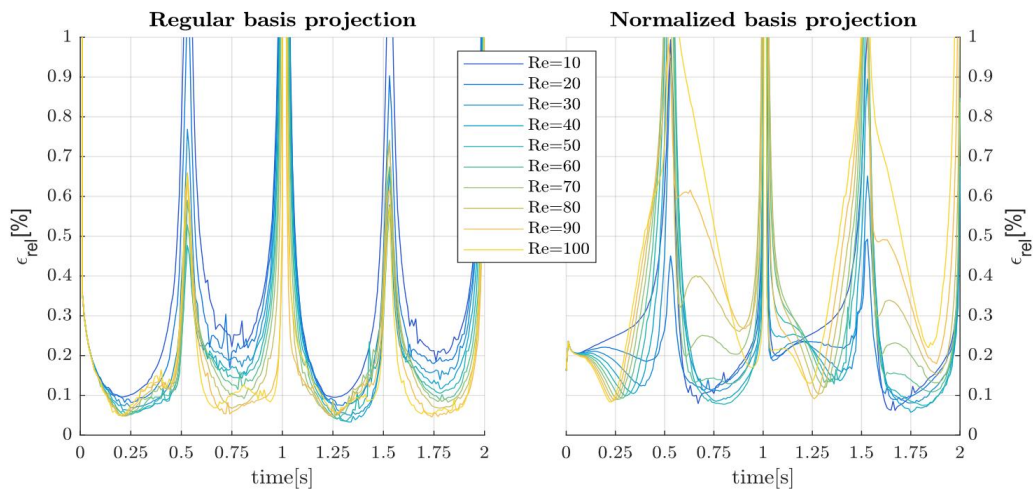
Fig. 6.16: (left) Relative error for a training set of regular snapshots is lower compared to training set of normalized snapshots(right) for equal basis size of 6.

The error is of similar scale but it can be seen that for the high Reynolds the basis performs slightly worse for the normalized vector training set scenario as compared to the regular vector training set scenario. This is supported by average error over time and the range of Reynolds numbers, at an average error of 0.39% using the regular vector training set for a basis and 0.45% for the normalized vector training set.

The same exercise was repeated for a basis containing 9 modes including a calculation of the average error which was 0.28% and 0.15% for the regular vector and normalized vector training sets bases respectively.
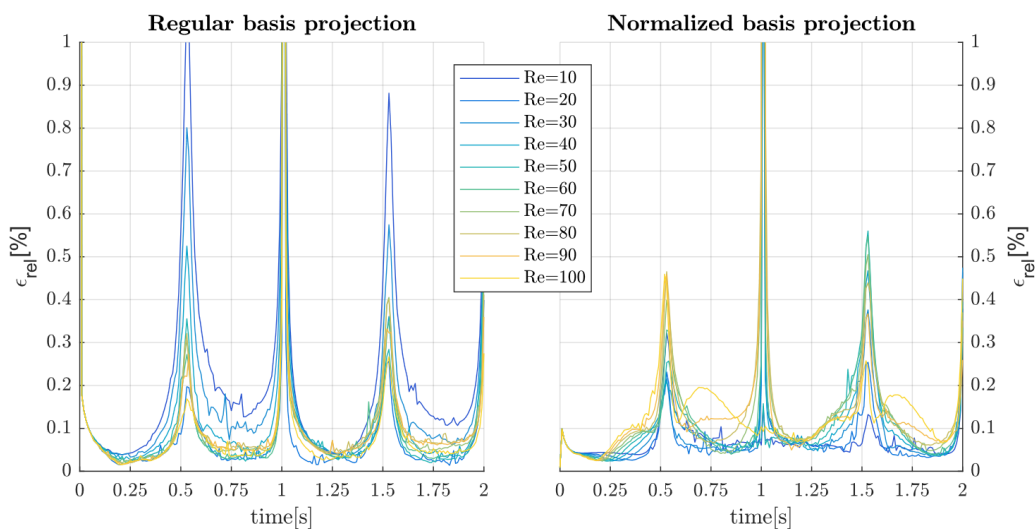
Fig. 6.17 - (left) Relative error for a training set of regular snapshots is higher compared to training set of normalized snapshots(right) for equal basis size of 9.

Partially this diminished average error using normalized vectors, is due to the peaks being lower during the phases of 0 pressure. This reduction implies that the cases are better represented during these phases of the flow. This is not completely

unsurprising as snapshots with low reynolds number flow even compared to Re_{max} within individual simulations now have the same magnitude as those at Re_{max}.

Qualitatively, it can also be remarked that the error for the higher reynolds numbers has gone up slightly but the error for the lower reynolds numbers has diminished. At this scale of the error it is debatable that this diminished error has any effect on the model outcome. However, the normalized basis vectors approach results in a basis that performs marginally better compared to the use of regular training vectors.

Lastly, the basis vectors derived from normalized training vectors are visualised below in fig. 6.18. The first 2 modes are very similar to those derived using regular training vectors. However, the patterns for the other modes are not comparable between the regular and normalized approach. This by itself is not surprising as multiple basis representations are possible for the same space. However, compared to the Basis derived from regular training vectors, more of the modes below seem to better resemble the size and shape of the vortex created after the expansion. However, more analyses are required to describe the functional difference between the two descriptions.
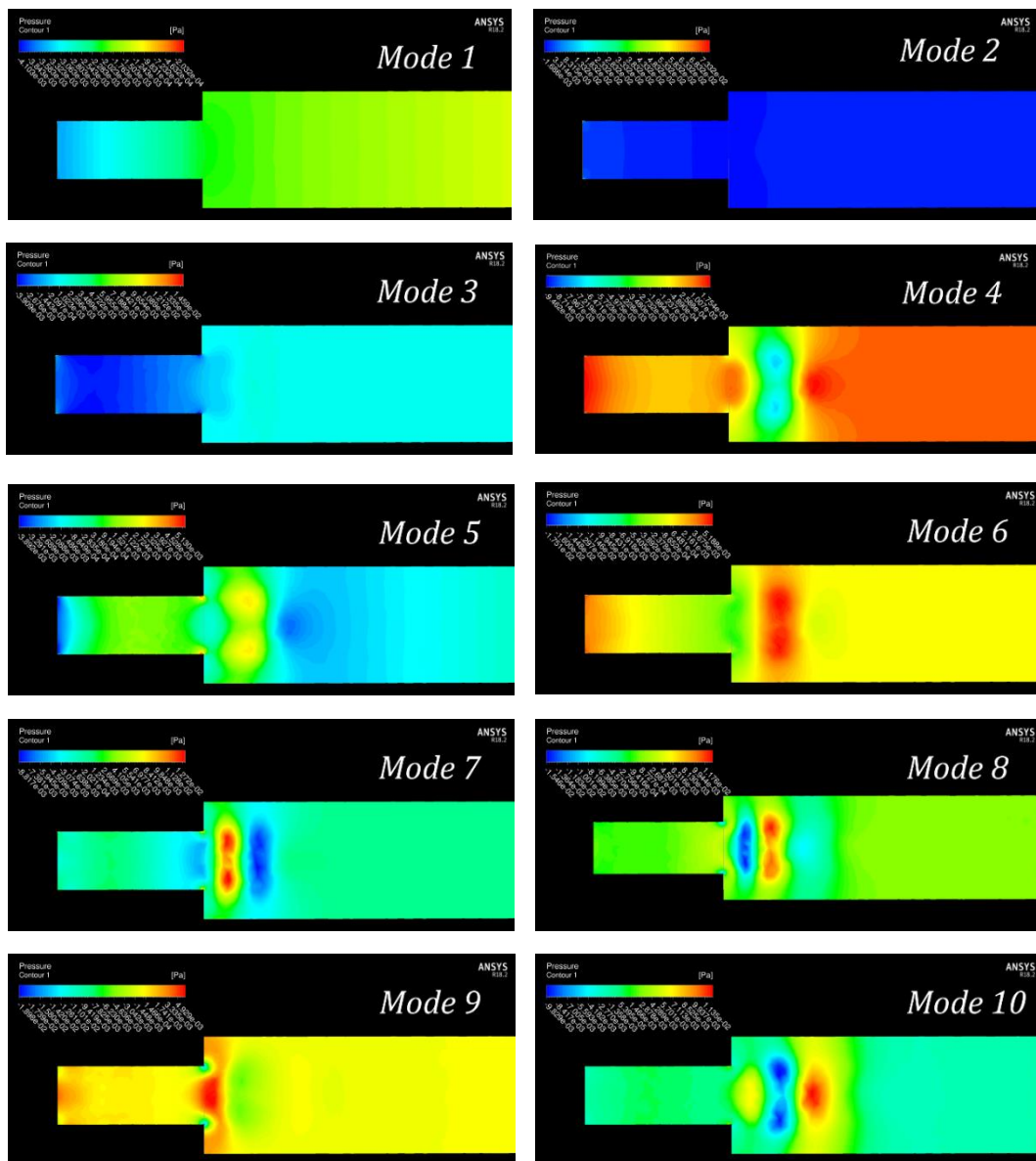
Fig. 6.18 - The first 10 modes of the pressure field for the sudden expansion from

the 3-training set scenario from normalized training data.

6.6. Transient Reduced order model

Lastly a reduced order model was trained within the working range of the parameter

space of the model, i.e. a single parameter $10 \leq Re_{max} \leq 100$. For this purpose,

the reduced basis resulting after the vector normalisation was used. The ROM was

subsequently compared to the FOM by calculating the average error over time for all signals and subsequently calculating the minimum, maximum and average error over all Re_{max} in the working range for a given basis size. The results of this training stage can be observed in fig. 6.19 below:
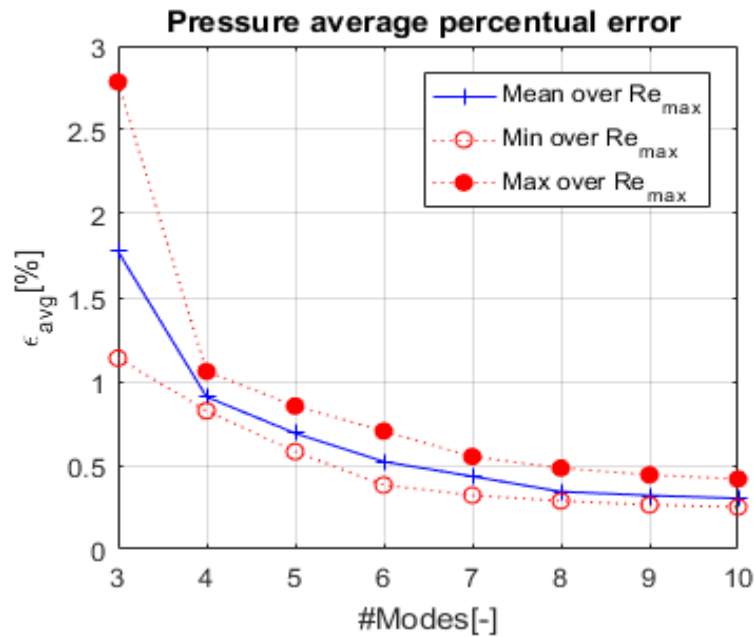
Fig 6.19 - Average percentual ROM error given the basis size as number of modes. For a basis size of 4 modes, the overall average error goes below 1%.

At the previously chosen basis size of 9 modes from the SVD process, it can be seen that the average percentual error is below 0.45[%]. Additionally, it was remarked upon close inspection that the maximum absolute percentual error of the ROM was below 4[%] for all values of Re_{max} within the range.

The offline training phase of the model is in the order of minutes once the simulation data has been acquired from the traditional Fluent simulation. Data

acquisition from Fluent is in the order of hours while it was observed that the evaluation of the ROM given an input parameter is of the order of seconds, depending on the computer used for evaluation. As such a speedup of approximately 99,9% is achieved for the end-user of the ROM.

6.7. Discussion

In this chapter the concept of steady-state and transient ROM generation using ANSYS ROM builder has been explored. The steady-state ROM example demonstrated that different modes represent different physical effects. A similar statement can be made regarding the transient ROM, although the relationship between modes is more complex and far less intuitive due to its transient characteristics.

In the current study the steady-state example effectively only serves to highlight the process of SVD decomposition. No ROM has been made in this case as it is not expected to be clinically relevant in many cases. Cardiovascular flow has pulsatile characteristics in the large arteries and only steady-state characteristics in smaller arteries. It is not unthinkable to define steady-state models even for highly time dependent flows as for example considering all flows at a similar characteristic time in a cardiac cycle. However, it is expected that most of the testcases for cardiovascular flow merit transient ROM generation.

For the transient ROM generation process an attempt was made to analyse the required amount of training data and the required number of modes for SVD basis

generation. The general answer to these questions seems to be that it depends on the basis requirements. Both the available training data and the number of modes determine what behaviour can be represented given the reduced basis. For the current study a choice was made to favour similar performance for all testcases in the Reynolds number range. This is a scenario where it is assumed that every point in the input parameter space is equally important. Were this not the case, then question that arises in our study is: If some points in the input parameter space are less important, why simulate those points at all?

Continuing this approach further effort was made to remove the scale difference between simulations as this scale is favoured in SVD basis generation. This increased the required basis size, but the resulting basis is ultimately more capable of representing the feature space.

Lastly, a ROM was derived for the pressure of the sudden expansion. While this model might not be accurate enough for all engineering purposes, at an average error below 0.45[%] it is arguably more than sufficient to be useful for qualitative or explorative analyses in clinical practice. Where necessary, a FOM simulation can be carried out after an explorative analysis if the ROM analysis is not deemed sufficient for particular cases.

 Future work includes repeating the reduced order modelling process described above for the 3D vector velocity field. An explorative study was carried out

revealing that the velocity field shows bigger spatial variation. As a result, more modes are required for the reduced basis and the estimated number for this specific setup is approximately 20 modes. However, a formal analysis and results have not been included and remain as future work.

Additional future work includes automation of training set size and basis size. Selection. For reduced order modelling techniques to be relevant in clinical practice it is required that someone trains and runs these models. In the humble opinion of the author, the number of specialisms required in order to start from patient-specific data collection, go through all clinical and engineering steps and manually arrive at a patient-specific reduced order model are not practically manageable for a single person. Therefore, either specialised simulation personnel should be present in the clinic or some steps in the full process need some form of automation.

Chapter 7

7. Conclusions

7.1. Conclusions and future work

The modelling of cardiovascular physics has had a very rich history for centuries and potentially some time to come. Whereas studies in the past might have started out only out of pure interest for some, it is recognised evermore that there is a significant potential to make a difference in the day to day clinical work. However, the physics involved are complex due to its Multiphysics and Multiscale nature which has led to many technical and academic advances in the last 50 years but few translational projects of significant value. Additionally, the advances in availability of computational power are a relatively new phenomenon which are only just now starting to open up opportunities outside of research centres. This thesis has sought to address some of the aspects that can create hurdles along the way to translate academic research to clinically relevant implementations. Model order reduction can greatly aid this translation

Chapters 2 to 4 are very closely interconnected and seek to address the problems in assigning proper boundary conditions. In the opinion of the author, proper specification of boundary conditions is one of the main problems to perform accurate simulations for cardiovascular systems.

The first hurdle that occurs is : "How do we obtain sufficient patient-specific data to feed our models?" Often this question is phrased as : "Given a certain data set, what is the best cardiovascular simulation we can possibly perform?". Chapter 2 seeks to highlight that perhaps both phrasings of the question are important, i.e. it

is important to both seek what can be done with currently collected data but perhaps as important, to seek what data should be collected in the future and how, in order to add more value. It is absolutely crucial that a 2-way dialogue exists between researchers and clinicians. The clinical data used in chapter 2 was not measured with enough rigor to be of direct use in prescribing boundary conditions. However, in a real clinical setting pressure measurements are not available and often many data uncertainties exist that are clearly out of the control of anyone performing the measurements.

It is readily acknowledged that multiscale modelling approaches to represent BCs is a more consistent and more successful approach. The WK models were introduced in chapter 3 as the simplest lumped parameter model for the purpose. It can be parameterised using patient-specific data and some simple model assumptions but the details of this are not explicitly treated in this thesis. However, an attempt was made to provide an efficient open-source implementation of the models to prevent researchers having to implement their own novel version for every study design. In addition, considerations are given with regards to accuracy as a function of the time-step, as often these considerations are lacking in most studies. Chapter 3 explored the error introduced solely by the coupling of the windkessel to aid in future decision making of other researchers seeking to use the model.

Chapter 4 then goes into the stability of model coupling in general. In a research or academic setting, it is often doable to troubleshoot simulations by hand and by the grace of the extensive knowledge of the researcher. Model parameters can be changed, time-step size and mesh element density can be explored, etc. However, in a clinical setting this is impractical if not impossible due to the sheer volume of cases and the different specialties that clinicians compared to researchers.

Having stable model couplings reduces the efforts to translate models to a clinical setting significantly. The main result of chapter 4 is suggestion of a central difference coupling for all couplings in a multiscale approach where the considered time integration is relevant and is potentially relevant for increased stability in FSI simulations. However, the current study only addresses the subject for lumped parameter models and future work is required to explore central difference couplings in multiscale workflows. Additionally, future work includes a more rigorous energy analysis to explore the mechanism behind the implicit instability as this occurs in many settings.

Fluid-structure interactions are highly relevant for simulations of the large arteries. However, a partitioned approach requires iterations between a fluid and structural model often inflating the computational cost tenfold. Therefore, a closer look was taken at the compressible fluid model by Brown [72], capable of running at significantly reduced cost, in order to try and improve the model's accuracy. While a possible way of improving on the model was found, it was not implemented under

the current work and this would be the most immediate future work: To implement an additional correction term and explore the usefulness of the method in more clinically relevant cases.

Lastly and potentially one of the most interesting novel avenues is the reduced order modelling approach described in chapter 6. Different data requirements from simulation were considered to obtain a reduced basis representation of the pressure field and train a reduced order model with relative success. A sudden expansion is a very harsh transition that does not occur in the human body but serves as a case for transportable large coherent structures. These can occur in the cardiovascular system therefore making this model relevant and it is highly relevant in other engineering fields, for example in aeronautics.

There is a large body of future work for this subject as mentioned in the chapter discussion. The most immediate future work being a repetition of the process for 3D velocity fields. Pressure and velocity are the main quantities of interest in any CFD study. It is expected that the velocity field features are more complex and therefore are more difficult to represent bringing with it potentially different considerations with regard to training data. But in order to use these models in practice, some recommendations or automation with regards to training data requirements should exist. Subsequently, an attempt should be made to apply these techniques to more realistic vessels, to explore what can already be done for model order reduction for cardiovascular flows.

Bibliography

[1] E. J. Benjamin, P. Muntner and S. S. e. al., "Heart Disease and Stroke Statistics—2019 Update: A Report From the American Heart Association," *Circulation,* vol. 139, 3 2019.

[2] M. Nichols, N. Townsend, R. Luengo-Fernandez, J. Leal, A. Gray, P. Scarborough and M. Rayner, european cardiovascular disease statistics 2012, European Heart Network, Brussels, European Society of Cardiology, Sophia Antipolis, 2012.

[3] A. Timmis, N. Townsend and S. Logstrup, "European Society of Cardiology: Cardiovascular Disease Statistics 2017," *European Heart Journal,* vol. 39, pp. 508-579, 11 2017.

[4] M. McClellan, N. Brown, R. M. Califf and J. J. Warner, "Call to Action: Urgent Challenges in Cardiovascular Disease: A Presidential Advisory From the American Heart Association," *Circulation,* vol. 139, 2 2019.

[5] H. M. Krumholz, S.-L. T. Normand and Y. Wang, "Trends in Hospitalizations and Outcomes for Acute Cardiovascular Disease and Stroke, 1999–2011," *Circulation,* vol. 130, pp. 966-975, 9 2014.

[6] S. M. K. E. N. Marieb, Essentials of Human Anatomy & Physiology, Global Edition, Pearson, 2017.

[7] C. Vlachopoulos, M. O'Rourke and W. W. Nichols, McDonald's Blood Flow in Arteries, Taylor & Francis Ltd., 2011.

[8] D. H. Bergel, "The dynamic elastic properties of the arterial wall," *The Journal of Physiology,* vol. 156, pp. 458-469, 5 1961.

[9] J. B. Cheung and C. C. Hsiao, "Nonlinear anisotropic viscoelastic stresses in blood vessels," *Journal of Biomechanics,* vol. 5, pp. 607-619, 11 1972.

[10] Y.-C. Fung, Biomechanics, Springer New York, 1993.

[11] E. L. Bradley and J. Sacerio, "The velocity of ultrasound in human blood under varying physiologic parameters," *Journal of Surgical Research,* vol. 12, pp. 290-297, 4 1972.

[12] "Determinants of pulse wave velocity in healthy people and in the presence of cardiovascular risk factors: `establishing normal and reference values'," *European Heart Journal,* vol. 31, pp. 2338-2350, 6 2010.

[13] G. G. Belz, "Elastic properties and Windkessel function of the human aorta," *Cardiovascular Drugs and Therapy,* vol. 9, pp. 73-83, 2 1995.

[14] V. M. Barodka, B. L. Joshi, D. E. Berkowitz, C. W. Hogue and D. Nyhan, "Implications of Vascular Aging," *Anesthesia & Analgesia,* vol. 112, pp. 1048-1060, 5 2011.

[15] N. A. Shirwany and M.-h. Zou, "Arterial stiffness: a brief review," *Acta Pharmacologica Sinica,* vol. 31, pp. 1267-1276, 8 2010.

[16] S. Glasser, "Vascular Compliance and Cardiovascular Disease A Risk Factor or a Marker?," *American Journal of Hypertension,* vol. 10, pp. 1175-1189, 10 1997.

[17] G. D. Santis, P. Mortier, M. D. Beule, P. Segers, P. Verdonck and B. Verhegghe, "Patient-specific computational fluid dynamics: structured mesh generation from coronary angiography," *Medical & Biological Engineering & Computing,* vol. 48, pp. 371-380, 2 2010.

[18] A. G. Brown, Y. Shi, A. Marzo, C. Staicu, I. Valverde, P. Beerbaum, P. V. Lawford and D. R. Hose, "Accuracy vs. computational time: Translating aortic simulations to the clinic," *Journal of Biomechanics,* vol. 45, pp. 516-523, 2 2012.

[19] M. Zhou, O. Sahni, H. J. Kim, C. A. Figueroa, C. A. Taylor, M. S. Shephard and K. E. Jansen, "Cardiovascular flow simulation at extreme scale," *Computational Mechanics,* vol. 46, pp. 71-82, 12 2009.

[20] T. W. Secomb, "Hemodynamics," *Compr Physiol.,* vol. 6(2), p. 975–1003, 2017.

[21] P. D. Morris, A. Narracott, H. Tengg-Kobligk, D. A. S. Soto, S. Hsiao, A. Lungu, P. Evans, N. W. Bressloff, P. V. Lawford, D. R. Hose and J. P. Gunn, "Computational fluid dynamics modelling in cardiovascular medicine," *Heart,* vol. 102, pp. 18-28, 10 2015.

[22] F. M. White, Fluid Mechanics, McGraw-Hill Education - Europe, 2015.

[23] O. Reynolds, Papers on Mechanical and Physical Subjects Volume 3; The Sub-Mechanics of the Universe, Cambridge University Press, 1903.

[24] W. H.K. Versteeg, An Introduction to Computational Fluid Dynamics, Pearson education limited, 2007.

[25] J. N. Reddy, An Introduction to the Finite Element Method, McGraw-Hill, 2006.

[26] Mechanical APDL, Theory Reference, ANSYS, 2019.

[27] Y. Zhang, V. H. Barocas, S. A. Berceli, C. E. Clancy, D. M. Eckmann, M. Garbey, G. S. Kassab, D. R. Lochner, A. D. McCulloch, R. T. Son-Tay and N. A. Trayanova, "Multi-scale Modeling of the Cardiovascular System: Disease Development, Progression,

and Clinical Intervention," *Annals of Biomedical Engineering,* vol. 44, pp. 2642-2660, 5 2016.

[28] R. Chabiniok, V. Y. Wang, M. Hadjicharalambous, L. Asner, J. Lee, M. Sermesant, E. Kuhl, A. A. Young, P. Moireau, M. P. Nash, D. Chapelle and D. A. Nordsletten, "Multiphysics and multiscale modelling, data–model fusion and integration of organ physiology in the clinic: ventricular cardiac mechanics," *Interface Focus,* vol. 6, p. 20150083, 4 2016.

[29] A. Quarteroni and A. Veneziani, "Analysis of a Geometrical Multiscale Model Based on the Coupling of ODE and PDE for Blood Flow Simulations," *Multiscale Modeling & Simulation,* vol. 1, pp. 173-195, 1 2003.

[30] N. Westerhof, F. Bosman, C. J. D. Vries and A. Noordergraaf, "Analog studies of the human systemic arterial tree," *Journal of Biomechanics,* vol. 2, pp. 121-143, 5 1969.

[31] M. Anliker, R. L. Rockwell and E. Ogden, "Nonlinear analysis of flow pulses and shock waves in arteries," *Zeitschrift für angewandte Mathematik und Physik ZAMP,* vol. 22, pp. 217-246, 3 1971.

[32] F. Migliavacca, R. Balossino, G. Pennati, G. Dubini, T.-Y. Hsia, M. R. Leval and E. L. Bove, "Multiscale modelling in biofluidynamics: Application to reconstructive paediatric cardiac surgery," *Journal of Biomechanics,* vol. 39, pp. 1010-1020, 1 2006.

[33] H. J. Kim, I. E. Vignon-Clementel, C. A. Figueroa, J. F. LaDisa, K. E. Jansen, J. A. Feinstein and C. A. Taylor, "On Coupling a Lumped Parameter Heart Model and a Three-Dimensional Finite Element Aorta Model," *Annals of Biomedical Engineering,* vol. 37, pp. 2153-2169, 7 2009.

[34] S. Sankaran, M. E. Moghadam, A. M. Kahn, E. E. Tseng, J. M. Guccione and A. L. Marsden, "Patient-Specific Multiscale Modeling of Blood Flow for Coronary Artery Bypass Graft Surgery," *Annals of Biomedical Engineering,* vol. 40, pp. 2228-2242, 4 2012.

[35] A. Krishnamurthy, C. T. Villongco, J. Chuang, L. R. Frank, V. Nigam, E. Belezzuoli, P. Stark, D. E. Krummen, S. Narayan, J. H. Omens, A. D. McCulloch and R. C. P. Kerckhoffs, "Patient-specific models of cardiac biomechanics," *Journal of Computational Physics,* vol. 244, pp. 4-21, 7 2013.

[36] H. Gao, Q. Long, S. K. Das, J. Halls, M. Graves, J. H. Gillard and Z.-Y. Li, "Study of carotid arterial plaque stress for symptomatic and asymptomatic patients," *Journal of Biomechanics,* vol. 44, pp. 2551-2557, 9 2011.

[37] P. D. Morris, D. Ryan, A. C. Morton, R. Lycett, P. V. Lawford, D. R. Hose and J. P. Gunn, "Virtual Fractional Flow Reserve From Coronary Angiography: Modeling the

Significance of Coronary Lesions," *JACC: Cardiovascular Interventions,* vol. 6, pp. 149-157, 2 2013.

[38] B. T. Tang, C. P. Cheng, M. T. Draney, N. M. Wilson, P. S. Tsao, R. J. Herfkens and C. A. Taylor, "Abdominal aortic hemodynamics in young healthy adults at rest and during lower limb exercise: quantification using image-based computer modeling," *American Journal of Physiology-Heart and Circulatory Physiology,* vol. 291, pp. H668--H676, 8 2006.

[39] C. A. Taylor and C. A. Figueroa, "Patient-Specific Modeling of Cardiovascular Mechanics," *Annual Review of Biomedical Engineering,* vol. 11, pp. 109-134, 8 2009.

[40] U. Morbiducci, D. Gallo, D. Massai, F. Consolo, R. Ponzini, L. Antiga, C. Bignardi, M. A. Deriu and A. Redaelli, "Outflow Conditions for Image-Based Hemodynamic Models of the Carotid Bifurcation: Implications for Indicators of Abnormal Flow," *Journal of Biomechanical Engineering,* vol. 132, 8 2010.

[41] U. Morbiducci, R. Ponzini, D. Gallo, C. Bignardi and G. Rizzo, "Inflow boundary conditions for image-based computational hemodynamics: Impact of idealized versus measured velocity profiles in the human aorta," *Journal of Biomechanics,* vol. 46, pp. 102-109, 1 2013.

[42] D. Gallo, G. D. Santis, F. Negri, D. Tresoldi, R. Ponzini, D. Massai, M. A. Deriu, P. Segers, B. Verhegghe, G. Rizzo and U. Morbiducci, "On the Use of In Vivo Measured Flow Rates as Boundary Conditions for Image-Based Hemodynamic Models of the Human Aorta: Implications for Indicators of Abnormal Flow," *Annals of Biomedical Engineering,* vol. 40, pp. 729-741, 10 2011.

[43] G. S. Stergiou, G. Parati, C. Vlachopoulos, A. Achimastos, E. Andreadis, R. Asmar, A. Avolio, A. Benetos, G. Bilo, N. Boubouchairopoulou, P. Boutouyrie, P. Castiglioni, A. Sierra, E. Dolan, G. Head, Y. Imai, K. Kario, A. Kollias, V. Kotsis, E. Manios, R. McManus, T. Mengden, A. Mihailidou, M. Myers, T. Niiranen, J. E. Ochoa, T. Ohkubo, S. Omboni, P. Padfield, P. Palatini, T. Papaioannou, A. Protogerou, J. Redon, P. Verdecchia, J. Wang, A. Zanchetti, G. Mancia and E. O'Brien, "Methodology and technology for peripheral and central blood pressure and blood pressure variability measurement," *Journal of Hypertension,* vol. 34, pp. 1665-1677, 9 2016.

[44] T. Müller, "Two dimensional and four dimensional hemodynamic and motion of the thoracic aorta - functional investigations prior to thoracic endovascular aortic repair," 2013.

[45] A. Volk and C. J. Kähler, "Density model for aqueous glycerol solutions," *Experiments in Fluids,* vol. 59, 4 2018.

[46] E. LÉVÊQUE, F. TOSCHI, S. H. A. O. L. and J.-P. BERTOGLIO, "Shear-improved Smagorinsky model for large-eddy simulation of wall-bounded turbulent flows," *Journal of Fluid Mechanics,* vol. 570, pp. 491-502, 1 2007.

[47] J. Blazek, "Turbulence Modeling," in *Computational Fluid Dynamics: Principles and Applications*, Elsevier, 2015, pp. 213-252.

[48] J. SMAGORINSKY, "GENERAL CIRCULATION EXPERIMENTS WITH THE PRIMITIVE EQUATIONS," *Monthly Weather Review,* vol. 91, pp. 99-164, 3 1963.

[49] W. L. Oberkampf and T. G. Trucano, "Verification and validation in computational fluid dynamics," *Progress in Aerospace Sciences,* vol. 38, pp. 209-272, 4 2002.

[50] O. Frank, "Die Grundform des Arteriellen Pulses," *Zeitschrift für Biologie 37, 483-526,* 1899.

[51] N. Westerhof, J.-W. Lankhaar and B. E. Westerhof, "The arterial Windkessel," *Medical & Biological Engineering & Computing,* vol. 47, pp. 131-141, 6 2008.

[52] Y. Shi, P. Lawford and R. Hose, "Review of Zero-D and 1-D Models of Blood Flow in the Cardiovascular System," *BioMedical Engineering OnLine,* vol. 10, p. 33, 2011.

[53] J. Hron and S. Turek, A Monolithic FEM/Multigrid Solver for an ALE Formulation of Fluid-Structure Interaction with Applications in Biomechanics, Springer Berlin Heidelberg, 2006, pp. 146-170.

[54] M. Heil, "An efficient solver for the fully coupled solution of large-displacement fluid–structure interaction problems," *Computer Methods in Applied Mechanics and Engineering,* vol. 193, pp. 1-23, 1 2004.

[55] M. A. Fernández and J.-F. Gerbeau, Algorithms for fluid-structure interaction problems, Springer Milan, 2009, pp. 307-346.

[56] S. Piperno, C. Farhat and B. Larrouturou, "Partitioned procedures for the transient solution of coupled aroelastic problems Part I: Model problem, theory and two-dimensional application," *Computer Methods in Applied Mechanics and Engineering,* vol. 124, pp. 79-112, 6 1995.

[57] C. A. Felippa, K. C. Park and C. Farhat, "Partitioned analysis of coupled mechanical systems," *Computer Methods in Applied Mechanics and Engineering,* vol. 190, pp. 3247-3270, 3 2001.

[58] M. E. Moghadam, I. E. Vignon-Clementel, R. Figliola and A. L. Marsden, "A modular numerical method for implicit 0D/3D coupling in cardiovascular finite element simulations," *Journal of Computational Physics,* vol. 244, pp. 63-79, 7 2013.

[59] M. A. Fernández, "Coupling schemes for incompressible fluid-structure interaction: implicit, semi-implicit and explicit," *SeMA Journal,* vol. 55, pp. 59-108, 9 2011.

[60] W. A. Wall, D. P. Mok, J. Schmidt and E. Ramm, Partitioned Analysis of Transient Nonlinear Fluid Structure Interaction Problems Including Free Surface Effects, Springer Berlin Heidelberg, 2000, pp. 159-166.

[61] P. L. Tallec and J. Mouro, "Fluid structure interaction with large structural displacements," *Computer Methods in Applied Mechanics and Engineering,* vol. 190, pp. 3039-3067, 3 2001.

[62] L. Formaggia, A. Quarteroni and C. Vergara, "On the physical consistency between three-dimensional and one-dimensional models in haemodynamics," *Journal of Computational Physics,* vol. 244, pp. 97-112, 7 2013.

[63] P. Reymond, P. Crosetto, S. Deparis, A. Quarteroni and N. Stergiopulos, "Physiological simulation of blood flow in the aorta: Comparison of hemodynamic indices as predicted by 3-D FSI, 3-D rigid wall and 1-D models," *Medical Engineering & Physics,* vol. 35, pp. 784-791, 6 2013.

[64] A. Quarteroni, S. Ragni and A. Veneziani, "Coupling between lumped and distributed models for blood flow problems," *Computing and Visualization in Science,* vol. 4, pp. 111-124, 12 2001.

[65] K. Laganà, R. Balossino, F. Migliavacca, G. Pennati, E. L. Bove, M. R. Leval and G. Dubini, "Multiscale modeling of the cardiovascular system: application to the study of pulmonary and coronary perfusions in the univentricular circulation," *Journal of Biomechanics,* vol. 38, pp. 1129-1141, 5 2005.

[66] H. Gharahi, B. A. Zambrano, D. C. Zhu, J. K. DeMarco and S. Baek, "Computational fluid dynamic simulation of human carotid artery bifurcation based on anatomy and volumetric blood flow rate measured with magnetic resonance imaging," *International Journal of Advances in Engineering Sciences and Applied Mathematics,* vol. 8, pp. 46-60, 2 2016.

[67] A. Jonášová and J. Vimmr, "Noninvasive assessment of carotid artery stenoses by the principle of multiscale modelling of non-Newtonian blood flow in patient-specific models," *Applied Mathematics and Computation,* vol. 319, pp. 598-616, 2 2018.

[68] E. Lo, L. Menezes and R. Torii, "Impact of Inflow Boundary Conditions on the Calculation of CT-Based FFR," *Fluids,* vol. 4, p. 60, 3 2019.

[69] P. D. Morris, D. Ryan, A. C. Morton, R. Lycett, P. V. Lawford, D. R. Hose and J. P. Gunn, "Virtual Fractional Flow Reserve From Coronary Angiography: Modeling the

Significance of Coronary Lesions," *JACC: Cardiovascular Interventions,* vol. 6, pp. 149-157, 2 2013.

[70] P. Causin, J. F. Gerbeau and F. Nobile, "Added-mass effect in the design of partitioned algorithms for fluid–structure problems," *Computer Methods in Applied Mechanics and Engineering,* vol. 194, pp. 4506-4527, 10 2005.

[71] C. Förster, W. A. Wall and E. Ramm, "Artificial added mass instabilities in sequential staggered coupling of nonlinear structures and incompressible viscous flows," *Computer Methods in Applied Mechanics and Engineering,* vol. 196, pp. 1278-1293, 1 2007.

[72] A. G. Brown, "Patient-specific Local and Systemic Haemodynamics in the Presence of a Left Ventricular Assist Device," 2012.

[73] A. C. L. Barnard, W. A. Hunt, W. P. Timlake and E. Varley, "A Theory of Fluid Flow in Compliant Tubes," *Biophysical Journal,* vol. 6, pp. 717-724, 11 1966.

[74] T. J. R. Hughes and J. Lubliner, "On the one-dimensional theory of blood flow in the larger vessels," *Mathematical Biosciences,* vol. 18, pp. 161-170, 10 1973.

[75] J. R., "Recherches sur la courbe que forme une corde tenduë mise en vibration"," *Histoire de l'académie royale des sciences et belles lettres de Berlin,* vol. 3, pp. 214-219, 1747.

[76] Y. C. Fung, P. Tong and X. Chen, Classical and Computational Solid Mechanics, WORLD SCIENTIFIC, 2015.

[77] D. Bessems, C. G. Giannopapa, M. C. M. Rutten and F. N. Vosse, "Experimental validation of a time-domain-based wave propagation model of blood flow in viscoelastic vessels," *Journal of Biomechanics,* vol. 41, pp. 284-291, 1 2008.

[78] C. G. Giannopapa, J. M. B. Kroot, A. S. Tijsseling, M. C. M. Rutten and F. N. Vosse, "Wave Propagation in Thin-Walled Aortic Analogues," *Journal of Fluids Engineering,* vol. 132, 2 2010.

[79] D. Lesage, E. D. Angelini, I. Bloch and G. Funka-Lea, "A review of 3D vessel lumen segmentation techniques: Models, features and extraction schemes," *Medical Image Analysis,* vol. 13, pp. 819-845, 12 2009.

[80] W. Kroon, W. Huberts, M. Bosboom and F. Vosse, "A Numerical Method of Reduced Complexity for Simulating Vascular Hemodynamics Using Coupled 0D Lumped and 1D Wave Propagation Models," *Computational and Mathematical Methods in Medicine,* vol. 2012, pp. 1-10, 2012.

[81] G. J. Langewouters, K. H. Wesseling and W. J. A. Goedhard, "The static elastic properties of 45 human thoracic and 20 abdominal aortas in vitro and the parameters of a new model," *Journal of Biomechanics,* vol. 17, pp. 425-435, 1 1984.

[82] F. Chinesta, R. Keunings and A. Leygue, The Proper Generalized Decomposition for Advanced Numerical Simulations, Springer International Publishing, 2014.

[83] C. Maccone, Ed., A simple introduction to the KLT (Karhunen—Loève Transform), Springer Berlin Heidelberg, 2009, pp. 151-179.

[84] H. Abdi and L. J. Williams, "Principal component analysis," *Wiley Interdisciplinary Reviews: Computational Statistics,* vol. 2, pp. 433-459, 6 2010.

[85] B. K. D. R. Hill, Elementary Linear Algebra, Prentice Hall, 2003.

[86] J. L. Lumley, "The structure of inhomogeneous turbulent flows," *Atmospheric Turbulence and Radio Wave Propagation, Moskow,* vol. ed by A. M. Yaglom and V. I. Tatarsky, pp. 166-178, 1967.

[87] E. Balmès, "PARAMETRIC FAMILIES OF REDUCED FINITE ELEMENT MODELS. THEORY AND APPLICATIONS," *Mechanical Systems and Signal Processing,* vol. 10, pp. 381-394, 7 1996.

[88] M. Frangos, Y. Marzouk, K. Willcox and B. B. Waanders, Surrogate and Reduced-Order Modeling: A Comparison of Approaches for Large-Scale Statistical Inverse Problems, John Wiley & Sons, Ltd, 2010, pp. 123-149.

[89] G. Berkooz, P. Holmes and J. L. Lumley, "The Proper Orthogonal Decomposition in the Analysis of Turbulent Flows," *Annual Review of Fluid Mechanics,* vol. 25, pp. 539-575, 1 1993.

[90] A. Chatterjee, "An Introduction to the Proper Orthogonal Decomposition.," *Current Science,* vol. 78, pp. 808-817, 2000.

[91] C. Eckart and G. Young, "The approximation of one matrix by another of lower rank," *Psychometrika,* vol. 1, pp. 211-218, 9 1936.

[92] M. B. Salem and L. Tomaso, "Automatic selection for general surrogate models," *Structural and Multidisciplinary Optimization,* vol. 58, pp. 719-734, 2 2018.

[93] S. Kamath, "Observations on the length and diameter of vessels forming the circle of Willis.," *Journal of anatomy,* vol. 133, pp. 419-423, 1981.

[94] J. E. Hall, Guyton and Hall Textbook of Medical Physiology, Elsevier LTD, Oxford, 2015.